Advancements in image sensor technology for soft X-ray spectroscopy in space: CIS detectors for the Auroral X-ray Imaging Spectrometer

Lawrence Stretton Jones

A thesis presented for the degree of

Doctor of Philosophy

Centre for Electronic Imaging

School of Physical Sciences

The Open University

June 2023

Abstract

Soft X-rays with energies below 2 keV are of tremendous scientific utility for planetary science but are particularly challenging to detect and analyse due to their low energies and short attenuation lengths. Solid state image sensor based X-ray detectors, derived from charge coupled devices (CCDs) and CMOS image sensors (CISs), have the potential to capture information about a soft X-ray flux in the time, spatial, and energy domains, and so are a potent scientific tool. Developing X-ray detector technology is enabling the application of soft X-ray imaging spectrometers in ever more demanding environments, with the current state of the art CIS promising the potential for high temperature, Fano-limited, performance.

This thesis investigates the use of solid state image sensors for soft- X-ray imaging spectroscopy in space-based applications. Specifically: an evaluation of the radiation damage experienced by the swept charge devices (SCDs) of the Chandrayaan-2 Large Area Soft X-ray Spectrometer (CLASS) which was shown to be within expectations and consistent with the requirements for continued science operation; and a study of X-ray detectors for the Auroral X-ray Imaging Spectrometer (AXIS) instrument aboard the Disturbed and quiet-time Ionosphere System at High Altitudes (DISHA) mission, resulting in the adoption of a novel CIS X-ray detector into the instrument design.

The AXIS study has found that the newly developed CISs are now equal to their CCD counterparts in some soft X-ray imaging spectroscopy applications, potentially enabling new science targets to be pursued. The successful recommendation to change the AXIS instrument X-ray detector from the more mature EMCCD CCD201-20 of the baseline design, to the less mature but better performing CIS221-X and its derivatives represents a milestone in the development of CIS X-ray detector technology.

Declaration

I hereby declare that no part of this thesis has been previously submitted to this or any other university as part of any other degree or professional qualification. This thesis has been wholly written by the undersigned, except for colleagues and others acknowledged in the text.

Lawrence Jones

2023

Dedication

To the team, gang, and soc.

Acknowledgements

Firstly, soft X-ray photons everywhere, who have done the thesis' *e-V* lifting, providing both puzzles and answers for three years most successfully.

Thanks also to the STFC and the Open University for their support, and studentship.

The contribution of my supervisors has been particularly heroic over a turbulent period. A leviathan thanks to Chiaki Crews, for sticking through the entire project, and to Andrew Holland for providing the nudges required to make sure good science was happening. Similar thanks to James Ivory for agreeing to be added to the team late on and providing the CIS expertise needed to work out what we were seeing with AXIS. Thank you to the sadly transient members, Matthew Soman, who rescued the project from disaster with a suggestion, and mission-proposal, involving pinholes and X-rays before swooping into the sunset, to Nathan Bush who did similarly, and James Endicott who put up with more rounds of 'graph-mageddon' than anyone should have to experience. Finally, to Konstantin Stefanov, who has been enormously generous with his time, knowledge, and experience.

Thank you to other members of the CEI who have been especially helpful, Tom Buggey, Ben Dryer, Oliver Heatherington, Anton Lindley-DeCaire, Tim Arnold, Zoe Lee-Payne, and Artur Klarecki.

A special thanks must go to the student cohort in SPS over the 2019-2023 period for helping hold the world together. I'll have missed some of you but thanks to: Saad Ahmed, Dan Evans, Bradley Kelman, Charlie Townsend-Rose, Imane Dazzazi, Harry Fox, Josh Wilde, Tara Hayden, Ben Man, Samuel Jackson, Lynge Lauritsen, Zak Smith, Tim Leese and of course Siobhan Patrick. Also to Ben Rozitis for the many PB-breaking training runs.

Finally thank you to my family for always being excited by (and supportive of) the increasingly obscure experiments and science.

Contents

Acronyms and Abbreviations

APS	-	Active Pixel Sensor
ATHENA	-	Advanced Telescope for High Energy Astrophysics
AXIS	-	Auroral X-ray Imaging Spectrometer
BDR	-	Baseline Design Review
BESSY II	-	Berlin Electron Storage Ring for Synchrotron Radiation
BOL	-	Beginning Of Life
BSI	-	Back Side Illuminated
C1XS	-	Chandrayaan-1 X-ray Spectrometer
CCD	-	Charge Coupled Device
CF	-	Con Flat (vacuum flange standard)
CGI	-	CoronaGraph Instrument (of Nancy Grace Roman Space Telescope)
CIS	-	CMOS Image Sensor
CLASS	-	Chandrayaan-2 Large Area Soft X-ray Spectrometer
CMOS	-	Complementary Metal Oxide Semiconductor
COTS	-	Commercial Off The Shelf
CTI	-	Charge Transfer Inefficiency

D-CIXS	-	Demonstration of a Compact Inexpensive X-ray Spectrometer
DISHA	-	Disturbed and quiet time Ionosphere-thermosphere System at High Altitudes
EMCCD	-	Electron Multiplying CCD
EOL	-	End of Life
FPGA	-	Field Programmable Gate Array
FSI	-	Front Side Illuminated
GEO	-	Geosynchronous Earth Orbit
GRB	-	Gamma Ray Burst
JANUS	-	Jovis, Amorum ac Natorum Undique Scrutator
JUICE	-	JUpiter ICy moons Explorer
LEO	-	Low Earth Orbit
NEIL	-	Non ionising energy loss
NGRST	-	Nancy Grace Roman Space Telescope
PTB	-	Physikalisch-Technische Bundesanstalt
QE	-	Quantum Efficiency
SAA	-	South Atlantic Anomaly
SBC	-	Supplementary Buried Channel
SCD	-	Swept Charge Device
SEE	-	Single Event Effect
SEGR	-	Single Event Gate Rupture
SEL	-	Single Event Latchup
SEU	-	Single Event Upset
SMILE	-	Solar Magnetosphere Ionosphere Link Explorer
SPENVIS	-	SPace ENVironment Information System
SWCX	-	Solar Wind Charge eXchange
T-e2v	-	Teledyne e2v
THESEUS	-	Transient High-Energy Sky and Early Universe Surveyor

1 Introduction

1.1 Summary

The constant development of image sensor technology is enabling more and more demanding X-ray spectroscopy to be conducted in the space environment. The arrival of X-ray optimised CMOS image sensors (CIS) has the potential to fulfil the requirements for moderate energy resolution imaging spectroscopy at very soft X-ray energies, while also introducing much improved radiation tolerance and higher frame rates than the more proven charge coupled device (CCD) technology. This thesis is largely focussed on the initial stages of the investigation into X-ray detectors for the Auroral X-ray Imaging Spectrometer (AXIS) instrument aboard the Disturbed and quiet-time Ionosphere System at High Altitudes (DISHA) mission, in which a CIS and an electron multiplying CCD (EMCCD) have both been considered. This is prefaced with the evaluation of radiation damage in the Chandrayaan-2 Large Area Soft X-ray Spectrometer (CLASS), an active instrument utilising swept charge devices (SCDs), a CCD derivative that makes drastic design compromises to achieve the same results now being demonstrated by CISs. Ultimately, it is the conclusion of this body of work that newly developed CISs are now equal to their CCD counterparts in some soft X-ray imaging spectroscopy applications, potentially enabling new science targets to be pursued.

This is not a sudden development; the gradual improvement of CIS technology has brought them closer and closer to parity with CCD quality. This has been largely driven by improvements in manufacturing techniques and quality reducing the sources of noise, reducing the contribution of manufacturing non-uniformities, in CISs. Though presented as different technologies, ultimately all X-ray detectors considered within this body of work rely on the same basic processes. The collection of photo-generated charge, localisation of this charge within pixels, and conversion to voltage for readout is common to all detectors considered. CCDs achieve this with a minimum number of active components resulting in high uniformity and low complexity. CISs use higher complexity resulting in a

lower reliance on large, finely tuned, custom, analogue structures, enabling their implementation in commercial CMOS processes. The improvement in manufacturing to the point of mitigating the increased implementation complexity has enabled CIS to achieve performance approaching that of the simpler CCD, but with additional benefits.

Soft X-ray imaging spectroscopy has many scientifically useful applications, though the instruments of this thesis will address only two. At soft X-ray energies (roughly 100 eV to a few thousand eV), many physical processes can be identified uniquely from the energy of emitted photons. Specifically, electron transitions to the K-shell of all elements with atomic numbers from 7 (nitrogen) to 32 (germanium) produce X-rays in the 0.3-10 keV range. The CLASS instrument has used this to map the surface abundance of many lighter elements across the surface of the moon from orbit, taking advantage of surface excitation by solar radiation. The AXIS instrument will make similar observations of excitation in the Earth's auroral regions to answer questions related to aeronomy (the study of the high atmosphere) and the composition of the inner Van Allen belt.

Capturing information about the energy, time and location of each detected X-ray is demanding for any sensor. Forgoing wavelength dispersive mechanisms in an instrument limits energy resolution due to the inclusion of Fano noise associated with charge generation by X-rays, while time and positional information often requires a careful trade-off between spatial resolution and signal to noise ratio in the data. However, such is the density of information available that any improvements in detector technology are often directly translated into improved science results. This is demonstrated well by CLASS, which (and whose predecessors, back to the early space age) has turned key performance improvements into brand new detection and mapping capabilities. The translation of technology to science improvement is promising for AXIS, which may be able to harness improvements in CIS technology to achieve its science aims.

This thesis begins with an overview of the AXIS instrument in chapter 2, its science goals and baseline design from which the work of this thesis has followed. Chapter 3 is an overview of solid-state image sensor technology, including detail on physical mechanisms enabling the detection of incoming photons, the various architectures employed by these sensors and finally the various noise sources encountered when using a sensor of this type. Chapter 4 outlines the use of solid-state sensors for the detection of X-rays in a photon counting mode, including the changes from the general case of chapter 3 and the additional sources of uncertainty. This chapter also covers the nature and effect of radiation damage on solid state image sensors, the chief challenge faced when designing space-based detectors. Chapter 5 covers the evaluation of the CCD236 SCDs aboard CLASS, and the measurements of

radiation damage in these detectors. Chapters 6, 7 and 8 focus on the X-ray detector of the AXIS instrument. Chapter 6 records the initial X-ray detector trade-off and the first demonstration of CIS suitability for AXIS and finally chapters 7 and 8 cover the further measurements and analysis of device behaviour used to follow up some of the outstanding questions posed by the work of chapter 6.

The primary outcome of the body of work represented by this thesis has been the successful recommendation to change the AXIS instrument X-ray detector from the higher technology readiness level (TRL) EMCCD CCD201-20 of the 2019 baseline design, to the lower TRL but better performing CIS221-X and its derivatives. This represents a milestone in the development of CIS X-ray detector technology and is expected to contribute to the continuing maturation and adoption of CIS X-ray detectors.

1.2 Research goals

The work of this thesis ultimately aimed to identify and test an X-ray detector for the AXIS instrument. For AXIS the research goals were to:

- Complete trade-off of different X-ray detectors for the AXIS instrument:
    - Use, and build, theoretical models to permit comparison of detectors of dissimilar technologies.
    - Perform demonstration testing of specimen X-ray detectors.
- Upon identifying the CIS221-X as the preferred X-ray detector for AXIS:
    - Verify energy resolution and charge collection properties to confirm benefits of novel pixel design features.
    - Provide an initial estimate of maximum CIS221-X operating temperature for AXIS.

Analysis of the CLASS SCDs did not fit into this line of work directly, however work for CLASS greatly informed the AXIS X-ray detector investigation and provided a demonstration of X-ray detectors in the space environment. For CLASS the research goals were to:

- Measure performance degradation of CCD236 and compare the measured values to pre-launch predictions.
- Inform continued science operation by identifying and accounting for the emergence of undesired performance.

1.3 Publications arising from this work

Jones, L. S., C. Crews, J. Endicott, and A. D. Holland. 2022. “Evaluation of the Performance of the CCD236 Swept Charge Devices in Lunar Orbit Using In-Flight Data.” Journal of Instrumentation 17(07):C07013.

Jones, L. S., C. Crews, M. Soman, J. Ivory, and A. D. Holland. 2022. “Evaluation of Sensors for the Detection of Energy Resolved Very Soft X-Ray Fluorescence.” P. 43 in X-Ray, Optical, and Infrared Detectors for Astronomy X. Vol. 8848, edited by Andrew D. Holland and J. Beletic. SPIE.

Townsend-Rose, C., Buggey, T. W., Ivory, J., Stefanov, K. D., **Jones, L. S**., Hetherington, O., & Holland, A. D. 2023. “Characterization, quantum efficiency, and radiation hardness of a CMOS image sensor optimized for soft x-ray astronomy”. Optical Engineering + Applications, 12678–25. SPIE.

1.3.1 Technical notes

Open_AXIS_TN_01, *Detector trade-off study for the AXIS instrument on DISHA-H*, M. Soman, **L. Jones**

Open_AXIS_TN_02, *Experimental measurements with candidate detectors for the AXIS instrument on DISHA-H* M. Soman, **L. Jones**

Open_AXIS_TN_03*, Conclusions and Recommendations following initial study on candidate detectors for the AXIS instrument on DISHA-H*, C. Crews, **L. Jones**

2 The Auroral X-ray Imaging Spectrometer

This chapter covers the scientific background and starting point for the investigation of AXIS. This is intended to provide the context for the more detailed background of chapters 3 and 4, and investigations of following chapters. This chapter includes a summary of the current state of auroral X-ray observations, to which AXIS is intended to contribute, and the baseline design of the AXIS instrument, from which the work of this thesis has been derived.

2.1 Observations of the Earth's X-ray aurora

The study of the Earth's aurora permits investigations into space weather in the region it has greatest effect on modern infrastructure and impact on humans. Generated by the precipitation of energetic particles into the Earth's atmosphere, all parts of the spectrum of auroral electromagnetic emissions provide information on the magnetosphere and high atmosphere itself. Monitoring X-rays, however, has a major advantage over the more easily accessible optical emissions in that they can be observed on both the day and night sides of the Earth (Stadsnes et al., 1997).

The aurora is a consequence of radiation trapped in the innermost regions of the Earth's magnetosphere, the region defined by its magnetic field, interacting with the atmosphere. The Earth's magnetosphere, generated by the planet's internal magnetic dynamo (Schubert and Soderlund, 2011), and is heavily deformed by incoming solar radiation (Eastwood et. al. 2015). The boundary between the region dominated by the Earth's magnetic field and the surrounding volume dominated by the interplanetary magnetic field is labelled the magnetopause. In the direction of the sun, solar wind compresses and deforms the geomagnetic field, while away from the sun the magnetosphere extends into the geotail. At the poles of the magnetic field energetic particles can be transported down along the field lines which intersect the Earth's atmosphere, and surface, generating the auroras. These include particles previously trapped in the field (in the Van Allen belts, discussed later in section 4.5), and radiation that has been able to cross the magnetopause.

2. The Auroral X-ray Imaging Spectrometer

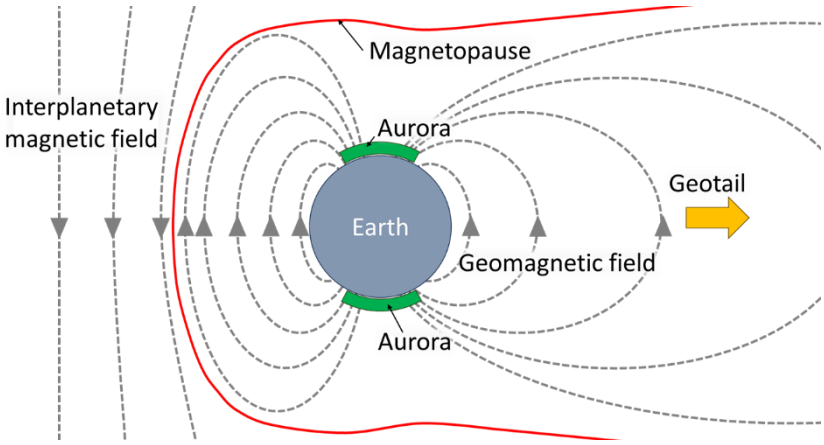

Figure 2.1. A simple diagram of the Earth's magnetosphere and major features relevant for this work including the Earth's auroras. Diagram is not to scale, additionly in reality the field is further distorted by the tilt of the Earth's magnetic field and the connection of interplanetary and geomagnetic field lines.

X-ray emissions from the aurora have two primary components in the soft X-ray range: fluorescence from atmospheric atomic species: nitrogen and oxygen; and bremsstrahlung emissions from the deceleration of electrons as they precipitate out of the inner Van Allen belt. Measurement of the bremsstrahlung spectrum can provide information on the energies of the electrons and the energy deposited by them into the high atmosphere (Luhmann, 1976; Luhmann & Blake, 1977). Resolving emissions spatially is expected to provide insights into the links between auroral spectral, spatial, and temporal behaviours and the solar wind, larger magnetospheric structures and the near Earth environment. Key observational goals of the instrument are to correlate solar wind and auroral behaviours and to observe the effects of magnetic reconnection on the Earth's nightside, by identifying precipitating electrons bouncing back from the geotail. Observations of neutral atom fluorescence are expected to permit the composition of the high atmosphere to be mapped, including the distribution of atomic species.

It is counter intuitivethat one of the most difficult X-ray auroras of the solar system to observe, in its entirety and at soft X-ray energies, is the Earth's (Branduardi-Raymont, 2017). This is largely because detailed observations require levels of performance commonly associated with astronomical telescope instruments while observing a target that is not an astronomical distance from the observing instrument, and therefore requiring an unusually large field of view. The other planets of the solar system have been the target of campaigns from various astronomical observatories. In particular, observations of Jupiter's X-ray aurora have helped determine the dynamics of the vast Jovian magnetosphere, providing insight into the current circulation methods and the role of the Jupiter's

satellites. This has required multiple observation campaigns from different missions including Chandra (Gladstone et al., 2002) (Figure 2.2) and XMM-Newton (Yao et al., 2021).

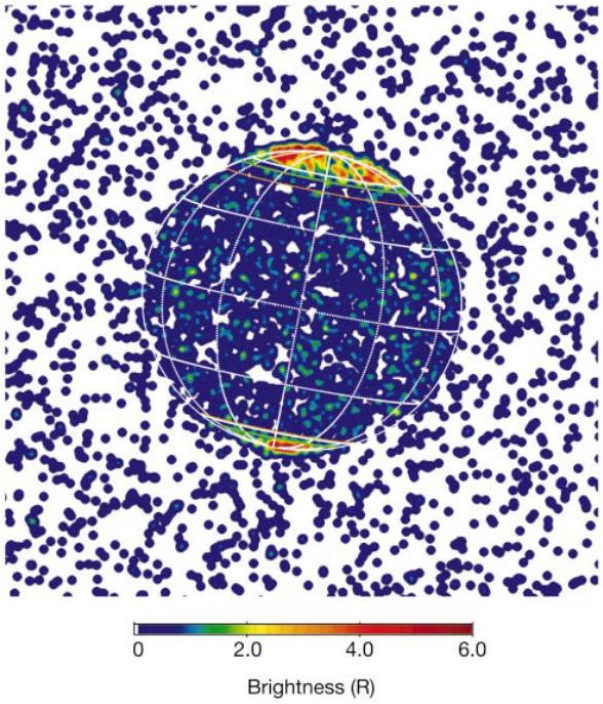

Figure 2.2. Jovian X-ray aurora observed by the Chandra X-ray Observatory. The instrument used for this observation did not have energy resolution capabilities. X-rays appearing beyond the disk of Jupiter are due to instrument and sky background sources. Figure credit: Gladstone et al. (2002), Figure 1.

Observation of the Earth's auroras, by contrast, are characterised by their easier accessibility, but lower availability of high quality, astronomical class, X-ray instruments. Early observations were made from balloons and sounding rockets, linking hard X-ray emissions (20 keV energy and greater) with solar and magnetospheric events (Stadsnes et al., 1997). Balloons permit observations without a rocket; however, their altitude limitations prevent them from observing X-rays of energies below 20 keV. Sounding rockets can avoid this limitation, though at the expense of far shorter observation periods (minutes) preventing sustained observations of anything but the shortest time-scale dynamics.

While satellite-based X-ray detectors had been used prior to 1996, the Polar Ionospheric X-ray Imaging Experiment (PIXIE) aboard Polar-1 (Imhof et al., 1995) was the first imaging camera placed in a high orbit to observe the entire auroral oval for long periods. Using a gas proportional counter and pinhole optic, PIXIE successfully observed the aurora from 1996 to 2008 at hard X-ray energies. The key science finding of PIXIE was the mapping of electron precipitation across the entire northern hemisphere (and

therefore energy deposition) (Østgaard et al., 2001). PIXIE's use of a gas proportional counter resulted in a lack of sensitivity to X-rays below 2 keV, though this was consistent with its goals for studying hard X-ray emissions between 2 keV and 60 keV.

In addition, there have been fortunate occasions when instruments intended for astronomy have been able to make key auroral observations. Of these the 1979 observation of electron precipitation by HEAO-1 and the 2004 observations of the northern auroral oval by the Chandra X-ray observatory are most relevant.

The High Energy Astronomical Observatory's (HEAO-1's) Cosmic X-ray instrument (Figure 2.3) operated in a pencil beam mode, with highly directional sensitivity (3^{o} FWHM) sweeping out the sky as the spacecraft spun, and using a proportional gas counter (Rothschild et al., 1978). This included unavoidable periods when the instrument was pointed at the Earth. The spacecraft was in a low inclination, near equatorial, orbit, and was thus unable to observe the polar aurorae, however it was able to discern emissions from low latitude regions (Figure 2.4), primarily at the conjugate point in the atmosphere from the South Atlantic Anomaly (SAA), which was understood to be a site of energetic particle precipitation into the atmosphere. The resulting data was used by Luhmann & Blake, (1977) to confirm and refine their bremsstrahlung emission models, subsequently widely used to link and describe the relationship between X-ray and electron populations.

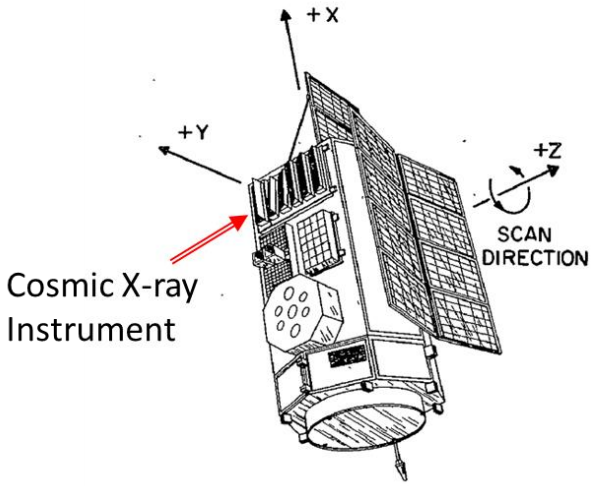

Figure 2.3. HEAO-1 with X-ray detectors (pointed along the +Y axis) and rotation axis marked. Six X-ray detectors tuned for different energy bands were used. These appear as the stack of boxes. Figure adapted from Figure 1 Rothschild et al. (1978).

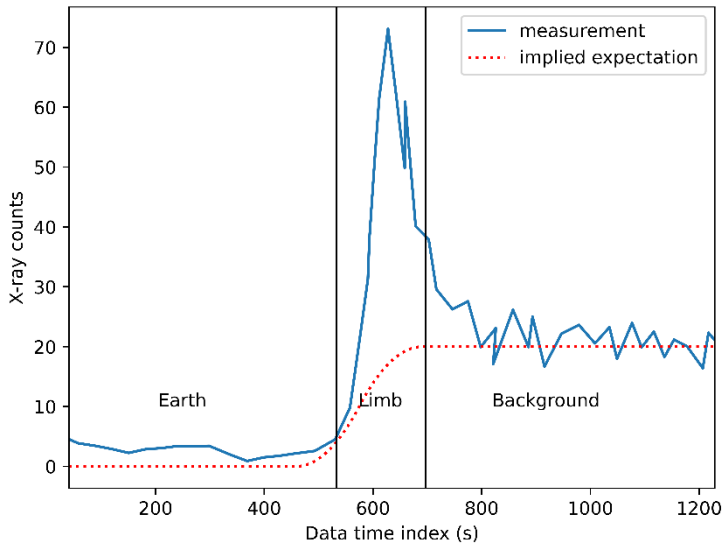

Figure 2.4. X-ray counts (all X-rays >150 eV) for altitude, measured by HEAO-1 on 20 September 1977, the expected X-ray behaviour has been indicated in red, and the three observation regimes highlighted: Earth, with very low counts; Limb, the atmospheric limb showing the observed excess of X-rays; and Background, background counts observed from astronomical sources. Because the instrument was rotating, the detector's field of view swept from the Earth to sky predictably with time. Figure adapted from Figure 2 of Luhmann et al. (1979).

Finally, in 2003 and 2004, key observations were made with the Chandra space telescope observing X-ray emission in the auroral regions (Bhardwaj et al., 2007). These observations used the High Resolution Camera (HRC) instrument, which itself uses a microchannel plate detector (MCP). This instrument was sensitive to X-rays between 0.1 keV and 10 keV, though lacked photon energy discrimination. Chandra was not designed for Earth observation, so the observations were achieved by pointing the telescope at a point behind the Earth on the celestial sphere and letting the Earth drift through the field of view while Chandra was at apogee. As well as providing information on the spatial distribution of X-ray fluorescence (Figure 2.5), the X-ray emissions were compared to electron precipitation spectra collected from under-flying earth observation satellites. These observations were used to strengthen the conclusion that the Earth's auroral X-ray emissions are largely the result of electron precipitation, rather than of heavy ions. However, the lack of energy resolution and limited number of observations left open questions concerning the relationship between atmospheric species fluorescence and electron bremsstrahlung contributions to overall X-ray production, and the variability of auroral soft X-ray emissions over short and medium timescales.

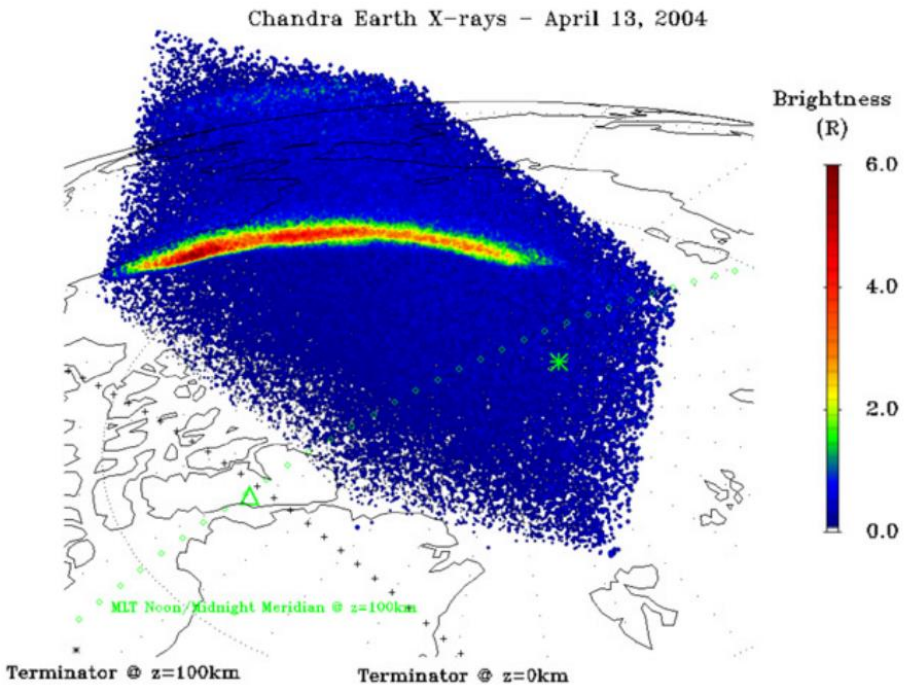

Figure 2.5. Auroral X-ray emissions observed by the Chandra HRC. Figure credit: Bhardwaj et al. (2007)

These are the science and observational gaps that AXIS seeks to address. A modern, dedicated, instrument capable of improving spatial and energy resolution of observations of the X-ray aurora at softer energies promises to improve our understanding of it and related phenomena. X-ray emissions in the 0.3 keV to 2 keV band are known to exist, and their properties have been predicted, however they are yet to be observed over long periods of time. By harnessing recent improvements in X-ray detector technology, AXIS is seeking to complete such observations with sufficient resolution in the energy (to resolve atmospheric fluorescence and bremsstrahlung) and spatial (to identify the origin of emissions within auroral structures) domains in a platform that can be dedicated to auroral science and aeronomy, ensuring adequate coverage in the time domain too.

2.2 AXIS baseline design

The starting point for investigations into the AXIS instrument was the baseline design approved as part of the Baseline Design Review (BDR) in 2019, described in Narendranath (2019) and summarised in Table 2.1. This called for an EMCCD, the CCD201-20, operating in photon-counting mode with spatial resolution provided by a 100 µm pinhole aperture (Figure 2.6). The design is intended to maximise spatial coverage and X-ray sensitivity while providing coarse spatial resolution to discriminate the location of auroral emission features.

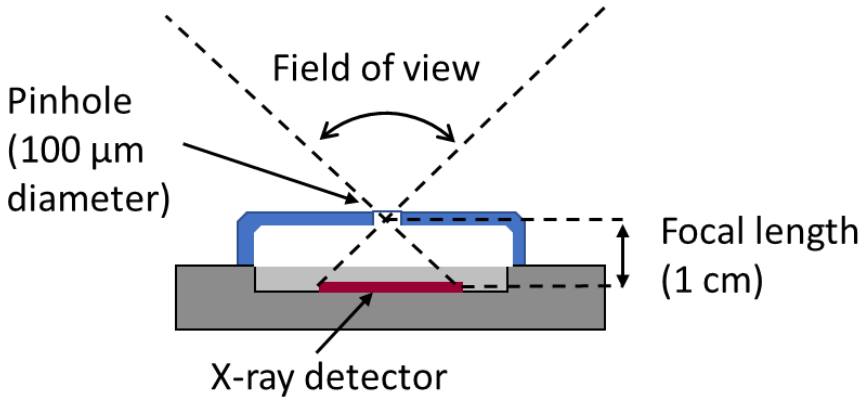

Figure 2.6. BDR design of the AXIS instrument of the DISHA mission.

In order to observe the desired spectral features, the instrument will be required to be sensitive across a range from 300 eV to 2000 eV with an energy resolution of no more than 100 eV at 500 eV. This is specifically to enable the separation of oxygen and nitrogen fluorescence, at 390 eV and 520 eV respectively. To screen optical light from the X-ray detector the instrument will incorporate an aluminium optical blocking filter (OBF), deposited directly on the X-ray detector itself. There is a direct trade-off between optical opacity and soft X-ray transmission for the optical blocking filter, therefore the deposited aluminium filter is expected to be made as thin as possible.

The requirements for spatial resolution are less demanding, the baseline design calls for a footprint of 5 km per pixel, though this is largely derived from the pixel sizes of the baseline X-ray detector and expected satellite orbit. A 110 ° field of view (FOV) will enable observations to be made over a large portion of the Earth visible during auroral overflights.

A pinhole aperture was selected as it forms a real image with a large field of view. It also has no dependence of focal length on photon energy. Using a 100 µm pinhole and a 10 mm focal length, AXIS is expected to have a total footprint of 600 km from the intended satellite altitude.

The CCD201-20, an EMCCD, was selected as the AXIS X-ray detector. This detector has attributes favourable to the application. The suppression of readout noise by the EM register was expected to have multiple benefits. The most immediate of these was the lowered noise floor of the detector, enabling the detection of very soft X-rays whose charge can easily be lost below the floor. Furthermore, as will be discussed in chapter 3, the suppression of readout noise permits the CCD201-20 to operate at higher pixel readout rates than a conventional CCD. For AXIS this was seen as a particular advantage as higher readout rates have the potential to reduce the noise contribution from

optical light leaking through the OBF. A reduction in measured OBF leakage would permit a thinner OBF to be used, giving similar performance whilst increasing sensitivity at low X-ray energies. Devices related to the CCD201-20 have previously been tested at very soft X-ray energies and shown to have good sensitivity even at the lowest end of the energy range required (Moody et al., 2017). Additionally, development associated with this detector's use in the Nancy Grace Roman Space Telescope's (NGRST) Coronagraph Instrument (CGI) has raised its TRL (to TRL-6, the highest level before demonstration in space) and explored many of the detector attributes relevant for space based applications (Harding et al., 2015).

Table 2.1. Summary of AXIS baseline design parameters.

Parameter	**Unit**	**Value**
Sensitivity range	*eV*	300-2000
Energy resolution	*FWHM @ 500 eV, eV*	<100
Operating temperature	*^{o}C*	-80
QE	*%*	>65
X-ray detector		CCD201-20
Field of view	*^{o}*	110
Pixel FOV	*km*	5
Sensitive area	*mm*	13x13
Pinhole diameter	*µm*	100
Pinhole focal length	*mm*	10
Optical blocking filter		1200 Å Al
Aurora X-ray rate	*count/s*	8
SWCX X-ray rate	*count/s*	0.04
Power	*W*	15
Mass	*kg*	17

The contents of the following chapters have been derived from work to validate this baseline design, from the perspective of the X-ray detector. This has included investigations a trade-off study of X-ray detectors to replace the CCD201-20.

3 Solid state image sensors

Solid State Image Sensors rely on the photo-electric effect to generate charge in response to an external photon source. The many methods of collecting and measuring the generated charge define the various architecture categories.

The history of widespread scientific solid state image sensors began with the invention of the Charge Coupled Device (CCD) by Boyle and Smith in 1970 (Boyle & Smith, 1970), for which they won the Nobel Prize in 2009. For space-based observatories the CCD has been the dominant imaging technology since its use aboard the Hubble Wide Field and Planetary Camera 1 (Janesick, 2001). However, ongoing improvements in semiconductor manufacturing uniformity and quality have enabled a growing role for Active Pixel Sensors (APS), a more complex architecture with large improvement potential for radiation hardness and most frequently made with the Complementary Metal Oxide Semiconductor (CMOS) process (Fossum, 1997).

This chapter will outline the physics and design of solid state image sensors. Starting with a brief introduction into the background semiconductor mechanics, photoelectric effect, and common semiconductor structures; continuing with a description of the CCD architecture (and relevant variants), the CMOS image sensor (CIS) architecture; and ending with a description of the common sources of noise in a solid-state image sensor, many of which are architecture independent. This description will address the general use of these classes of photon-detector under ideal conditions, the use of solid-state image sensors for the detection of X-rays, and under the hostile conditions of the space environment are covered by the next chapter.

The slightly cumbersome term ‘solid state image sensor’ is inclusive of both the CCD and CIS architectures as many of the mechanics and behaviours of these sensors are shared, and the work detailed in later chapters uses both architectures. The CCD and CIS, when referring specifically to their ability to detect photons, have been labelled ‘detectors’ in this chapter, and specifically ‘X-ray detectors’ through the rest of the thesis. The word ‘device’ has been restricted to single simple semiconductor structures.

3.1 Semiconductors and basic structures

All X-ray detectors considered by this thesis make use of semiconductor materials, specifically silicon, and physical processes to efficiently store and manipulate photogenerated charge. The two charge transport mechanisms available to a semiconductor, that of drift in response to an external electric field, and diffusion in response to a concentration gradient of charge carriers, permit the creation of controllable switches, amplifiers and storage structures that are all crucial to the function of an image sensor. The following is an overview of semiconductor physics in its application in the design and operation of image sensors, for further information Sze, (1985), provides a more complete coverage of semiconductor physics and its applications.

Semiconductors are a class of solid materials with a crystal structure and defined by the size of the forbidden energy gap between the energy states of the two outermost electron shells of their constituent atoms: that of the valance band responsible for chemical bonding of atoms into the crystal structure; and the conduction band of delocalised electrons, with a higher energy than the valance band. In an electrically insulating material this gap can be very large indeed, requiring significant energy to promote electrons to states in which they can act as charge carriers, such that thermal excitation of carriers is exceedingly rare. Within an electrical conductor the gap can be very small to non-existent. For a semiconductor this gap is on the order of a few eV, for example in silicon it is 1.12 eV.

Charge carriers, in this case electrons, may be promoted (ionised) from the valance band to the conduction band with the input of energy. This energy can either imparted by a variety of means: thermally, using large electric fields, or (usefully for an image sensor) via the deposition of energy by a photon. For the detectors of this thesis the photon energy transfer mechanism is the photo-electric effect, first described by Einstein, (1905) for which he also won the Nobel Prize in 1921. Conduction band charges may move freely in response to an external electric field and thus permit drift charge transport, defined by equation (3.1) where J_e is the drift current density magnitude, μ_e is the electron mobility of the semiconductor, E is the magnitude of the applied electric field and q is the magnitude of the carrier charge.

$$J_e = -\mu_e E q \tag{3.1}$$

This description requires two qualifications. Firstly, silicon, the sole semiconductor of relevance for the image sensors of this thesis, is an indirect bandgap semiconductor. The band structure of a silicon crystal, when plotted in both energy and momentum coordinates (Figure 3.1), has a misalignment between the highest energy state of the valance band and lowest energy state of the conduction band.

Therefore, the promotion of charge carriers is most efficient with the introduction of additional momentum from a lattice vibration (phonon). This is not the case in direct band gap semiconductors, for example in the compound semiconductor gallium arsenide, where the highest valance and lowest conduction energy states are aligned, and a momentum change is not required. This distinction is most relevant for the detection of higher energy photons

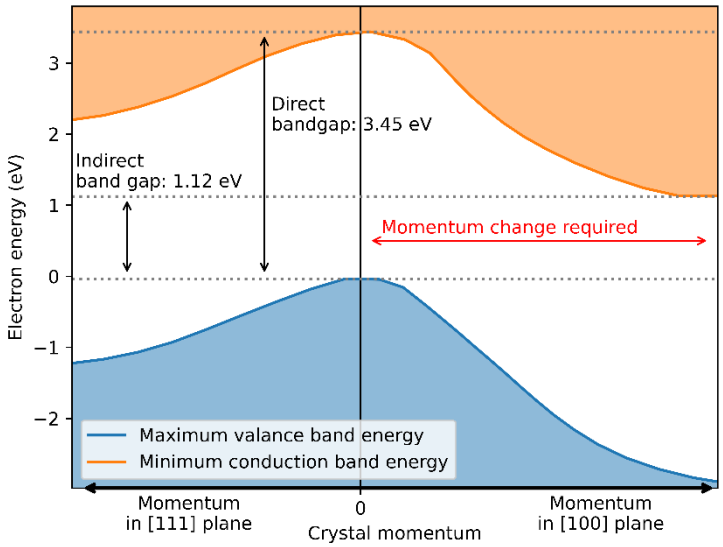

Figure 3.1. Energy-momentum band structure of intrinsic siliconshowing offset of conduction band minimum energy and valance band maximum energy. Adapted from Sze (1985) Fig. 1.12.

Secondly, the promotion of an electron occurs from a valance band covalent bond, and leaves behind a vacancy, or hole, where an electron could be. If an external electric field is applied to the semiconductor electrons will swap bond locations to fill the vacancy, in the same direction as the electrons flowing in the conduction band. This results in the hole travelling against the flow of valance electrons and practically acting as a charge carrier of the opposite (positive) charge. The hole carrier has similar properties, and behaviour with regards to drift current (equation (3.2)), to the negative electron charge carrier though generally hole mobility (μ_p) is far lower.

$$J_p = \mu_p E q \tag{3.2}$$

Under normal conditions the population of holes and electrons will be subject to random variations with thermal noise promoting carriers and electron-hole recombination maintaining an intrinsic carrier concentration n_i, which has a strong temperature dependence described

$$n_i^2 = \beta T^3 \, e^{-\frac{E_g}{kT}} \tag{3.3}$$

Where β is the product of the effective density of electron and hole states (a property of the semiconductor), E_g is the bandgap energy, k is the Boltzmann constant and T is the semiconductor temperature. The populations of holes and electrons will maintain equilibrium according to:

$$n_i^2 = n_e n_p \tag{3.4}$$

Which describes the intrinsic (n_i), electron (n_e) and hole (n_p) carrier concentrations.

In addition to drift current, charge carriers will also flow in response to their own concentration gradients:

$$J_e = \frac{\delta n_e}{\delta x} D_e q \tag{3.5}$$

$$J_p = -\frac{\delta n_p}{\delta x} D_p q \tag{3.6}$$

Introducing D_e and D_p the electron and hole diffusion coefficients respectively).

Diffusion current is readily exploited with the introduction of dopant impurity atoms to control the concentration gradients. Such dopants generally come from the two atomic groups neighbouring silicon's group IV. The dopant atoms substitute silicon atoms in the silicon crystal with either one too many (group V dopants) or one too few (group III dopants) valance electrons. The additional electron, or hole (absence of an electron), is very weakly bound and easily ionised resulting in an excess of charge carriers corresponding to the dopant type. Doped silicon is labelled according to the introduced charge carrier, n-type for the negative charge carriers introduced by a group V dopant, p-type for the positive charge carriers of group III dopant.

The main benefit of the dopant atoms is to introduce a population of charge carriers with a concentration largely independent of temperature, far larger than could be expected in an undoped, intrinsic, semiconductor. These introduced carriers are therefore said to the be the majority carriers (holes in p-type, electrons in n-type) while the opposite charge carriers are labelled the minority carriers. However, equation (3.4) is still valid. In an undoped silicon there is a large variation in the number of charge carriers with temperature, resulting in large changes in conductivity. In a doped region of silicon, the number of dopant-introduced charge carriers is fixed, and the minority charge carrier concentration will change instead. Because the minority charge carriers are not the primary

contributors to conductivity this in turn results in a far more stable material conductivity. This behaviour has limits at extremely low temperatures when the dopant charge carriers cannot be excited, and the semiconductor experiences 'freeze out', and also at very high temperature when the number of intrinsic carriers becomes comparable to the number of dopant carriers (Figure 3.2).

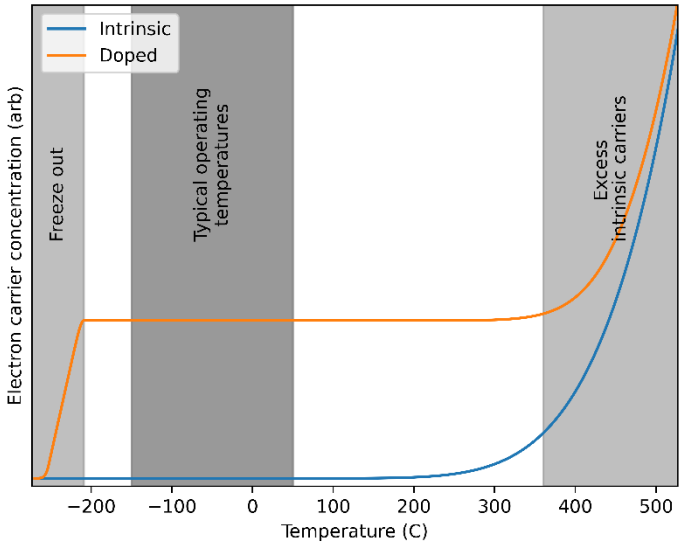

Figure 3.2. Intrinsic and extrinsic (doped) silicon conductivity for temperature. After Sze (1985) Fig. 1.23.

3.1.1 The MOS capacitor

The basic charge storage element for CCDs and CIS is the Metal Oxide Semiconductor (MOS) capacitor. In this structure a layer of oxide acts to electrically insulate a semiconductor from a metal contact. A large advantage when using silicon is the relative ease with which it oxidises to form silicon oxide, a highly effective insulator over which metal contacts can be readily applied. Applying a positive voltage to the metal contact will attract electrons in the semiconductor to the oxide-semiconductor interface, where they will combine with the dopant holes for a region depleted of holes (depleted region). Though this structure can be implemented in either polarity p-type silicon is by far the most common for CCDs and CISs.

The shape of the induced potential profile can be found by solving Poisson's equation in one dimension (equation (3.7)) for the semiconductor. In a standard p-type MOS capacitor, in the depletion region ($0 < x < x_p$) the space charge will be roughly equal to the acceptor dopant concentration (N_A), below the depletion region it will be equal to zero as there is charge neutrality:

$$\frac{d^2V}{dx^2} = \frac{\rho(x)}{\epsilon_s} \qquad \text{for } 0 < x < x_p \tag{3.7}$$

$$\frac{d^2V}{dx^2} = 0 \qquad \text{for } x > x_p \tag{3.8}$$

$$\rho(x) = qN_A \tag{3.9}$$

Where ϵ_s is the semiconductor (silicon) permittivity and $\rho(x)$ is the space charge density at a depth x below the insulator (Sze, 1985) (Figure 3.3). Making use of the fact that both the potential and electric field are continuous (that is $V(x)$ and $\frac{dV(x)}{dx}$ do not have discontinuities), that below the depletion region there is no net electric field and the potential is equal to the substrate voltage ($V(x_p) = V_{ss}$), and assuming that the oxide is thin $(V(0) \approx V_g)$:

$$V(x) = \frac{\rho(x)}{2\epsilon_s}x^2 - \frac{\rho(x)}{\epsilon_s}xx_p + V_g \tag{3.10}$$

Where:

$$x_p = \sqrt{\frac{2\epsilon_s}{\rho(x)}(V_g - V_{ss})} \tag{3.11}$$

The depletion region, in which there is a non-zero electric field, is highly useful for collecting free charge carriers produced by the photo electric effect, which will quickly flow via drift current.

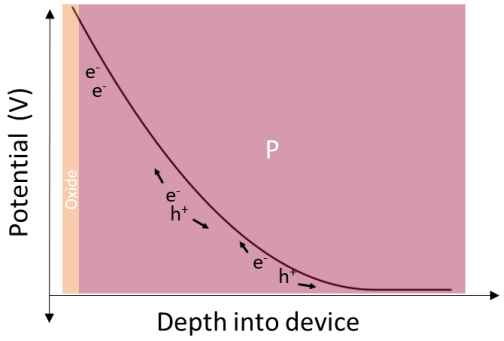

Figure 3.3. MOS capacitor showing accumulation of electrons.

An issue with the simple MOS structure is that collected charges are stored in a region immediately adjacent to the oxide interface. The interface between the silicon crystal lattice and silicon oxide leaves many vacant covalent bonds in the silicon crystal (Figure 3.4) that introduce mid-band gap energy states from which charge carriers can be more readily excited or absorbed.

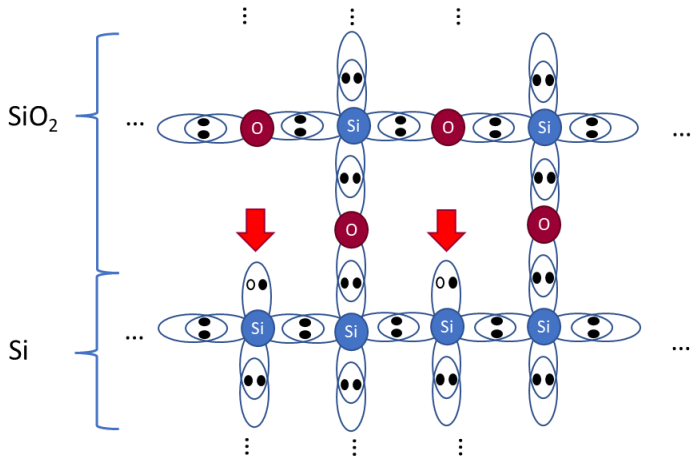

Figure 3.4. Silicon-silicon oxide interface with vacant bonds highlighted. Vacant bonds are also referred to as dangling bonds.

The solution commonly used is the introduction of a buried channel - a layer of n-type silicon between the oxide and p-type layer. Depletion of the new PN boundary means the n-region potential rises above the applied potential (voltage) of the gate, resulting in the profile of Figure 3.5, in which the photo-generated charge carriers (electrons) move upwards to the region of maximum potential, now separated from the traps at the oxide interface. This region is known as the buried channel because it has been moved away from the surface of the device. The buried channel implant size and dopant concentration are designed such that the entire thickness of the n-type layer is within the depletion region. This means that the initial, dopant introduced electrons will have diffused out of the buried channel and not interfere with the much smaller number of signal electrons.

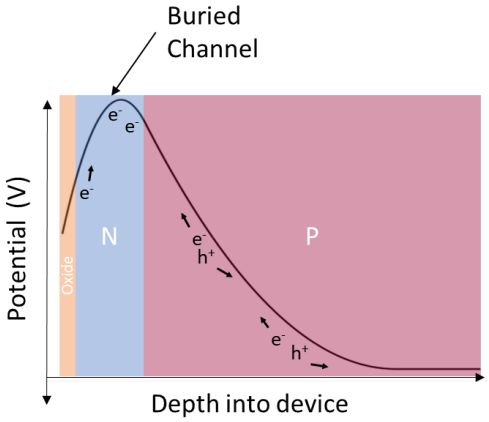

Figure 3.5. Schematic of electrical potential within a buried channel MOS capacitor.

However, this only solves half of the issue as the vacant oxide interface bonds are still free to act as sites of charge generation, greatly increasing the dark signal as discussed later (section 3.5.2). The

common mitigation for this is pinning - saturating the oxide interface with holes to suppress charge generation. This can be achieved either with a heavily p-doped (p^+) implant, or by introducing the holes electrically.

The former method is favoured by CIS because it can be achieved without the large clock amplitudes (> 5 V) used in CCDs. A heavily doped p-type implant will be added at the top of the pixel, forming a layer between the buried channel n-type region and the oxide interface. This also has the effect of decreasing the buried channel potential, a highly useful attribute for a CIS because this ensures that charge can be efficiently transferred into a readout circuit. For this reason almost all CIS will use pixels of a p^+-n-p pinned photodiode type (Stefanov 2022, pp. 2.11).

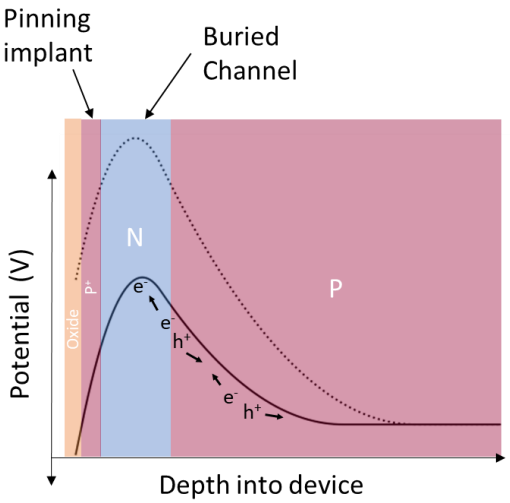

Figure 3.6. MOS capacitor with p^+ pinning implant showing movement of electrons and holes. Potential profile in absence of pinning implant has been included to demonstrate that this structure lowers the potential of the storage buried channel, making subsequent charge transfer more straightforward.

Alternatively, with control over both the oxide potential and substrate potential a CCD can simply raise the potential of the substrate until it is above that of the oxide. At this point holes will flow from the channel stop regions used to separate vertical columns of pixels where there is no buried channel acting as a potential barrier to the oxide interface where they act in much the same way as the p^+ implant. The new population of holes dominate over the n-type dopant electron carriers and invert the silicon polarity in a thin layer close to the oxide. For this reason, operating with the substrate potential raised in this way is known as inverted mode operation (IMO).

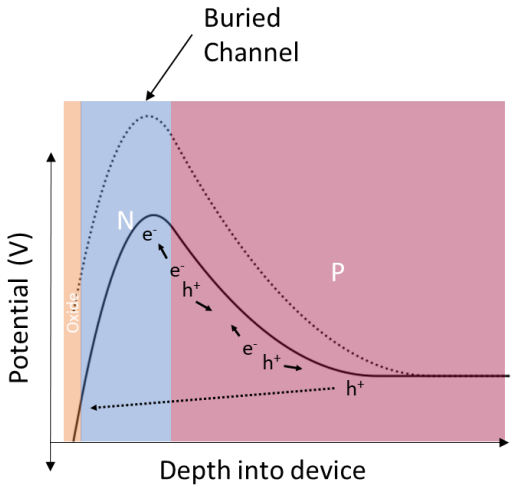

Figure 3.7. MOS capacitor in IMO showing movement of electrons and holes. For illustrative purposes a NIMO potential profile has been included with a matched substrate voltage to demonstrate reduced channel capacity. This profile is very similar to that of the pinned photodiode in Figure 3.6.

Both methods tend to reduce the capacity of the buried channel potential well. Therefore, in CCDs where large signals are expected inverted mode operation may not be used.

3.1.2 The MOSFET

The MOS field effect transistor (MOSFET), shown in Figure 3.8, is the primary active device encountered in the image sensors. When the gate is unbiased the region between the two n-wells acts as two back to back diodes and prevents the flow of charge from the source to drain terminals. However, by applying a sufficient, positive voltage to the gate terminal the silicon immediately beneath it becomes inverted as the gate potential attracts electrons and repels holes. This forms a conductive pathway between the two terminals through which current can flow. The conductance of the channel is controlled with the gate voltage.

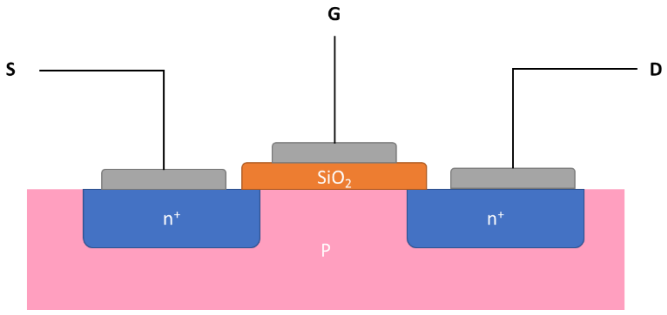

Figure 3.8. Basic structure of an n-channel MOSFET showing the two n-wells, the p-type substrate in which the inverted conductive channel is formed and the three terminals source (S), gate (G) and drain (D).

The channel formed beneath the gate is still resistive, therefore if the drain-source current is large a significant field can develop between the two n-wells. This will distort the distribution of charge carriers creating the conductive channel, leading to 'pinch off' effects. This will impede the flow of current, pushing the device into a saturation mode in which the current flowing between the source and drain terminals is largely independent of any small changes in V_{DS}.

In this saturation region the current flowing between the source and drain terminals is largely independent of the source drain voltage, and instead is dependent on the gate voltage and device properties. Equation (3.12) describes this relationship.

$$I_d = \frac{1}{2} k'_n \frac{W}{L} \left(V_{gs} - V_t\right)^2 \tag{3.12}$$

Where W and L are the physical width and length of the MOSFET charge conduction channel respectively, and V_t is the threshold voltage for the MOSFET below which the field of the gate is unable to form a conductive channel between the source and drain regions. k'_n is equal to $\mu_n C_{ox}$, the product of the MOS channel carrier mobility and the oxide capacitance per unit area, generally fixed by the manufacturing technology used (Sedra & Smith, 1998).

3.1.3 The Source Follower

The current produced by each pixel with a solid state image sensor is very small, even in image sensors collecting thousands of electrons and performing pixel readouts at MHz rates the maximum output current will be on the order of pico-amps.

Such small signals are prone to noise and can be hard to measure. It is therefore common practice to buffer signals prior to digitisation or transmission from the sensor chip. To conserve the limited number of electrons and provide sufficient gain the source follower is used (Figure 3.9 (a)), due to its very high input impedance. In this amplifier configuration an input voltage is applied to a transistor gate terminal, an output voltage is measured between the transistor source terminal and ground, effectively over a current sink that provides the transistor bias drain current.

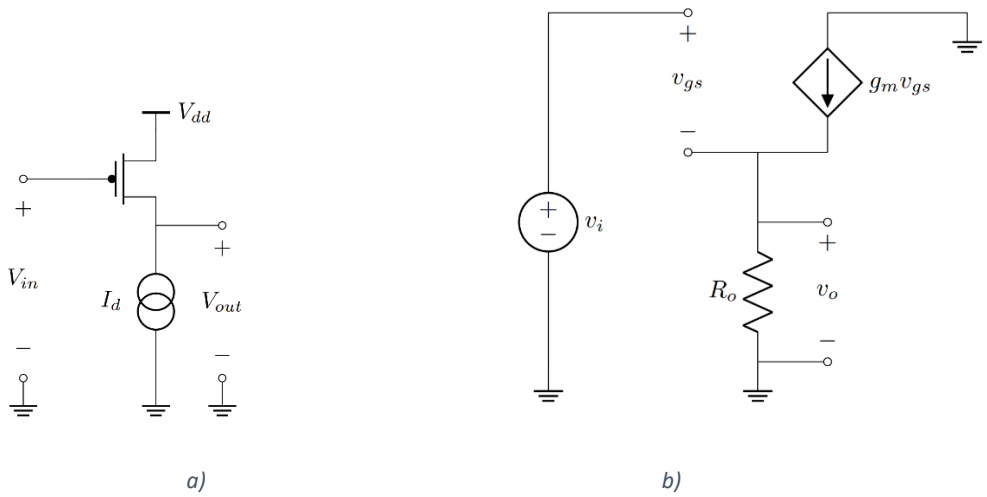

Figure 3.9 The source follower amplifier a) component circuit diagram and b) small signal equivalent circuit diagram (using the hybrid pi model for the transistor).

From Figure 3.9 (b):

$$v_o = R_o g_m v_{gs} \tag{3.13}$$

$$v_o = v_i - v_{gs} \tag{3.14}$$

Therefore, the voltage transfer function of the source follower is:

$$\frac{v_o}{v_i} = \frac{R_o g_m}{R_o g_m + 1} \tag{3.15}$$

Which is approximately equal to unity. However, the input impedance of the circuit is effectively infinite, buffering the input terminal from the output terminal. This is used in an image sensor to convert signal charge, as small as ones or tens of electrons, into voltage signals that can be used to drive output circuits, such as further amplifiers or ADCs. As the first stage of the readout electronics chain the source follower has the greatest impact on image sensor performance and is the primary source of electronics noise. Because of the noise susceptibility of the buffering stage, it is usually necessary to implement it embedded within the rest of the image sensor, as opposed to externally 'off-chip'. The source follower circuit is a simple structure that can be built within an image sensor to provide the required high gain.

3.2 The CCD

CCDs represent the current incumbent technology for space based instruments. Operating to read the charge through a single readout node (or one of very few nodes) they permit a high degree of photo response uniformity. The following is a brief description of the CCD architecture highlighting elements

relevant for this thesis. For more information Janesick (2001) provides a complete description of CCDs and their behaviours. In the archetypal CCD, displayed in Figure 3.10, packets of electrons produced by incoming photons are moved through the CCD, transferring the contents of one row of pixels to the next, until they reach the final row. From this final row they are transferred into a serial register, which moves packets horizontally until the readout circuit is reached.

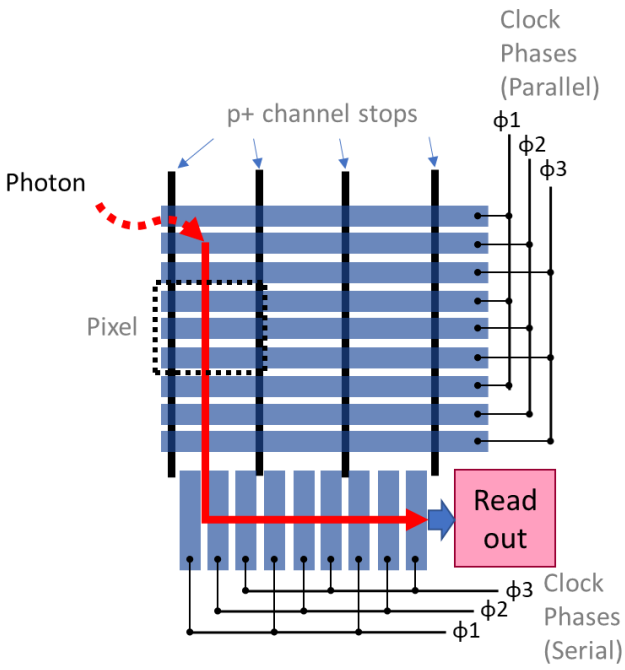

Figure 3.10. An example CCD showing the readout path for the charge collected in a pixel. Charge is initially confined to a pixel region by clock potentials and p^+ implant channel stops.

The charge collected in each pixel in the image area is confined to its original column by "channel stops" of p-type implant separating the vertical buried channels as per Figure 3.10. Both diagrams show a three phase CCD, which is the minimum number of phases in a CCD to ensure that the potential wells are always kept separate and control the direction of the charge movement. Two phase CCDs are possible with the introduction of intra-phase implant structures to direct charges. A greater number of phases can be used if higher full well capacity is required.

Raising a clock potential creates a storage well into which signal photo-electrons can flow. By pulsing the clock voltages on each of the three clock electrodes signal electrons can be confined to a single potential well that is gradually moved across the pixel array (illustrated in Figure 3.11).

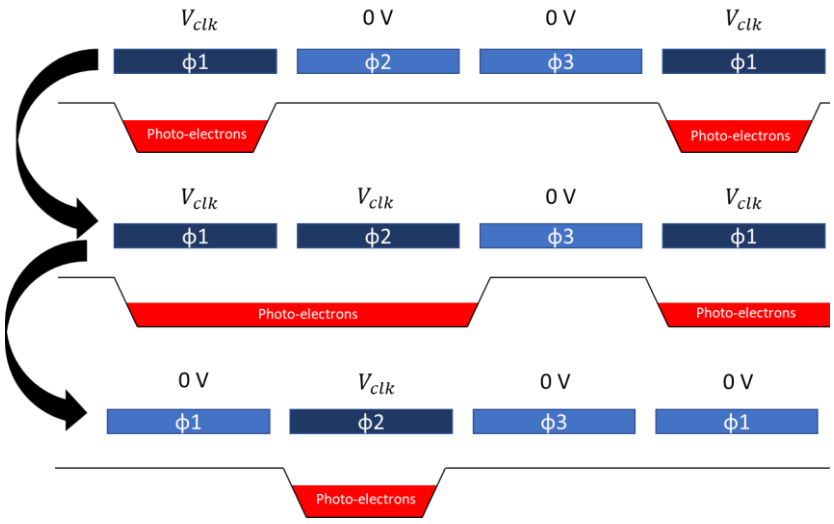

Figure 3.11. A single pixel transfer, showing the movement of the potential wells (and the contained photo-electrons) in response to the clock potentials.

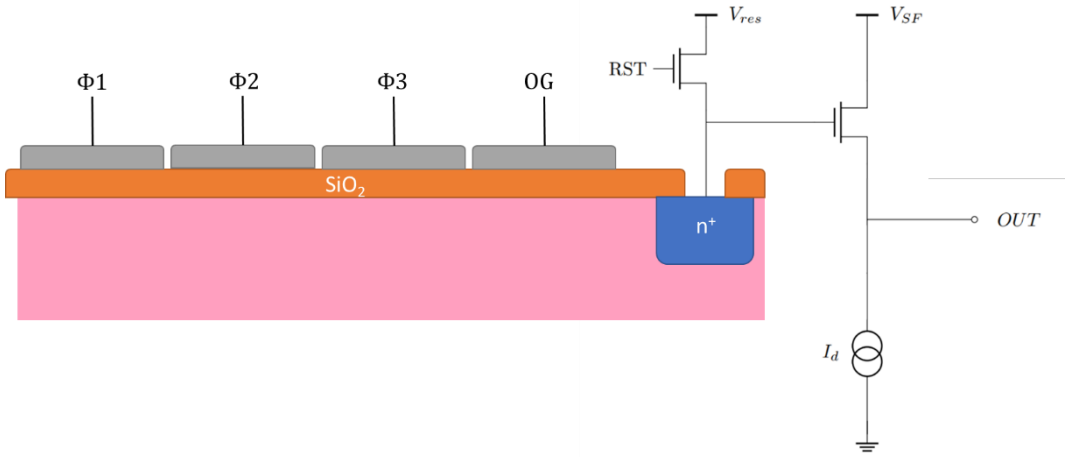

Figure 3.12. Output circuit of a CCD showing final serial clock electrodes n⁺ doped sense node (to ensure charge flows onto it from the final clock electrode) and a source follower.

At the end of the serial register charge packets must be converted into voltage signals for transmission off chip, achieved with the circuit of Figure 3.12, utilising a source follower to buffer the output signal. After completing the previous readout, the voltage on the sense node is reset to V_{res} by driving the reset transistor into conduction with the reset gate clock (RST). Then charge from the next pixel, waiting under the final clock electrode of the serial register, is moved to the sense node by driving the gate Φ3 low. The signal charge reduces the gate voltage of the source follower and results in a drop in the output voltage. This drop can be recorded by further (generally off chip) electronics and

converted into a digital pixel value. The OG (output gate) phase is biased to permit the flow of charge from the serial register to the sense node.

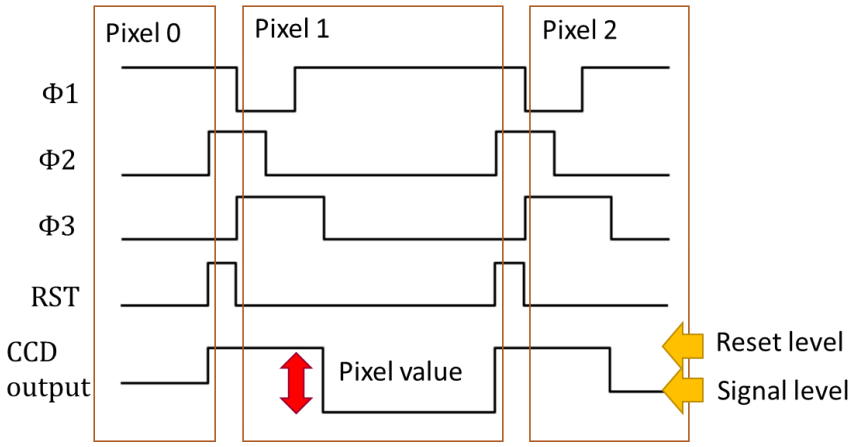

Figure 3.13. Clock timings for and typical idealised output of circuit in Figure 3.12. Showing the three serial clock phases, and transfer and reset pulses.When the third phase is driven low charge flows onto the sense node and results in a voltage drop at the output of the source follower.. This charge is swept away, ready for a new pixel readout, when the reset input is later pulsed.

Utilising the clock timings of Figure 3.13, the output of the CCD may be expected to be of the form demonstrated in that figure. The conversion gain of the readout circuit shown is given by equation (3.16), where the source follower Δv_g is generated by the collection of charge q_s on the sense node of capacitance $C_{sense\ node}$ (usually on the order of pF to ensure high output signal). The ratio of charge (in electrons) to output voltage is reported as the image sensor's charge to voltage factor (CVF).

$$\Delta v_g = \Delta v_i = \frac{q_s}{C_{sense\ node}} = \Delta v_0 \tag{3.16}$$

3.2.1 The EMCCD

The CCD architecture is extended in an Electron Multiplying CCD (EMCCD) with the addition of an electron multiplying register (EM register). Amplification of signals through the EM register suppresses the contribution of readout noise to a signal and enables the detection of signals as small as a single photo-electron at much higher framerates than is possible with as standard CCD (Jerram et al., 2001).

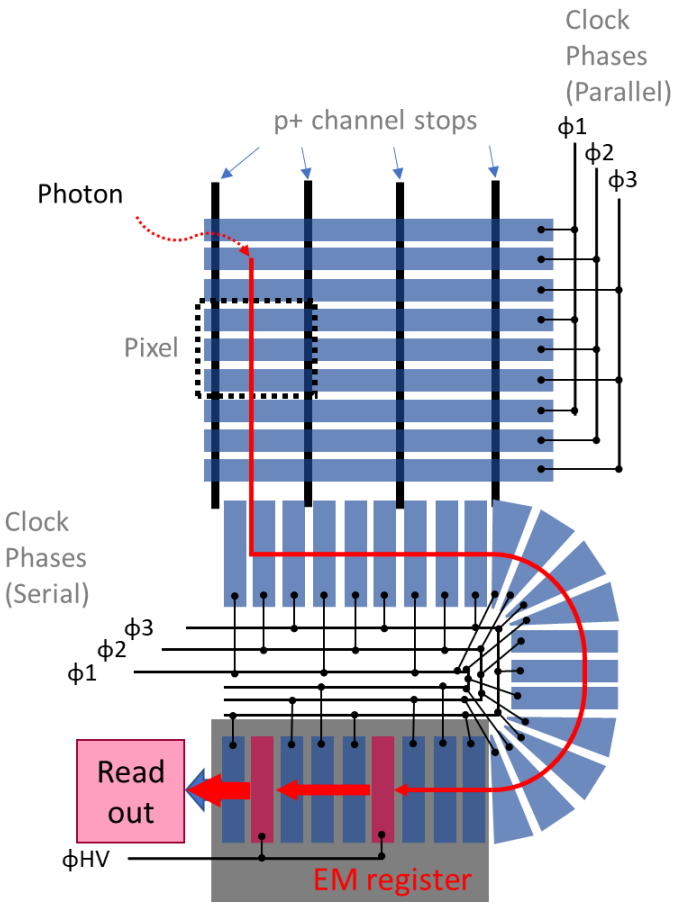

Figure 3.14. An example EMCCD showing the addition of the EM register. In practical implementations the EM register is often preceded by a short 180 º turn to ensure the EMCCD footprint remains an easily tessellated rectangular form.

The EM register operates by generating a large electric field between the charge storage wells of neighbouring register elements. As electrons pass through the regions of high field, they undergo impact ionisation and release more electrons into their original charge packet. The EM register is a carefully designed structure to ensure it performs optimally for an extended period. The precise details of the register, its behaviour and deeper physics are beyond the scope of this thesis. For a thorough consideration of the use of the EMCCD, focussed on its use in a space environment, Bush (2017) is an invaluable resource.

3.2.2 The SCD

Swept Charge Devices (SCDs) are a modification of the standard CCD architecture, intended for X-ray spectroscopy, that focus on collecting charge from a large area and gathering it at a small, low capacitance, readout node (Lowe et al., 2001). Unlike a CCD, charge from different initial regions is

combined during transfer which means that an SCD is unable to identify where charge is generated and cannot be used as an imaging sensor by itself. However, this combination also means that the SCD can readout its entire in fewer readout steps, only 120 are required to readout the CCD236, an SCD, as opposed to thousands for a typical CCD. This means that dark current is less of an issue, and the SCD can be operated at warmer temperatures reducing design demands placed on other instrument elements. Figure 3.15 shows a diagram of the modified electrode layout.

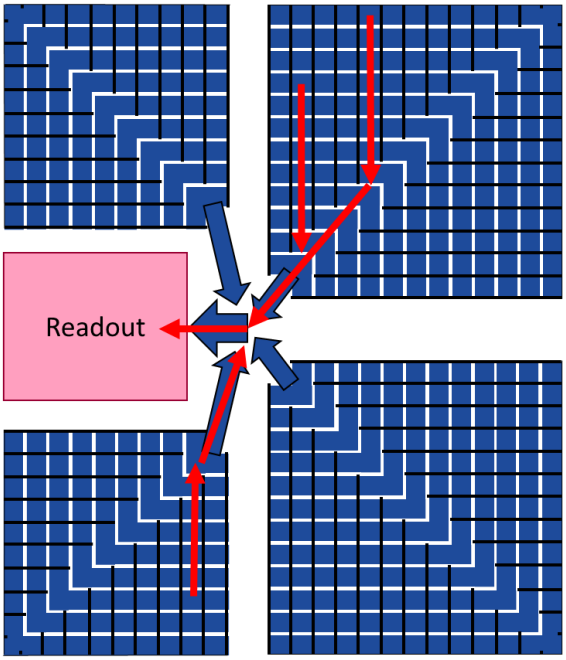

Figure 3.15. Simplified diagram of SCD clock electrode structure, with the readout path of several charge packets shown.

The SCD also offers a lower control complexity. There are fewer clock inputs required, because there is no distinction between serial and parallel pixel transfers, and further input reduction can be achieved with in pixel potential shaping implants, permitting readout of the entire SCD to be achieved with just two pixel clocks, and a further two clocks for the readout amplifier (e2v Technologies, 2007).

3.3 The CMOS image sensor

The CMOS image sensor (CIS) utilises the active pixel sensor (APS) architecture which differs from the CCD in that each pixel has its own readout circuit, shown in Figure 3.16. The conversion of signals from the charge to voltage domain simultaneously in many pixels permits far higher readout rates to be achieved than in CCDs, because the readout operation can be performed in parallel. However, the use of many readout circuits across the sensor results in the introduction of additional non-uniformities.

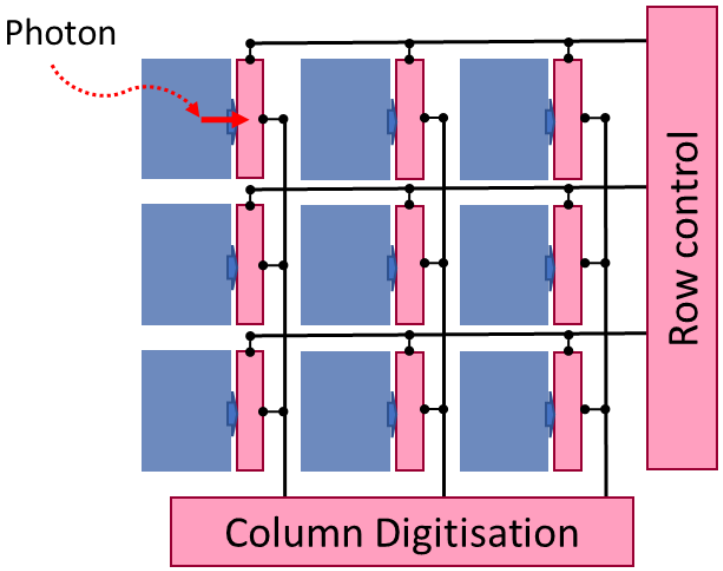

Figure 3.16. An example APS showing the readout path for the charge collected in a pixel.

Compared to the CCD, the APS has far higher on-chip complexity with transistors located within each pixel. Achieving sufficiently high process yield and uniformity was the reason for the initial dominance of the CCD, which could achieve both more easily. The current growing adoption of APSs has largely been the result of improvements in fabrication technology. Currently the most used technology for APS is the CMOS process favoured by semiconductor manufacturers. This current method of implementation of the APS is so closely associated with the manufacturing process that they will be referred to as CMOS Image Sensors (CIS). The assumption is that any APS will be implemented with CMOS techniques, and any CMOS image sensor will use the APS architecture.

CIS have been able to use improvements in fabrication technology to become highly integrated, either including functions previously implemented off-chip, such as the built-in ADCs of the CIS120 family (Teledyne e2v, 2017), or the more specialised functions such as energy harvesting (Cevik et al., 2015). Ultimately though, the advantage of CIS, over the CCD are the per-pixel readout, higher radiation tolerance and higher framerates allowing longer lifetimes when used in harsh environments, higher operating temperatures, and large imaging area (Fossum, 1993).

3.3.1 Pixel architectures

The most basic CIS pixel is the three transistor (3T) design shown in Figure 3.17. One transistor is used to reset the photodiode, a reset transistor; one transistor is used as a source follower; and a third transistor is used to enable the output, a row select transistor. A current sink is used to bias the source

follower during readout. The current sink, and the logic used to select pixels by row are generally provided by structures at the edge of the pixel array, rather than within each pixel.

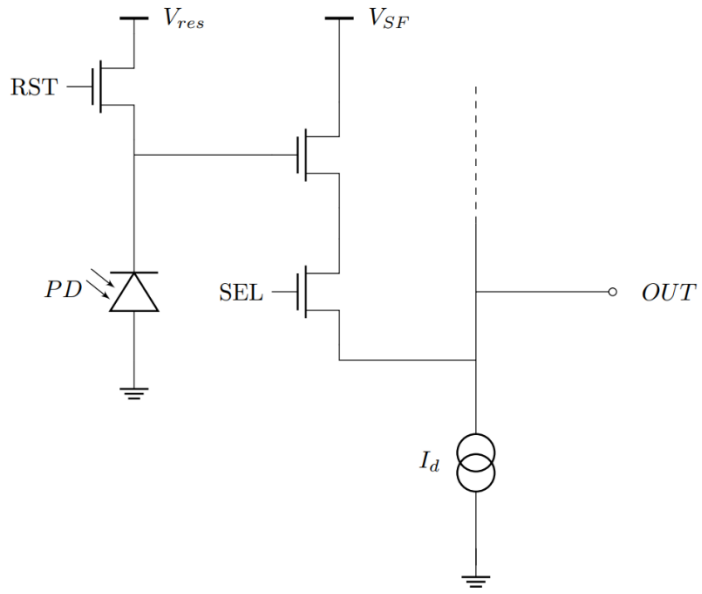

a)

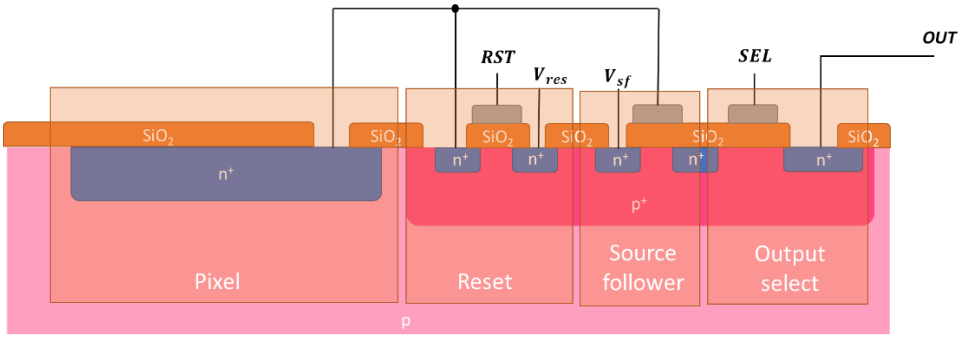

b)

Figure 3.17. 3T Pixel design circuit schematic, b) simplified 2D structure, not to scale (after Stefanov (2022)).

During normal operation charge generated in the photodiode accumulates at the photodiode cathode, itself connected to the gate of the source follower. When the time comes to read the pixel out, the row select transistor is put into full conduction and the source follower generates an output voltage proportional to the charge collected in the photodiode. Then the reset transistor is put into full conduction which drains the photodiode charge, allowing the pixel to be used again.

This circuit is very similar to the CCD output circuit shown in Figure 3.12, and indeed the output from an individual CIS pixel looks very like the output of a CCD pixel array. Therefore, subsequent readout steps are often very similar with the difference that they can be performed in parallel.

3.3.1.1 4T pixel

All CISs used during the work covered by thesis used the four transistor (4T) design (Figure 3.18), in which a transfer transistor is added to the basic 3T layout, and the photodiode, is replaced with a pinned photodiode.

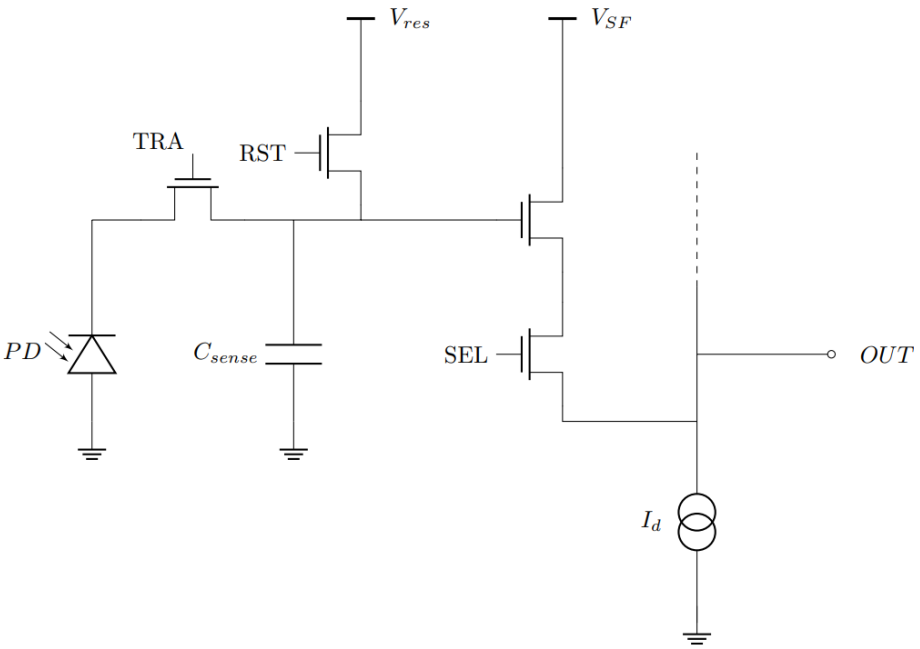

a)

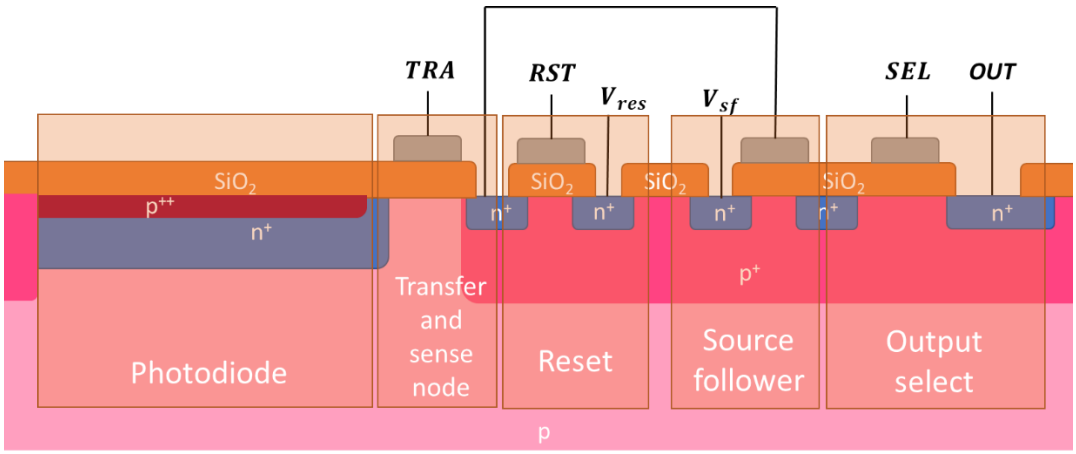

b)

Figure 3.18. The 4T pixel a) circuit schematic, b) simplified 2D structure (not to scale) including p++ pinning implant required for good charge transfer characteristics.

The additional transistor is the transfer gate. A drawback of the 3T design is that the voltage developed at the gate of the source follower relies on the capacitance of the photodiode. This signal voltage is related to the pixel capacitance (C_{pd}) by equation (3.17). Here the pixel capacitance has been used as the capacitance for the source follower sense node, as in equation (3.16)

$$V = \frac{q}{C_{pd}} \tag{3.17}$$

The photodiode design is generally driven by other design goals and therefore its capacitance can be quite large. This limits the charge-to-voltage conversion factor and could result in a very low pixel sensitivity limiting low light performance. The transfer gate transistor is added between the photodiode and the sense node. During readout the transfer gate is opened allowing charge to flow onto the sense node (Figure 3.19). The capacitance of the sense node is far lower than the photodiode, greatly improving the sensitivity of the pixel to small amounts of charge.

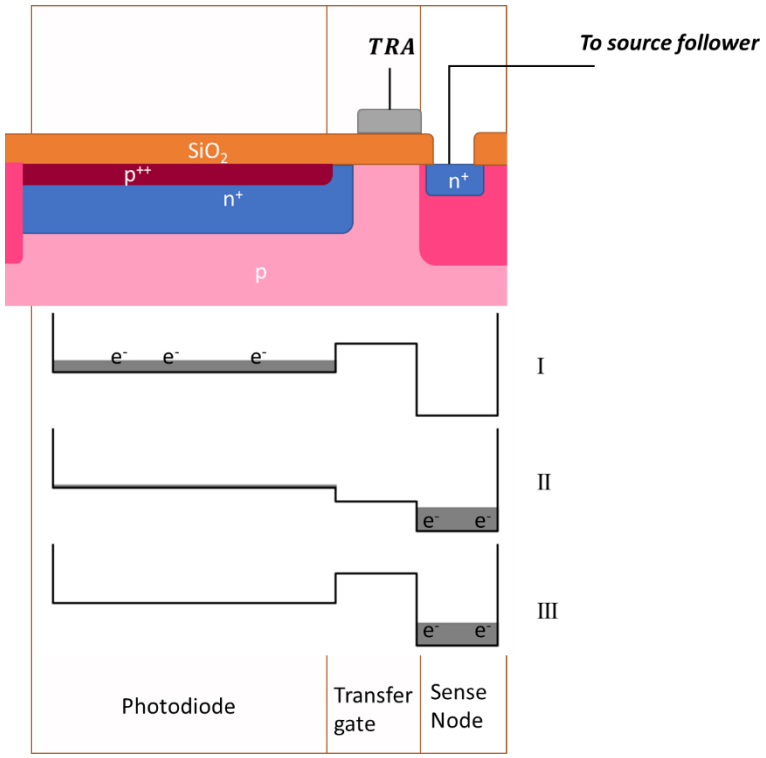

Figure 3.19. 4T pixel operation. I) Electrons collect in photodiode in response to incoming photons. II) Transfer gate potential is raised and a conductive path to the sense node is created and electrons flow across onto the sense node. III) Sense node is effectively independent of pixel, permitting readout and reset while photodiode collects more charge.

This transfer operation introduces additional requirement that all charge is moved from the photodiode to the sense node. Ensuring the completeness of this transfer is one of the motivations

for the inclusion of the pinned photodiode (see section 3.1.1) which pushes the potential of the photodiode below that of the sense node.

3.4 Sensitivity of solid-state image sensors

A key metric of sensor performance is its sensitivity to the photons of interest. Generally, this is recorded as a probability of detection for a given incident photon. For a large number of photons this is equivalent to number of photons detected as a proportion of the total number of incident photons.

3.4.1 QE

The probability of absorbing, and collecting, a given photon is labelled a solid-state sensor's Quantum Efficiency (QE). The QE of an image sensor is generally a combination of its ability to absorb incoming photons in photo-sensitive regions and its ability to transmit photons through preceding non-photosensitive (dead) layers. Because the transmission lengths of a photon through most materials changes with energy, the QE is specified as a function of photon energy.

For a standard CCD or CIS the design choices available are to either minimise the thickness of the front surface electrodes and insulating oxide deposited on the front side of the sensor, or to increase the thickness of the photo-sensitive volume. At the photon energies considered by the work of this thesis reflection and interference effects due to internal photon reflections do not impact QE.

3.4.1.1 Deep depletion

While much of a sensor will absorb incoming photons, not all of these regions will generate charges that can be captured and measured in a reasonable length of time. In particular, below the depletion region in the field free region, charge may be generated and, because within this volume the primary transport mechanism is diffusion, take a long time to reach the depletion region where they can be swept to the charge collection channel and measured. This length of time can exceed the recombination lifetime of the charges meaning that they recombine before being captured and are lost. Alternatively, they can spread far beyond their initial interaction location with implications discussed in subsequent chapters.

Therefore, minimising the field free region of an image sensor can be a key design objective. This can be done either by physically thinning the image sensor, removing material from the back surface until only depleted material remains, or maximising the depletion region thickness under the pixel MOS capacitors, as discussed in section 3.1.1.

3.4.1.2 Back surface Illumination

One of the ways to reduce the thickness of the initial dead layers is to bypass them completely. By thinning the sensor from the back surface, either by thinning the entire sensor or by etching a window behind the sensor pixels, it is possible to illuminate a sensor from behind, making it backside illuminated (BSI) (as opposed to frontside illuminated (FSI)). This effectively turns the sensor upside down, illustrated in Figure 3.20. Photons may therefore reach photo-sensitive volumes without traversing the front surface at all. This can have a significant benefit for QE for photons with a particularly short attenuation length.

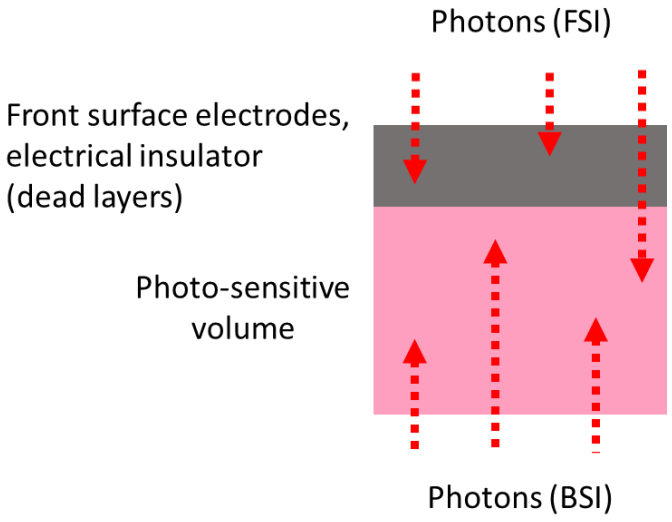

Figure 3.20. Direction of photon interactions in an FSI and BSI image sensor.

The back surface of an image sensor still has (much thinner) dead layers, these include SiO_2 that will grow directly on the back surface. The back surface silicon-silicon oxide interface has issues similar to those of the front surface which require the introduction of the buried channel. This necessitates back surface passivation techniques typically achieved with a p+-type implant close to the back surface (Moody et al., 2017), though this can introduce further regions of charge loss, resulting in a design push to minimise the p+ implant thickness (Hoenk et al., 2022).

3.4.1.3 The layer cake model

The layer cake model is a simple method for calculating the QE of an image sensor based solely on its physical properties. This method treats an image sensor as a set of strata, one of which the photo-sensitive layer. QE is therefore the proportion of incident photons that are absorbed in the photo-sensitive layer as opposed to being absorbed in the other, dead, layers, or passing through all strata and escaping the image sensor. This method has previously been verified, successfully predicting the

soft X-ray QE of both FSI (P. H. Smith et al., 2014) and BSI (Moody et al., 2017) image sensors. This model does not take reflections into account and is therefore limited to describing X-ray QE. A diagram of the standard FSI strata has been included in Figure 3.21.

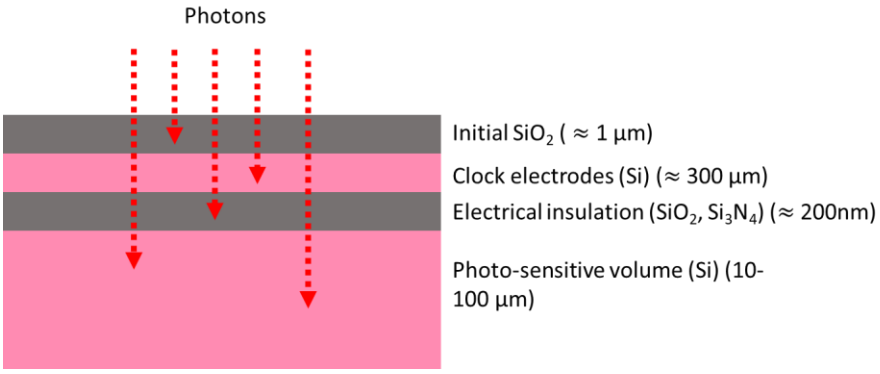

Figure 3.21. Example strata for a typical FSI CCD. Smith (2014 pp. 72) includes a detailed strata diagram used to model the CCD236.

Using this model, the QE of an image sensor can be described by the probability of photon absorption (non-transmission) in the photosensitive layers and the probability of transmission through all preceding non-photosensitive layers in Equation (2.28).

$$QE = (1 - P_{tran,ps-layer}) \prod_{dead\ layers} P_{tran} \tag{3.18}$$

The probability of transmission through any given layer is a function of the layer material and thickness, as per equation (3.19), which is derived from the Beer-Lambert law for the attenuation of radiation in a given medium.

$$P_{trans} = e^{-t/l} \tag{3.19}$$

Where t is the material thickness and l is the material attenuation length, a characteristic property of the material of the layer. The attenuation length value changes with material and photon energy. For the QE curves generated in this thesis attenuation values have been drawn from Henke, Gullikson, & Davis, (1993).

In addition to the basic QE prediction, it has been necessary to extend the model to measure the proportion of all photons that are absorbed in specific regions of the photo-sensitive volume. This can be done by running the QE model for each region.

This method can quickly generate QE predictions over a wide range of photon energies. However, it is limited in its representation of 3D structures. In CCDs or BSI sensors this is less of an issue as the

volumes dominating QE are homogenous, however predictions are less applicable for FSI CISs, where there are large differences in layer composition across the length and breadth of the sensor.

3.5 Noise in solid state image sensors

The image sensors of this thesis are intended to accurately measure the properties of incoming photons. This is made harder by noise, which can greatly increase the uncertainty in measurements made. For this reason, the following section introduces a number of common noise sources, the physical processes giving rise to them and their typical description during the analysis in later chapters.

3.5.1 Photon Shot Noise

The first source of noise in an image sensor is related to the photon source. The resulting uncertainty in the measurement of the number of photons is seen as shot noise. For an instrument observing many photons the number of observed photons will take a Poisson distribution with its λ parameter (describing the mean and variance of the distribution) equal to the expected number of received photons. The standard deviation of the number of photons is therefore equal to the square root of the mean number observed:

$$\sigma_{shot} = \sqrt{\mu_{signal}} \tag{3.20}$$

This noise source has no mitigation and forms an absolute noise floor for photometry measurements made with solid state imager sensors.

3.5.2 Dark Current

Dark current, or leakage current, is measured even in the absence of external light sources and is composed primarily of thermally generated electrons. Dark current is made significantly worse by lattice defects which can introduce mid-bandgap states that will generate charge carriers more often. Such defects can arise during manufacture, because of radiation damage, or occur along a material boundary due to atomic lattice mismatch. The Si-SiO_2 interface is a particularly severe source of dark current as discussed in section 3.1.2, the vacant Si bonds at the material boundary provide a ready source of free electrons. Dark current has a strong temperature dependence and can be mitigated by cooling the sensor. Any surface dark current can be mitigated by passivating the vacant bonds, usually achieved by introducing hydrogen to the interface to fill them. The dark current is primarily observed as dark signal, equal to the dark current (measured in electrons per second) multiplied by the integration period t_{int}:

$$e^-_{darksignal} = e^-_{darkcurrent} . t_{int} \tag{3.21}$$

As well as a mean signal value added to the photogenerated signal of each pixel, there is a variance in the number of dark current charges, which follows the properties of shot noise (equation (3.22)).

$$\sigma_{ds,shot} = \sqrt{\mu_{e^-_{ds}}} \tag{3.22}$$

3.5.2.1 Temperature dependence

In an idealised image sensor, specifically CCDs, there are two distinct regions of dark current generation: within the depleted regions of the image sensor, in and near the buried channel, and the undepleted regions. A full derivation of the two characteristic expressions below is given in Widenhorn et al. (2002) and Janesick, (2001, pp.605-622).

In the depletion region the concentrations of free carriers are far lower than the concentration of intrinsic carriers, therefore the dark current is a function of generation rate of carriers, described by Shockley Read Hall theory (Hall 1952; Shockley and Read, 1952). The n-type doping of the depletion region permits the simplification of the full generation-recombination expression into equation (3.23).

$$D_{e^-_{dep}} = \frac{x_{dep} A_{pix} n_i}{2\tau} \tag{3.23}$$

Where $D_{e^-_{dep}}$ is the depletion dark current in electrons a second, x_{dep} is the depletion layer thickness, A_{pix} is the pixel area, n_i is the intrinsic carrier concentration, and τ is the charge carrier generation-recombination lifetime.

Dark current originating in the undepleted region can instead be described by the diffusion current across the boundary at the bottom of the depletion region, itself a function of the minority carrier concentration (electrons in the p-type substrate) (equation (3.24)):

$$D_{e^-_{diff}} = \frac{D_n A_{pix} n_i^2}{x_{ff} N_A} \tag{3.24}$$

Where $D_{e^-_{diff}}$ is the dark current due to diffusion, D_n is the electron diffusivity, x_{ff} is the field free thickness in a thin image sensor, (it is replaced by L_n, the diffusion length, in much thicker sensors) and N_A is the acceptor dopant concentration.

Both dark current source expressions include the intrinsic carrier concentration (n_i), which has a strong temperature dependence (from equation (3.3)). As a vast simplification the total dark current may therefore be represented by equation (3.25):

$$D_{e^-} = D_{e^-_{diff}} + D_{e^-_{dep}} = AT^3 e^{\frac{-E_g}{kT}} + BT^{3/2} e^{\frac{-E_g}{2kT}} \quad (3.25)$$

Where A and B are constants based on the image sensor properties, and generally B is far greater than A. It can be observed, therefore, that at high temperatures the dark current from the field free region will tend to dominate. However, at lower temperatures at and below room temperature the depletion dark current is usually sufficient to describe observed behaviour.

3.5.2.2 Activation energy of dark current

It is common practice to express the measured dark current in such a way as to expose the expected $\exp\left(-\frac{E_g}{2kT}\right)$ dependence. Plotting the natural logarithm of measured dark current for the inverse of temperature (in Kelvin), an Arrhenius plot, permits the measurement of this term, called the activation energy, from the linear gradient of the points. An example is shown in Figure 3.22.

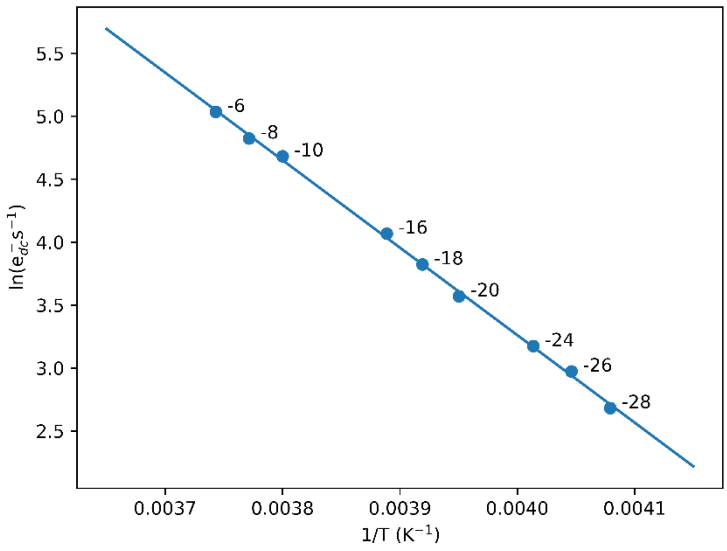

Figure 3.22. Example Arrhenius plot of dark current, showing the linear relationship between the two plotted parameters. The gradient (in - ln(e⁻s⁻¹) K) corresponds to the activation of the dark current in this sensor, 0.6 eV. The temperature (in °C) of each measurement point has been indicated.

This can provide a powerful tool for diagnosing atypical dark current behaviour, for example Widenhorn et al. (2002) uses this plot to identify the change between the diffusion and depletion dark current dominated temperature regimes, while the value of the activation energy can be used to track radiation damage, for instance Lofthouse-Smith (2021) chapter 7.

3.5.2.3 Characterising dark current

At, and below room, temperature the total dark current is dominated by the depletion dark current, resulting in the recommended characteristic equation of Janesick, (2001, pp.622) for the relationship between temperature and dark current in a buried channel CCD with the contribution from the surface suppressed, in electrons pixel^{-1}second^{-1} (equation (3.26)). This equation is the second term in (3.25), expressed with terms that can be measured in an image sensor experimentally.

$$e^{-}_{darkcurrent} = 2.5 \times 10^{15} A_p D_{FM} T^{1.5} e^{-E_g/(2kT)} \tag{3.26}$$

Where A_p is the pixel area, T is the image sensor temperature in Kelvin, E_g is the bandgap energy (which also has a temperature dependence, ignored here), and D_{FM} is a dark current figure of merit in $\mathrm{e^{-}s^{-}cm^{-2}}$, the dark current per unit area at a reference temperature. $e^{-}_{darkcurrent}$ is expressed in units of $\mathrm{e^{-}s^{-1}}$. In practice dark current can often be described with a single straight line fit in log space:

$$e^{-}_{darkcurrent} = 10^{aT+b} \tag{3.27}$$

Which can provide a simpler, empirical, description of dark current behaviour for quick interpolation of dark current behaviour between measurement points. The change of base from e to 10 is to aid measurement of the equation parameters from standard log-scale plots. The exclusion of the $T^{1.5}$ factor limits the temperature range over which this expression can be applied.

3.5.3 Charge Transfer Inefficiency

Charge transfer inefficiency (CTI) refers to the loss of charge from a charge cloud to defects and traps in the charge storage areas of an image sensor. This charge is often released later and, in CCDs, will 'smear' point sources in the readout direction as charge is captured and later released into a different charge packet. In addition to any effects on the mean value of a signal, uncertainty associated with charge absorption and emission introduces a random component to the charge loss. The contribution of CTI to overall pixel noise can be described by equation (3.28) (Janesick 2001, pp 656).

$$N_{CTI} = \sqrt{2\ CTI\ N_P\ n_{e^-}} \tag{3.28}$$

Where N_{CTI} is the rms noise contribution of CTI to the value of any given pixel, CTI is the per-transfer inefficiency value, N_p is the number of transfers for a pixel (up to thousands in a large CCD), and n_{e^-} is the number of electrons in the transiting signal packet. The CTI is dependent on image sensor properties, temperature, and operation parameters including the transfer clocking scheme. As such, optimisation of CTI for a specific CCD for a specific application can be demanding and require in-depth investigation (for example, Buggey (2021)).

3.5.4 Image Lag

Many of the issues associated with CTI in CCDs are less evident in CISs, with only a single transfer required per pixel. However, the problem is not avoided, instead of appearing in the same image, 'smeared' charge can simply appear in later pixel readouts, producing ghost-images. Complete charge transfer in CIS is not assured, especially in large pixel CIS it can be challenging to create a lateral potential gradient to attract electrons to the sense node.

Uneven potentials in the pixel can lead to small potential barriers and pockets (Stefanov, 2022). Barriers will prevent the flow of electrons out of a pixel and can trap a large number. Electrons so trapped will only pass through the barrier slowly, or not at all. Potential pockets will trap small numbers of charge carriers, the trapped carriers will be released thermally into subsequent readouts.

Finally, in 4T pixels is possible to fill the potential well of the sense node such that charges 'spillback' into the transfer gate. This spillback charge can subsequently be transferred back into the photodiode, where it will also appear in future pixel readouts (Ivory, 2021).

In a well-designed 4T CIS the image lag is negligible, assisted by the pinned photodiode. In larger pixels specialised designs can be used to ensure a potential gradient across the entire pixel, including the introduction of additional pinning implants to encourage the photo-generated charge to be stored in a smaller region (Heymes, Stefanov, et al., 2020), or shaping the initial pinning implant to ensure a lateral potential gradient (Shin et al., 2010).

3.5.5 Readout noise

Readout noise is a catch all term used to describe the electrical noise seen at the output due to the readout (charge transfer and amplification) circuits. There are three primary sources of this electrical noise: thermal or Johnson-Nyquist noise, 1/f noise, and flicker (also called random telegraph signal (RTS) or 'popcorn') noise. The mechanism by which this noise is embedded into output data is labelled reset noise.

Thermal noise (Johnson, 1928; Nyquist, 1928) is a common source of noise in electronic systems, primarily the result of thermal variations in carrier movements and material conductivity. When considering thermal noise, the primary source is at the readout node during the pixel readout reset, where it is described by equation (3.29).

$$e^-_{reset,\,rms} = \frac{\sqrt{k_B T C}}{q} \tag{3.29}$$

Where k_B is Boltzman's constant, T is the sensor temperature in Kelvin, and C is the sense node capacitance and q is the electron charge. While further amplification and digitisation stages generate further Johnson noise, the noise of the initial stage is usually dominant.

In addition to the 'white' Johnson noise, 1/f noise is also commonly observed in the readout circuits of solid state image sensors. These are introduced by the transistors of the readout circuit and are thought to be due to traps in the MOSFET channel or in the gate oxide, modulating current. These noise sources have a spectral power density inversely proportional to their frequency. In particularly small transistors the effect of single traps can be distinguished with step changes in output signal as charge is absorbed or released from individual traps. This results in random telegraph signal (RTS), also known as flicker noise, illustrated in Figure 3.23.

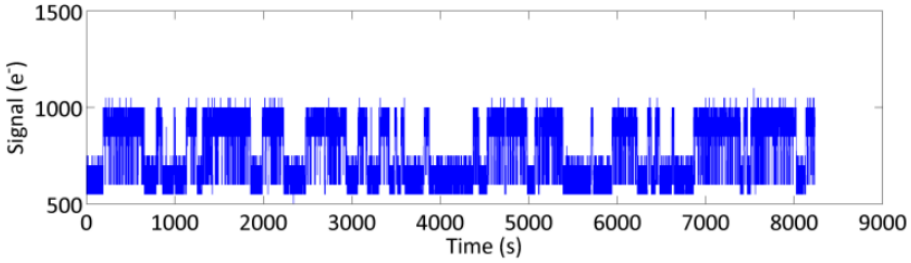

Figure 3.23. RTS noise observed in an irradiated CIS. This noise is named for its apparent similarity to an on-off shiftkeyed telegraph waveform. Figure adapted from Figure 7.11 of Dryer (2013).

Practically, the mechanism for reset noise is demonstrated in Figure 3.24. Thermal noise driven variations in the reset level are captured when the reset level is measured, adding a variable voltage to the actual measured value (which is also changing due to other noise sources).

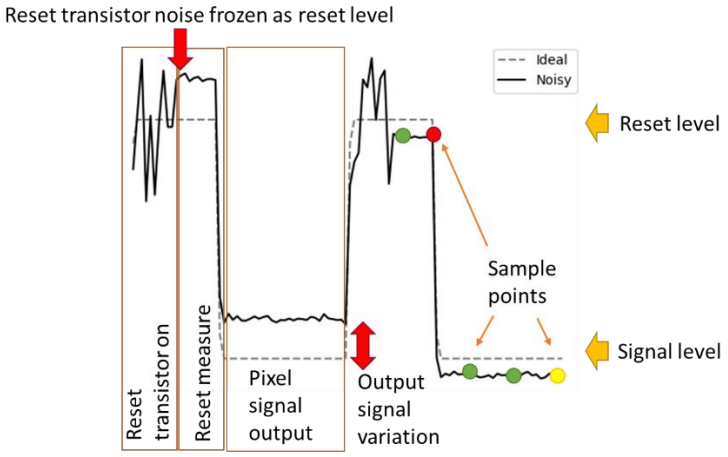

Figure 3.24. Manifestation of output electronics noise in measured data in two example pixel readout cycles. Noise on the output transistor results in a high uncertainty in reset level.

Reset noise can be eliminated with correlated double sampling (CDS), either in an analogue implementation such as dual slope integration (DSI) or using multiple digital samples. The most basic form of CDS involves taking a sample of the output signal level before and after charge has been transferred onto the sense node (using the yellow and red measurement points), with the pixel value being calculated as the difference between the two samples. Adding further samples to the reset and signal levels (including the green measurement points) can help reduce the contribution of the source follower transistor.

All CDS methods are effectively applying a bandpass function to the noise spectrum with a lower cut-off determined by the total time range over which samples are taken (more samples over a longer readout period decrease the lower cut-off), and an upper cut-off determined by the spacing of sample points (more tightly spaced points will result in a higher frequency cut-off). There is therefore a design trade-off for the method of readout sampling where the CDS sample timing can be optimised for the expected noise spectrum. For the work that follows the simple assumption that more time spent on sampling the output signal results in lower electronics noise describes the observed results well. For better readout noise behaviour, especially in a single readout CCD, there is a direct trade-off with the framerate that can be achieved.

3.5.6 EM register noise (EMCCD)

The EM register of an EMCCD is intended to suppress the noise contribution of the readout amplifier and electronics, however it also acts as a noise source itself as the impact ionisation gain mechanism is stochastic and so the number of electrons added by each stage is variable. This source of noise is unavoidable if the EM register is used to provide substantial gain.

The size of the EM register's noise contribution is derived in Robbins & Hadwen, (2003) and Tutt, et al. (2012), generally the high-gain approximation of the EM noise contribution is used and expressed as a combination of the photon shot noise and EM noise:

$$\sigma_{\mathrm{EM}}^2 = (\alpha + 1)\, \mu_{signal} \tag{3.30}$$

Thus, for an optical imaging sensor ($\alpha = 1$), the signal dependant shot-like noise is $\sqrt{2}$ times greater at high EM register gain.

3.5.7 Non-Uniformities

In the ideal sensor, every pixel has the same response to incoming photons and has identical noise characteristics. However, manufacturing tolerances and damage may cause pixels to diverge from the mean values for dark current generation (dark current non-uniformity (DCNU)), sensitivity, and CVF

and QE (photo-response non-uniformity (PRNU)). This is a particular problem for CISs, as the readout circuit in each pixel may have a different gain and offset value. CCDs, with their single readout circuit for many pixels do not experience this issue to the same extent.

PRNU in a CIS is largely driven by physical properties of each pixel, and of associated row and column drivers. Therefore, there have been attempts to calibrate and correct the PRNU of a single CIS permitting data from proof of concept characterised image sensors to approach theoretical performance limits (Dryer, 2013; Wu et al., 2023).

3.5.8 Uncertainty noise budget model

This thesis includes trade-off studies which have considered many sensors, some of which were not available for immediate testing. It has therefore been necessary to predict the total noise of each image sensor based on underlying physical and performance parameters.

Fortunately, because most of the noise sources encountered are not correlated, the total noise in the image sensor σ_{tot} may be calculated by equation (3.31):

$$\sigma_{tot} = \left(\sum \sigma^2\right)^{1/2} \tag{3.31}$$

$$= \left(\sigma_{shot}^2 + \sigma_{DC}^2 + \sigma_{readout}^2 + \cdots\right)^{1/2} \tag{3.32}$$

Crucially this noise model does not capture the smearing effects of CTI and image lag. Additionally, it does not handle non-linearity well, so must be used with caution when sensors are operating near saturation levels.

3.6 Summary

This chapter has outlined the physics of solid-state image sensors, a selection of the architectures in use, and outlined many of the noise sources present in any measurement made with these image sensors. CCDs and CISs are powerful tools for detecting many types of radiation, though the work of this thesis focusses on their capabilities as X-ray detectors, which is described in the next chapter.

4 Detection of X-rays in solid state image sensors

This chapter describes the use of solid state image sensors for the detection of X-rays primarily within the 300 eV to 2000 eV range, in a photon counting mode. Photon counting, or measuring the interactions of individual photons, enables new methods of analysis useful for science. Ultimately many of the behaviours observed in these X-ray detectors, and the challenges that must be overcome, are related to those of the more generic image sensors of the previous chapter. There is, however, a greater focus on the accurate collection of charge generated by incoming photons and a greater freedom to perform data reduction without removing information useful for further science. This chapter begins with an overview of three past and current missions using different X-ray detectors, outlines some of the specific mechanisms and sources of uncertainty relevant for the use of silicon based X-ray detectors, covers the key steps used in X-ray data reduction which are used implicitly throughout the rest of the thesis, and ends with an overview of the effects of the space radiation environment on X-ray detector performance.

4.1 Example X-ray missions

Three key missions for the material of this thesis are: XMM-Newton, a flagship mission from the 1990s with a strong influence on all subsequent space-based X-ray detector design; SMILE, a planned mission to observe the interactions of the Earth's magnetosphere and the solar wind using a state of the art large format CCD as an X-ray detector; and THESEUS, a planned multi-wavelength astronomical observatory expected to use a novel CIS X-ray detector. These three missions represent only a small fraction of all past and current activity for space-based X-ray detectors, selected for their relevance in providing context for the ideas surrounding the current state of the art and expected future developments addressed by this thesis. These three missions also illustrate some of the breadth of science that may be completed with an X-ray sensitive instrument.

4.1.1 XMM-Newton

The X-ray Multi-Mirror mission (XMM-Newton), and the contemporaneous Chandra X-ray telescope, represented an entirely new level of X-ray astronomy capability when launched in 1999. XMM-Newton in particular offered a vastly increased effective area (driven by a larger telescope aperture), enabling the detection of far fainter X-ray sources than had previously been seen (Lumb et al., 1996). Key to

these improvements were the CCD X-ray detectors of the spacecraft's European Photon Imaging Camera (EPIC). The increased effective area has resulted in XMM-Newton being able to observe the X-ray emissions of diffuse objects, leading to important discoveries relating to the nature of Solar Wind Charge Exchange (SWCX) in cometary comas, the aurorae of Jupiter (also reported in section 2.1), and the natures of supernovae and active galactic nuclei, among others (Lumb et al., 2012).

Of the three EPIC focal planes, two made use of MOS-CCDs: CCDs of the form presented in section 3.2. These detectors enabled energy dispersive energy resolution of 140 eV at 6.4 keV, adding capability for imaging spectroscopy observations using the entirety of the X-ray flux arriving at the X-ray focal plane. As of 2023, XMMNewton continues to perform important science functions, with its successor, the Advanced Telescope for High Energy Astrophysics (ATHENA), only planned to become operational in the late 2030s (ESA, 2022).

4.1.2 SMILE

The Solar Magnetosphere Ionosphere Link Explorer (SMILE) mission is currently planned to launch in 2024. Its primary scientific focus is to investigate the interactions between the Earth's magnetosphere and solar wind, with an instrument suite and planned mission profile that will enable it to observe the entire dayside magnetosphere boundaries for extended periods of time (Raab et al., 2016).

SMILE will make these observations from the apoapsis of a highly elliptical orbit. Its observations of soft X-rays are expected to permit the identification and mapping of specific interactions between solar wind and the neutral atoms in the Earth's exosphere labelled, SWCX. Observations of SWCX are possible in the soft X-ray range, which covers most of the critical emission energies expected. This requires the use of an imaging spectrometer with sufficient energy resolution to separate the X-ray energy components of different processes. Alongside the X-ray detector, imaging of the UV aurora is required to build an understanding of the internal configuration of the magnetosphere.

Directly relevant for the work of this thesis is the Soft X-ray Imager (SXI) instrument: a soft X-ray imaging spectrometer intended to make the SWCX observations. This instrument will use two large X-ray optimised CCDs with performance requirements roughly equivalent to those of the AXIS X-ray detectors considered in chapter 6. These CCDs, CCD370s, represent the state of the art for large format X-ray CCDs, with a sensitive area almost 8 cm square, on-chip binning to aid X-ray charge collection built into the pixel array (Soman et al., 2018), and incorporating design features intended to reduce the effect of radiation damage on performance (Hall et al., 2017).

4.1.3 THESEUS

The Transient High Energy Sky and Early Universe Surveyor (THESEUS) was a mission proposed for the ESA M5 call, intended to search large areas of the sky for gamma-ray bursts (GRBs) and other energetic events in the early universe. It was expected to work alongside upcoming gravitational wave observatories and transient event observatories to identify highly energetic events, and provide precise localisation information for follow up observations by other ground and space based telescopes (Amati et al., 2018). To do this, an array of telescopes and detectors sensitive to a wide variety of photon energies, over fields of view exceeding one steradian, were planned.

The instruments proposed for THESEUS were not intended as primary scientific observation tools for known phenomena, but rather act as surveyors for unknown transients. These were expected to include many GRBs from the early universe, with redshifts that mean emitted radiation is received in softer X-ray energies too. Such events are expected to provide information on the nature of early stars and therefore the evolution of stellar populations to the present day.

Most relevant for this thesis, the Soft X-ray Imager (SXI) was proposed to consist of four telescopes, sensitive to X-rays from 300 eV to 6000 eV. During initial design phases it was determined that the spacecraft design was not going to enable X-ray detector operating temperatures required by traditional CCDs to be met (McHugh et al., 2020). Therefore, CIS X-ray detectors were baselined for their faster readout speeds and resulting ability to operate at warmer temperatures. Though the already available CIS120 was explicitly identified at the time, this design choice was directly responsible for the development of the X-ray optimised CIS221-X which is the focus of much of chapters 6 to 8.

4.2 X-ray detection theory

A key property of X-rays, as opposed to lower energy photons, is their high energy relative to the 3.5 eV direct bandgap or 1.1 eV indirect bandgap energies of silicon. This means that X-rays can release a large amount of charge within a silicon X-ray detector. This thesis is concerned with X-rays of energies between 300 eV and 2000 eV, generally labelled soft X-rays.

4.2.1 X-ray fluorescence

Following a sufficiently energetic excitation process an electron can be promoted from the K-shell in an atom to a higher energy shell. To shed excess energy during later relaxation an electron will emit a photon with an energy equal to the relaxation transition. The relaxation energy transitions of each

atom are unique to its species. The relative energies (or properly, wavelengths) of X-ray emission were a key components in the development of atomic models in the early 20th century (Moseley, 1913).

The energy of the emitted photon is dependent on the species of the atomic nucleus and the electron shell transition made. Within the context of this thesis only transitions between the K, L, and M shells have been observed. Very high energy resolution would reveal further differentiation between transitions associated with more complex behaviours, such measurements are not possible with the methods of this thesis. The transitions follow the naming scheme as per Figure 4.1. Of the three transitions labelled, $K\alpha$ and $K\beta$ are most relevant for the testing and science applications of this thesis. Kα lines are generally much more prominent than Kβ lines, and so are most commonly used in measurement of X-ray detector performance.

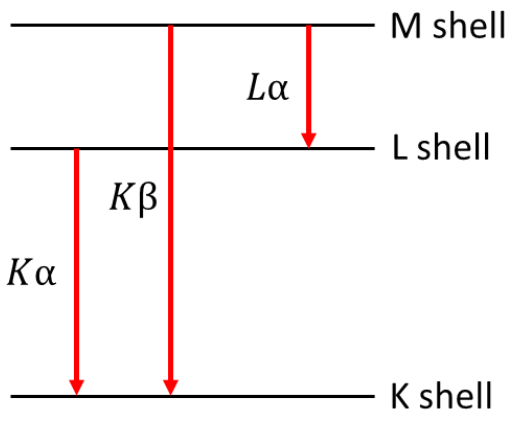

Figure 4.1. Standard terminology for X-ray fluorescence energies related to electron relaxation steps. $K\alpha$ fluorescence is by far the most common followed by $K\beta$. As a lower energy transition, $L\alpha$ fluorescence is generally not observed at X-ray energies for lighter elements.

Therefore, when observing the fluorescence of a target of known composition (either in the lab or in a science instrument) the observed spectrum of X-ray energies often contains a set of peaks with energies corresponding to electron transition energies in the atomic species of the target. These are referred to throughout the thesis by the standard convention, using the atomic species in which the fluorescence has originated, and the electron transition. For instance, in Figure 4.2 a typical spectrum produced in a small lab test chamber is displayed showing the intended silicon and oxygen fluorescence, and stray fluorescence from the rest of the chamber. The values for fluorescence energies for all subsequent work have been derived from Lifshin, (1999).

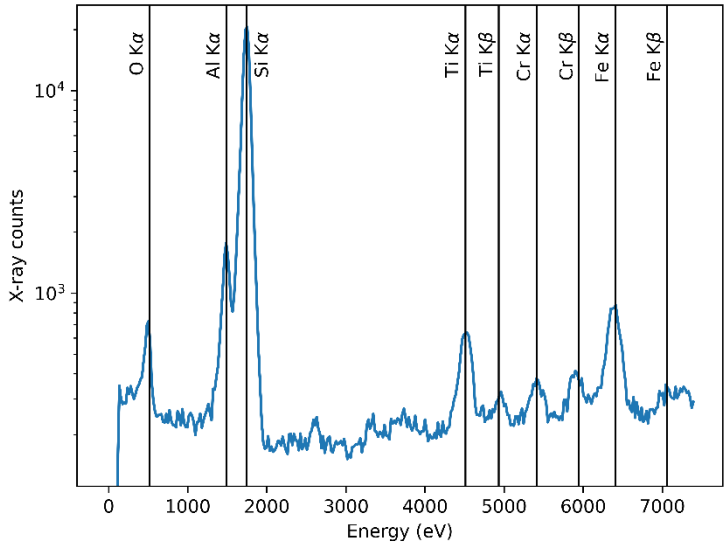

Figure 4.2. Example X-ray spectrum fluoresced from an SiO_2 target. The X-rays fluoresced from specific elements can be separated by energy. In addition to the silicon and oxygen fluorescence, fluorescence from the aluminium fluorescence target holder, chromium bolts and steel chamber is also observed.

4.2.2 Charge generation

At soft X-ray energies, the dominant charge production mechanism is the photo-electric effect. Whereas optical photons only have sufficient energy to excite a single electron, soft X-rays can excite many. After the absorption of an X-ray photon and promotion of an electron to the conduction band (as per section 3.1), excess energy is dissipated into neighbouring atoms which can excite further electrons generating a cloud of photoelectrons in the vicinity of the initial interaction site. At incident X-ray energies above 1839 eV (the K-shell electron transition energy of silicon) there is also the possibility that the incoming X-ray will instead excite a silicon atom that subsequently emits a fluorescence Si Kα X-ray, resulting in two additional observed charge clouds: one corresponding to the energy of the initial X-ray minus the 1740 eV fluorescence Xray energy (named an 'escape peak' on the X-ray spectrum); and another, generally close by, generated by the X-ray fluorescence from the silicon atom.

Because of the fixed energy requirement to promote an electron into the conduction band, the number of generated electrons (n_{e^-}) is calculated in silicon by equation (4.1), where E_{ph} is the X-ray energy in eV and ω is the energy to electron conversion factor, typically taking a value of 3.65 eV/e^- (Mazziotta, 2008).

$$n_{e^-} = \frac{E_{ph}}{\omega} \tag{4.1}$$

This relationship permits the energy of incoming X-ray photons to be inferred from the amount of charge they are observed to generate. This makes it desirable to measure the charge from each individual photon, this method of detector operation is termed a photon-counting mode (for example Figure 4.3).

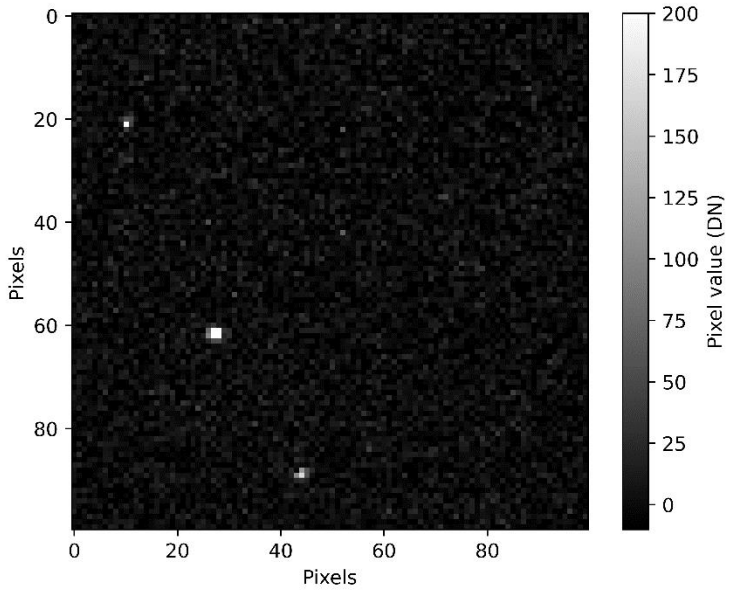

Figure 4.3. Example frame from an X-ray detector showing several observed X-rays. These appear as bright spots, brighter spots correspond to more energetic X-rays.

If each recorded X-ray is sufficiently isolated from other X-rays, and so the energy of each can be recorded, it is possible to use the data derived from the detector for imaging spectroscopy: the extraction of spectral information at each point in a recorded image (Figure 4.4). This can have large scientific utility, permitting the identification and localisation of processes responsible for X-ray emissions that are detected with the same instrument and at the same time.

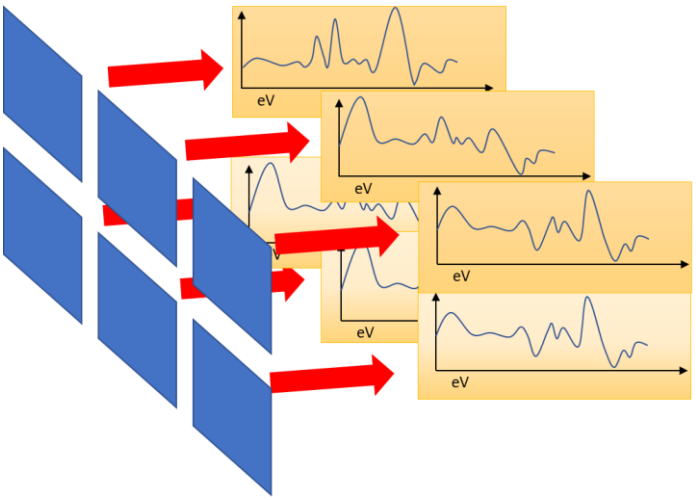

Figure 4.4. Imaging spectroscopy: the extraction of spectral parameters alongside spatial resolution.

Some modifications are required to a solid-state image sensor to optimise it for X-ray detection. X-ray charge clouds, especially in the soft X-ray range, contain far fewer electrons than the normal image sensor saturation levels. Therefore, the gain of the readout circuit will often be adjusted, sacrificing the unused range to provide greater sensitivity (Soman et al., 2018). In space-based applications, an X-ray detector will also be exposed to significant levels of optical light, which produce unwanted background signals, therefore an optical blocking filter blocking optical photons but with a high transmission index for X-rays, will generally be used in X-ray instruments.

4.2.3 Interaction depth

The detection of very soft X-rays is characterised by the extreme range of attenuation lengths of the X-rays within silicon, ranging from just 60 nm at 200 eV, to 14 µm at 1830 eV. The attenuation length of a photon has a direct impact on the probability of interaction at a given depth, which is determined by the Beer-Lambert law also used in the layer cake model of section 3.4.1.2.This means that typically the entire thickness of an X-ray detector will be used to collect photon energy (Figure 4.5) and the behaviour of electrons in each layer of the detector is of interest (Holland, 2013). An important distinction to be made is that while early CCD based X-ray detectors were frontside illuminated, and therefore concerned with high energy X-rays being collected in the regions far from the charge collection channel, the modern X-ray detectors considered by the later chapters of this thesis are backside illuminated, and therefore are concerned about low energy X-rays for the same reason.

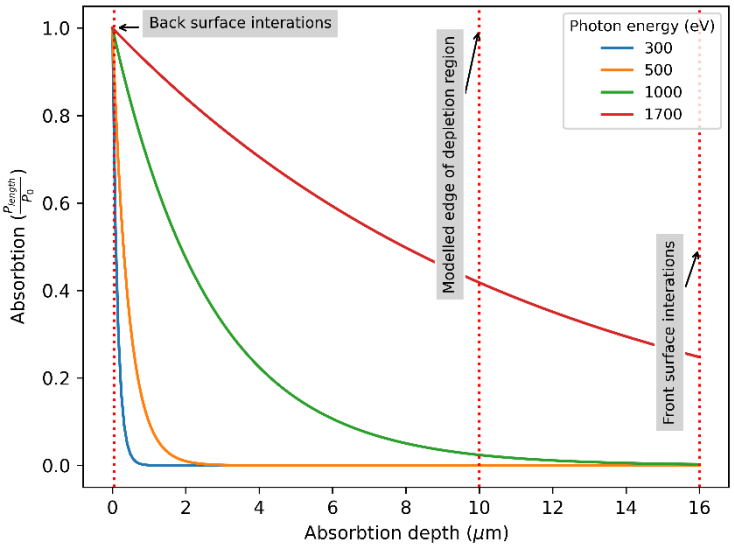

Figure 4.5. Absorption for depth in an example BSI 16 µm thick detector showing the relevance of back-surface, front-surface, field-free and depletion region interactions. Low energy X-rays will be almost entirely absorbed within the first micron of silicon, whereas higher energy X-rays can be expected to be absorbed throughout the detector thickness.

X-ray events interacting in the depletion region are the most straightforward to analyse, as X-ray generated charge is quickly drawn to the charge collection volumes by the region's potential gradient (illustrated in Figure 4.6). This generally results in compact charge collection areas that are straightforward to identify and analyse.

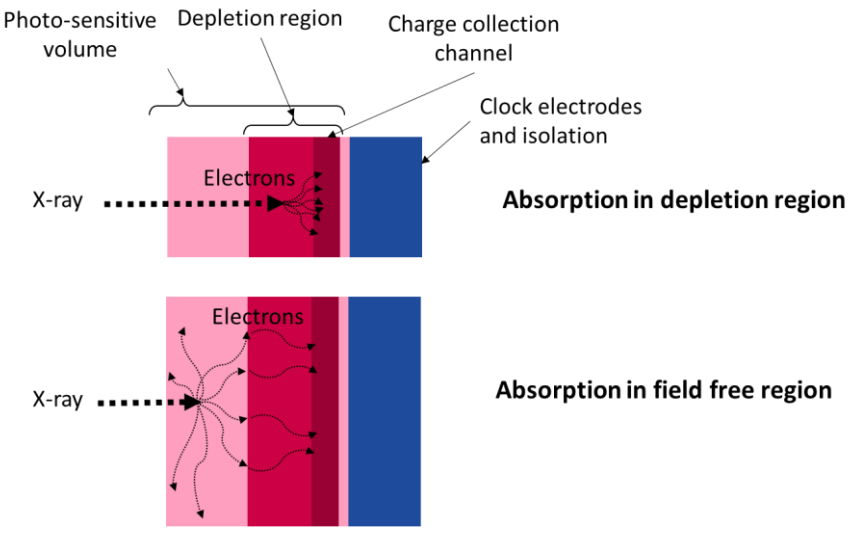

Figure 4.6. Illustration of charge absorption in field free region of a solid state image detector.

In an X-ray detector that is not fully depleted, that is the depletion region extending from the buried channel does not reach the back surface of the X-ray detector, the charge cloud from events interacting in the field free region is largely unconstrained in its expansion. Whereas the charge from

events that occur in depletion region is quickly swept into the charge collection channel by the potential gradients, charge in the field free region propagates by diffusion in all directions. The collection of charge from these events relies on the charges eventually reaching the depletion region and being swept away. This is not guaranteed and it is quite possible for X-ray generated charge to diffuse well beyond any reasonable region that may be used to consider an X-ray event, or remain uncollected and recombine into the silicon lattice (also shown in Figure 4.6) (Lumb & Holland, 1988).

Finally, X-rays absorbed very close to the back surface (much less than 1 μm from the back surface) interact with the region of increased complexity there. Typically, interactions in this thin layer have been analysed in the context of UV photon detectors (Janesick, 2001 pp. 195-214), due to the short attenuation length of photons at those energies, however they are also relevant at the softest X-ray energies.

4.3 X-ray data reduction and processing

The following is a summary of the X-ray data reduction process used during all work in later chapters. This pipeline is common among space-based CCD X-ray detectors because of the low computational complexity and large reduction in data volume that may be achieved.

To retrieve X-ray data from a frame of pixels, or stack of frames, recorded by an X-ray detector data processing is completed in three steps. First, frames are processed to remove systematic pixel offsets and filter known defective pixels. Then X-rays, as individual X-ray interaction events, are identified, generally by filtering pixels by value and identifying the pixel of the greatest value in any given area. Finally, the pixels neighbouring an identified incident pixel are processed to reconstruct any events that have resulted in charge being shared across multiple pixels. Processing the X-ray data in this way can drastically reduce its size, and corresponding storage and transmission requirements, with a minimal impact on the data's science utility. For this reason, detection and reconstruction algorithms are usually implemented on board a space based instrument. Raw frames are rarely transmitted to the ground.

4.3.1 Image calibration

The intention of image calibration is to remove any systematic effects of the X-ray detector on the data. The first step for any of the detectors of this thesis is the removal of the base offset on all pixel values, which is the result of background signal: optical light leakage, dark current generation, and deliberate offset used to prevent non-linear behaviour in the readout amplifiers and ADC. This is generally achieved by measuring a 'dark pixel value' in a set of frames with no X-rays.

This step can also include pre-screening of any pixels known to produce erroneous data, for instance due to dark current defects, to ensure that they do not contaminate further data analysis.

4.3.2 Event detection

X-rays are detected as pixels with a value above a threshold. Event detection proceeds on the basis that X-rays generate more electrons than would be expected solely from noise sources. The threshold is set to avoid false X-ray detections, often three to five times the pixel rms noise value is chosen depending on how critical the rejection of false X-rays is. It is also useful to collect groups of adjacent detected bright pixels which are likely to be related to the same X-ray. Detected X-rays will often then be extracted from the image into small regions of interest (ROIs), centred on the brightest pixel in any grouping of adjacent bright pixels, for further analysis.

4.3.3 Event reconstruction

The ideal X-ray interaction, for the detectors and application of this thesis, is recorded in a single pixel. However, often pixel-edge and field free interactions will result in X-ray charge being collected in multiple pixels. Depending on the application, such detections could be discarded. However, there are often significant gains in sensitivity to be made by reconstructing such events and including them in further X-ray analysis (Owens et al., 1994).

Generally, reconstruction is completed by including neighbouring pixels in the detected event if they too exceed a secondary, reconstruction, threshold. Such algorithms have been used in a variety of space based instruments, from many generations of instrument, including the SMILE-SXI (Randall et al., 2020), with modifications to account for CTI; CLASS aboard Chandrayaan-2 (P. H. Smith, 2014), adapted for use with the SCDs of that instrument; and the EPIC instrument aboard XMM-Newton (Pigot et al., 2000), though with restrictions to suit the computation available at the time. Thresholds are usually selected, either ahead of time or dynamically, at a certain level above the background noise level. Additional information can be included alongside any raw event estimated values, including a map of included pixels; the values of surrounding pixels; or the estimated event interaction location, which may be calculated to a sub pixel-precision using centroiding (Soman et al., 2013). With a good understanding of the charge transport behaviour events can often be reconstructed (Lumb & Holland, 1988), however charge transport mechanisms including diffusion and multiple pixel recorded events leave have a large effect on reconstructed event quality (Bootsma et al., 2000).

4.3.4 An example

An illustrative example application of the X-ray detection and reconstruction process is shown in Figure 4.7. Starting with a calibrated image in the top left, pixels with values greater than the detection threshold (200 eV) are identified in the top right. Then, groups of pixels are further analysed to identify the pixel with the greatest value in each 5x5 region, which is inferred to be the pixel in which the X-ray was incident (bottom left). Finally, the pixels in which X-ray charge has been collected are identified (with a reconstruction threshold (60 eV)) (bottom right) and used to calculate a reconstructed event value. Following initial data processing further analysis of X-ray events is possible, to improve rejection of false X-ray events or generate better estimates of X-ray event values.

The example image was captured with a CCD201-20 observing magnesium and fluorine X-ray fluorescence. The example reconstructed X-ray events have odd shapes, the leftmost X-ray does not appear to have spread uniformly. This is because, in this detector, the reconstruction threshold is generally best to set quite low as the per-pixel noise penalty for pixel inclusion is small. This means that pixels with little collected charge at the edge of the X-ray event can be included, however these pixels are prone to being pushed above or below the noise floor resulting in the odd shapes.

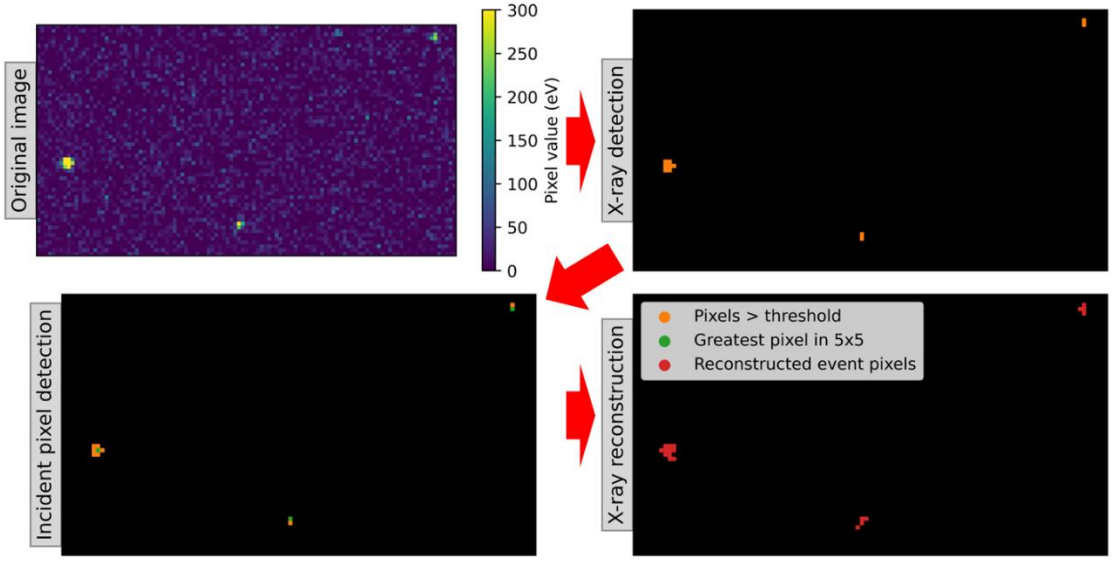

Figure 4.7. Example processing of image extract in top left to extract likely X-ray events. Colour scale in raw image has been chosen to highlight pixel values close to detection and reconstruction thresholds (200 eV and 60 eV respectively), the three pixels in which an X-ray is inferred to have been incident have values well above this scale.

4.4 Noise and uncertainty mechanisms

A key challenge of the use of solid state image sensors for the detection of X-rays is the understanding, and mitigating where possible, of the various noise sources affecting the eventual output measurement. Many of the noise sources are derived directly from noise within the detector, covered in section 3.5, so shall not be repeated here. Some sources are specific to the interaction of high energy photons with the sensor and photon counting.

Generally, these noise sources will manifest as an increase in uncertainty in the energy measured in any given event and result in a loss of energy resolution.

4.4.1 Fano noise

Charge generation uncertainty due to variance in energy absorption in a medium was identified first in gas-based detectors (Fano, 1947). Similar mechanisms mean that there is an irreducible variance in the number of charges generated by an X-ray in any silicon X-ray detectors.

This noise source affects photon counting detectors, it is often used to replace the shot noise seen when measuring the arrival of many photons at an optical sensor modified by some value, a Fano factor, which is determined by the X-ray detector material.

$$\sigma_{fano}^2 = F.E_{ph}/\omega$$

Where F, is the Fano factor, takes the value of 0.115 in silicon (Alig et al., 1980), E_{ph} is the photon energy in eV, and ω is the eV to electron conversion ratio. The Fano noise is due to uncertainty associated with the absorption of energy and generation of charge, the correlation of charge generation sites in the vicinity of the absorption volume leads to sub-Poissionian behaviour: a Fano factor of less than 1. Though Fano factor commonly appears in the noise budget equations of this thesis as a replacement for photon shot noise, it is a separate noise source.

Fano noise is the fundamental limit of energy dispersive spectral resolution (providing the values of Figure 4.8). While better energy resolution may be achieved, it requires wavelength dispersive instrument elements such as gratings. Such additions distribute photons spatially in proportion to their energy and greatly increase computational complexity when attempting imaging-spectroscopy.

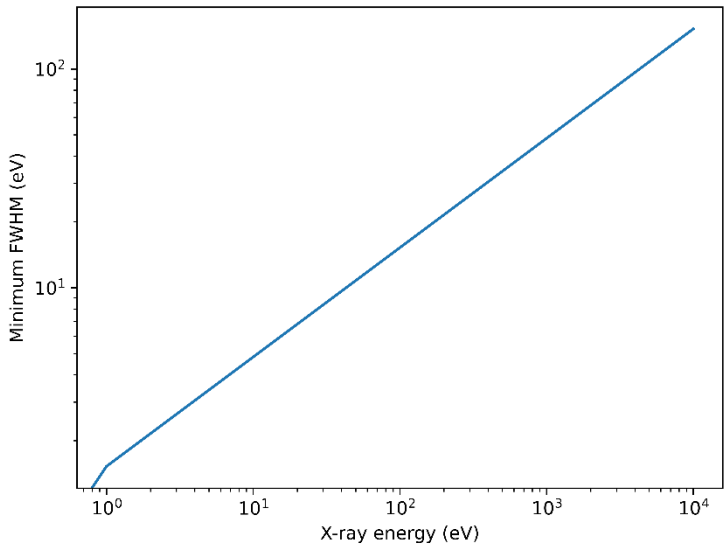

Figure 4.8. Minimum X-ray peak FWHM in a silicon-based X-ray detector due to Fano noise.

4.4.2 Pileup

A clear issue with trying to record individual photon interactions is the possibility of multiple interactions affecting any given pixel, given the term pileup. This is usually solved by lowering the photon flux, reducing the arrival rate of photons for any given pixel, or increasing the detector framerate, reducing the probability of multiple photons arriving at a pixel within the same frame. Pileup can create energy spectrum artifacts, peaks at multiples of bright fluorescence peaks, or as a combination of any bright peaks. Usually, this is less of an issue in flux constrained scientific applications, however it can be readily induced under laboratory conditions with a strong X-ray source, demonstrated in Figure 4.9.

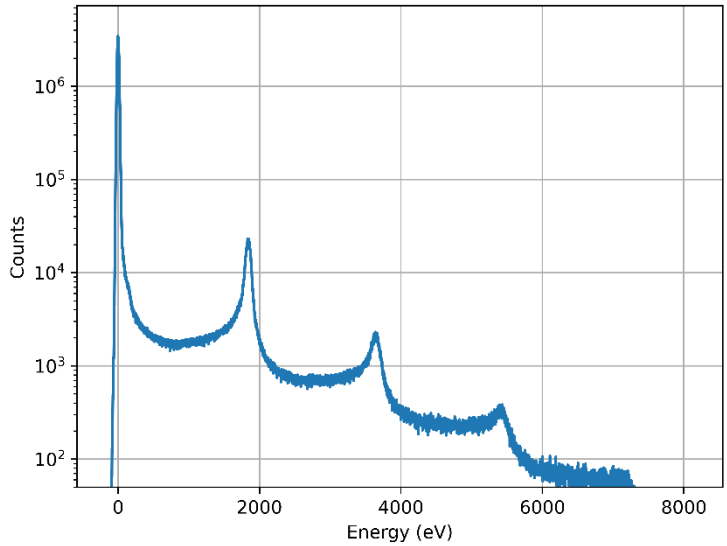

Figure 4.9. 1900 eV X-ray raw pixel energy spectrum showing primary X-ray peaks and subsequent peaks formed by pileup. This spectrum was collected at the BESSY-II synchrotron soft X-ray beamline which can produce high X-ray fluxes.

4.4.3 Event reconstruction uncertainty

An unavoidable issue with the method of event reconstruction described in section 4.3.3 is that the thresholding of pixels will introduce additional uncertainty into the measurement of the value of any given event. This will occur both because an uncertain amount of charge will be excluded by thresholding, and because an unknown (ahead of time) number of pixels are added into each event increasing the amount of per-pixel noise.

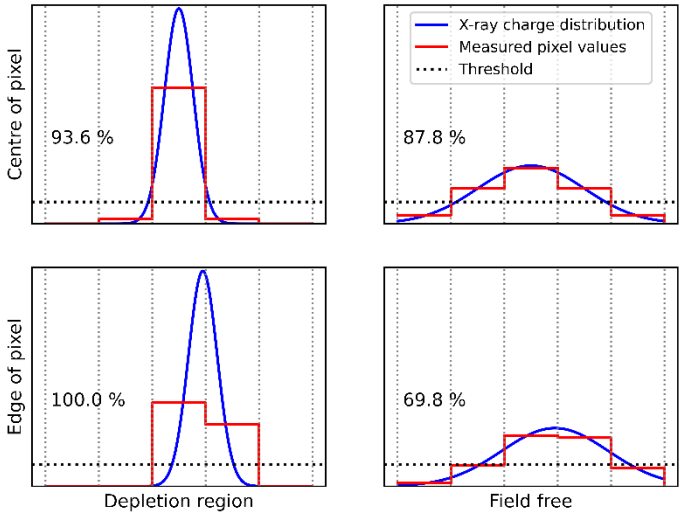

Figure 4.10. A one dimension illustration of reconstruction thresholding resulting in the exclusion of charge in four archetypal events with the same integral value. The percentage of event charge recovered by summing pixels above the example threshold is indicated in each plot.

Event reconstruction can exclude the most X-ray generated charge when many pixels contain close to the reconstruction threshold values' worth of charge, itself an appreciable portion of the total charge expected, illustrated in Figure 4.10. This occurs in two situations. The first is when X-ray charge is expected to spread over many pixels, for example due to a large field free region, in this case recovering the tails of the charge distribution can become challenging and we may expect many pixels containing X-ray charge to fall below it. In the second situation a very noisy detector necessitates a high reconstruction threshold, in which case even moderate charge spreading can result in much charge being excluded. In both scenarios the amount of charge excluded can be minimised by simply reducing the reconstruction threshold, however it will be shown that this is not suitable for most X-ray detectors and that there is a trade-off between charge exclusion and the inclusion of per-pixel noise which often leads to a minimum viable reconstruction threshold.

The recovery of distribution tails is seen as a particular concern in modern X-ray detectors for upcoming flagship astronomy missions. These are expected to use small pixel, thick, detectors in which charge is highly likely to spread beyond incident pixels. The issue of this uncertainty is driving the exploration of more exotic event reconstruction methods (LaMarr et al., 2022).

This source of uncertainty is highly dependent on device properties and can be greatly enhanced or mitigated by X-ray data handling. For this reason, chapter 6 includes a more thorough prediction of the reconstruction uncertainty mechanisms.

4.5 Effects of the space environment

A key attribute of the instruments considered by this thesis is their location in the space environment. This has a critical impact on the achievable performance of the X-ray detectors used because of radiation, and radiation induced damage. The effects on X-ray detector performance range from gradually increasing noise through to catastrophic device failure. This section covers the composition of the radiation environments encountered by the instruments of this thesis, and how these environments are understood to affect detector operation.

The effects of radiation damage are a major difference in the behaviour of ground-based and space-based X-ray detectors. To a small extent ground-based X-ray detectors are affected by the space radiation environment though shielding from 100s of kilometres of atmosphere can effectively minimise issues. Radiation shielding for a space-based detector is not nearly as generous, design constraints mean that there is a large pressure to minimise the mass allocated to shielding structures. Therefore, there is often a question on the upper bound on radiation that can be tolerated by a detector.

The effects of the space radiation environment are replicated before flight by subjecting X-ray detectors to doses equivalent to those expected to be encountered during flight, usually requiring the use of specialised facilities to act as a controllable source of radiation. These irradiations seek to replicate the effects of the radiation environment expected to be encountered, though usually with far higher dose rates to ensure experiments can be completed in a reasonable length of time. Such planned irradiations are a key step in the characterisation of a detector prior to flight. This is to confirm an X-ray detectors behaviour meets requirements at expected end of life radiation doses, and to provide information to instrument operators and users about likely detector behaviour (Parsons et al., 2020). Such experiments have not been performed within the body of work covered by this thesis, though the results of previous irradiations are critical to the findings of chapter 5 and are strongly recommended as follow on work from chapters 6 to 8.

4.5.1 The space radiation environment

The source of most radiation affecting the X-ray detectors for the instruments of this thesis is the sun, as the local source of photons, electrons, protons, and heavier ions. The steady outflow of energetic

particles is known as the solar wind. Solar emissions have a high degree of variability on both long and short timescales. The 11 year solar cycles are characterised by variation between periods of low and high activity. At the time of writing the Sun is at the peak of solar cycle 25 (SILSO World Data Center, n.d.), meaning that analysis of past data from CLASS and projections for AXIS are both more concerned with conditions during quieter periods of the cycle. On shorter timescales solar flares and coronal mass ejections (CMEs) can result in significant enhancements of local radiation levels, particularly protons and heavy ions (Janesick, 2001 pp. 723). Extra-solar radiation is also a concern during periods of quieter solar activity, when the sun's magnetic field is weaker.

The impact of the radiation environment experienced by an instrument on its performance makes the accurate estimation of the environment critical during instrument design. There is often a large degree of complexity of the radiation environment, especially the relationship between shielding and mission parameters to the nature and size of the dose received. Throughout the work of this thesis ESA's space environment information system (SPENVIS) (Heynderickx et al., 2002) has been used. SPENVIS incorporates different models of trapped, solar and galactic radiation, alongside interfaces for inputting spacecraft coordinates and shielding structures to generate dose estimates.

4.5.1.1 Low Earth Orbit

For Earth orbiting X-ray detectors the effect of radiation trapped in the Earth's magnetic field must also be considered. The radiation environment of low Earth orbit (LEO) is dominated by the Van Allen Belts, regions of trapped charge resulting from the Earth's magnetic field capturing and trapping incoming charge particles. The Van Allen Belts consist of an inner and outer belt, the inner primarily consists of both electrons and protons, while the outer is dominated by electrons, concentration maps are shown in Figure 4.11 along with the altitudes of typical satellite orbits. In both regions charged particles travel along the magnetic field lines, getting reflected between the north and south poles.

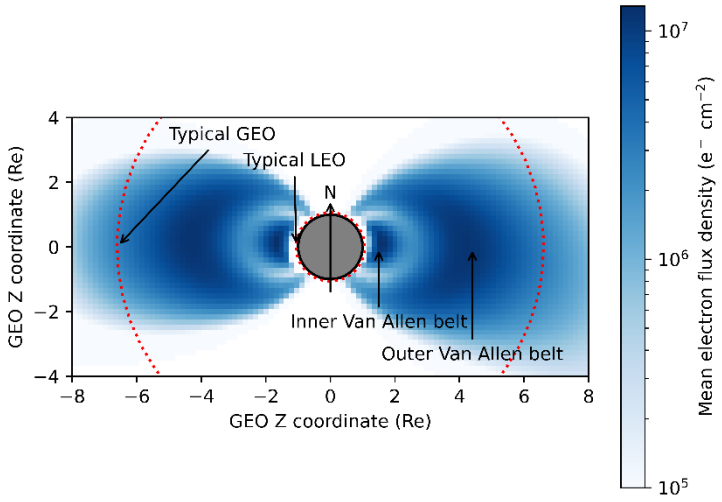

a)

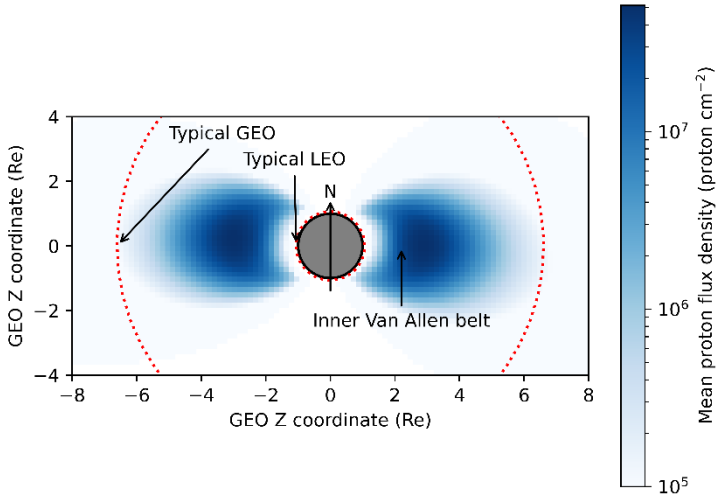

b)

Figure 4.11. A map of (a) trapped electron and (b) trapped proton flux densities due to the Van Allen belts in the near Earth environment. Charged particle fluxes have been drawn from the IRENE model of the Earth's trapped radiation environment (Ginet et al., 2013). The model time was set to noon, the Sun (and Earth's prime meridian) are to the right of the figure. Two typical orbital altitudes have been labelled, satellites on these orbits as shown would pass over the Earth's poles. Axis units are in Earth radii.

The belts have their greatest altitude over the equator. Away from the equator the altitude of the belts decreases until they intersect with the atmosphere in the polar regions, the Auroral horns. In addition, an offset in the Earth's magnetic dynamo, the origin of its field, results in a region of increased particle density over the South Atlantic, the South Atlantic Anomaly (SAA) (Figure 4.12). Though these macroscopic features are largely consistent there is a high degree of variability in the

radiation fluxes, shapes, and sizes of the Van Allen belts. The belts over any given part of the Earth's surface are subject to both diurnal variations and variations due to changes in solar activity.

The complex structure, variation, and composition of the Earth's trapped radiation environment make the use of thorough, verified, modelling tools particularly important. The SPENVIS interface has been used throughout this thesis.

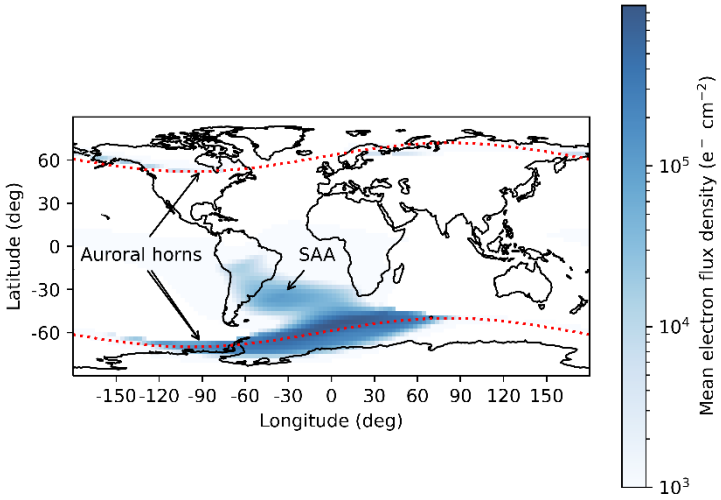

a)

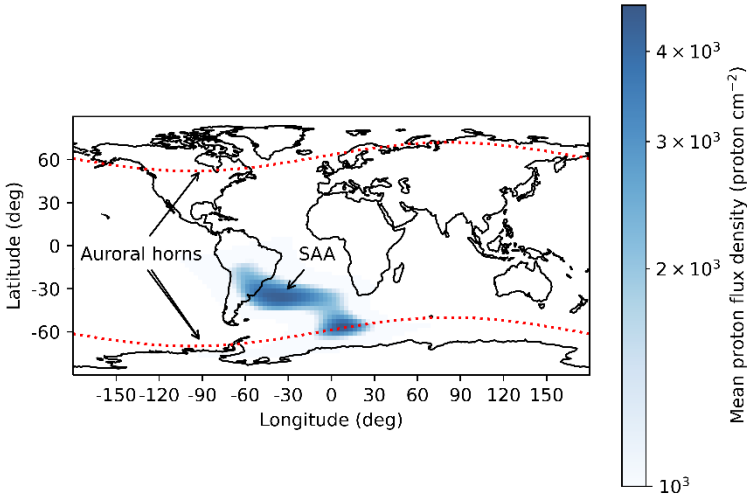

b)

Figure 4.12. Map of mean a) electron, and b) proton flux at 400 km altitude overlaid over a map of the Earth, showing the Auroral horns and SAA. Charged particle fluxes have been drawn from the IRENE model of the Earth's trapped radiation environment (Ginet et al., 2013)*. Model date was set to 20 April 2023, on which day the Auroral horns were not expected to be prominent at the modelled altitude.*

4.5.1.2 Instrument secondary radiation

In addition to any incoming radiation from external sources, an X-ray detector is also subject to any secondary radiation from the instrument in which it is housed (Hall et al., 2018). This can include the introduction of background signals (particularly for an X-ray detector), or the creation of secondary particle showers with the potential to damage the detector in the same way as external radiation.

As behaviour that depends on both the external radiation environment, the structure of the X-ray detector's instrument, as well as the X-ray detector itself, secondary radiation is an ongoing area of research (for instance the work of Davis (2021)).

4.5.1.3 Shielding

For the instruments of this thesis the radiation shielding of the X-ray detectors has been primarily composed of aluminium, and when analysed made use of spherical shell models in which shielding is simplified to a spherical shell of uniform composition and thickness. Where scope and resources permit, however, more complex shielding and modelling methods can provide critical reductions in, and insights into, the actual radiation environment likely to be experienced by an X-ray detector.

The experience of previous missions has shown the importance of detailed simulations to model the effect of the spacecraft structure, including the optic (Prigozhin et al., 2000). Furthermore, heterogeneous shielding structures, including graded-Z shielding, have been proposed for future X-ray observatories as a way of reducing secondary radiation experienced by X-ray detectors (von Kienlin et al., 2018).

4.5.2 Radiation effects on X-ray detector performance

Incoming radiation can interact with an X-ray detector in one of two ways: electrically, ionising the device material; or through nuclear collisions, that is non-ionising effects. Of the two, ionising effects are often be dealt with most easily, as this is what the detectors are intended to measure. However, there are still some damage mechanisms that must be accounted for: single event effects in active devices built into the detector, and the introduction of background non-science signals. Non-ionising damage can lead to long term irreversible damage, including CTI and dark current enhancement, which can determine the maximum period of operation for an X-ray detector in a given environment.

4.5.2.1 Ionising effects

Ionising particles are distinguished as generating free charge as they traverse a volume. Ionising particles can be protons, photons of energies much higher than the X-ray photons of this thesis, or heavier ions.

In a neutral, field free, region of a detector ionising effects can have a very low impact as generated charge will usually recombine. However, in regions with an electric field, or a diffusion gradient, the generated electron hole pairs may separate. This can lead to the generation of background signals. In silicon oxide, because hole carriers have a far lower mobility, this can also result in many positive charges building up within the silicon oxide layers. In a MOS capacitor or MOSFET these will shield the active silicon from the gate voltage and result in a higher required gate electrode voltage for equivalent behaviour, termed flatband voltage shift (Janesick, 2001 pp. 760). Both processes require the presence of electrical fields, in an inactive image sensor charge will recombine and the effects of the radiation will be less. For this reason, image sensors will often be turned off while traversing regions of high radiation intensity.

The standard unit used to quantify ionising radiation dose in X-ray detectors is the rad(Si), the specification for silicon is required as dose is absorption medium dependent.

4.5.2.2 Single event effects

The sudden deposition of charge from a single particle of incoming ionising radiation can have a large effect on semiconductor devices. These are collectively known as single event effects, they include:

- Single event upsets (SEU), in which the deposition of charge changes a memory state.
- Single event latch up (SEL) in which the deposition of energy triggers the activation of a parasitic thyristor in CMOS manufactured devices (Johnston, 1993).
- Single event gate rupture (SEGR) when the ionised track left behind by a high energy radiation particle can result in a conductive path through a layer of previously insulating material. Most commonly occurring in the clock isolation oxide (Sexton et al. 1997), SEGR can cause catastrophic damage via ohmic heating.

Single event effects (SEEs) were a particular concern during initial development of space based CIS (Rushton, 2018) due to the integration of computational and memory elements and thin oxides associated with CMOS manufacturing techniques. However, mitigation strategies implemented at a chip design stage and in supporting electronics mean that these effects are no longer explicitly considered for the X-ray performance of current X-ray detectors, instead the greater focus is on CTI and dark current enhancement, and instrument background.

4.5.2.3 Instrument background

A clear issue facing a charge sensitive X-ray detector is the charge generated by incident radiation particles interfering with science signals. Incident radiation of concern can be of any type with ionising

effects, protons, electrons, and photons with energies outside of the science ranges of interest including cosmic rays. Cosmic rays can be detected even in ground based testing (critical for chapter 7 of Murray, (2008)), with the potential for a large amount of charge generated in many pixels for obliquely incident rays. This can pose a risk of saturating a down-link limited instrument if all pixels with deposited charge are detected and reported as X-ray events (Pigot et al., 2000).

Instrument background signal can be mitigated in a variety of ways, the most obvious being the rejection of reported X-rays with energies outside the expected science bands. Oblique cosmic rays produce long continuous streaks within a single frame, which can be identified and used to screen any associated event detections. Finally, machine learning has been trialled for rejection of background signals during observations of diffuse X-ray sources with a low brightness. Because the expected X-ray flux is low, and well distributed, there are further gains that may be made employing machine learning to identify non-oblique charged particle interactions and secondary particle spray (Wilkins et al., 2022).

Finally, X-ray fluorescence of the instrument itself can be an issue, particularly if the instrument is made of elements that fluoresce at important energies for science objectives. This has been seen in the XMM EPIC cameras with the distribution of X-rays at Cu Kα, Si Kα, and Al Kα energies having a close correlation with the expected location of copper, silicon and aluminium within the instrument (Lumb et al., 2002).

4.5.2.4 Non ionising effects

Incoming particles, both charged and uncharged, also have the potential to displace atomic nuclei within the silicon lattice, leading to defects that can display altered behaviour with regard to charge generation and recombination. If the energy deposited by the incoming radiation particle is greater than the energy required to dislocate an initial atom the initially dislocated atom (the primary knock-on atom (PKA)) will gain the excess as kinetic energy and can dislocate further atoms in the lattice, leading to a cluster of defects in a small volume (Janesick, 2001 pp. 787).

In the ideal silicon based X-ray detector there are very few unique atomic species, silicon, dopants, oxygen, nitrogen, and contamination carbon, bound into largely uniform crystal structures. For this reason, defects can largely be attributed to a specific dislocation (or dislocation complex) with known, and explored properties (Watkins, 2000). The work of this thesis does not address specific defects, instead looking at the cumulative effect of many such defects. While the cumulative number of defects is approximately proportional to dose, the effect, and evolution, of lattice defects is complex.

Non ionising damage effects are proportional to the non-ionising energy loss (NIEL) of incoming radiation. It is common practice to express non-ionising doses as an equivalent dose of particles at a fixed energy, as this simplifies comparisons to test data generated with a population of mono-energetic mono-species particles. Within the context of this thesis the NIEL scaling values of Srour et al. (2003) have been used implicitly, and non-ionising radiation doses expressed as an equivalent fluence of 10 MeV proton cm^{-2}, intended to be broadly representative of the conditions in LEO (Bush, 2018).

4.5.2.5 CTI degradation

The creation of lattice defects associated with non-ionising damage has a large impact on CTI by generating low energy charge trapping sites. These can lead to a large enhancement in CTI observed in a space based detector and severely impact the accurate collection of charge from individual X-ray events. CTI in response to radiation damage in the space environment is an ongoing area of research with the effect of cryogenic irradiation and thermal annealing being of particular interest for future (Parsons et al., 2020), and active, instruments. The CCDs of the Euclid mission VIS instrument expected to be launched in 2023 will include defect, trap, characterisation capabilities for this reason (Cropper et al., 2018).

The increase in CTI will increase X-ray event value uncertainty and reduce energy resolution. Depending on the charge trap time constants CTI can also introduce skew into X-raw event profiles, smearing the charge from an X-ray across pixels readout after the initial pixel. This can also increase uncertainty in estimates of the interaction location, reducing spatial resolution.

A common mitigation technique for CTI in CCDs intended for use in radiation environments is the use of a supplementary buried channel (SBC), an additional n^+-type implant to ensure that charge collected is stored (and is transported) through only small section of each pixel. This reduces the effect of traps outside this area and increases the radiation dose that a detector can receive before exhibiting an equivalent level of CTI to an unmodified device. An SBC is one of the two modifications made to the CCD201-20 of chapter 6 for the CCD311 radiation hard variant (Morrissey et al., 2023), while the CCD236 of chapter 5 includes SBC-like structures to improve radiation tolerance (Smith 2014 pp. 73-79).

4.5.2.6 Dark current degradation

The creation of lattice defects also increases the rate of thermal charge carrier generation, increasing dark current. The shot noise associated with dark current generation will reduce energy resolution and reduce the sensitivity of the detector to very low energy X-rays.

Additionally, incoming radiation has the potential to increase dark current by disrupting dark current passivation. This is specifically an issue for front surface oxide passivation, where the vacant Si-SiO_2 interface bonds are commonly neutralised by flooding this region with hydrogen. Incoming energetic particles can break an H-Si bond, the hydrogen atom is then free to combine with another free hydrogen atom, form molecular hydrogen, and diffuse out of the detector (Janesick, 2001 pp 757).

4.5.3 Other design considerations

The investigations of this thesis have been enabled by the emergence of new demanding X-ray spectroscopy applications in a technology environment that is increasingly valuing resource constrained instrument implementations (Millan et al., 2019). This includes the emergence of CubeSats as useful scientific tools in swarms and hazardous situations (NASEM, 2016). At the same time, the promise of a new class of X-ray detector based on CISs are beginning to show (Heymes, Stefanov, et al., 2020; Narukage et al., 2020). Therefore, there has been an effort, and success, in implementing science grade X-ray instruments with lower demands on the instrument design. From this perspective the following results chapters may be divided into: an analysis of CCD based low-resource X-ray detectors; the comparison of a high resource CCD and low resource CIS detectors for a demanding application; and further verification of the immature CIS technology to support a decision, from the perspective of science potential, that is heavily weighted by engineering design considerations.

For the X-ray detector developments covered by this thesis the most important further consideration of the instrument environment is the thermal control of the X-ray detector. To achieve their near optimum performance, CCD-based X-ray detectors require operation temperatures well below standard spacecraft operation temperatures. This places a large heat load on the rest of the spacecraft which itself can face severe thermal radiation limits (in the extreme case of CubeSats the total thermal radiation from the spacecraft is limited to a few tens of watts (Selva & Krejci, 2012)). Furthermore, cooled CCDs can act as cold traps collecting any outgassed materials from the rest of the instrument. This effectively adds additional dead layers on the illuminated surface of the device, severely impacting soft X-ray sensitivity. The loss of soft X-ray sensitivity due to condensing contaminant layers is an ongoing concern for the Chandra ACIS, with contaminant build up continuing decades after launch (Plucinsky et al., 2022). This has led to a development pressure for a high temperature, science quality, X-ray detector

4.6 Summary

CCDs and CISs can be used as highly effective X-ray detectors, converting incoming X-rays into packets of charge that can be measured like those originating from photons of other, longer, wavelengths. The mechanism for energy absorption in an X-ray detector means that there is a predictable relationship between the number of charge carriers generated by a photon, and its energy. Operating in a photon-counting mode leads to new ways of interpreting the data collected with an X-ray detector, permitting imaging spectroscopy, the recovery of information in the spatial, energy and time domains, a potent scientific tool. Estimating the energy of each incoming photon is affected by noise sources which restrict the achievable energy resolution. Careful handling of X-ray data is required to ensure that further uncertainty is not embedded into data following event reconstruction.

Finally, the space environment is a defining characteristic of the X-ray instruments considered by this thesis. Without the shielding provided by the atmosphere at ground level, X-ray detectors are degraded by radiation in the space environment. For interplanetary instruments this is largely dominated by the solar wind and cosmic rays. For instruments in low Earth orbit this is dominated by the trapped radiation of the Van-Allen belts, protons and electrons trapped by the Earth's magnetic field concentrated into toroidal regions with high concentrations. Irradiation can act to increase the effect of dark current and CTI by introducing lattice defects and disturbing the carefully constructed structures of an X-ray detector. It can also result in entirely new sources of noise and failure, fluorescing the instrument itself, and leading to a variety of single event effects.

5 Evaluation of soft X-ray detectors in lunar orbit

This chapter covers analysis of the radiation damage experienced by SCDs in lunar orbit, and verification of the damage observed against expectations derived from ground-based testing. Within the context of the work covered by this thesis, this analysis provided experience with the data produced from a soft X-ray photon-counting spectrometer during flight. In addition, the development of the SCD was a direct response to some of the challenges posed by space-borne CCDs that are also addressed by the CIS X-ray detectors evaluated later. The analysis of this chapter is focussed almost entirely on energy resolution and energy spectra because the SCDs are not imaging detectors.

The SCDs under investigation are the X-ray detectors used by the Chandrayaan-2 Large Area Soft X-ray Spectrometer (CLASS), an instrument aboard the Chandrayaan-2 currently in orbit around the moon. Launched in 2019, CLASS has continued operation well beyond its originally planned 12-month lifetime and has been able to map the surface abundance of a variety of metals including, for the first time, sodium across most of the lunar surface (Narendranath et al., 2022). The work within this chapter was completed largely at the request of the instrument operators to verify the SCDs were behaving as expected and ensure that they were still suitable for completing the lunar science goals of CLASS.

The primary focus of the investigation has been to spot changes in noise behaviour that might have indicated radiation damage. With the information available the total noise in each device could be measured at many different stages of the mission and dark current could be measured before and after CLASS's transit to the moon. Basic modelling indicated that CTI would not be observable in the available data.

The work of this chapter sits apart from the work of chapters 6 to 8, because of its focus on CLASS, as opposed to AXIS, and use of a highly streamlined SCD rather than current state of the art X-ray detectors. Therefore section 5.1 briefly covers the background and specific context of the CLASS SCDs. Ultimately analysis of the SCDs highlighted the challenges faced by space borne X-ray detectors, and the SCD itself represents an initial attempt to tackle the issues with CCDs addressed by the detectors considered for AXIS.

The work within this chapter provided confirmation of earlier CEI results (in particular Smith (2014)) and was used to assist the CLASS instrument calibration team. The results presented in section 5.3.1 appeared in (Jones, Crews, Endicott, et al., 2022).

5.1 Background

5.1.1 CLASS

The CLASS instrument is intended to map the elemental composition of the Lunar surface by detecting soft X-ray emissions excited from the surface of the moon by incident solar radiation. The composition of the lunar surface is important for answering key planetary science questions relating to the formation of the moon itself and the history of the inner solar system, due to its relative age. Additionally, an understanding of the elemental abundances is critical for the future utilisation of lunar resources to support upcoming space missions and development. Observation of soft X-ray fluorescence permits simultaneous identification of elements present in the material of the first few centimetres of the lunar surface, and a measurement of their abundance. Making these observations from an orbiting platform permitted CLASS to achieve near global coverage in its first year of operation (Narendranath et al., 2021). Instruments using this principle were flown as early as 1968, aboard Luna 12 (Cheremukhin et al., 1968), and have been re-flown, harnessing technology improvements for increased performance on many more missions. CLASS sought to improve on these previous measurements with an extended energy sensitivity range, which has permitted the identification of sodium and oxygen for the first time with this method (Narendranath et al., 2021, 2022).

CLASS (image in Figure 5.1) consists of 16 CCD236 swept charge devices, optimised for soft X-ray photon counting, collimators to restrict the field of view of the X-ray detectors, and the associated supporting electronics and hardware (Radhakrishna et al., 2020). The CCD236s are organised into four sets of four, each set is labelled a ‘quad’, with signal processing and temperature control largely completed on a quad-by-quad basis. The CCD236 is the focus of this chapter and will be described in more depth later. The collimators consist of a gold coated copper grid which define a 12.5 km field of view footprint on the lunar surface, and mapping is achieved by correlating observed fluorescence time with the footprint location. The collimator is also used to support an aluminium optical blocking filter designed to prevent optical photons from reaching the detectors. Previous missions had demonstrated the importance of protecting the X-ray detectors while transiting to the moon, therefore the SCDs and collimators were covered with a shield door prior to arrival at the moon. This was made of aluminium that was approximately 12 mm thick. The opening mechanism was one-shot, meaning that once the door was opened it could not be closed again. Attached to the inside of the

door was the final component of interest to this investigation, a set of iron-55 X-ray sources used for SCD calibration. Prior to launch and before science operation commenced these were used to assess the performance of the SCDs. They provided strong, reliable fluorescence peaks because of their proximity to the detectors.

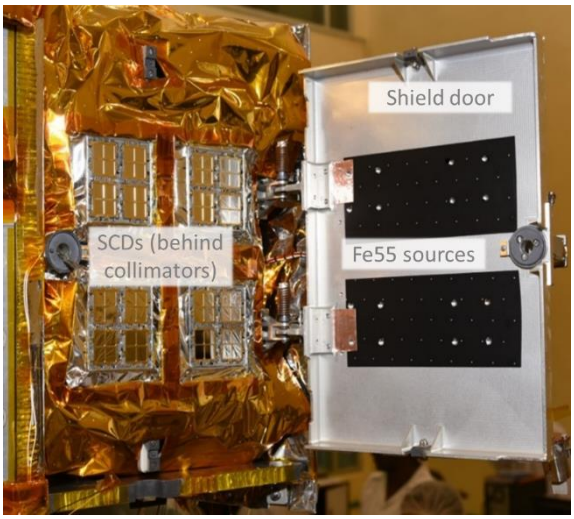

Figure 5.1. CLASS before launch with various elements indicated. Image credit: ISRO.

CLASS is mounted alongside the other lunar observation instruments of Chandrayaan-2 and is kept pointing in the nadir direction as the satellite orbits.

To achieve global coverage, Chandrayaan-2 was placed in a polar orbit around the moon with an average altitude of 100 km. The angle between the solar vector and the plane of this orbit is not fixed but changes slowly with time. The requirement for incoming solar radiation to fluoresce the observed X-rays means science operations are conducted as the spacecraft crosses above the dayside of the moon. For the same reason the better observations are generally made during periods of high solar activity and the best observations have been made as a solar flare reaches the moon (Narendranath, Pillai, and Sharan 2019). Finally, CLASS can be used as a limited particle detector for more than X-rays, and there have been repeated observations of anomalous activity from the instrument as it passes through the geotail, the trailing portion of the Earth's ionosphere.

Initially Chandrayaan-2 was planned for launch in 2016, however it was delayed until mid-2019. Though it was intended for a mission lifetime of a year, science operations are continuing. The change in timing has affected the irradiation experienced by the instrument to the different levels of solar activity in 2016 and 2019. Furthermore, continued operation has permitted CLASS to take advantage of the increase in solar activity associated with the start of solar cycle 25. As of mid-2023, science operations are continuing.

5.1.2 D-CIXS and C1XS

CLASS is directly derived from a line of predecessor lunar soft X-ray spectrometer instruments. The heritage of these instruments fed into the design of CLASS and provided some insight into the expected performance of CLASS prior to its flight. The Demonstration of a Compact Inexpensive X-ray Spectrometer (D-CIXS) flown aboard SMART-1 in 2003 (Grande et. al. 2003) and the Chandrayaan-1 X-ray Spectrometer (C1XS) flown aboard Chandrayaan-1 in 2009 (Grande et. al. 2009), used SCDs for XRF mapping of the lunar surface. Both instruments used the CCD54, an earlier version of the CCD236 SCD used by CLASS. Both instruments successfully operated around the moon and returned at least initial data. However their coverage of the moon was not completed, and the detection of sodium by C1XS (Athiray et al., 2014) indicated the potential of further investigation. The evolution across the three instruments have shown a gradual improvement in energy resolution, as shown in Figure 5.2, attributed to the better shielding and lower dose received by the C1XS SCDs compared to the D-CIXS SCDs, and then the improvements of the CCD236 over the CCD54, as discussed below in section 5.1.3.

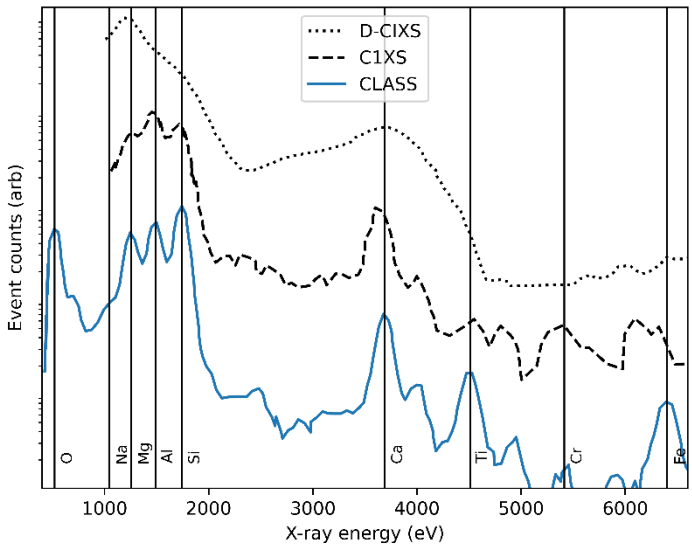

Figure 5.2. Comparison of spectra produced by D-CIXS, C1XS and CLASS showing the gradual improvement in energy resolution. Spectra have been offset to improve readability. Data credit: Grande et al., (2007) *(D-CIXS),* S. Narendranath et al., (2011) *(C1XS),* S. Narendranath et al., (2021) *(CLASS).*

5.1.3 Swept charge devices and the CCD236

The X-ray detectors of CLASS, SCDs, have been introduced in section 2.2.2. CLASS used second generation SCDs, the CCD236 (Figure 5.3), developed from the earlier CCD54 used in C1XS and D-CIXS (Holland & Pool, 2008). Tapered clock electrodes and additional doped regions were added to reduce the charge storage volume. Along with similar measures in the diagonal charge transfer channels, these design changes were intended to reduce the cross section of charge clouds and therefore reduce

their susceptibility to interaction with radiation induced lattice defects, and thus to CTI. The CCD236 also featured an increased sensitive area, increased to four times the CCD54, using a four-quadrant layout which was intended to improve performance in low-flux conditions.

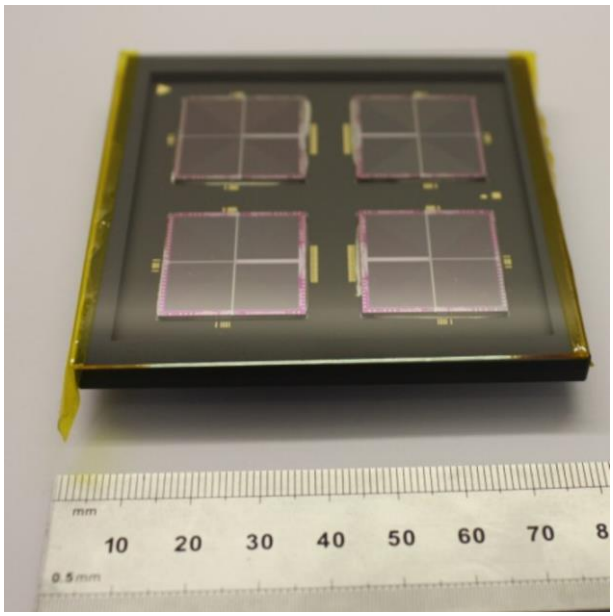

Figure 5.3. A quad package of four CCD236 SCDs, ruler marked in mm for scale. Image credit: Phillipa Smith.

To evaluate the performance of the SCDs during flight, an understanding of the CCD236's behaviour was required. This has been achieved using modelling to interpret the device characteristics, and with reference to ground testing of the X-ray detectors prior to launch.

5.1.3.1 Quantum Efficiency

The QE of the CCD236, estimated using the layer cake model of section 3.4.1.3, is adequate across the energy range of interest for CLASS (> 0.5 from 1 keV to 7 keV), though its QE below 2 keV is hampered because it is a frontside illuminated device. The CCD236 is not fully depleted, leading to partial charge collection at energies at which the additional field free volume contributes significantly to QE. The modelled QE of the CCD236, including estimates of the relative number of split events, is shown in Figure 5.4. These values are known to have good agreement with experimental measurements (P. H. Smith et al., 2014).

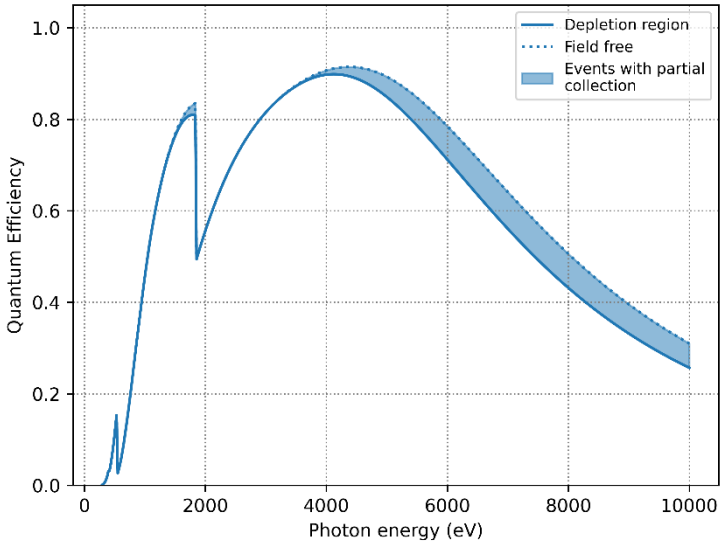

Figure 5.4. QE of the CCD236 showing the 'layer cake' QE prediction which is known to have good agreement with the actual device QE in the range of energies tested (200 eV – 2 keV) (P. H. Smith et al., 2014). *The expected depletion region (solid line) and field free region (dashed line) QE values have both been plotted.The shaded region indicates events that are expected to be absorbed in the field free region.*

5.1.3.2 Energy resolution

Modelling of the CCD236's noise also highlighted its ability to provide good energy resolution over a wide energy range. The FWHM values calculated using the device noise parameters, shown in Figure 5.5, indicates that the sensor achieves energy resolution comparable to the best equivalent CCD or CMOS devices. While designed for operation at -20 °C, and operated at -40 °C aboard CLASS, the CCD236 can provide good energy resolution at higher temperatures.

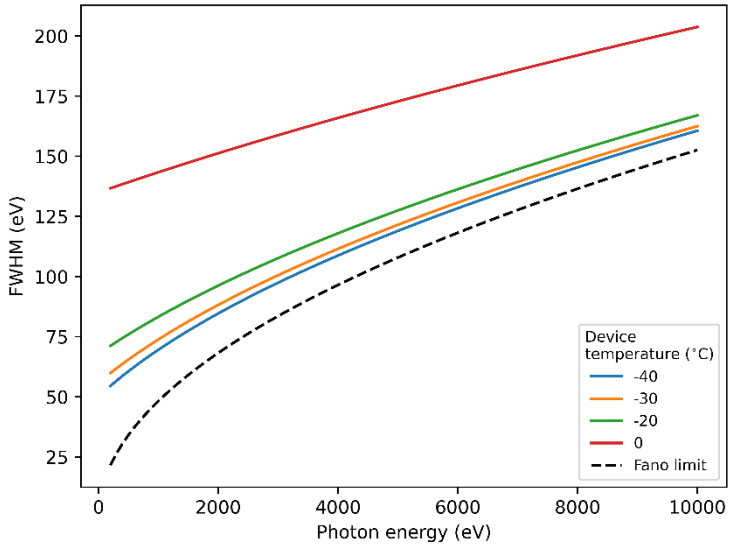

Figure 5.5. CCD236 predicted FWHM for X-ray energy, using the datasheet readout noise and dark current values.

5.1.3.3 Response to irradiation

Previous work completed within the CEI built an understanding of the likely behaviours of the CCD236 after irradiation. This involved controlled irradiations of CCD236 and subsequent characterisation. The target of these investigations was to measure the increase in noise sources and device properties that are understood to be heavily affected by radiation damage.

J. Gow et al. (2015), J. Gow et al. (2012), and Smith et al. (2012) measured the dark current and energy resolution of the CCD236 after irradiations to a 3×10^8 protons cm^{-2} and 5×10^8 protons cm^{-2} 10 MeV equivalent fluence. These fluences were selected to represent the end-of-life dose of the CLASS SCDs. The time and cost associated with a device irradiation often means that only a few fluence values can be explored, therefore testing under worst case conditions was prioritised. When measuring the energy resolution of the CCD236 before and after irradiation Gow and Smith identified a possible linear trend (Figure 5.6). This permits the interpolation of estimated spectral resolution for irradiation fluences within the tested range.

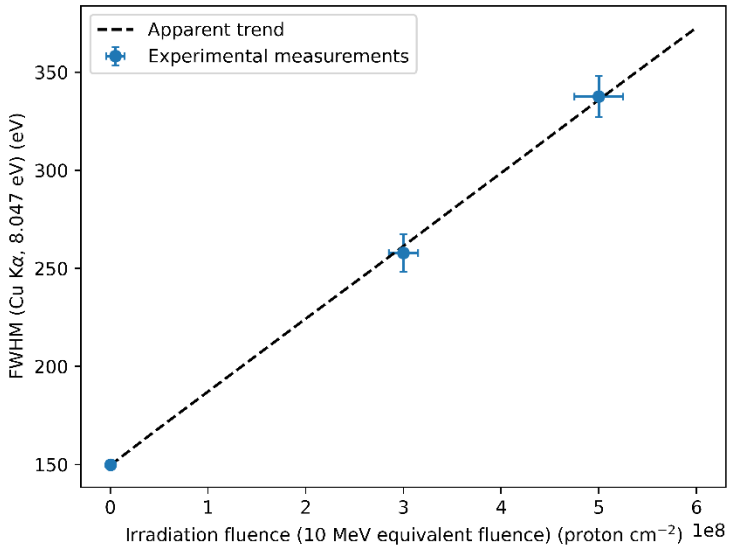

Figure 5.6. Cu Kα FWHM, a proxy for device noise, for device irradiation, reproduced from (Smith, 2014). FWHM is dependent on device noise.

Smith et al. (2015) measured the CTI before and after a proton irradiation to a 5×10^8 protons cm^{-2} 10 MeV equivalent fluence (results in Table 5.1). Spatial information was reintroduced to the SCD readout by using a copper shield to mask all but a small portion of the SCD under test. Their results indicated that an increase in CTI was mostly seen in the vertical and horizontal transfers, rather than in the diagonal channel. The large errors in the measurements were attributed to the small number of transfers made within the device limiting the CTI that was observable.

Table 5.1 CTI measurements of the CCD236 before and after irradiation from Smith et al. (2015). CTI expressed as portion of charge lost per transfer.

Readout path	**Irradiation (protons cm^{-2} 10 MeV equivalent fluence)**	
	0	**5×10^8**
Horizontal	$(8.7 \pm 6.6) \times 10^{-5}$	$(9 \pm 1.8) \times 10^{-4}$
Vertical	$(1.1 \pm 6.7) \times 10^{-5}$	$(8 \pm 1.9) \times 10^{-4}$
Diagonal	$(1.0 \pm 1.1) \times 10^{-4}$	$(0.5 \pm 6.8) \times 10^{-5}$

5.1.3.4 Expected irradiation

To predict the behaviour of the SCDs aboard CLASS their irradiation fluence was re-predicted, taking advantage of the findings of the previous investigation. Although the period covered by the data roughly corresponded to the expected transfer and one year at the Moon mission timeline used by Gow and Smith to plan their irradiations, the mission parameters had changed significantly since their

prediction. It was also thought to be useful to build an understanding of the intermediate levels of irradiation, for which there is now also flight data.

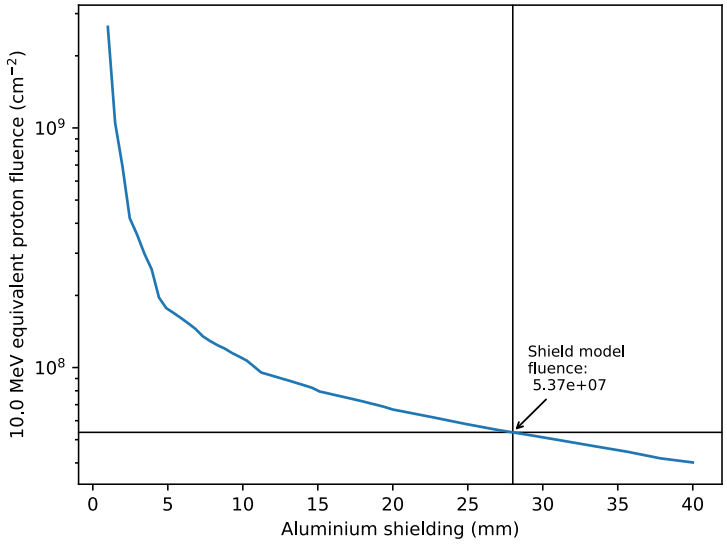

Figure 5.7. CLASS SCD dose for shielding thickness with dose at modelled thickness indicated.

The irradiation fluence prediction was made using the Space Environment System (SPENVIS) (Heynderickx et al., 2002), the orbit parameters of Chandrayaan-2 during its transfer and arrival at the Moon, and the shielding model used in Smith et al., (2012). The expected dose for shielding thickness is shown in Figure 5.7. Transit to the moon includes time spent in the trapped radiation environment of the Earth, while the radiation environment at the moon is dominated by the Sun. SPENVIS indicated a total irradiation fluence of 5.37×10^7 protons cm^{-2} 10 MeV equivalent fluence during transit to the Moon dominated by transit through the Van Allen belts, and negligible further dose received once there (until February 2021). This dose is far less than earlier predictions, primarily because solar activity was extremely low during this period, as shown in Figure 5.8.

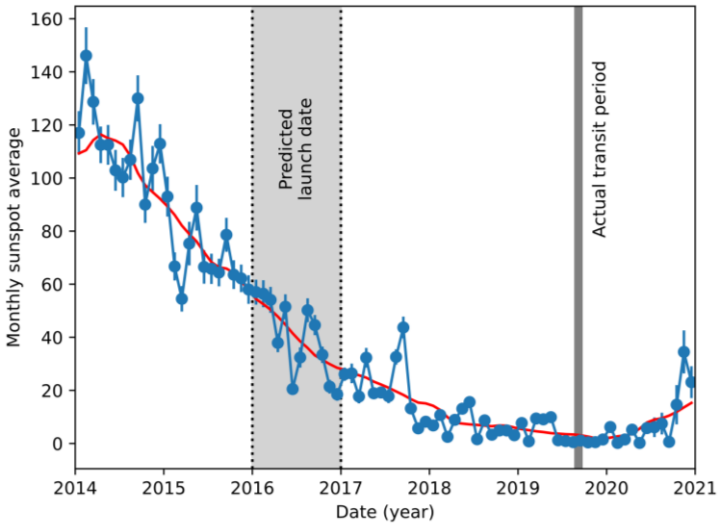

Figure 5.8. Solar activity, represented by the number of sunspots, during the end of Solar Cycle 25 showing the dates that Chandrayaan-2 was initially expected to launch, and when it eventually made the transit to the Moon. Data credit: (SILSO World Data Center, n.d.)

5.2 In-flight data

Three separate datasets were provided by the instrument operators to enable the evaluation of the SCDs aboard CLASS. Partially processed data or 'Level 1 data' was available covering large periods of time and had been partially pre-calibrated enabling the quick analysis of instrument performance required during the opening stages of this investigation. Raw instrument data, or 'Level 0 data', enabled the examination of the performance of individual SCDs, though for more constrained time periods. Finally, calibration information from the early stages of the mission provided clear information that could be used to assess the initial states of each SCD.

Level 1 (L1) data is the format provided by the instrument operators to the wider lunar science community. It consists of pre-processed spectra from each 8 seconds of CLASS operation, combining the events from all operating SCDs after calibration. This data format was useful for examining the broad instrument properties quickly because the combination of events enabled the rapid detection of faint X-ray fluorescence. In addition to the spectra from the SCDs, Level 1 data is packaged alongside instrument information, including its location and orientation.

Level 0 (L0) data from the satellite was largely representative of the raw data produced by the CLASS instrument. Data reduction performed by the instrument itself meant that this data format was a list of time- and origin-stamped events rather than raw SCD readout values. The inclusion of SCD numbers meant that events recorded in this format could be separated by the SCD that recorded them,

permitting the analysis of individual SCDs. The arrangement and numbering of the SCDs, used throughout the rest of this chapter, is shown in Figure 5.9.

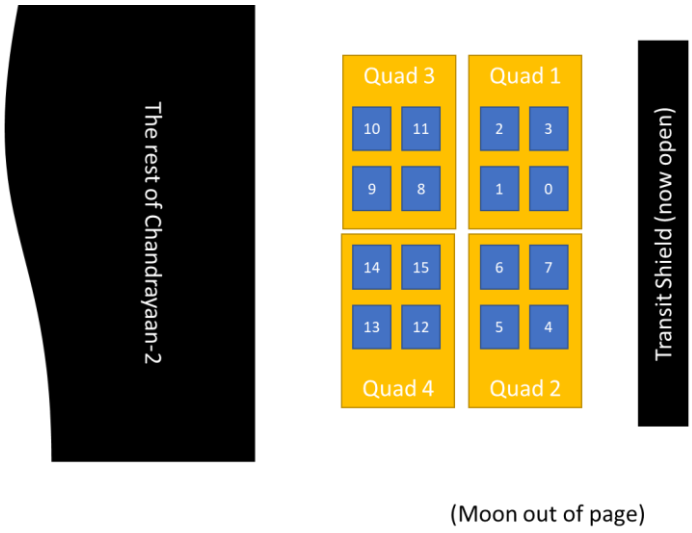

Figure 5.9. Arrangement and numbering of CLASS SCDs and quads.

An example spectrum produced from level 0 data, using events from SCD6, has been included as Figure 5.10.

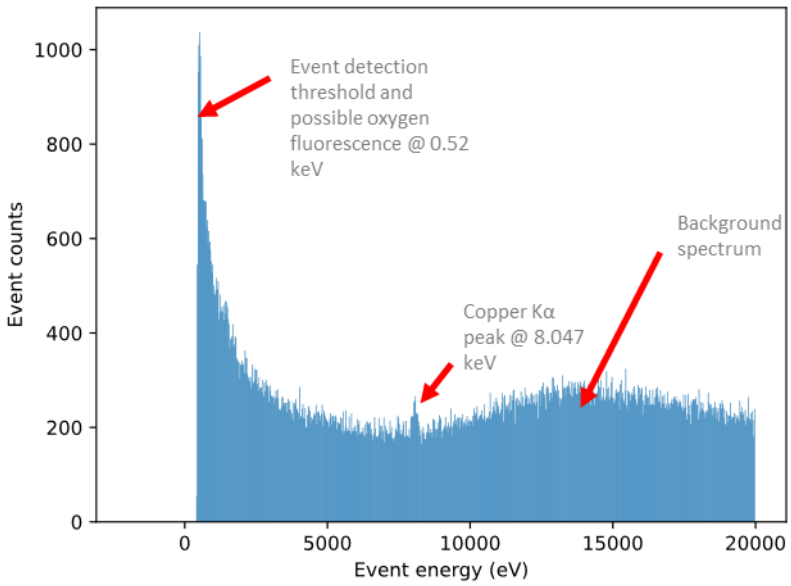

Figure 5.10. Example spectrum generated from Level 0 data from SCD6 in October 2019. Various spectral features have been highlighted.

In addition to the list of events, the level 0 data also included some basic housekeeping information including SCD temperature. The level 0 data was available as two separate datasets, the first included sparse periods of operation adding to many hours' worth of data in October 2019, almost immediately

after science data-collection had begun. The second included 11 minutes of data collected in February 2021.

Finally, the instrument operators provided information gathered during SCD calibration prior to launch and just after arrival at the Moon. This data consisted of FWHM measurements made from the Mn Kα peaks generated by the calibration sources on the shield door at a range of temperatures which provided a wealth of information on the starting condition of each SCD. The calibration data for SCD6 has been shown in Figure 5.11.

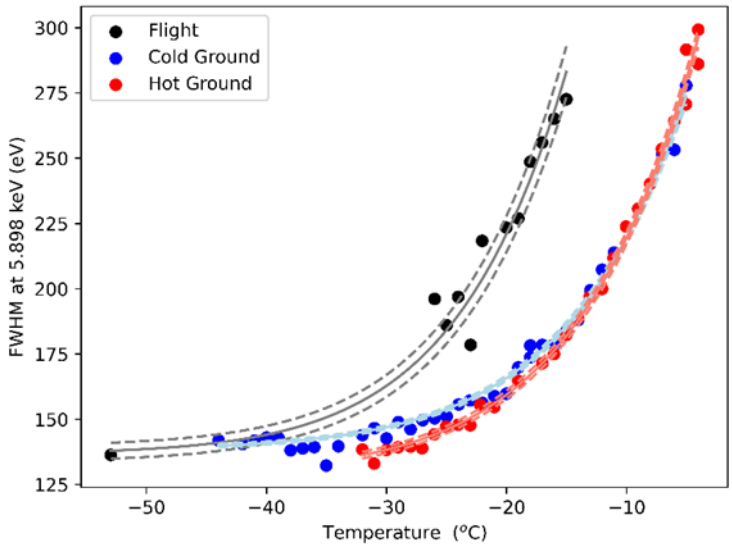

Figure 5.11. CLASS SCD6 energy resolution vs temperature. "Flight" dataset was collected upon arrival at the Moon, prior to shield door opening, ground collected data was separated into hot and cold datapoints, separating measurements made while warming the sensor up (hot soak) or cooling it down (cold soak). The benefits of operating at -40 °C are evident.

Because the SCDs do not record X-ray event positional data, and information about the spread of event charge is removed by the data reduction that occurs within CLASS, the following analysis proceeded based on the behaviour observable across the population of X-rays recorded. This behaviour was chiefly expressed in the observed width of fluorescence peaks and recorded, as per the calibration data, as FWHM.

5.2.1 Initial data parsing

Prior to beginning of analysis of SCD behaviour, an assessment of the available information was required. This included the identification of issues with the data, for example stray light which required the exclusion of certain SCDs, and verification of software to measure FWHM in the available level 0 and level 1 data, which had to be automated due to the datasets' size.

5.2.1.1 Disqualification of fourth quadrant

Examination in the relationships between housekeeping parameters identified optical light leakage issues being experienced by the SCDs of quad 4 (SCDs 12-15). This issue had been flagged by the instrument operators and is thought to have occurred because the collimator for this quad is loose. The issue can be observed by plotting the modal pixel value in each SCD, reported as a zero-offset housekeeping value in the level 0 data, over the course of a few hours (shown in Figure 5.12). The period of this signal in SCDs 12-15 corresponds to the orbital period of Chandrayaan-2 around the Moon.

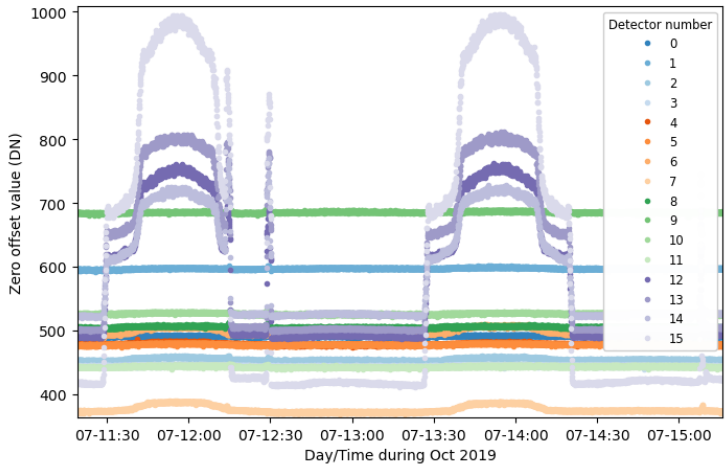

Figure 5.12. Zero offset for time during 7 October 2019. The zero offset is representative of the mean SCD signal. Light leakage into SCDs 12 to 15 appears as an increase in the mean value in a cycle with a period corresponding to the Chandrayaan-2 orbital period and duty cycle corresponding to the time Chandrayaan-2 spends above the sunlit side of the moon.

Using an overlap in the coverage of L0 and L1 data, and their associated housekeeping information, it was possible to explore the relationship between the zero offset value and the instrument solar phase angle (between the instrument boresight and Sun vector) (Figure 5.13). This further indicated there is a strong correlation between the position of the satellite and the zero offset of quad 4 SCDs. This has implied an intriguing relationship between the optical light leakage and solar phase angle. The leakage is apparently not occurring through the front of the collimator as this would result in a gradual increase in zero offset around 90 ° as the spacecraft crossed the lunar terminator. Though beyond the scope of this analysis, it has been suggested that tracking the optical light leakage for spacecraft orientation may enable a more precise understanding of the mechanism for the leakage.

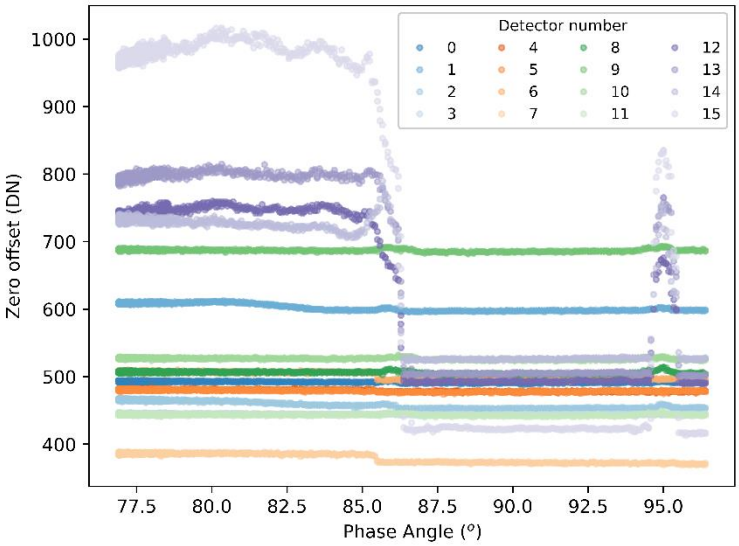

Figure 5.13. Zero offset for solar phase angle during 7 October 2019. Plotting data for solar phase angles reveals more information about zero offset behaviour in figure 5.12.

5.2.1.2 Solar phase angle relationships

As identified during irradiation dose prediction, solar activity was very low during the period covered by the available data (Figure 5.8). This resulted in very few fluorescence X-rays being observed from the lunar surface. To assess the performance of the SCDs it was therefore necessary to observe X-rays fluoresced from the instrument itself, which were slightly less faint purely due to their proximity to the SCDs. The iron-55 X-ray sources, which provided the strong fluorescence lines for calibration purposes before the shield door was opened, were removed from the instrument field of view, and did not contribute to the population of X-rays observed later.

The primary fluorescence source in the instrument was the collimator, which produced copper and aluminium fluorescence peaks observable in both L0 and L1 data. To verify methods used to measure peak width automatically, the prominence of these instrument peaks was tracked through the available L1 data. The prominence with respect to solar phase angle was measured, rather than with respect to time, as this was expected to be less affected by transient spikes in solar activity.

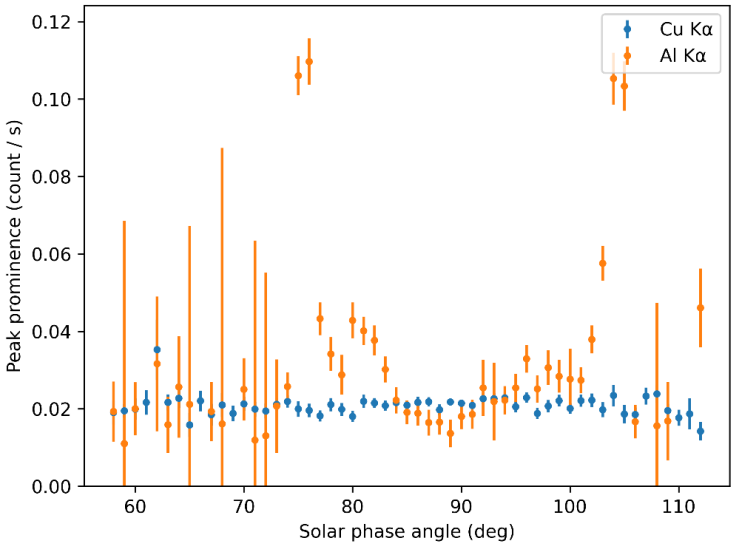

Figure 5.14. Prominence of the two collimator fluorescence peaks for solar phase angle in October 2019, measured using the L1 data. This provided confidence in searching for copper fluorescence peak across the L0 data.

Figure 5.14 shows that the copper Kα line at 8.047 keV was consistently available, whereas the aluminium Kα line at 1.487 keV was more variable, and far more prominent at some angles. This increased confidence that peak measurements were able to use either fluorescence line, with the aluminium being preferred but the copper occasionally being required. An explanation for the consistency of the copper fluorescence, compared to the aluminium fluorescence is illustrated in Figure 5.15: at 90° solar phase angle (represented by view *C*) the physical cross section of the aluminium blocking filters is low. At solar phase angles closer to those represented by view *A* the aluminium filter has a large physical cross section but is quite thin so interacts with few incoming particles. Aluminium fluorescence is thought to be greatest at intermediate angles (such as B) where incoming particles approaching obliquely are presented with a larger cross-section but also an increased thickness of aluminium, and therefore interact to the greatest extent. Meanwhile the copper collimator structure presents a consistently large and thick cross section.

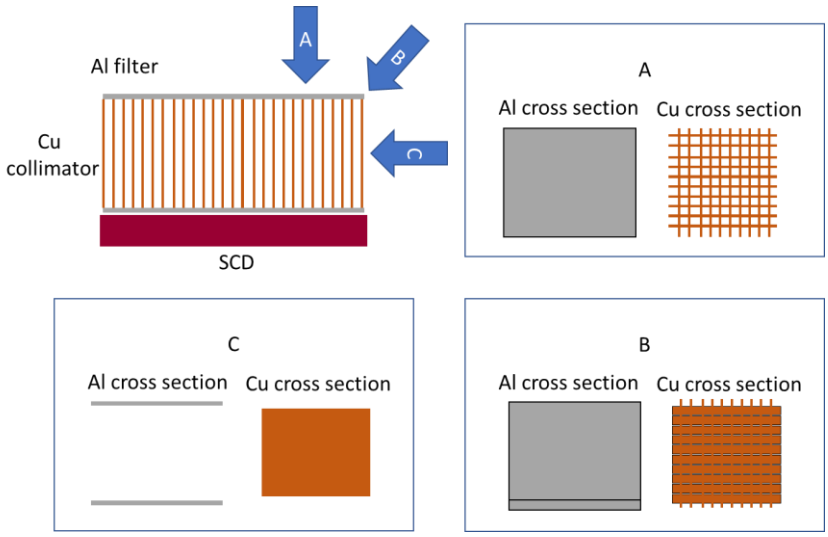

Figure 5.15. Rough comparison of cross section presented to incoming radiation by the Cu collimator and Al filter from various directions. These visualisations were used to understand Figure 5.14.

5.2.1.3 The quality of fluorescence peaks

The quality of the observed fluorescence peaks varied between the two level 0 datasets analysed. The fluorescence observed in 2019 was very faint and required the aggregation of much data to form unambiguous peak profiles, whereas a large signal was seen in the 2021 dataset. Analysis of the spectra that could be formed by slicing the 2019 data by time indicated that spectra made with a small number of events tended to result in the peak finding algorithm finding narrower peaks, or misfitting to statistical noise, whereas spectra made with a larger number of events had prominent peak profiles, but that these were wider than expected. This is illustrated in Figure 5.16: the peak of (b) is well defined whereas the peak of (a), in a spectrum in which the amount of data has been restricted to result in roughly an equal number of events per histogram energy bin to the 2021 spectrum (c), is questionable. Finally, Figure 5.16 (c) shows the peak found in the 2021 spectrum, showing a good peak profile. The increase in peak width for increasing numbers of events is likely a result of longer-term drifts in device behaviour, given that such spectra generally represented the events collected over the course of an hour, depending on the continuity of available data.

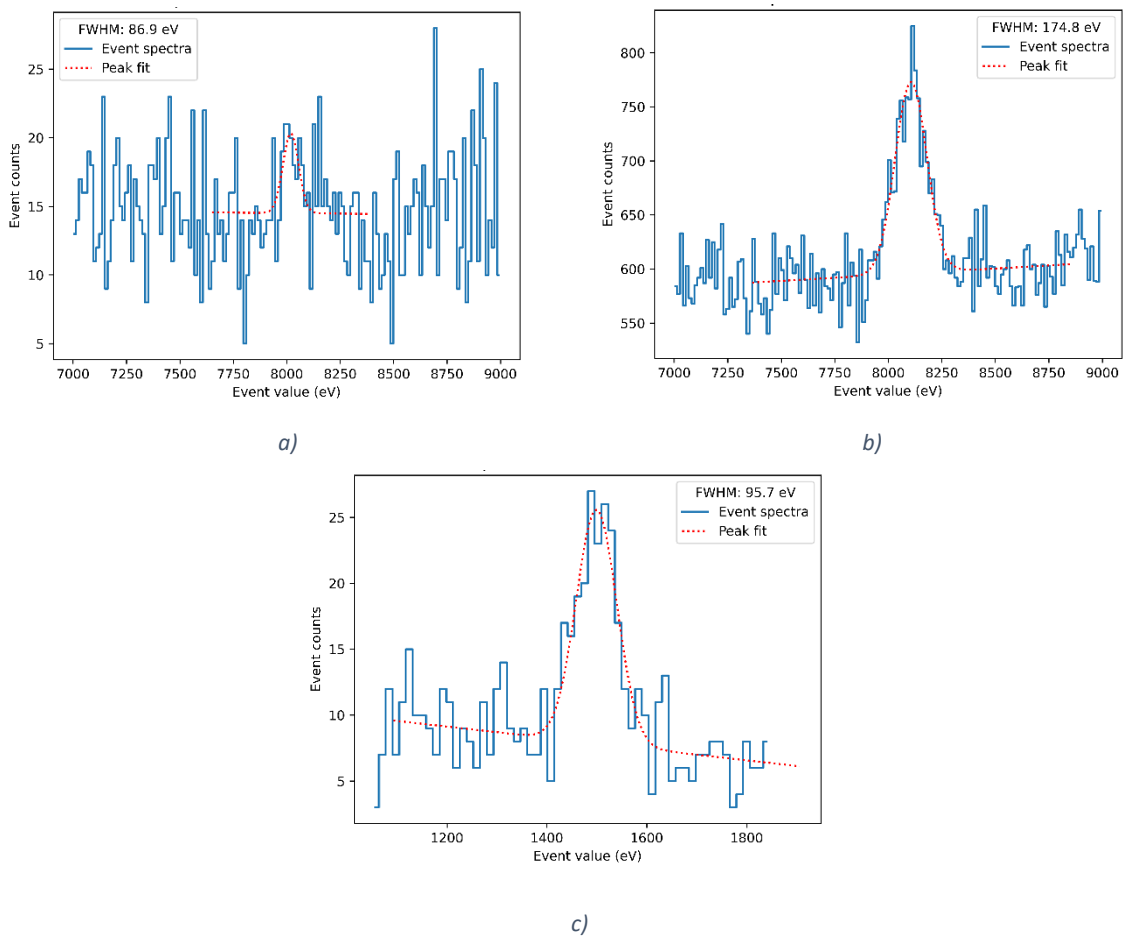

Figure 5.16. Example extracts from spectra and example peak fits derived from data from SCD6 showing (a) a 2019 spectrum and Cu Kα peak with an equal number of events to the 2021 spectrum (spotting the peak requires prior knowledge that it is likely to be there), (b) a 2019 spectrum and Cu Kα peak with more events showing the better-quality peak, and (c) a fit to the 2021 spectrum, made of all available events; note that in this case the Al Kα peak has been used.

Therefore, the SCD noise measurements for 2019 were estimated using many peak fits, slicing the available data, and down selecting the peaks measured based on the error in the noise implied by the fit (rejecting errors greater than 7 e^-) which removed faint, unreliable, peaks and the measured FWHM in bin widths (rejecting peaks narrower than 2 bins), to reject fits to single anomalous bins. The FWHM values measured from each of the spectra was then analysed as a population, with the population mean and variance being used for the estimates of device FWHM and uncertainty in FWHM.

Only the Al Kα fluorescence peak could be observed in the data available from 2021, and its uncertainty was derived from uncertainty in the peak fit, which was provided by the fitting algorithm. This peak was sufficiently prominent to be less ambiguous than those found in 2019. The prominence of the aluminium peak, and lack of corresponding copper peak may indicate an external source of Al Kα X-rays possible the intended lunar surface fluorescence.

5.3 In-flight noise measurements and radiation damage assessment

Using the information available it was possible to track some performance changes of the CLASS SCDs over the course of their first year in orbit. Of particular interest was the change in performance due to radiation damage. This analysis was limited by the data available from the CLASS SCDs and the equivalent data from ground-based tests. Comparisons indicated that there were three possible areas of investigation: the progression of spectral resolution, in FWHM, of the flight SCDs compared to the linear trend indicated by ground-based tests; the increase in dark current implied by the calibration curves; and changes in fluorescence peak shape due to CTI.

5.3.1 Total noise development

The total noise in each SCD, manifesting as energy resolution, was expected to increase linearly with irradiation according to the behaviour observed by J. P.D. Gow et al. (2015), presented in Figure 5.6. This enabled a direct comparison between degradation in energy resolution expected due to the irradiation predicted by SPENVIS and the change in energy resolution for each SCD.

The predicted irradiation dose to the CLASS SCDs during transit to the Moon and the linear trend of Figure 5.6 implied that following transit the devices should exhibit a noise increase of 8.7 e^- rms at -30 °C. To see this difference in the data, the FWHM at $-30\,^{\circ}\mathrm{C}$ was interpolated from the flight and cold ground curves of the calibration data from each SCD (the calibration data from SCD 6 has been presented in Figure 5.11). The ground and flight FWHM values were converted from units of eV to e^- rms noise values. Their difference was then calculated in quadrature, because the additional noise was not expected to be correlated with earlier noise sources:

$$n_{diff} = \sqrt{n_{flight}^2 - n_{ground}^2} \tag{5.1}$$

The calculated differences, along with the predicted increase and the experimental values measured by J. P.D. Gow et al. (2015) have been plotted in Figure 5.17. There is good agreement between the predicted and measured values. Furthermore, a map of noise increase values according to the location of SCDs in CLASS (Figure 5.18), with reference to the SCD arrangement described in Figure 5.9, indicates that there are no spatial correlations for the noise increase observed. This does not affect the lack of correlation implied by equation (5.1).

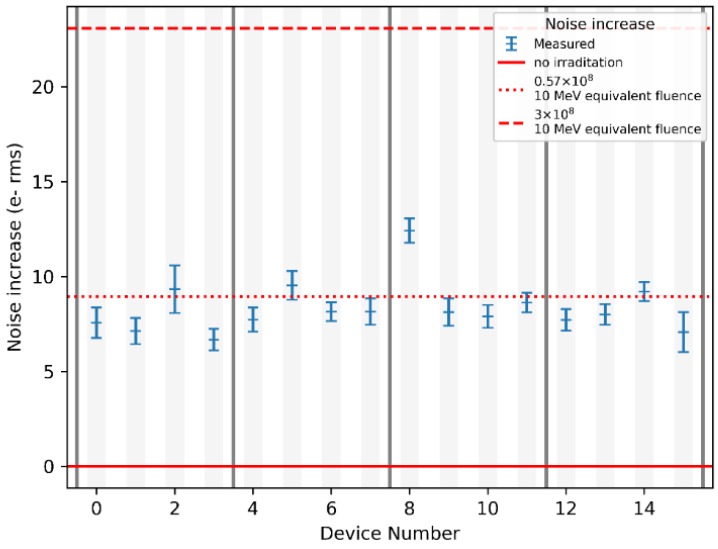

Figure 5.17. Noise observed at -30 °C after transit to the moon (blue) compared to previous predictions based on Gow et al., (2012) (red). The 0.57 × 10^8 proton cm^{-2} 10 MeV equivalent fluence value has been interpolated from the zero dose and 3 × 10^8 proton cm^{-2} experimental values from J. P.D. Gow et al., (2015).

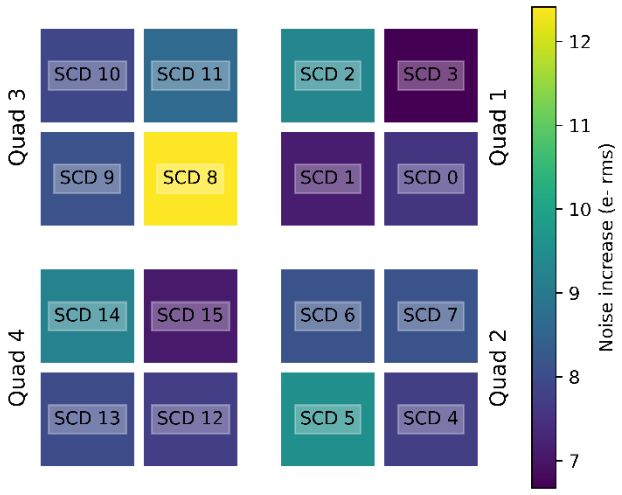

Figure 5.18. Measured noise increases in each SCD (plotted in Figure 5.17) mapped onto a representation of the arrangement of the SCDs in CLASS.

With little further irradiation predicted after arrival in 2019 until February 2021, little increase in noise was expected. For this comparison, the X-ray peaks measured in the level 0 data were used. As mentioned in section 0, peak measurements in these two datasets used different fluorescence peaks, Cu Kα (8.047 keV) in 2019 and Al Kα (1.487 keV) in 2021. When comparing the noise values calculated from peaks of different energies, the Fano noise component was removed using equation 5.2, where F is the Fano factor in silicon, and E is the peak energy, in eV.

$$n_{e^-rms} = \sqrt{n^2_{e^-\,rms,tot} - \frac{F.E}{\omega}} \tag{5.2}$$

Furthermore, the data was down selected based on SCD temperature, so that a fair comparison could be made between the two datasets. Unlike the calibration data, energy peaks were not strong enough to produce a noise estimate at a specific temperature due to insufficient X-ray fluorescence events. These measurements instead used data collected with SCD temperatures between -40 °C and -35 °C. Unexpectedly some SCDs showed a decrease in noise, therefore the noise difference equation (5.1) was adapted so that the noise difference represented whether a noise source had been added or removed, as per equation (5.3). Shown in Figure 5.19, a range in noise differences were measured, however they were centred on 0 e^- difference. Therefore, little difference in noise behaviour can be inferred overall. Because this measurement made use of in-flight data, the SCDs of quad 4 could not be used due to their optical light leakage issues. There was no apparent correlation between the noise behaviour observed and SCD location (Figure 5.20).

$$\begin{aligned} \Delta n_{e^-rms} &= \sqrt{n^2_{e^-rms,2021} - n^2_{e^-rms,2019}} \quad \text{if} \quad n^2_{e^-rms,2021} \geq n^2_{e^-rms,2019} \\ &= -\sqrt{\left|n^2_{e^-rms,2021} - n^2_{e^-rms,2019}\right|} \quad \text{if} \quad n^2_{e^-rms,2021} < n^2_{e^-rms,2019} \end{aligned} \tag{5.3}$$

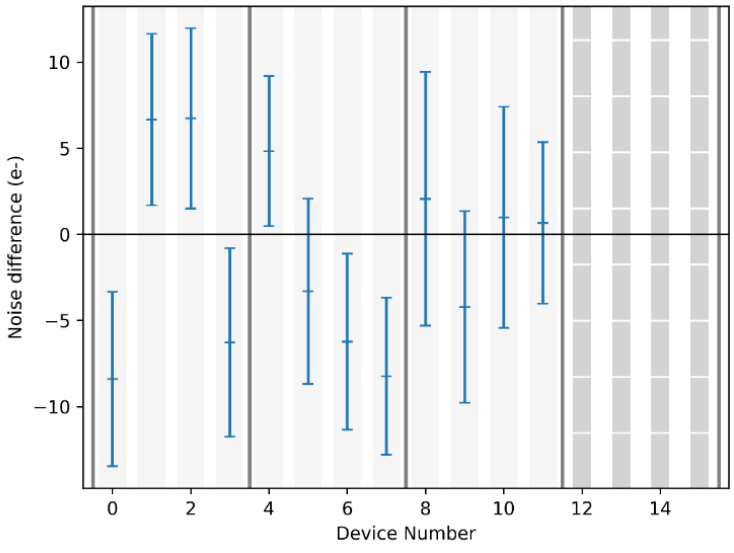

Figure 5.19. Difference in noise between 2019 and 2021; devices with stray light have been removed.

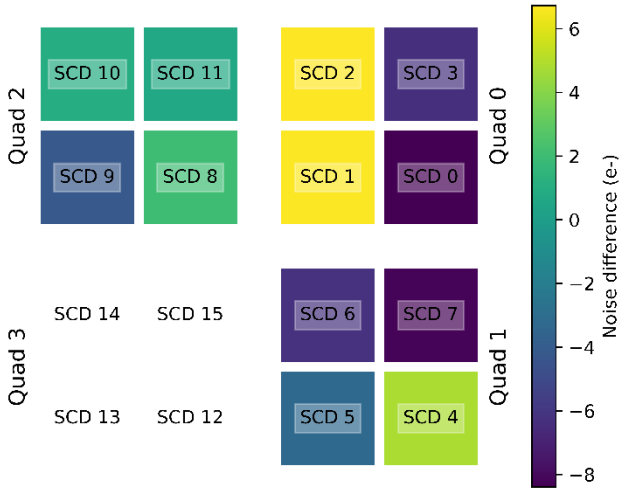

Figure 5.20 Measured noise difference from 2019 to 2021 in each SCD (as per Figure 5.19), mapped onto a representation of the arrangement of the SCDs in CLASS.

5.3.1.1 Discussion

The total noise exhibited by the SCDs appeared to change as expected during the two intervals available for analysis. This builds confidence in the predictions made by ground-based irradiation and testing campaigns. The analysis of total noise has indicated that the SCDs of CLASS remain suitable for science, and the observed damage after transit implies their total radiation dose is likely to be far less than the initially expected end of life dose.

One of the issues facing the comparisons made using in-flight data from 2019 was the high uncertainty of FWHM measurements made from the collimator fluorescence peaks. As previously discussed, this was largely due to the low SNR of these peaks; the fluorescence was faint and building spectra with a sufficient number of events necessarily also included background signal. Simply building a spectrum with the greatest amount of data possible proved counterproductive as the peaks in these spectra had consistently larger FWHM values. This is thought to be because the inclusion of data from a larger period of Chandrayaan 2's orbit embedded any instrument variations due to changing environmental conditions.

The measurements of total noise build confidence in the trend of changes to FWHM with irradiation fluence predicted by ground-based irradiations. The current energy resolution exhibited is better than the minimum required for continued science operation, and by extrapolating expected noise increase with further radiation damage, it is predicted that the SCDs should continue to operate sufficiently well for at least double the current irradiation fluence.

5.3.2 Dark current

The increase in dark current generation is a useful tool for understanding the degradation of the Si-SiO interface and the generation of lattice defects in the pixel wells both of which, while present in an unirradiated device, will increase following irradiation. The traditional method for measuring dark current, tracking changes in dark signal with integration/exposure time, is not possible using the data returned by CLASS because of the data-reduction steps taken by the instrument.

5.3.2.1 Dark current model

Instead, the dark signal expressed in the data has been inferred by modelling the temperature dependant variance of the calibration data made available for the CLASS SCDs. Similar data from ground-based testing before and after controlled irradiation is available from Gow, Holland, and Pool (2009) and Smith et al. (2012). The dark signal behaviour inferred from each dataset has been expressed as the expected dark current (in $e^- s^{-1}$) at a set temperature (-30 °C).

It was expected that the change in variance for temperature could be modelled by capturing the behaviour of the various temperature dependent noise sources. For the CCD236 these were expected to be readout noise, and dark current, as described in section 2.5. An addition to these some small contribution to the noise measured by FWHM-derived variance could be expected from CTI and Fano noise, though these have been omitted.

Therefore, the expected noise variance for temperature function is described by equation (5.4), which includes the introduction of $\sigma^2_{constant}$ to represent the temperature invariant noise sources:

$$\sigma^2 = \sigma^2_{readout} + \sigma^2_{darksignal} + \sigma^2_{constant} \quad (5.4)$$

And:

$$\sigma^2_{darksignal} = e^-_{darksignal}$$

Which includes the contribution of readout noise, shot noise from dark signal and the combined noise contribution from other sources expected to be constant for temperature ($\sigma^2_{constant}$). Dark current and readout noise were modelled with equation (3.26) and equation (3.29) (with reset noise being the dominant component of readout noise) of chapter 3 respectively. To a curve fit solver[1] this can be represented as:

$$\sigma^2 = f(T, C, D_{FM}, \sigma_{constant})$$

[1] The author used the curve fit solver available in the sciPy.optimize Python package.

Where T is the device temperature, C is the readout node capacitance used to scale readout noise, and D_{FM} is the dark signal figure of merit used to scale dark current. Once the values for C, D_{FM} and σ_{static} had been estimated by the curve fit solver, the parameters were used to predict the dark current that would be measured at any given temperature.

5.3.2.2 Fits to data

Figure 5.21 shows the initial noise model fit to ground-based variance data from Gow, Holland and Pool (2009). Good agreement was achieved between the fit and data points, and fitted parameters took reasonable values for offset and readout noise.

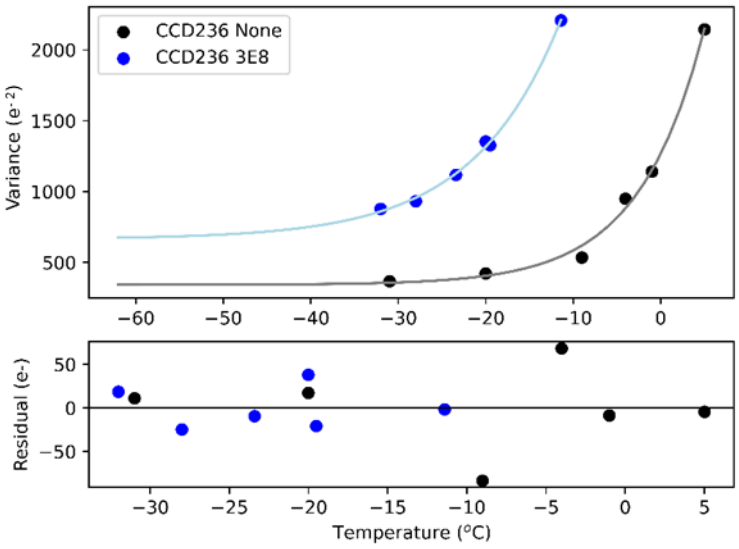

Figure 5.21. Variance for temperature measured during ground-based testing before and after a 3 x 10^8 proton cm^{-2} 10 MeV equivalent fluence irradiation (Gow et al., 2009).

Verification of the dark current parameters derived by the model used the dark current reported by Gow et. al. shown in Figure 5.22. This shows good agreement between the model and reported values for the unirradiated device, however for the irradiated device there is some divergence at lower temperatures. This is thought to be due to two factors. Firstly, the data from the irradiated device does not extend into the flatter region of the variance curve, which is thought to have reduced the ability of the curve fitting algorithm to accurately fit to the data. Secondly, the reported dark current measurement has also been inferred, as reported by Gow et. al. the reported measurement is derived from the increase in noise seen at the reported temperature from some unspecified colder temperature. In situations where the dark current is low this is expected to be accurate, however after irradiation dark current could be measurable even at lower temperatures and this may have introduced systematic offsets into their data.

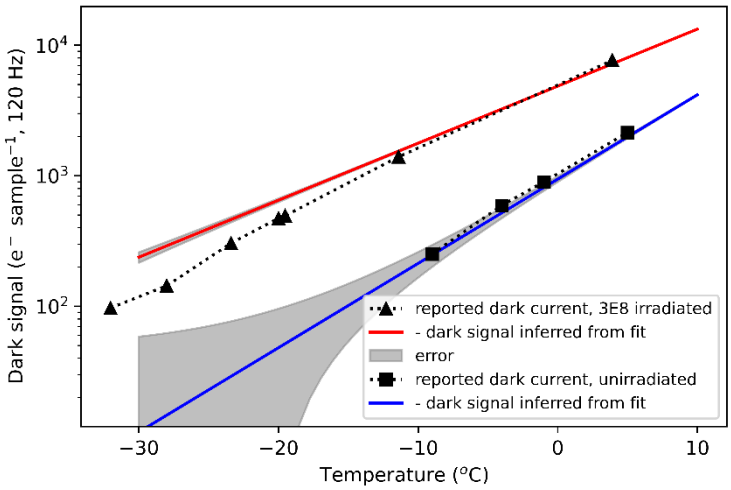

Figure 5.22. Dark current implied by model fit compared to dark signal measurements reported by Gow et al.

Finally, the model was able to derive fits for the CLASS data. Shown in Figure 5.23, the model was able to fit to the large number of ground points with minimal residual error, however because the flight datapoints are sparser, and exhibit greater scatter, the fits to flight data were generally less certain.

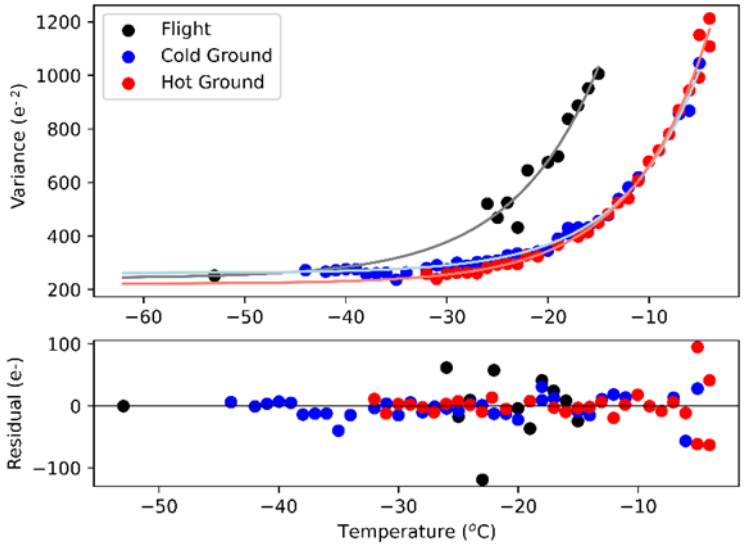

Figure 5.23. Noise curve fitted to data from CLASS calibration, SCD6. The three traces show variance in the device measured during flight and then during cold soak and hot soak pre-flight testing.

5.3.2.3 Dark current measurement

Figure 5.24 reports the apparent dark current (at -30 °C) exhibited by the CLASS SCDs and measured following ground-based irradiations for irradiation fluence, according to the dark current model. For

the CLASS SCDs, the SPENVIS irradiation fluence prediction of 0.54 × 10^8 proton cm^{-2} (10 MeV equivalent) has been used.

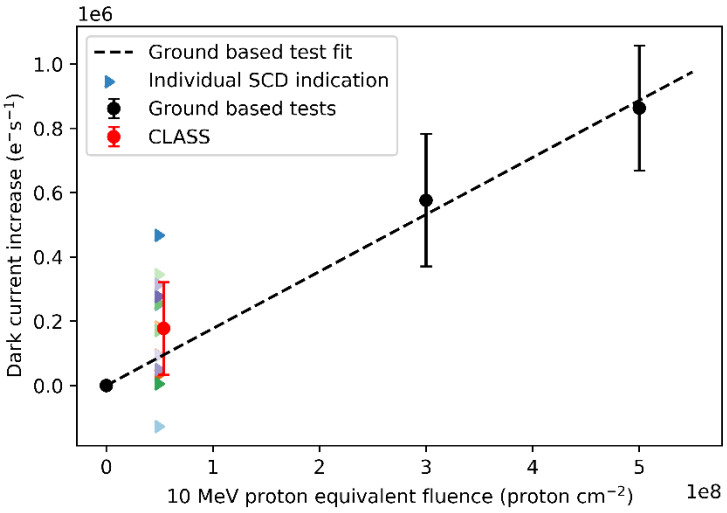

Figure 5.24. Dark current increase estimated from various datasets at -30 °C. The colour of the carets used to indicate the results from individual SCDs correspond to the colours of Figure 5.25

The CLASS SCDs measurements indicate the SCDs are, on average, exhibiting dark current consistent with the expected irradiation fluence and the results of previous investigations. Though no data is available at irradiation fluences equivalent to that experienced by the SCDs, the average behaviour of the SCDs is consistent with the trend implied by the ground-based tests. Figure 5.25 re-plots these values as irradiation dose normalised dark currents, permitting a better representation of the individual CLASS SCDS. The high uncertainty of the dark current measurements masks any behaviour for a single device, however, there appear to be no exceptional SCDs in the CLASS array. Furthermore, with reference to the SCD arrangement described in Figure 5.9, there does not appear to be any correlation between higher dark current and SCD location, illustrated in Figure 5.26.

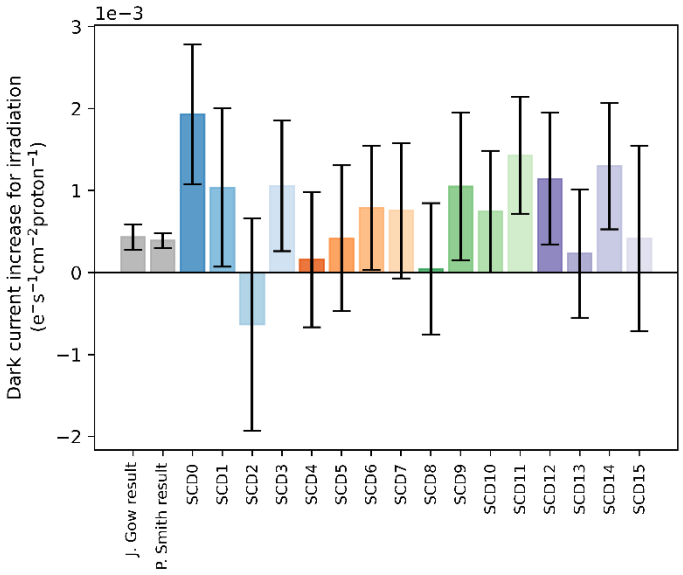

Figure 5.25. Dark current at -30 ºC, normalised to irradiation fluence for ground based irradiated SCDs and CLASS SCDs.

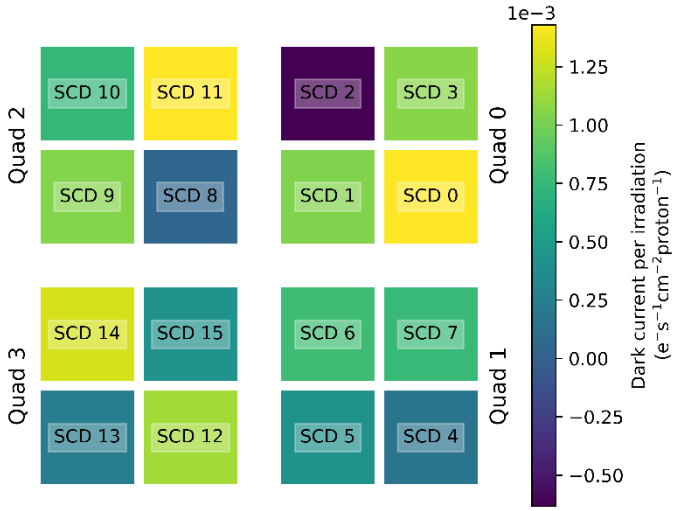

Figure 5.26. MAP of CLASS SCD dark current values (without error), showing no apparent spatial correlation of devices with very high or very low dark current values.

5.3.2.4 Discussion

The CLASS devices have displayed slightly higher dark current than was consistent with linear interpolation of the ground testing data, at the estimated irradiation dose expected to have been experienced by the CLASS SCDs. This result was not necessarily an indication that the SCDs of CLASS are all experiencing more dark current than might have been expected from ground-based tests. The method used to derive dark current values has used pre-processed data which will have embedded

variations in device operation or data handling in an opaque manner. Therefore, the apparently high dark current measured aboard CLASS was not perceived as alarming. Alternatively, some reassurance may be derived from the fact that the absolute values were not far more than those observed in ground tests and that the CLASS results were within 1-2 sigma of each other and had no apparent spatial correlation. That is, no region of the instrument was showing higher dark current which may have been indicative of localised damage or increased radiation dose.

Finally, further measurements of dark current in the manner described here are unlikely. With the instrument now operating in a science mode whenever there are fluorescence peaks observable temperature variation will be far less than required to observe the temperature dependent behaviours observed in the calibration curves. Furthermore, at science operation temperature (≈ -40 ^{o}C) dark current generation is generally quite low, so until radiation damage has become significant dark current behaviour will be masked by other noise sources. This analysis has only been possible with the calibration data from CLASS when a large temperature range was probed, and the calibration sources were providing a consistent flux of X-rays.

5.3.3 Charge transfer inefficiency

Key to the analysis of the CLASS SCDs has been their architecture making direct analysis of noise parameters hard, or heavily reliant on good signal to noise properties. Investigation into CTI has been largely frustrated by the loss of positional information in the SCD during charge transfer. In this section a method for measuring CTI in the CCD236 is proposed and discussed, however it was not applied to the science data as the effects intended to be observed are easily obscured for low irradiation fluences. Smith et al. (2015) used a copper shield to restrict the regions of a device exposed to incoming X-rays and thereby measured CTI by comparing the X-ray values recorded from different regions. This test required the used of an adjustable copper shield and is not repeatable aboard CLASS.

The transfer path of the pixels of the CCD236 means that there is not an equal distribution of pixels for charge transfer steps. In general, there are more pixels with more transfer steps to the readout node, best illustrated by the CCD236 schematic of section 2.2.2. Therefore, we may expect an uneven distribution of CTI-induced charge loss across all X-ray events recorded in the SCD as the distribution of pixels for number of transfers is not uniform. There are more pixels at the edge of the CCD236 (see Figure 3.15), these pixels also have a greater number of transfer steps before they are readout. While each pixel will have a normally distributed output of X-ray values, the total SCD output will consist of many such distributions, shifted by CTI and dominated at the lower value end by the edge of array pixels (Figure 5.27). A simple Monte Carlo model was used to explore the effect of CTI on the recorded

event value probability distributions, which was expected to be reflected in the fluorescence peak shapes.

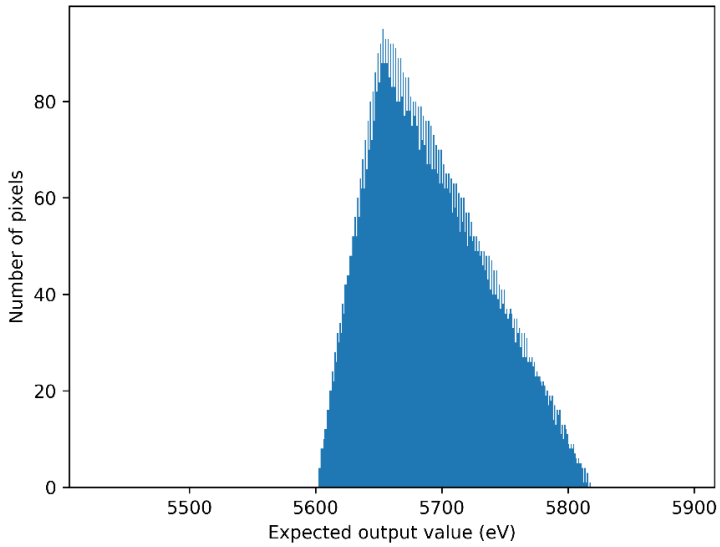

Figure 5.27. Histogram of expected output values from the different pixels of a CCD236 for a 5.9 keV photon, accounting for an arbitrary, fixed, low CTI charge loss per transfer. Skew in the peak is due to the device geometry, there are more edge pixels which require more readout steps, than centre pixels, which do not.

CTI has been modelled as an average charge loss per pixel transfer, with the probability of charge loss in any given transfer described by equation 3.28, with N_p set to one for any given transfer, and n_e- set to an expected number of Mn Kα electrons (accounting for Fano noise), and assuming the CTI variance is approximately equal to the mean charge lost. Because X-ray events are sparse across the SCD, only the effects of charge absorption have been accounted for. Similarly, the effect of trap sites being filled prior to the arrival of an event packet has not been modelled or included.

The parameters of this model were tuned with the results of Smith et al. (2015) to ensure that the model outputs matched experimental observations. Figure 5.28 compares Figure 7 of Smith et al. (2015) to the model output, showing the good agreement resulting from the parameter tuning. Specific properties that were sought to be replicated included the distribution of charge loss values, shown in Smith's work with the colour map, and the range of peak energies exhibited for the different pixel locations.

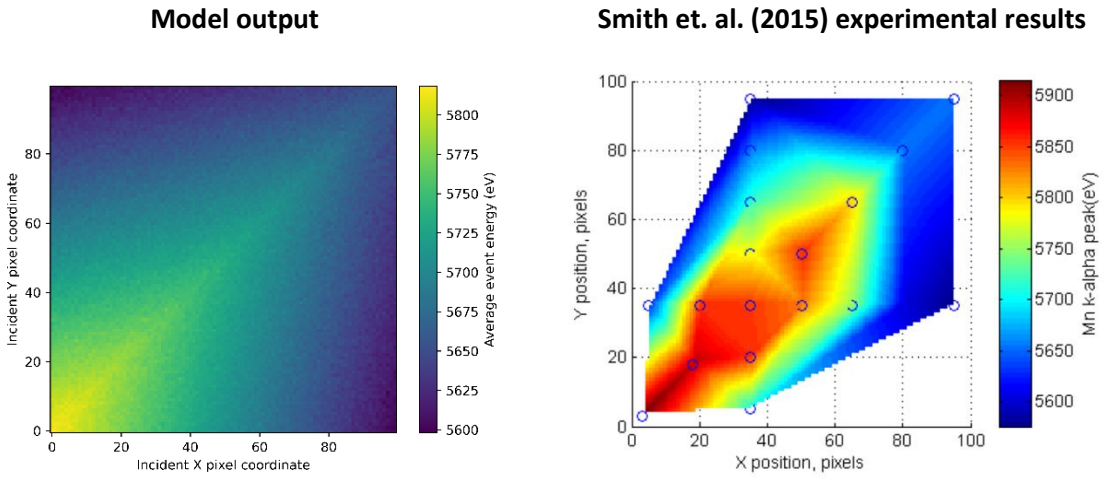

Figure 5.28. Comparison of mean event value for pixel coordinates from (a) model output and (b) Smith et al. (2015) Figure 7. The mean event values of (b) have only been measured at the blue circles, and the colourmap has been interpolated.

The interaction of lattice defects and photo-generated charge is non-trivial and has strong dependencies on the transfer speeds and device temperature. Because the SCDs aboard CLASS are operated at a similar temperature, with the same readout scheme and comparable charge packets as those tested by Smith et al., it has been assumed that the behaviour of the flight SCDs will be similar to that seen during ground testing, and that a model with fixed charge loss rates will approximate the observed behaviour.

However, the effect of the modelled CTI, on fluorescence peaks similar to those available in the CLASS data, was far too small to observe. Noise sources were able to easily obscure the distortion in event values. In Figure 5.29 the CTI model has been applied to a sample of 5.9 keV X-rays, as well as Fano noise, the minimum additional event uncertainty expected. The skew generated by the CTI model is just visible, but largely obscured by the normally distributed uncertainty of the Fano noise. In the data available from the SCDs of CLASS this effect is not expected to be observable as the actual fluorescence peaks seen are of a worse quality.

It is hypothesised that the CTI skew may become observable towards the end of the CLASS instrument's life when solar radiation is fluorescing stronger peaks and the SCDs have accumulated more damage and exhibit more CTI.

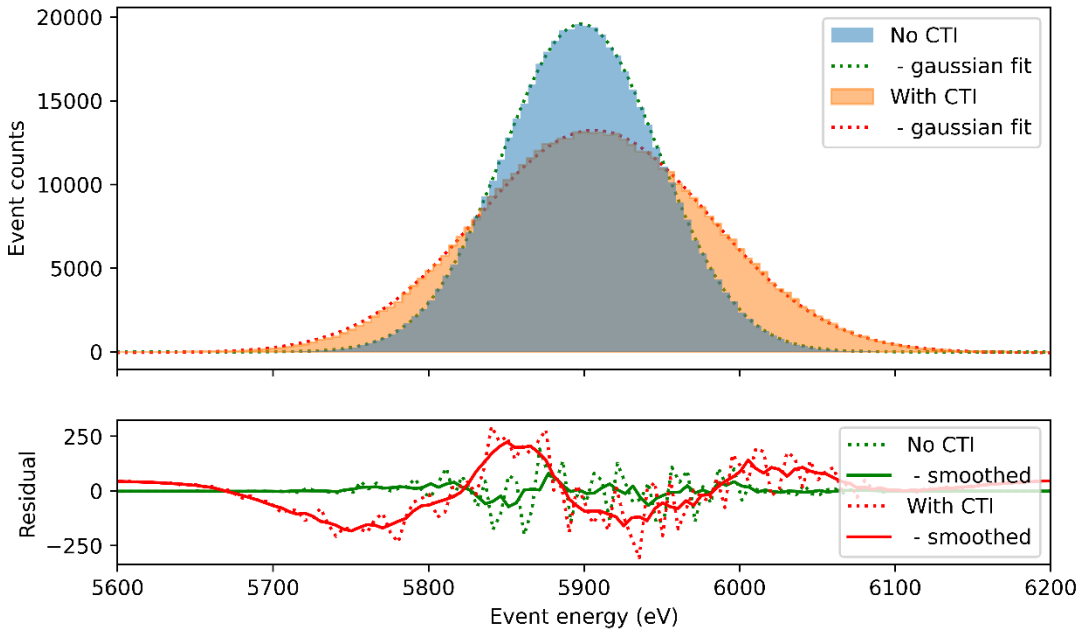

Figure 5.29. Distribution of Mn Kα (5.898 keV) event values with Fano noise and without, or with, effects of CTI predicted by the model. The CTI peak has been recentred, as it would in real data where the conversion gain was unknown. The difference between gaussian fit and CTI histogram is highlighted in the residual plot.

5.4 Conclusions

The degradation in energy resolution exhibited by the SCDs of the CLASS instrument is consistent with expected radiation dose. Apart from the optical light leakage of quad 4, all SCDs continued to perform to a level consistent with the science goals of CLASS up to the final time-period covered by available data in February 2021. This has permitted CLASS to be operated beyond its expected mission lifetime of one year in lunar orbit and gather useful data as solar activity has begun to increase with the start of solar cycle 25.

Three indications of performance degradation following irradiation have been explored and compared to pre-flight predictions. The progression of total noise in each SCD is well within expectations. The increase in dark current seen in the CLASS SCDs is more than was indicated by ground-based irradiations, however significant variation in dark current behaviour due to annealing was seen in the ground-based tests which may explain apparent differences. Finally, the effect of CTI was explored and determined to be too subtle to observe with confidence.

The CCD236 has shown itself to be a resilient X-ray detector, capable of continuing to operate following the irradiation of an interplanetary mission.

5. Evaluation of soft X-ray detectors in lunar orbit

6 AXIS X-ray detector trade-off

This chapter presents a trade-off study of the candidate X-ray detectors for AXIS, including a review of the X-ray detectors and their suitability for instrument requirements, and a side-by-side experimental performance comparison for soft X-ray detection in the 300 eV to 2000 eV range. This was intended to reduce the number of X-ray detectors to be considered during more in-depth testing, as well as providing initial suggestions for the instrument design.

Ultimately the X-ray detectors under consideration could be split into three categories: EMCCDs as proposed in the baseline design, CISs under development for other instruments, and standard CCDs also under development for other X-ray instruments. EMCCDs and CIS are the primary candidate architectures due to their potential ability to achieve low noise performance under the operating conditions imposed by AXIS. Standard CCDs have been able to achieve high levels of X-ray imaging spectroscopy performance for decades, and therefore are worth including in the comparison as a benchmark, though X-ray detectors with this architecture cannot achieve the required framerates for AXIS.

This chapter is in three sections, an initial overview of the detectors under consideration, a theoretical evaluation, and an experimental trial of X-ray detectors available at the time of the investigation. The energy performance initial evaluation and experimental testing sections of this chapter were published in Jones et al. (2022).

6.1 X-ray detector candidates

Starting with the baselined CCD201-20, a range of X-ray detectors were identified for evaluation based on the potential performance benefits that they can provide for AXIS. This includes the CCD201-20 derived CCD311, and CIS that potentially meet performance requirements: the CIS120 and CIS221-X.

The CCD201-20 (Figure 6.1) is the baseline design X-ray detector, chosen for its comparatively high framerate, low noise and moderate TRL (TRL-6), as introduced in section 2.2. The CCD201-20 is an ideal detector for schedule and cost requirements as it is already commercially available.

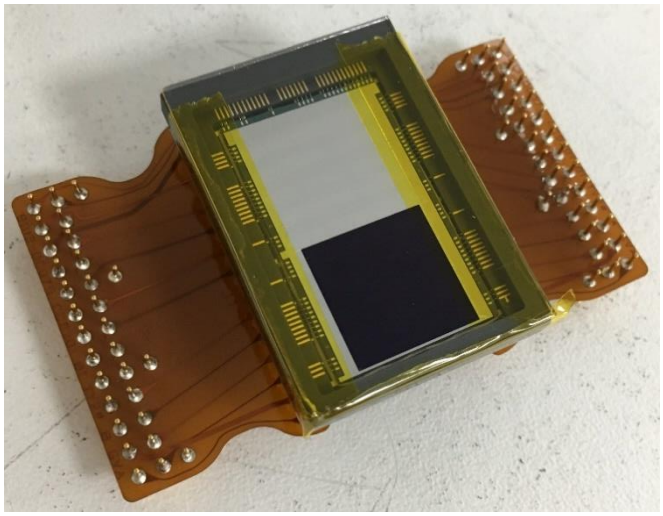

Figure 6.1. CCD201-20 used in this investigation, mounted on electrical interface flexi circuits. The protective glass cover is used to prevent the X-ray detector being damaged during handling and is removed before tests.

NGRST CGI work for the CCD201-20 has led to the development of the CCD311, which includes modifications to the CCD201-20 design to improve radiation hardness. These include narrowed charge tranpost channels to reduce charge transfer inefficiency (CTI) and overspill drains to protect the gain register against aging (Bush et al., 2021). These EMCCDs are under development specifically for NGRST, therefore there are some concerns about their availability. For the purposes of this study, the CCD311's unirradiated performance is expected to be equivalent to the CCD201-20.

A drawback of EMCCDs for the purposes of the AXIS instrument is the excess EM noise, generated by the stochastic processes of the EM register which adds additional X-ray energy uncertainty (Robbins & Hadwen, 2003), as outlined in section 3.5.6. When operating at the gain levels required to achieve the desired noise suppression, the resulting signal-dependent X-ray event signal variance increases from 0.115 times the signal (Fano noise in silicon) to 1.115 times the signal. Alternative X-ray detectors with acceptable performance for AXIS, but without the penalty of the EM register, offer the potential for increased energy resolution. Developments in CIS technology promise soft X-ray imaging spectroscopy performance comparable to CCDs and EMCCDs, with potential advantages for AXIS. They use the active pixel sensor (APS) architecture with charge to voltage readout conversion in each pixel (discussed in section 3.3), resulting in increased readout speed and radiation tolerance. This should permit the candidate CIS X-ray detectors to operate at higher temperatures and for a longer mission duration.

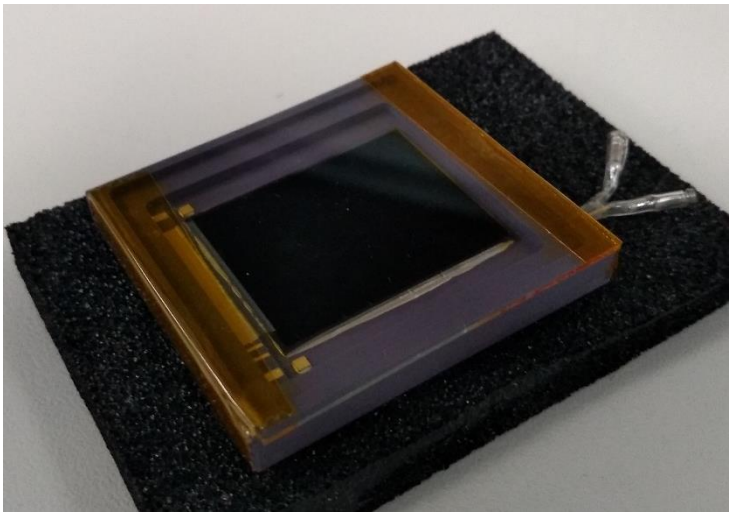

Figure 6.2. CIS120 image sensor used in this investigation. The uniform surface colour indicates that this is a backside illuminated (BSI) X-ray detector.

The CIS120 CIS manufactured by Teledyne e2v (Teledyne e2v, 2017) (Figure 6.2) is intended as a general-purpose image sensor. It features a 20 mm × 20 mm image area with 10 µm square pixels and a full well capacity of 39,000 e^-, using architectures inherited from the CIS115 due to fly aboard JUICE's JANUS camera (Soman et al., 2016). The CIS120 and its derivatives integrate many additional on-chip functions including readout and pixel driving. All interactions with the chip including setup, frame grabbing, and data transfer occur over digital interfaces.

The CIS221-X (Figure 6.3) is a test X-ray detector resulting from development of the CIS120 architecture to improve soft X-ray performance (Heymes, Stefanov, et al., 2020). It includes deep depletion extension implants to permit reverse bias and full depletion of the epitaxial layer (as per Stefanov et al. (2018)); three pixel variants of increased pixel size (40 µm square) to reduce X-ray event charge sharing; reduced readout noise and increased charge to voltage factor to improve performance at lower X-ray energies; and additional pinning implants to reduce the charge storage volume within each pixel and reduce image lag. The CIS221-X is expected to demonstrate key technologies and design features that will enable the development of future scientific CIS X-ray detectors. Initial testing of the CIS221-X has demonstrated near Fano-limited energy resolution (Heymes et al., 2022), in which the energy resolution approaches the limit of Fano noise associated with charge generation by X-rays.

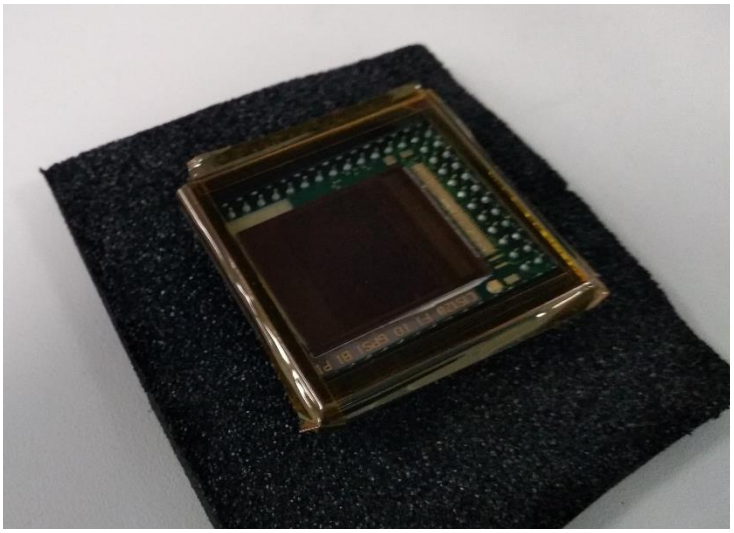

Figure 6.3. CIS221-X X-ray detector used in this investigation, mounted in an interim PCB package. Only a frontside illuminated (FSI) device was available at the time of this study, in which X-rays must first traverse the detector control structures to reach the X-ray sensitive silicon.

Prior work for THESEUS has identified that the variant 3 40 µm pixels have the best performance (Heymes et al., 2022), therefore, for this study only that variant has been considered.

Finally, the CCD370 has been included for initial theoretical comparisons between the candidate X-ray detectors and the current state of the art X-ray optimized detector. The CCD370 is a large area X-ray optimized CCD, designed for use in the Solar wind Magnetosphere Ionosphere Link Explorer (SMILE) Soft X-ray Imager (SXI) (Soman et al., 2018). Compared to a standard CCD, these X-ray detectors have an increased charge to voltage factor, enhanced back-surface passivation, and are intended to be used in a 6×6 pixel binning mode, resulting in an effective pixel size of 108 µm × 108 µm. Charge transfer inefficiency (CTI) is a particular concern for the CCD370 due to its large photosensitive area (8 cm × 8 cm), so many of the mitigation measures included in the CCD311 are also used in the CCD370. This X-ray detector is a useful benchmark for evaluating the performance of the EMCCD and CIS alternatives, however it is immediately disqualified from consideration as it will not be available in the time frame required for AXIS.

Table 6.1. Summary of devices included in this study.

	CCD201-20	**CCD311**	**CIS120**	**CIS221-X**	**CCD370**
Technology	EMCCD	EMCCD	CIS	CIS	CCD
Pixel pitch (µm)	13	13	10	40	108[2]
Sensitive area (mm x mm)	13.3 x 13.3	13.3 x 13.3	20.5 x 20.5	20.5 x 20.5	81.2 x 68.2
Thickness (µm)	16	16	16	35	16
Readout noise (e^-)	< 1[3]	< 1[4]	6	3	5.3
Framerate (Hz)	10	10	20	80	0.4
Radiation hardness	Low	Moderate	High	High	Moderate
Technology readiness for space envirnoment	Moderate	Moderate	Low	Low	Moderate
Availability	COTS	Unknown	COTS	Test device	Unavailable

6.2 Initial evaluation

The first comparison of the candidate X-ray detectors was performed using their reported parameters and to predict their performance prior to more in depth and time demanding experimental trials. The evaluation included evaluation of: energy performance, the FWHM of X-ray peaks, and sensitivity across the X-ray energy range of AXIS; event reconstruction properties of the X-ray detectors; spatial performance of the detectors, field of view, spatial resolution in the AXIS footprint, and possible pinhole modifications; and the impact of achievable framerates.

[2] With on-chip binning

[3] At an EM gain of 450 e^-/e^-

[4] At an EM gain of 450 e^-/e^-

6.2.1 Energy Performance

Understanding the differences between the candidate X-ray detectors began with an extrapolation of each detector's properties into key performance characteristics. The three key performance metrics that were explored in this way were: sensitivity (the ability of each X-ray detector to absorb X-rays); detectability (the expected yield of well reconstructed X-ray events compared to the total number of events absorbed); and energy resolution (the X-ray fluorescence peak FWHM that may be expected from each detector).

6.2.1.1 Sensitivity

The sensitivity of the candidate X-ray detectors was predicted using a layer-cake model, as discussed in section 3.4. All X-ray detectors were modelled as backside illuminated (BSI), with an enhanced back surface passivation used to reduce the non-sensitive back surface layer, and including the optical blocking filter planned for AXIS (strata detailed in Table 6.2), with the resulting QE predictions plotted in Figure 6.4. This method does not take horizontal structures into account, therefore because the vertical cross-section of all the candidate X-ray detectors other than the CIS221-X are very similar, they may be represented with the same layer cake model.

Table 6.2. Strata for QE model used in Figure 6.4.

Layer	**Material**	**CCD201, CIS120**	**CIS221-X**
Optical Blocking Filter	Al	*(AXIS nominal thickness)*	*(AXIS nominal thickness)*
Oxide	SiO_2	2 nm	2 nm
Passivation layer	Si	*(T-e2v enhanced process nominal thickness)*	*(T-e2v enhanced process nominal thickness)*
Field free region	Si	8 µm	0 µm
Depletion region	Si	8 µm	32 µm

The layer-cake method was extended to predict the proportion of X-rays expected to be absorbed in the field-free region of the partially depleted devices (CCD201-20, CIS120, CCD370) by plotting two traces for these devices: including and excluding the field-free region. At energies where the QE is significantly higher including the field-free region it is expected that the total population of observed X-rays will be dominated by field-free absorbed X-rays. The charge generated by such X-rays are far more likely to spread over many pixels before being collected.

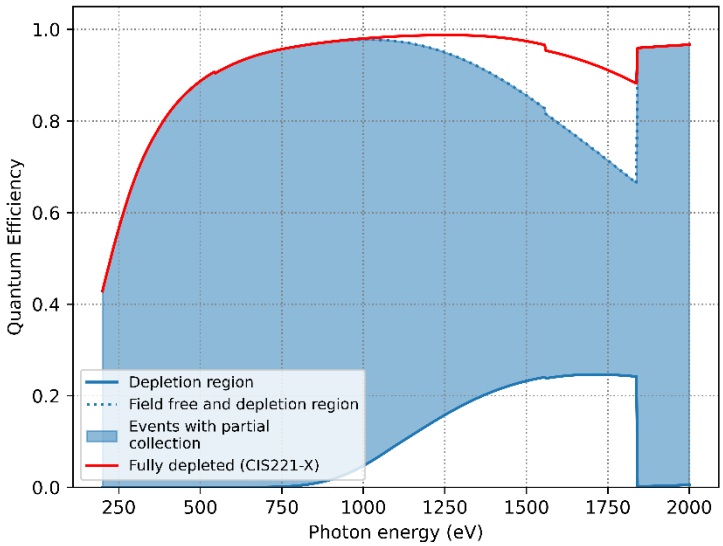

Figure 6.4. X-ray quantum efficiency predictions from 250 eV to 2000 eV showing the layer cake prediction for the CCD201-20, CIS120 and CCD370 in blue and the CIS221-X in red.The impact of the field free region in the partially depleted devices (not the CIS221-X) has been indicated, the dashed trace indicates the QE including the field free region, the solid trace without. The shaded region is representative of the proportion of X-rays that could be expected to be absorbed in the field-free region.

This model indicated that all candidate X-ray detectors have sufficient sensitivity (QE >0.7) over the required energy range. Below 1 keV the populations of X-rays in the partially depleted devices are very likely to be dominated by split events, though precise behaviour is beyond the scope of the model. This has implications for detectability, because split events will be harder to detect because less charge will be collected in any single pixel, and for energy resolution, because events spread over multiple pixels will be more affected by per-pixel noise.

The BSI version of the CIS221-X not yet available, therefore the QE of FSI versions of the X-ray detectors was also modelled, shown in Figure 6.5. Due to the thicker initial dead layers in an FSI device, the QE for very soft X-rays is far lower. Clearly, such devices would be unsuitable for use in AXIS, however, some device properties are testable if X-rays above 1 KeV are used. FSI CIS are doubly penalised: because these detectors are manufactured in semiconductor foundries with a wider range of applications the fabrication process is not optimised for image sensors, and therefore the front surface structures are far thicker, almost 6 µm of oxide, polysilicon, and silicon nitride, as opposed to around 1 µm for the CCDs considered.

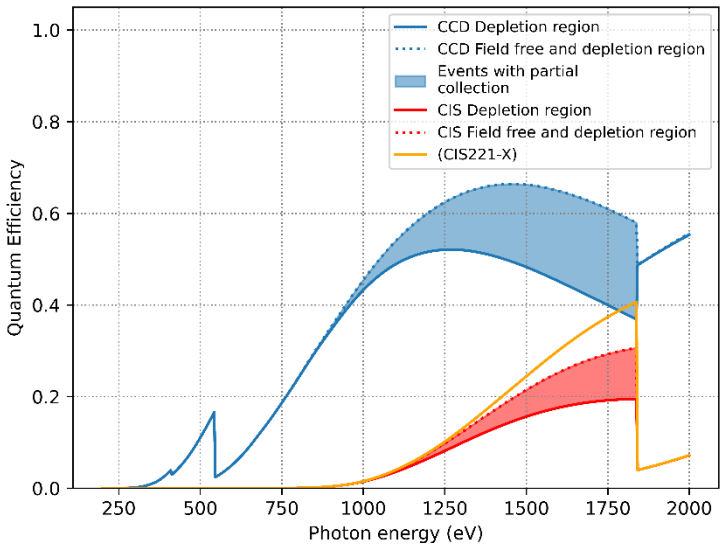

Figure 6.5. Sensitivity for front illuminated versions of devices under consideration for photon energy. The double traces are marked as per Figure 6.4, though certain behaviours are inverted because devices are FSI.

6.2.1.2 Detectability

Assuming complete charge collection, detectability is the probability that the charge of an X-ray event (e^-_{X-ray}, the number of electrons expected from the X-ray of energy E_{ph}) added to the noise of the detector (a random variable with standard deviation σ_{pix}) will exceed a detection threshold (γ_{thresh}), and can be expressed as equation (6.1). Detectability is primarily an issue at the lower end of the energy range of interest. Assuming that the noise of the device is largely Gaussian the detection probability may be expressed by equation (6.1) (and presented in Figure 6.6):

$$P_{detect} = \frac{1}{2}\left(1 - \mathrm{erf}\left(\frac{\gamma_{\mathrm{thresh}} - e^-_{X-ray}}{\sigma_{pix}\sqrt{2}}\right)\right) \tag{6.1}$$

The X-ray event threshold is often a multiple of the per pixel rms noise (for example, (Randall et al., 2020)). This is selected to ensure maximum detectability of X-rays whilst suppressing the number of noisy pixels falsely identified as X-rays. For the following predictions a detection threshold of 5 times the rms noise value has been used (this takes a value from < 1 eV in the EMCCDs to > 5 eV in the CIS120), to reflect the harsh event identification criteria that will be required to ensure the low-flux, low-energy X-ray events have a high signal to noise ratio.

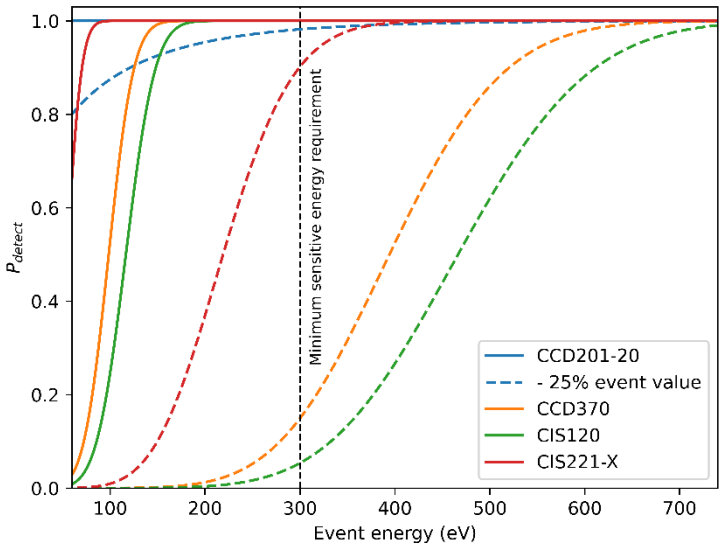

Figure 6.6. Event detection probability for energy in the four modelled devices. 25 % trace indicates roughly how the X-ray detectors would be expected to perform for split events in which the splitting is due to charge spread in the field free region.

Figure 6.6 highlights the large advantage of EMCCDs over the other X-ray detectors. Because readout noise is suppressed, X-ray charge is straightforward to separate from noise, even for very low X-ray energies. This means that even X-ray charge clouds split across multiple pixels will be identifiable. On the other hand, because of their higher readout noise, the CCD370 and both CIS show worse detectability behaviour. While all three are predicted to be able to detect single pixel events, the CCD370 and CIS120 show a low detection probability for split events from X-rays of energies that extend into the range of interest.

Alternatively, we may use equation (6.1) to predict event detection probability at a fixed energy but with noise increased above the baseline model including Fano noise, nominal dark signal, and readout noise. This is illustrated in Figure 6.7 at 390 eV for additional noise up to 30 e^- rms (equivalent to an extra 900 dark signal electrons).

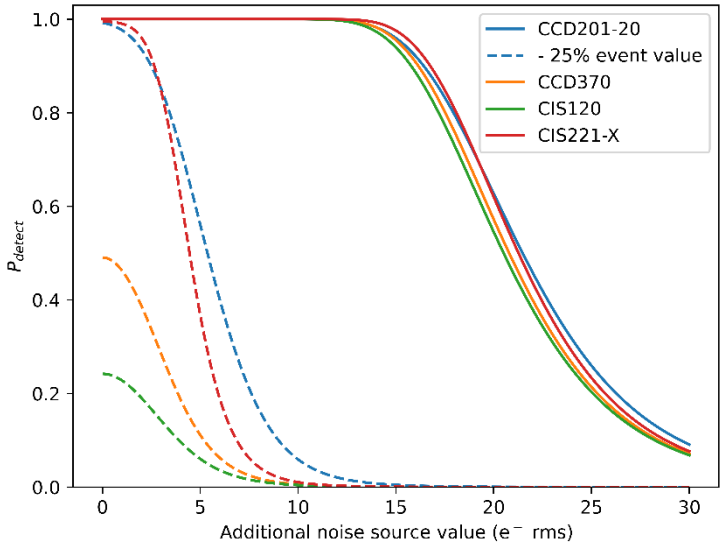

Figure 6.7. X-ray detection probability for a fixed energy, 390 eV (nitrogen Kα), with increasing noise from a hypothetical additional noise source.

The split event 25% trace shows a marked difference between the X-ray detectors. The CCD370 and CIS120 are not suitable for split event detection at this energy. The CIS221-X and the CCD201 quickly become unusable for detecting split events in the presence of additional noise, indicating that these devices, when considering split events, have a much lower excess noise budget of around 5 e^-.

6.2.1.3 Energy Resolution

Achieving the required energy resolution of AXIS, a peak FWHM of 100 eV at 500 eV, will be critical for enabling in-depth analysis of data and distinguishing atmospheric component fluorescence from the electron bremsstrahlung. The total noise in the measurement of any given X-ray has been modelled with equation (6.2) after section 3.5, which represents a best-case scenario.

$$\sigma_{X-ray,e^-} = \sqrt{\frac{F.\,\mathrm{E}_{\mathrm{X-ray}}}{\omega} + \sigma^2_{readout}} \tag{6.2}$$

Where F is the Fano factor (0.115 in silicon, 1.115 for an EMCCD including the EM register excess noise (Tutt et al., 2012)), E_{X-ray} is the X-ray energy in eV, ω is the conversion ratio between eV and e^- in silicon (approximately 3.65 eV/e^-) and $\sigma^2_{readout}$ is the readout noise of the device. It has been assumed that in the final instrument design the operating temperature will be selected to ensure negligible dark current, and this method does not capture more complex sources of noise including event reconstruction and CTI. The noise of an X-ray peak, in electrons rms, can be converted into energy resolution (FWHM), in eV, using equation (6.3):

$$FWHM_{eV} = 2.355 \,.\, \omega \,.\, \sigma_{X-ray,e^-} \tag{6.3}$$

Using the total noise values for each X-ray detector (calculated using equation 1.3), the predicted FWHMs of X-ray peaks for each X-ray detector were calculated and plotted in Figure 6.8.

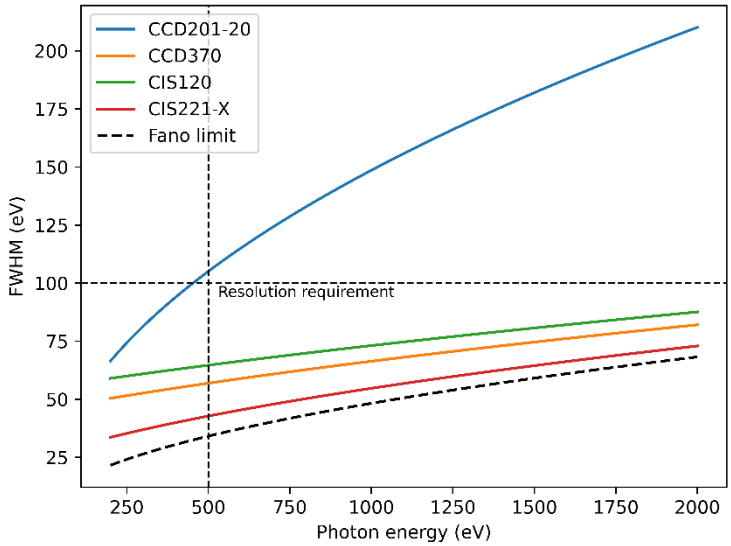

Figure 6.8. Energy resolution predictions for all X-ray detectors, expressed as FWHM.

The effect of the EM gain on the energy resolution of the CCD201-20 (as discussed in section 3.5.6) results in it not meeting the 500 eV energy resolution requirement. The CCD201-20 is not discounted at this point, however, as its expected performance is only slightly worse than required, and it shows far better detectability properties than the other candidate detectors.

Like the method used for detectability in Figure 7, we may instead resolve equation 3 while varying the noise parameter, rather than energy, as shown in Figure 6.9. Exploring the energy resolution at 500 eV, the predicted resolution of the CIS and CCD370 is only degraded beyond the required resolution with an additional noise source of > 8 e^- rms, indicating that detectability is the limiting performance parameter rather than resolution. The CCD201-20 begins with marginal energy resolution requirement compliance and so has a noise budget of 0 e^- rms, though as the noise source modelled in this plot has not been suppressed by the EM gain (that is, it is modelled as occurring within each pixel).

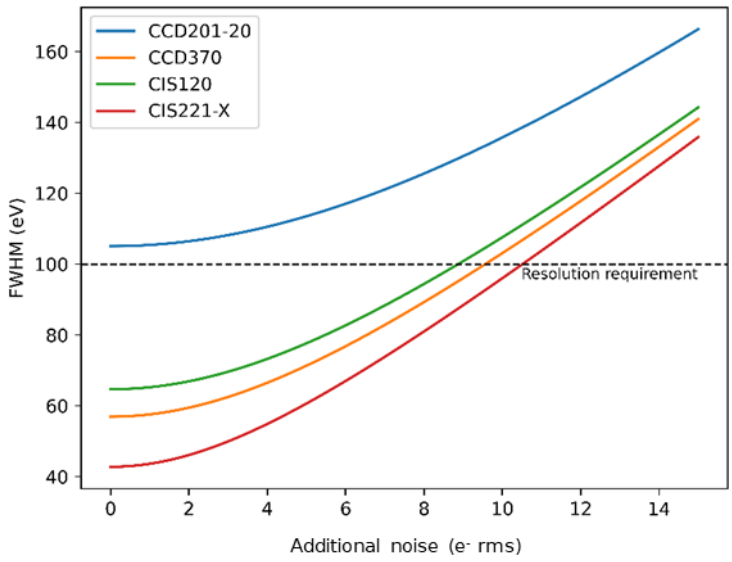

Figure 6.9. X-ray energy resolution for 500 eV X-rays energy with increasing noise provided by an additional noise source.

6.2.1.4 Energy performance requirements summary

The baseline CCD201/CCD311 has been maintained as an option for AXIS, despite concerns about its energy resolution. With sufficient, sensitivity, and ability to detect low energy X-rays according to the modelling presented, the EMCCD meets the instrument's other energy requirements. Of the candidate replacement X-ray detectors only the CIS221-X measures equally well. While all non-EMCCD X-ray detectors exhibit good noise, the full depletion and large pixels of the CIS221-X, which reduce the chance of event splitting, mean that it is not penalised for its per-pixel noise which is higher than the EMCCDs'.

6.2.2 Event reconstruction

A key difference between the candidate X-ray detectors is the way in which their properties modify the effect X-ray event reconstruction has on their performance. When using the dual thresholding techniques of section 4.3 threshold values for optimum performance will vary. With reference to the common approaches to reconstruction in chapter 4, the AXIS instrument will be required to operate with a low flux of science X-rays making the usage of all grades of X-ray important. This means an understanding of the likely performance of each X-ray detector for the reconstruction of low-grade X-ray events was necessary. This behaviour does not have a simple relationship to X-ray detector properties, therefore more detailed analysis has been completed.

The following is an attempt to provide a mathematical description for additional uncertainty introduced by the process of collecting the X-ray generated electrons into a region of noisy pixels and reconstructing the recorded pixels values back into an estimated X-ray energy value. Though other

reconstruction processes exist, pixel thresholding techniques have been modelled because they are the most relevant for AXIS.

To reiterate from section 4.2, the extraction of meaningful X-ray data from raw data usually occurs in two steps after image calibration: the first identifies high signal pixels likely to be containing X-ray generated charge; the second step involves the analysis of the surrounding pixels to identify any also containing X-ray generated charge. Both steps are generally completed using thresholding techniques and the thresholds are set using an understanding of the detector noise.

To understand the effect of event reconstruction on apparent X-ray detector performance for AXIS, a model for the reconstruction process has been built and explored. The findings have informed the data handling procedures used in this and following chapters. To maintain some level of tractability the more complex processes of event profiling and pixel rejection based on expected X-ray event shapes (illustrated by figure 1 of Pigot et al. (2000)) have been ignored. This means that there are only two sources of noise introduced or affected by the reconstruction process, charge excluded during reconstruction and total per-pixel noise.

6.2.2.1 Charge distribution

Ultimately, the key properties of interest are seen as the combined behaviour of all X-rays in a population. Therefore, the first step to understanding the effects of event reconstruction is to predict the distribution of pixel values that could be expected from a starting population of X-rays.

The charge collected in each pixel associated with an event is dependent on the pixel location, the X-ray interaction location and depth, the energy of the photon, and the parameters associated with the X-ray detector's properties. That is, the probability that a pixel has a given signal may be expressed by equation (6.4).

$$P(n_{e^-}) = f\left(x_{pix}, y_{pix}, x_{ph}, y_{ph}, z_{ph}, E_{ph}, param_{detector}\right) \tag{6.4}$$

Where $P(n_{e^-})$ is the probability of n_{e^-} electrons being collected in a pixel; x_{pix} and y_{pix} are the pixel coordinates (in column and row indices); x_{ph}, y_{ph} and z_{ph} are the coordinates of the initial X-ray interaction; E_{ph} is the X-ray photon energy; and $param_{detector}$ is an array of device parameters including pixel geometry, semiconductor properties and operating conditions.

When evaluating (6.5) certain simplifications can be made. In a sufficiently large detector, performance will be dominated by pixels well away from the array edge. In this case values for x_{pix} and y_{pix} can be resolved relative to the pixel in which an X-ray is incident, without considering X-ray events that spill out of the image area. If we are considering interaction and pixel coordinates relative

to the incident pixel, values for x_{ph} and y_{ph} are restricted to values representing the area of the incident pixel. If exploring the properties of an X-ray population they can be modelled as having a uniform distribution. z_{ph} has been measured from the back (illuminated) surface, the distribution of z_{ph} values for a population of X-rays have an exponential probability distribution, the Beer-Lambert law of section 3.4.1.4. For the purposes of this analysis E_{ph} was fixed. The required detector parameters ($param_{detector}$) are dependent on the method of charge distribution modelling. These parameters represent the properties of the X-ray detector and are largely specific to a single detector. However, for the purposes of this analysis only pixel geometry parameters have been changed, and the properties of the semiconductor left the same. The equations from Pavlov and Nousek (1999) were used for modelling charge transport behaviour in field-free and depleted regions of a CCD, as these had previously been identified as a good predictor of event charge distribution (Soman, 2014).

The inclusion of the charge collection from equations Pavlov and Nousek (1999) makes the evaluation of $P(n_{e^-})$ non-trivial. Therefore, to probe the reconstruction properties of each detector, a set of Monte-Carlo trials were run using the charge distribution model to convert an expected population of X-rays into an expected population of recorded X-ray events.

6.2.2.2 Charge exclusion uncertainty

The probability that a pixel is included in an event is defined in equation (6.5). That is, the probability that the X-ray generated signal of a pixel, added to any noise, is greater than the detection threshold:

$$P_{included} = P\left(n_{e^-,X-ray} + n_{e^-,pixel} > \gamma_{thresh}\right) \tag{6.5}$$

Where $n_{e^-,X-ray}$ is the X-ray generated charge; $n_{e^-,pixel}$ is the charge contributed, or removed, by noise with a variance of σ_{pix}; and γ_{thresh} is the inclusion threshold value, expressed as charge. In this equation both $n_{e^-,X-ray}$ and $n_{e^-,pixel}$ are random variables, rather than the mean or rms values. If we assume the noise in each pixel of the detector is roughly Gaussian, the probability of inclusion for a given signal level, threshold and rms pixel noise is provided by equation (6.1), which the detection probability is equal to the inclusion probability, and the X-ray charges are instead replaced by the expected number of electrons due to an X-ray (in both the incident and surrounding pixels). That is:

$$\mathrm{P}_{included} = P_{detect}$$
$$n_{e^-,X-ray} = \bar{e_{X-ray}}$$

Where:

$$P_{included} = 1 - P_{ignored} \tag{6.6}$$

The dependence of the probability of a pixel being ignored on the threshold value and pixel value have been illustrated in Figure 6.10.

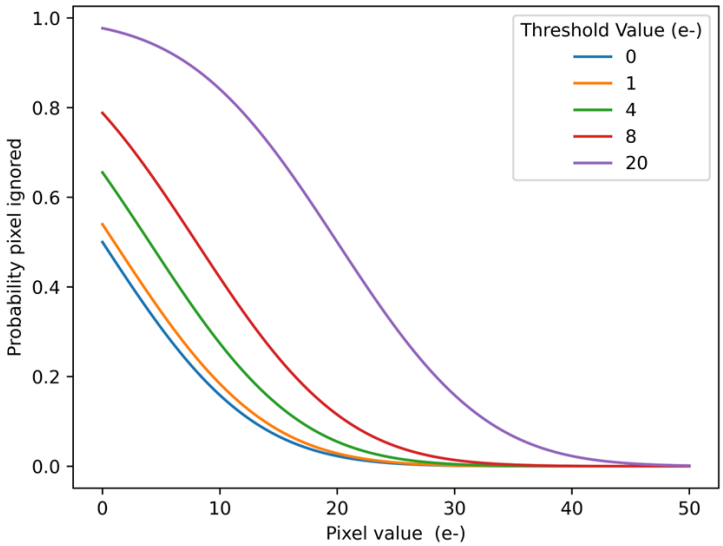

Figure 6.10 Probability of pixel exclusion for various threshold values, using 10 e⁻ rms pixel noise.

The charge lost from a given pixel, for a given a distribution of pixel values, will have a distribution described by equation (6.7):

$$Q_{lost} = n_{e^-,X-ray} P\left(ignored \middle| n_{e^-,X-ray}\right) P\left(n_{e^-,X-ray}\right) \tag{6.7}$$

Where the term Q_{lost} is the amount of charge excluded following a pixel being ignored, and $P\left(ignored \middle| n_{e^-,X-ray}\right)$ is the probability that an X-ray is ignored, given it produces $n_{e^-,X-ray}$ electrons. This implies that the mean charge lost from any given pixel will be given by equation (5.2).

$$Q_{lost} = \int_0^{Q_{ph}} n_{e^-,X-ray} P\left(ignored \middle| n_{e^-,X-ray}\right) P\left(n_{e^-,X-ray}\right) \delta n_{e^-,X-ray} \tag{6.8}$$

Where Q_{ph} is the maximum charge expected from an event. The total lost charge can then be found by summing the mean charge lost values across the pixels containing charge from an X-ray event, using the distribution of expected pixel values from the Monte Carlo trials:

$$\mu_{lost,tot} = \Sigma \mu_{Q_{lost}} \tag{6.9}$$

And more importantly the variance in charge lost can be found by summing the variance in charge lost across all event pixels:

$$\sigma^2_{lost} = \Sigma \sigma^2_{Q_{lost}} \tag{6.10}$$

This σ_{lost}^2 represents the uncertainty associated with the exclusion of charge from a reconstructed event. In an ideal X-ray detector this value stays low, either because noise is low, so any X-ray event charge puts a pixel above any reconstruction threshold, or because the amount of charge spread beyond an initial pixel is very low. This is a source of event uncertainty with a direct impact on energy resolution.

6.2.2.3 Per-pixel noise

There is also a penalty for including pixels when measuring an X-ray, in the form of additional per-pixel noise sources. This will mean that the noise exhibited by a population of X-rays due to per-pixel noise will generally exceed the value for per-pixel noise in a single pixel. Over the region of interest around the incident pixel the total variance included from per-pixel sources is given by:

$$\sigma_{inc}^2 = \sigma_{pix}^2 \,.\, \mathbb{B}\left(P_{included,i,j}\right) \tag{6.11}$$

Where $\mathbb{B}\left(P_{included,i,j}\right)$ is a Bernoulli trial for the inclusion of pixel i,j, which will have a probability of inclusion determined by the expected value for pixel i,j, as per equation (6.5) using the pixel value determined by equation (6.4). The mean value of $\sigma_{inc}^2$is representative of the effective per-pixel noise across the population of reconstructed events. That is:

$$\sigma_{pixel,tot} = \sqrt{\sum\nolimits_{i,j} P_{included,i,j} \times \left(\sigma_{pix}\right)^2} \tag{6.12}$$

6.2.2.4 Reconstruction noise

The total rms noise of the reconstruction process is:

$$\sigma_{event,tot} = \sqrt{\sigma_{pixel,tot}^2 + \sigma_{lost}^2} \tag{6.13}$$

In practice the additional noise due to the inclusion of many pixels is anti-correlated with the uncertainty associated with excluding charge and limits the range of behaviours the model can describe accurately to those close to optimum.

6.2.2.5 Application to AXIS X-ray detectors

This simplified model of the effect of event reconstruction permits the rapid exploration X-ray detector performance. The reconstruction model was applied to simplified examples of the X-ray detectors considered for AXIS to determine the best reconstruction threshold to use for each. The three detectors could be represented with three archetypes: a low noise, high charge spread detector

(CCD201-20 or CCD311); a high noise, high charge spread detector (CIS120); and a high noise, low charge spread detector (CIS221-X). The CCD370 was not modelled.

The first archetype was distinguished by very low per pixel noise, but small pixels and a larger field free region, representative of the EMCCDs under consideration. Evaluation of the charge distribution with the Pavlov and Nousek model indicated that the majority of identified X-rays would be spread across many pixels. This resulted in the performance illustrated in Figure 6.11, showing that the penalty for including many pixels was low while the noise introduced by excluding pixels with a high reconstruction threshold was predicted to be high. Therefore, when analysing X-ray data from the EMCCDs considered in the following chapters, a very low threshold has been used.

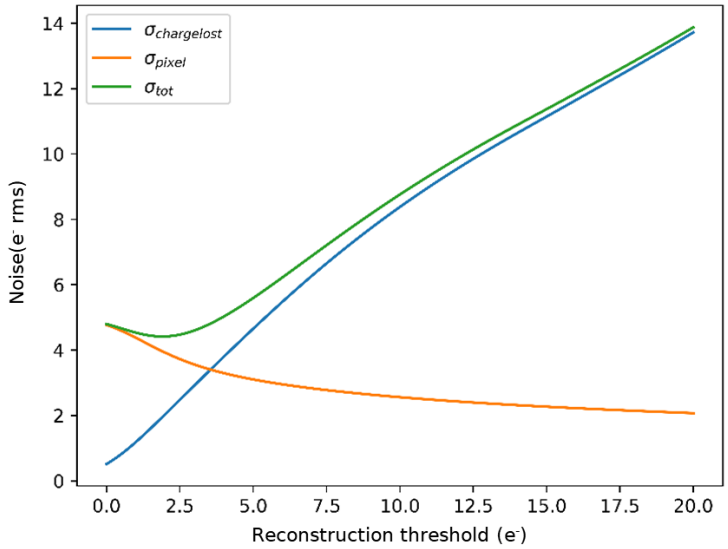

Figure 6.11. Modelled reconstruction noise for 1400 eV X-rays in the CCD201-20, for reconstruction threshold.

Evaluation of a second archetype with small pixels and relatively high-per pixel noise, like the CIS120, indicated that there is a trade-off to be made between the per-pixel noise and excluded charge uncertainty, illustrated in Figure 6.12. This indicates that these X-ray detectors are likely to face a significant penalty for including more than single-pixel events. While, qualitatively, the behaviour of the high noise detector looks similar to the low noise detector, the optimum point occurs at a threshold value of around 18 e^-, and the total noise is much higher than the low noise detector at that point.

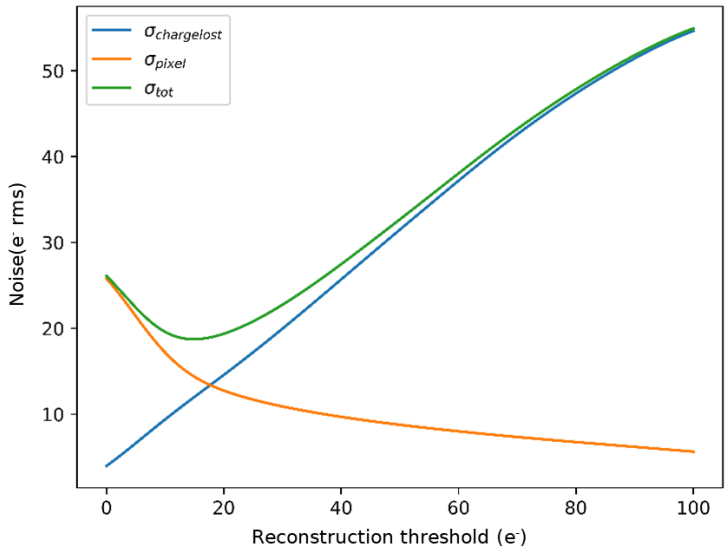

Figure 6.12. Modelled reconstruction noise for 1400 eV X-rays in an approximate model of the CIS120, for reconstruction threshold.

Finally, looking instead at the CIS221-X (with large pixels, fully depleted, but still high per-pixel noise) indicated a relationship opposite to that of the EMCCD-like model. Here, the exclusion uncertainty was seen to level off quite quickly meaning there is little additional penalty for a high reconstruction threshold (illustrated in Figure 6.13). This is because most X-ray interactions are recorded in a single pixel, according to the charge distribution model. The population of split pixel events is either quickly subjected to charge exclusion or consists of events that can be well reconstructed even with high reconstruction thresholds, for instance interactions with 50 % of the signal recorded in two pixels. However, because these X-ray detectors will be required for a range of X-ray energies, choosing a reconstruction threshold as close to the start of the plateau as possible has been deemed best.

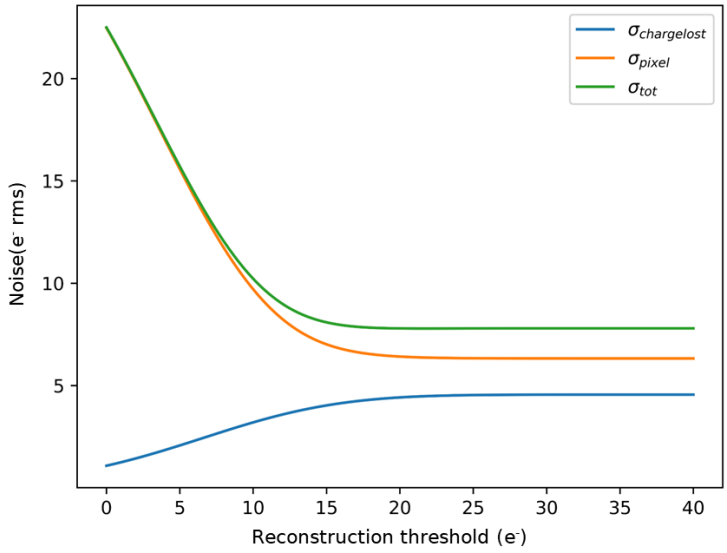

Figure 6.13. Modelled reconstruction noise for 1370 eV X-rays in an approximate model of the CIS221-X, for reconstruction threshold.

6.2.3 Spatial performance

The AXIS spatial requirements were derived from the baseline design (summarised in Table 2.1 of section 2.2), which indicate a spatial resolution of 5 km and an instrument footprint width of 600 km are required.

These spatial resolution performance metrics are largely driven by the design of the X-ray optic, rather than the detector. Even so, each X-ray detector was tested for compliance with the spatial requirements of the instrument with the baseline AXIS pinhole camera. In cases where there was a significant performance benefit, the effect of modifying the optic to better suit each of the X-ray detectors was explored.

6.2.3.1 Instrument field of view

The AXIS instrument baseline specifies the use of a pinhole camera with a 1 cm focal length and 100 µm pinhole in a 2 mm thick aluminium sheet, part of an aluminium and tungsten shield for the X-ray detector, shown in Figure 6.14. In the absence of further specification, the pinhole has been assumed to be of the knife-edge type, made of two conical bores cut from either side with good FOV properties. Optical photons will be blocked by an aluminium optical blocking filter applied directly to the X-ray detector.

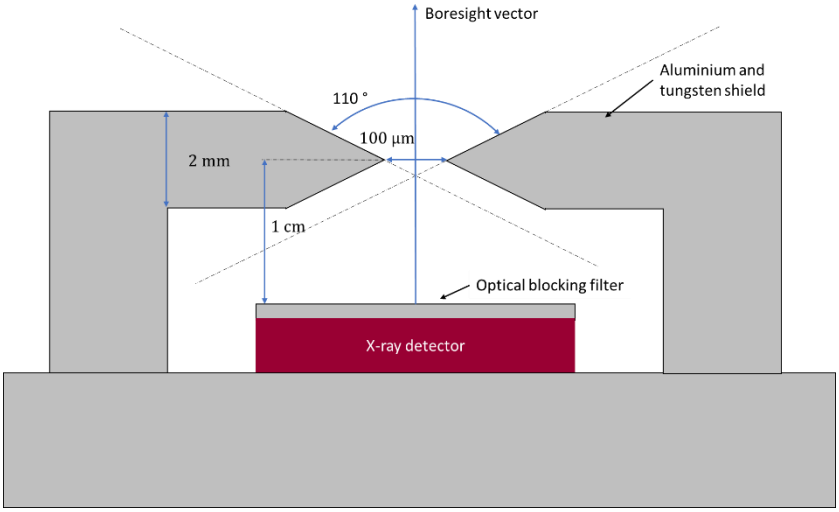

Figure 6.14. Sketch of AXIS pinhole camera. Not to scale.

When considering very 'thin' pinholes, the aperture can be considered as a hole in a 2D plane, resulting in large simplifications of characteristic expressions (Shokouhi et al., 2009). Practical pinholes are generally formed in a sheet with non-zero thickness, however. This can result in the pinhole self-shadowing, resulting in much lower sensitivity to incoming photons from high off-boresight angles. Additionally, some transmission of incoming photons through the pinhole material can be expected, especially near the tip of the knife-edge, which can lead to a larger effective aperture area (Metzler et al., 2001). However, self-shadowing effects are not expected (because the pinhole opening angle is larger than the instrument field of view required for the baseline design footprint width) and the attenuation length of X-ray photons at the energies of particular interest for science are very short. Therefore, for the purposes of the trade-off study the ideal pinhole approximation has been used. It should be noted that the effective aperture area (A_θ) does decrease with increasing angles off boresight, proportional to $sin^3\theta$ (Metzler et al., 2001):

$$A_\theta = A_0 \times \sin^3(\theta) \tag{6.14}$$

Where A_0 is the maximum aperture effective area, in this case it has been assumed to be the geometric area, and θ is the angle between the boresight vector and a ray traced between the focal plane and a point in the FOV through the pinhole. This is independent of the pinhole geometry, provided that the complicating self-shadowing and pinhole transmission behaviours are not impacting performance. For $\theta = 55\,°$ (the maximum value for θ in the baseline design with the 110 ° opening angle), A_θ is approximately $0.55\,A_0$. This will reduce the expected X-ray flux at the edge of the FOV. However, for the purposes of this X-ray detector trade-off the effect is less critical and is assumed to have an acceptable impact on the science performance of the instrument.

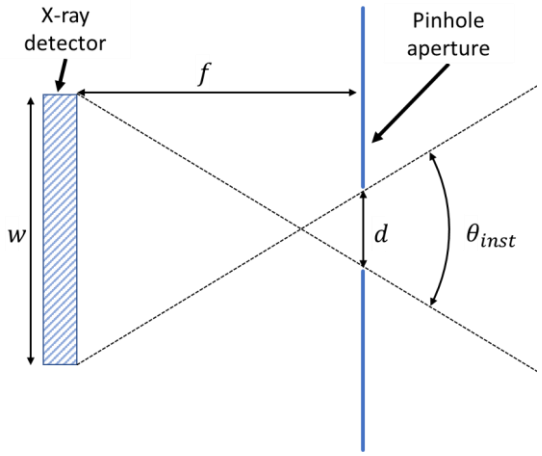

Figure 6.15. Schematic of ideal pinhole aperture.

To ensure adequate flux across the X-ray detector, it is expected that the FOV of the instrument will be restricted by the size of the X-ray detector rather than the opening angle of the pinhole. In this case equation (6.15) can be used to determine the instrument FOV:

$$\theta_{inst} = 2\tan^{-1}\left(\frac{w}{2f}\right) \tag{6.15}$$

Where w is the width (or length assuming the detector is square) of the X-ray detector, and f is the focal length of the X-ray optic (as per Figure 6.15). Figure 6.16 shows the relationship between X-ray detector sensitive area dimensions and FOV, for the current focal length of 1 cm, demonstrating that the CCD201-20 under-fills the area illuminated by the baseline pinhole.

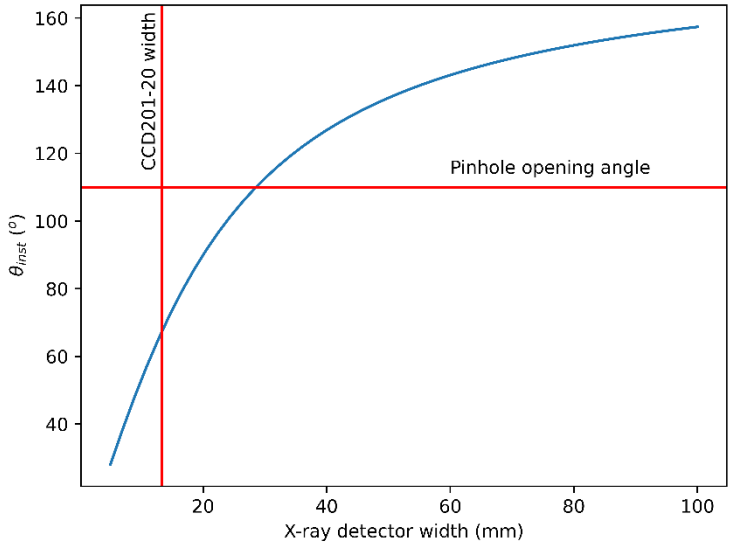

Figure 6.16. Instrument FOV angle for X-ray detector width (with 13.3 mm CCD201-20 labelled), for pinhole optic using 1 cm focal length.

The spatial performance of AXIS is also dependent on spacecraft altitude and the altitude from which the X-ray emission originates. A diagram of this geometry is shown in Figure 6.17, with the AXIS instrument baseline values labelled. Though the instrument footprint is commonly defined at the surface of the Earth, the height of X-ray emission has been included because X-rays are known to be produced at altitudes in excess of 200 km (Luhmann et al., 1979), for which the instrument footprint is considerably smaller.

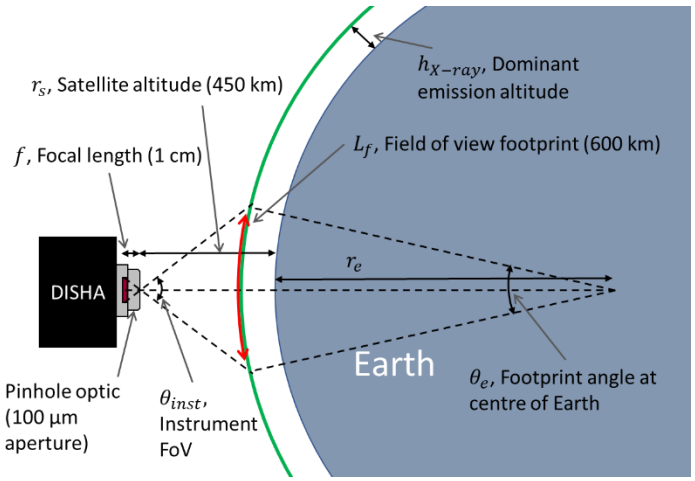

Figure 6.17. Diagram of instrument and target geometry with baseline dimensions in nadir pointing mode. H_{X-ray} can take a value between 20 and 200 km depending on auroral structure.

Evaluation of Figure 6.17 allows for the derivation of equation (6.16), which describes the observation footprint width (L_f) of AXIS given the expected X-ray emission altitude (h_{X-ray}), the radius of the Earth (r_e), and half the angle subtended by the footprint at the centre of the Earth (θ_e).

$$L_f = (r_e + h_{X-ray}).\theta_e \tag{6.16}$$

Where θ_e is itself a function of the instrument FOV (θ_{inst}) and satellite altitude (r_s).To derive expressions for θ_{inst} and θ_e the simplified geometry of Figure 6.18 was used where the pinhole of AXIS is placed at D, the centre of the Earth at E and half of the FOV footprint along the arc A_1A_2. Here, $y = r_e + h_{X-ray}$, $x = r_e + r_s$, $\theta = \theta_{inst}/2$, and $\phi = \theta_e/2$. For simplicity of expression, all equations relating to the geometry of AXIS use radians, however the results are reported in degrees for consistency with other documents.

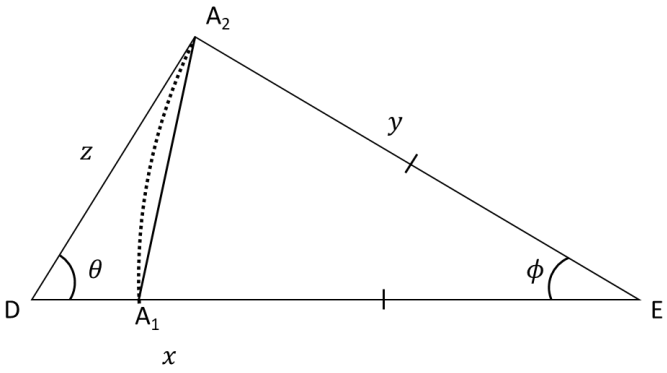

Figure 6.18. Simplified viewing geometry of AXIS.

From Figure 6.18, the expression (6.17) can be derived:

$$\frac{\sin\theta}{y} = \frac{\sin(\pi - \theta - \phi)}{x} = \frac{\sin(\theta + \phi)}{x} \tag{6.17}$$

Therefore:

$$\phi = \sin^{-1}\left(\frac{x\sin\theta}{y}\right) - \theta \tag{6.18}$$

And:

$$\theta = \tan^{-1}\left(\frac{\sin\phi}{\frac{x}{y} - \cos\phi}\right) \tag{6.19}$$

Or, expressed in the original instrument parameters:

$$\theta_e = 2\sin^{-1}\left(\frac{(r_e + r_s)\sin\left(\frac{\theta_{inst}}{2}\right)}{r_e + h_{X-ray}}\right) - \theta_{inst} \tag{6.20}$$

$$\theta_{inst} = 2\tan^{-1}\left(\frac{\sin\left(\frac{\theta_e}{2}\right)}{\frac{r_e + r_s}{r_e + h_{X-ray}} - \cos\left(\frac{\theta_e}{2}\right)}\right) \tag{6.21}$$

Equations (6.16) and (6.20) can be used to relate the instrument FOV to the instrument footprint, shown in Figure 6.19.

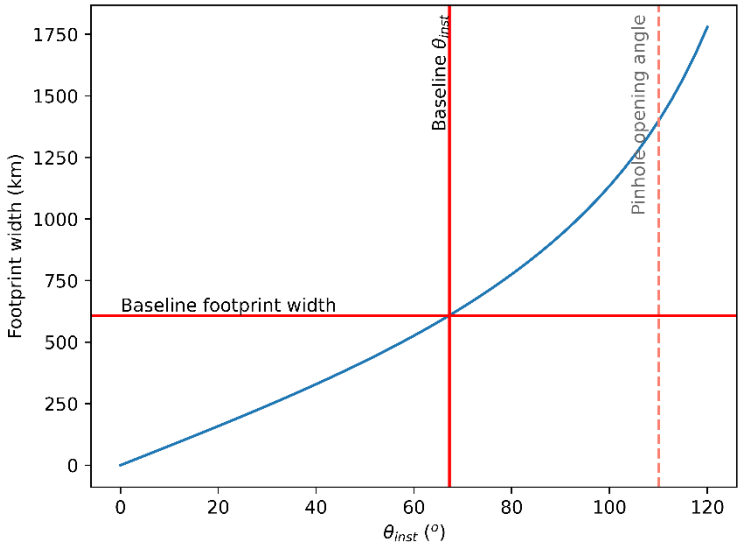

Figure 6.19. Instrument FOV footprint width for AXIS instrument opening angle, with the baseline design parameters indicated. Footprint width is limited by the X-ray detector size at focal plane rather than the pinhole opening angle.

6.2.3.2 Spatial Resolution

The effective spatial resolution of the instrument is limited by the size of the pinhole aperture and projection geometry. To a first approximation, the spatial resolution of a soft X-ray detector (as part of the instrument) is limited by the pixel size, although it can be improved by more detailed analysis of identified X-ray events and centroiding (Soman et al., 2013), or degraded if the MTF of the X-ray detector is particularly poor. The pinhole aperture (baselined as 100 µm) is larger than the detector pixel pitch, and therefore we assume here that the spatial resolution on the focal plane will be roughly equal to the aperture diameter. When projected into the footprint area, the resolution at the footprint altitude (x_{min}) is described by equation (6.22).

$$x_{min} = \frac{d.R}{f} \tag{6.22}$$

Here, R is the distance between the pinhole and the footprint altitude and d and f are aperture diameter and focal length of the instrument as before. The spatial resolution of the instrument may be calculated as function of focal length, as plotted in Figure 6.20.

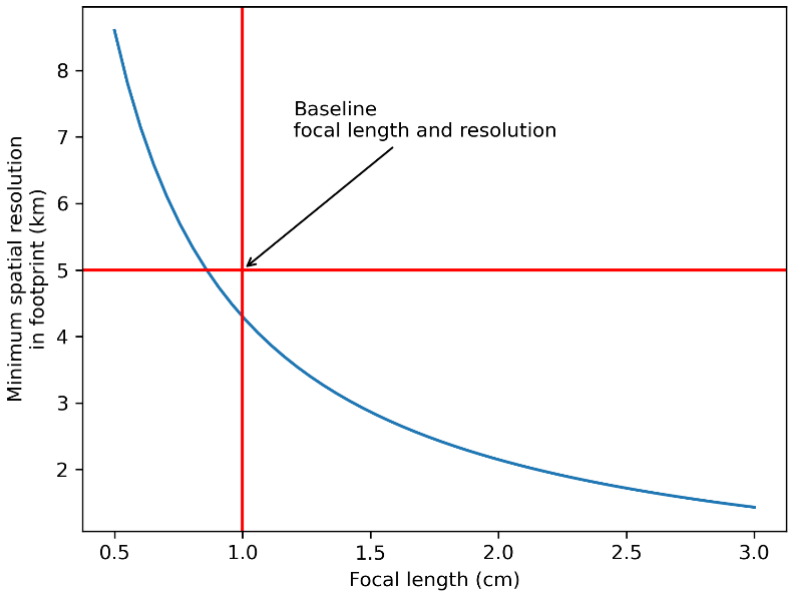

Figure 6.20. Pinhole-limited spatial resolution of instrument for varying focal length, using the baseline 100 µm pinhole diameter.

The maximum wavelength of the X-rays to be observed by AXIS is approximately 4 nm, less than a thousandth of the baseline pinhole aperture diameter. Therefore, diffractive effects are not expected to impact instrument performance.

6.2.3.3 X-ray detector suitability

From the expressions derived above, it is evident that only two properties of each X-ray detector are relevant for the spatial performance of AXIS: sensitive area and pixel pitch. These have been summarised in Table 6.3.

Table 6.3. Trade-off X-ray detector properties relevant for spatial performance.

	CCD201-20	**CCD311**	**CIS120**	**CIS221-X**	**CCD370**
Technology	EMCCD	EMCCD	CIS	CIS	CCD

Pixel pitch (µm)	13	13	10	40	108[5]
Sensitive area (mm x mm)	13.3 x 13.3	13.3 x 13.3	20.5 x 20.5	20.5 x 20.5	81.2 x 68.2

If the baseline design was used, all X-ray detectors are equal in size or larger than the baseline CCD201-20 and therefore able to cover an equivalent area in the focal plane, and all X-ray detectors have sufficient pixel pitch to achieve the required spatial resolution. The CCD370 is the only X-ray detector with a pixel pitch large enough, after binning, to become pixel limited, as opposed to aperture limited for spatial resolution.

However, the different X-ray detectors may enable an improvement in the pinhole performance. The larger detectors overfill the area illuminated by the pinhole in the baseline design, intended for the smaller CCD201-20. Increasing the focal length of the instrument has the potential to both increase the area illuminated by the pinhole and relax requirements on the pinhole diameter which may enable a larger pinhole to be used for increased X-ray flux.

Equation (6.23) expresses the ideal instrument focal length in terms of X-ray detector width and required FOV, derived from equation (6.15). Equation (6.24) describes the maximum permissible pinhole diameter for required spatial resolution, instrument focal length, and distance to the X-ray emission region, derived from equation (6.22). Finally, equation (6.25) relates the expected X-ray flux Φ_d for a given pinhole diameter *d*, using the simple pinhole model and the baseline design pinhole diameter and flux, d_0 and Φ_0 respectively. The baseline design, summarised in section 2.2, has a Φ_0 of 8 count/s.

$$f = \frac{w}{2\,tan\left(\frac{\theta_{inst}}{2}\right)} \tag{6.23}$$

$$d = \frac{x_{min} \cdot f}{R} \tag{6.24}$$

$$\Phi_d = \Phi_0 \times \left(\frac{d}{d_0}\right)^2 \tag{6.25}$$

[5] With on-chip binning

These formulas have been applied to the candidate X-ray detectors to determine the ideal X-ray optic parameters, summarised in Table 6.4.

Table 6.4. Suggested pinhole parameters for candidate X-ray detectors.

	CCD201-20	**CCD311**	**CIS120**	**CIS221-X**	**CCD370**
Sensitive area (mm x mm)	13.3 x 13.3	13.3 x 13.3	20.5 x 20.5	20.5 x 20.5	81.2 x 68.2
Focal Length (mm)	10	10	15.4	15.4	61.1
Pinhole Diameter (µm)	100	100	154	154	611
X-ray Flux (count s^{-1})	**8**	**8**	**19**	**19**	**298**

The CIS X-ray detectors and CCD370 all enable higher X-ray fluxes, which will improve instrument performance by reducing minimum sensitivity thresholds and the time required to produce scientifically useful data when observing the aurora, whilst maintaining the required spatial resolution. The CCD370 has a greatly improved performance over the alternative detectors. However, it must be reiterated that the CCD370's inclusion in the trade-off is largely illustrative as it is highly unlikely to be available for the instrument. In this case, it illustrates why large focal planes are advantageous. Furthermore, though a large instrument would deliver better performance it would also increase the instrument weight and cost.

6.2.3.4 Considerations for the CIS221-X

While the assumption during the trade-off study was that AXIS would use a CIS221-X derivative, there is also the possibility that an unmodified CIS221-X could be viable as an X-ray detector. This could be completed in two ways.

In the first, only the variant 3 pixels would be used providing the best pixel performance and enabling AXIS to make best use of the results and findings relevant to THESEUS, which has focussed on this, the best performing, variant. This would reduce the sensitive area to a 20.5 mm x 5.125 mm rectangle. While not ideal, if the CIS221-X could be oriented correctly this could result in a lower impact on performance. Operating the detector with the long edge perpendicular to the direction of travel would result in a minimal loss in spatial resolution or coverage, as the variant 3 pixels would eventually observe the regions that should have been covered by the rest of the detector. However, this would result in a reduction of the expected X-ray flux by 75 %.

In the second, one or more of the other pixel variant regions could be used to extend the sensitive area in addition to the variant 3 pixels. The variant 2 pixels have worse image lag properties than the variant 3 pixels, which should manifest as greater event value uncertainty and therefore worse energy resolution. Using the detector in this manner would result in a roughly equal X-ray flux to the baseline design. The worse performance of the variant 2 pixels makes this the less preferred option.

In this initial trade-off study the use off the CIS221-X was regarded largely as a representation of future X-ray detectors, and therefore only the performance of the variant 3 pixels has been modelled and tested.

6.2.4 Framerate

Finally, a consideration of the framerate achievable by each candidate X-ray detector is required. A high framerate, and short integration and readout time is important for three reasons:

1. Sensitivity at the lowest X-ray energies is particularly important for AXIS, and negatively influenced by optical blocking filters. To achieve maximum sensitivity below 500 eV the optical blocking filters must be made as thin as possible. However, this also makes them less effective at functioning as optical filters and transmission of optical photons becomes more of a concern. This is a particular issue for AXIS, as its primary objectives include observations of the Earth's dayside. Large optical light leakage will manifest like an increase in dark current.
2. The DISHA-H satellite is not intended for a high orbit; at the baseline 450 km the instrument will have a velocity of almost 8 km s^{-1} relative to the aurora. To adequately map recorded X-rays to locations within the aurora, down to the 5 km resolution required, seconds-long exposures are not possible.
3. A high framerate is also useful for supressing the effect of dark current. Photon counting soft X-ray imaging spectroscopy is primarily concerned with dark signal, and not dark current, because photons are recorded and extracted with a single frame. Faster framerates result in higher permissible dark current.

By suppressing readout noise with the EM gain, EMCCDs can employ fast readout amplifiers and digitisers. The Teledyne-e2v EMCCDs have demonstrated pixel readout rates in excess of 10 MHz (Harding et al., 2015). The CCD201-20, with 1024 by 1024 pixels, could therefore be expected to achieve a framerate of 10 Hz. This can be done with little degradation in its sub-electron noise performance and is the primary reason for its selection in the baseline design.

The parallel nature of the CIS readout means the CIS120, and CIS221-X, outperform the EMCCDs framerate with some margin. The CIS120 is able to achieve a framerate of 20 Hz (Teledyne e2v, 2017). The CIS221-X is built on the CIS120 architecture, where the 40 µm pixels are made with the standard 10 µm pixel readout sequencers and digitisers, but with only one pixel per 16 connected. Skipping the unconnected, dummy rows (columns cannot be skipped) should permit a framerate of 80 Hz.

The CCD370, uses a standard serial pixel readout and to achieve adequate noise performance the recommended readout rate is 100 kHz (Soman et al., 2018). Though it does have two output nodes, acting to halve the time required to readout a frame, its 751 by 631 pixels take a minimum of 2.37 seconds. This framerate of 0.4 Hz lowers its suitability for AXIS significantly.

6.3 Experimental trial

Practical demonstrations of the candidate X-ray detectors were performed with X-rays within the AXIS energy range to measure X-ray event uncertainty, particularly the difference between this value and ideal Fano-limited performance (in which the noise is limited by Fano noise). All detectors were tested by exposure to soft X-rays from several fluorescence targets, though for brevity only select results have been presented below. The CCD201-20, CIS221-X and CIS120 were tested, the CIS311 was expected to have unchanged behaviour to the CCD201-20 unirradiated and the CCD370 was not available for tests.

6.3.1 Test chamber

For the evaluation of X-ray detectors for AXIS a dedicated test setup was constructed. Key contributions of the author to the AXIS chamber included construction and commissioning, and the development of the cold head control software capable of unsupervised temperature slewing across the temperature range required for the AXIS investigation. The chamber design was based on the test chamber used during evaluation of the CIS221-X for THESEUS (Heymes et. al. 2022).

The test equipment of Figure 6.21 and Figure 6.22. It was designed to be flexible enough to permit most characterisation tests to be conducted without requiring chamber components to be changed, which would have required a pressure and temperature cycle for each change. The apparatus consisted of a vacuum chamber built as a 6-way cross. The five available flanges (the 6th being used as the chamber base) were used for:

1. A connection to a vacuum pump
2. An electrical feedthrough used to control an array of LEDs
3. An X-ray tube

4. A wheel of X-ray fluorescence targets mounted on a motorised rotary manipulator
5. A drive board and TEC-based cooling system

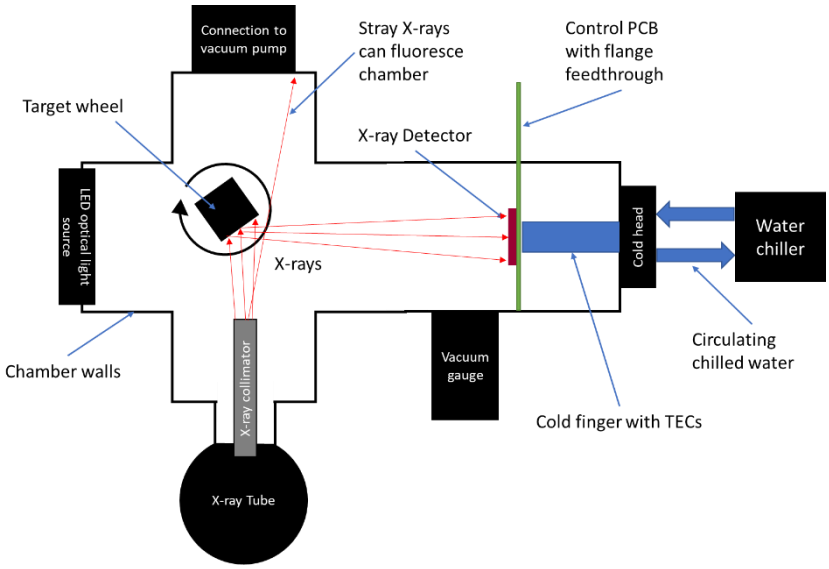

Figure 6.21. A top-down schematic diagram of experimental apparatus used for X-ray detector tests.

X-rays were generated with an Oxford Instruments Jupiter 5000 X-ray tube. The produced X-rays were used to fluoresce targets with known chemical compositions, as per section 4.2.1. The fluoresced X-rays were detected by the X-ray detectors. The fluorescence targets were mounted on a rotating wheel to expose them to the X-ray tube beam. This included copper (primary fluorescence energies at roughly 8 keV) and aluminium (primary energies at roughly 1.4 keV) targets used during the trade-off study and silicon dioxide (primary energies at 1.7 keV and 0.5 keV) and boron nitride (primary energy at 0.3 keV) targets used in later chapters.

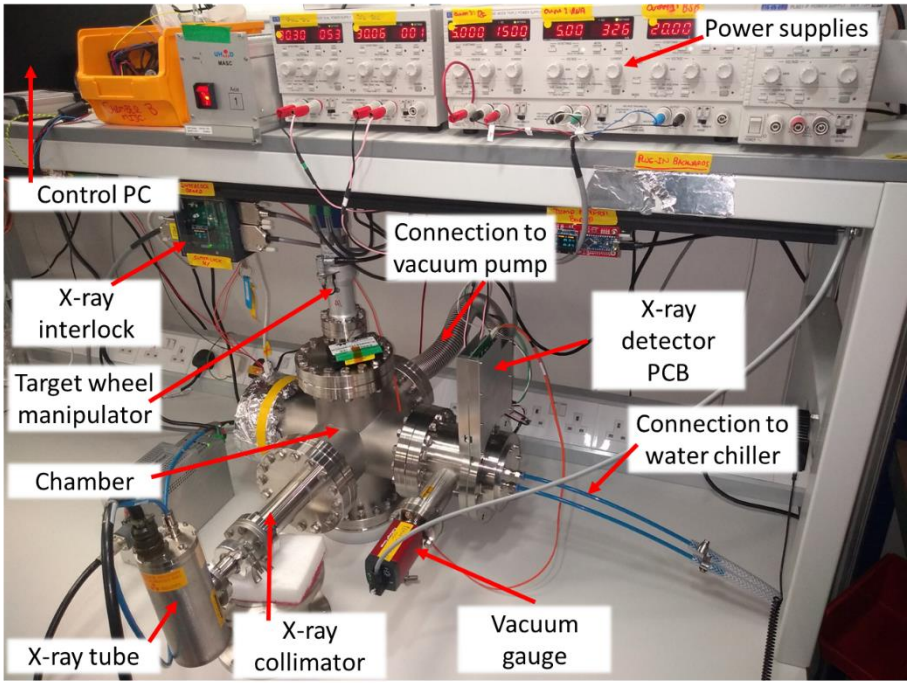

Figure 6.22. Apparatus used for the work in the AXIS study with components labelled.

Accurate temperature control of the X-ray detector was achieved using a Peltier thermo-electric cooler (TEC) based cold finger. To enable longer experiment runs, the operation of this system was automated, with a control system implemented specifically for this investigation. The control system, written in python (by the author), permitted unsupervised temperature slews between -45 ^{o}C and +20 ^{o}C, included PID and slew limiting control loops operating in asynchronous control threads, and included an automatic safety shutdown to protect the X-ray detector from excessive heat.

All elements of the test setup were operated automatically. Serial communications were used: to control the power supplies for the cold finger and X-ray detector; to send commands to and grab frames from the X-ray detector; to control the target wheel manipulator; and to toggle the X-ray interlock 'enable' to turn the X-ray tube on and off. Manual operation of the vacuum pump and water chiller was retained as these devices were not expected to be required to change operation during experimental runs. Experiment runs were completed with an author written python library which managed all serial communications and abstracted many apparatus operations for ease of future readability of experiment operation scripts,

The hardware of the test chamber was largely unchanged from the initial design used in the THESEUS test campaigns (Heymes et al., 2022; Stefanov et al., 2022). Apparatus changes were primarily software based, focussed on improving integration of control and test automation. Of these, the cooling system control was the largest point of difference.

6.3.2 CCD201-20

The CCD201-20 was not tested in the CIS221-X chamber due to flange compatibility issues. The only differences to the chamber used and the test apparatus described above was a slightly longer throw between the fluorescence target and X-ray detector, and a calibration iron-55 source placed in the X-ray detector field of view producing a steady flux of Mn Kα and Mn Kβ X-rays. A typical spectrum of X-ray event energies observed with this device is shown in Figure 6.23 (with an aluminium target).

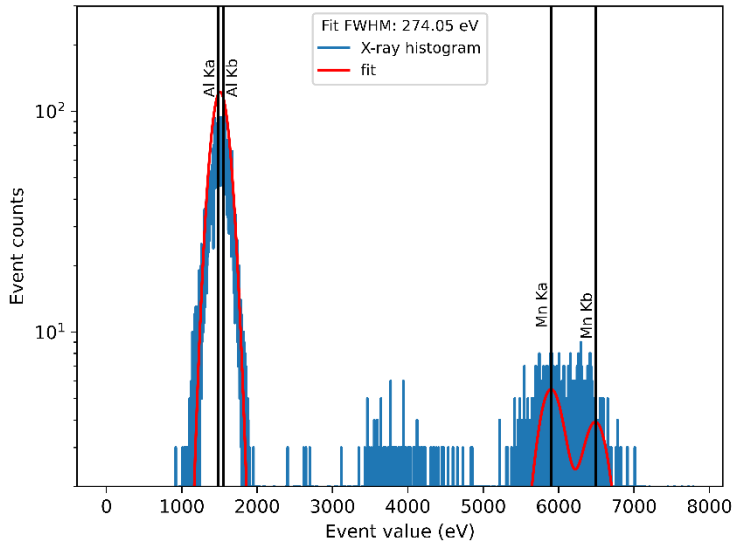

Figure 6.23. Typical X-ray fluorescence spectrum observed with CCD201 using an aluminium target; fit parameters given are for the aluminium Kα peak at 1487 eV.

The FWHM observed for the aluminium peak was consistent with a noise source equal to 23 e^- rms, in addition to the expected Fano and low readout noise. FWHM, and measured noise, could be reduced by down selecting the detected events, at the cost of event yield. For instance, restricting event selection to single pixel events quickly reduced the FWHM to the Fano noise limit, but excluded 80% to 100% of detected X-rays. The reason for this is shown in Figure 6.24, the 'mean X-ray' of all X-rays detected in the aluminium fluorescence line. The mean event indicates that for the average X-ray a considerable portion of the total X-ray generated charge collected was gathered in pixels other than the central one in which the X-ray was initially incident. This spreading is primarily caused by the diffusion of charge in the field free region close to the back surface of the X-ray detector.

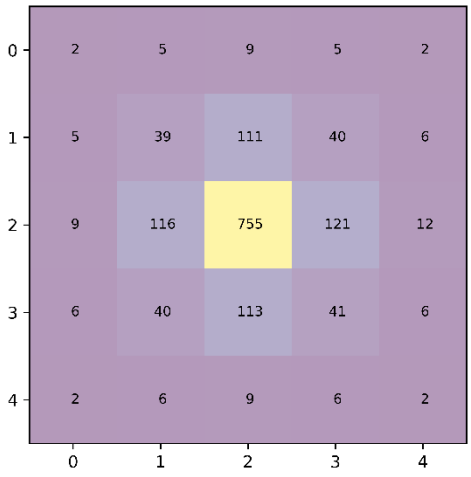

Figure 6.24. Mean value of pixels for all aluminium Kα X-rays (1490 eV) detected in the CCD201. Pixel values are in eV.

Another issue was the effect of charge smearing, as can be seen in Figure 6.24 (and Figure 6.25): pixel values surrounding the central, incident, pixel have a bias to the right, which corresponds to the readout direction (up then left). This is a known behaviour associated with both CTI and CCD clock timing issues observed in prior experiments (Kotov et al., 2021).

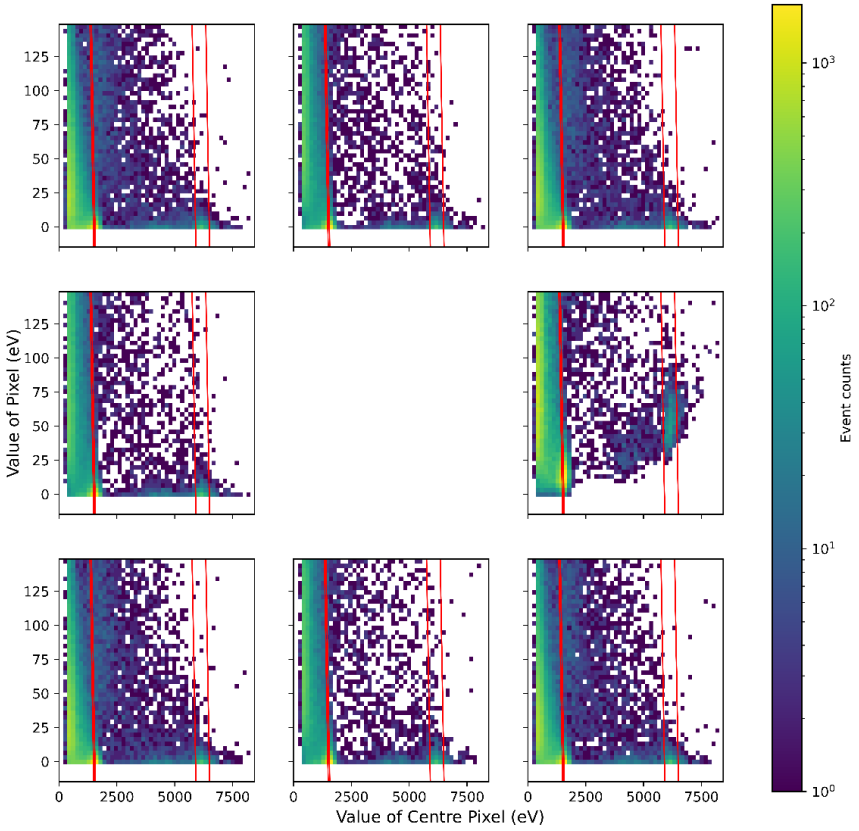

Figure 6.25. Distribution of pixel values in pixels neighbouring X-ray incident pixels of all detected X-rays in Aluminium target dataset. Red vertical lines indicate expected location of Al Kα, Mn Kα and Mn Kβ X-ray events. Plot indicates that the values of the centre and centre right pixel have a distinct correlation, shown by the upwards trend for higher centre pixel values, identifying a potential charge smear issue.

Overall, the CCD201-20 displayed performance sufficient for AXIS, including demonstrating low energy X-ray detection capability and near ideal energy resolution, following event down selection. Further work on event detection and operation optimization in this device may enable more accurate reconstruction and detection of events or lower the event yield penalty for down selecting detected X-rays to improve energy resolution.

6.3.3 CIS221-X

All analyses of the CIS221-X used the 40 µm third variant pixels, which have been shown to have the best performance in previous testing (Heymes et al., 2022). The population of X-rays observed was dominated by interactions within a single pixel. Fitting to the resulting spectrum indicated that the noise due to the X-ray detector was 8 e^- rms above the expected Fano and readout noise and therefore within the margin for the device to achieve the energy resolution performance required by AXIS.

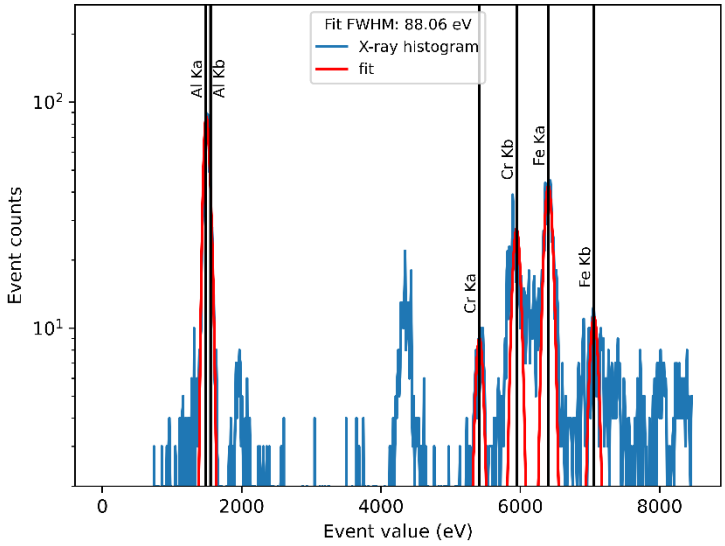

Figure 6.26. Typical X-ray fluorescence spectrum observed with CIS221-X using an aluminium target; some secondary fluorescence peaks are generated by the test chamber. Fit parameters given are for the Al Kα peak at 1487 eV.

The dominance of single pixel events is seen in the 'mean event' for the aluminium peak (Figure 6.27). No event down-selection has been conducted, and yet the energy collected is clearly dominated by the central pixel, and negligible energy was collected from pixels in the outer 5x5 ring. The CIS architecture does not introduce the event skew seen in the CCD201-20 (Figure 6.30).

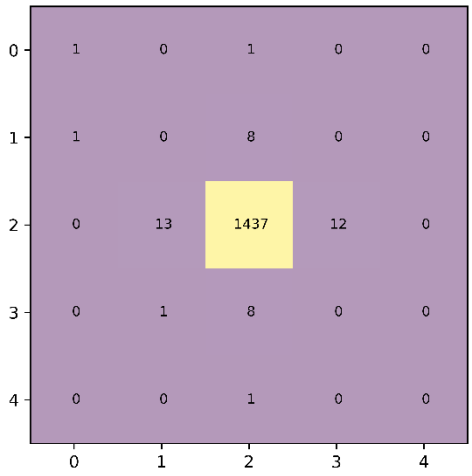

Figure 6.27. Mean value of pixels for all aluminium Kα X-rays (1490 eV) detected in the CIS221-X. Pixel values are in eV.

While <1 keV X-rays could not be observed, observation of the X-ray detector noise floor was possible. The noise floor represents a minimum energy below which any X-rays cannot be distinguished from pixel noise. This is shown in Figure 6.28, which compares the spectrum of X-ray events in the 0 to 2000

eV region from Figure 1.23 to a corresponding background spectrum (with no threshold applied), collected with the X-ray tube turned off. This plot demonstrates that the large increase in "events" incorrectly identified at low energies correspond to pixels that have equivalent signal due to noise. This indicates that the lowest X-ray energy that could confidently be identified in the CIS221-X is around 350 eV. In addition, many of the background events above 200 eV are due to consistently noisy, or hot pixels, which are an ongoing area of investigation.

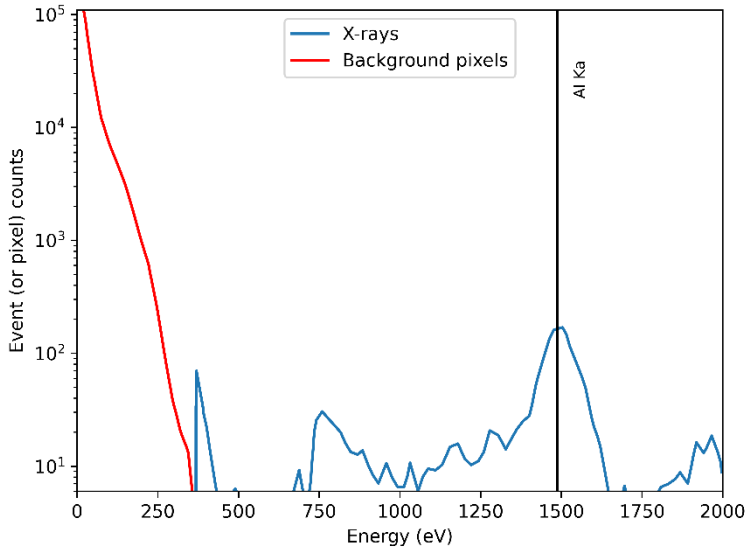

Figure 6.28. Comparison of energy spectra at <2 keV. Comparison between calculated event values and pixel values in dark frames illustrating noise floor in FSI CIS221-X.

This is a good indication that the CIS221-X is capable of the performance required by AXIS. The performance of the X-ray detector below 1 keV has not been explored because of the large attenuation of these X-rays in the dead layers of the front surface of this front-illuminated test device. The observed noise floor is not truly representative of the performance of a back illuminated X-ray detector, as X-rays of energies close to the observed noise floor would suffer charge spreading near the back surface. Additionally, the performance of the CIS221-X after irradiation has not yet been explored but will provide key information on its suitability for AXIS. The energy resolution and sensitivity seen, however, leaves considerable margin for radiation-induced degradations.

6.3.4 CIS120

The energy resolution of the CIS120 was measured with X-rays fluoresced from the copper target (shown in Figure 6.29) because lower energy X-rays proved to be particularly challenging. Stray X-rays produced further fluorescence lines from other chamber elements, ranging from 4500 eV to 7000 eV. The Cu Kα peak had a FWHM of 571 eV, indicating the presence of an extra 59 e^- (rms) of noise

contributing to event uncertainty in addition to the expected Fano, dark current, and readout noise sources. Some amount of additional noise had been predicted in the event reconstruction model of section 6.2.2.

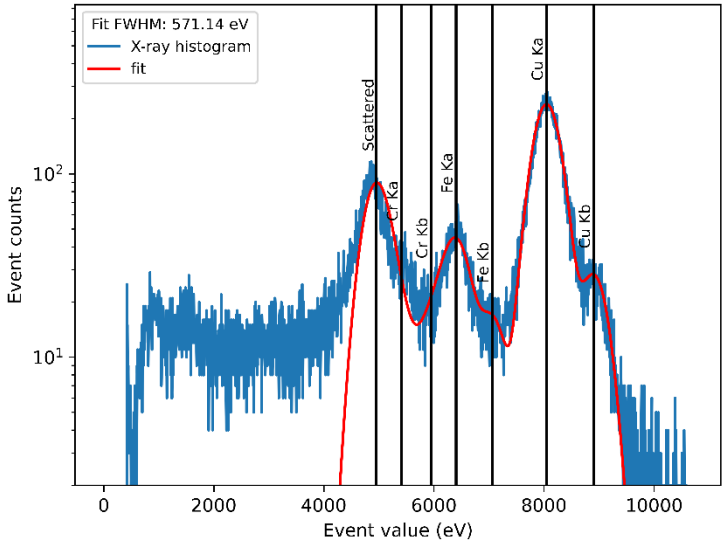

Figure 6.29. Spectrum from CIS120 using a Cu fluorescence target, and fit. Reported FWHM is for the CU Kα peak. Fluorescence from the test chamber is also observed.

The mean X-ray observed in the CIS120 (Figure 6.30) showed similar event spreading to the CCD201-20, indicating that the charge generated by incoming X-rays was usually spread over more than one pixel (6 on average). This meansethat the split event behaviour described in Figure 6.6 and Figure 6.7 is likely to be more appropriate for assessing the performance of this detector.

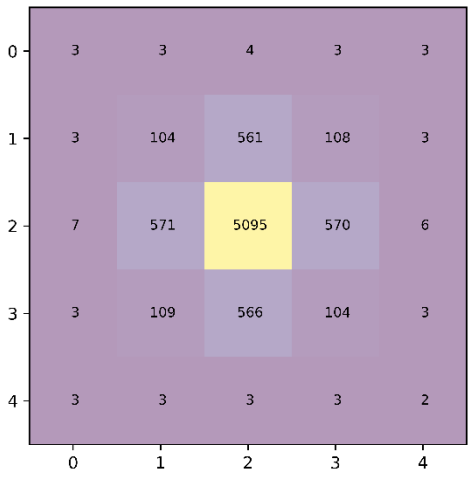

Figure 6.30. Mean value of pixels for all copper Kα X-rays (8042 eV) detected in the CIS120. Pixel values are in eV.

The performance of the CIS120 was not sufficient for AXIS. Readout noise was sufficient to obscure the signal from most X-rays below 1 keV, as the per pixel noise in the device tests was 24 e^- rms, above the datasheet values of 4 e^-. The charge from X-ray events was regularly split over many pixels (as shown in Figure 6.30), in a manner like the CCD201-20, resulting in the high additional noise from event reconstruction seen when fitting to the fluorescence spectra. The presence of a large field free region at the back surface of the device allows X-ray generated charge to spread across many pixels, compounding issues associated with the large per-pixel noise in this device. Energy resolution was therefore insufficient to resolve X-rays of energies below 2 keV.

6.3.5 Trial summary

In this experimental trial of specimen X-ray detectors for AXIS the CCD201-20 and CIS221-X displayed the most favourable performance. Of the two the CIS221-X exhibited a better energy resolution, as was expected from the initial evaluation. Noise was observed in both detectors, in addition to the expected read noise and Fano noise components. In the CCD201-20 it could be removed by down selecting events, which came at a cost of sensitivity. The CIS120 tested did not have sufficient performance for AXIS, and additional noise exhibited was not mitigated by down selection. The results of the experimental trials are summarised in Table 6.5.

Table 6.5. Summary of experimental trial results.

	CCD201-20	**CIS221-X**	**CIS120**
X-ray peak FWHM (eV)			
(Al Kα @ 1487 eV)	274	88	-
(Cu Kα @ 8047 eV)	-	-	571.14
Extra noise (e^- rms)	23	8	59
X-ray profile skew	Yes	No	No
X-ray charge spreading	Yes	No	Yes

6.4 Trade-off conclusions

Initial investigations of X-ray detectors for use in the AXIS instrument have had to consider devices with very different properties. To be useful as a soft X-ray detector for the auroral observations a high

readout speed and low noise floor is required, for which there are different design solutions. EMCCDs, with on-chip electron multiplication, supress the noise of faster readout electronics but incur a noise penalty that pushes them beyond the required 100 eV FWHM at 500 eV by a few eV. CIS, with a high degree of parallelisation, achieve faster readout rates but are the more technologically immature solution.

A model to describe the event reconstruction process was developed and used to predict the most favourable data processing for the X-ray detectors to be considered in the AXIS study. Applied to simplified models of detectors it has predicted a contrast between the event reconstruction behaviours of an EMCCD analogue and a CIS221-X analogue and suggested that the CIS120 performance would be poor.

Consideration of the spatial resolution and field of view requirements of AXIS has indicated that these are not the limiting factor for the instrument design. However, the larger sensitive area of the CIS under consideration appears to offer advantages in terms of expected X-ray flux, increasing the expectation from the baseline design of 8 count s^{-1} for the CCD201-20 to 19 count s^{-1} for a full size (20.5 mm $\times$ 20.5 mm pixel array) CIS.

In experimental testing, the CCD201-20, unirradiated, satisfies the requirements for AXIS. However, performance degradation due to irradiation during flight may prove problematic. Additional sources of X-ray energy resolution degradation including CTI and dark signal may quickly reduce the ability of the EMCCD to perform well enough below 1 keV. The CCD311 offers increased resilience to radiation damage which may mitigate these effects. These X-ray detectors have demonstrated the ability to approach their theoretical energy resolution limits, and further optimizations may permit these limits to be reached without corresponding losses to X-ray detectability.

The CIS120 did not satisfy the requirements of AXIS, despite favourable results in initial modelling. The CIS120 is unlikely to be suitable for AXIS. However, the CIS221-X shows more promising performance in this first test of its soft X-ray detection capability. Modelling and initial experiments suggest that the CIS221-X meets the energy resolution requirements of AXIS, though follow up tests with BSI X-ray detectors to test sub-1 keV sensitivity and after irradiation to evaluate likely in-flight performance will greatly improve understanding of this X-ray detector.

Of the alternatives considered, the CCD311 and CIS221-X were viable X-ray detectors for this application. Though both X-ray detectors had low TRL at the time of the study, the development and testing of these devices is tied to other instrument development programs and their use was expected

to be de-risked if mission timelines aligned favourably. Availability of test detectors and hardware and stronger predicted, and observed, performance when compared to the other X-ray detectors resulted in a significant level of interest in the CIS221-X for AXIS. Therefore, while two X-ray detectors were recommended by this study, the CIS221-X was the subject of immediate further testing and analysis.

7 CIS221-X performance with soft X-rays

Once the trade-off study had established the CIS221-X as a viable option for AXIS, further investigation was required to better understand the operation of this novel CIS X-ray detector. This was motivated in two ways, firstly to better understand the performance of the CIS221-X and secondly to enable a better description of the benefits the CIS221-X could provide to AXIS.

The most demanding requirements of AXIS relate to the lowest energy X-rays. These short attenuation length X-rays which produce small numbers of electrons are subjected to the most challenging charge transport to the charge collection region of the pinned photodiode and are most easily obscured by noise, charge sharing and loss to the back surface. While some estimates for the suitability of the CIS221-X at low energies could be made during the trade-off study, the subsequent availability of BSI CIS221-X X-ray detectors (specifically CIS221-X SN: 21094-07-23), and data collection at Berlin Electron Storage Ring for Synchrotron Radiation II (BESSY II), have permitted a deeper investigation into this device.

BESSY-II is a near ideal monoenergetic X-ray source, allowing an exploration of the best case X-ray spectra that can be recovered from the CIS221-X. This has permitted a verification of the X-ray detector energy resolution, event reconstruction behaviours predicted in section 6.2.2, and for the properties of the back-surface partial collection regions to be probed. Prior investigations at the CEI have enabled a comparison between the CIS221-X and the CCD97, an EMCCD closely related to the CCD201-20.

7.1 BESSY-II

The Physikalisch-Technische Bundesanstalt (PTB) soft X-ray beamline at the BESSY II provided an excellent source of monochromatic X-rays with no background signal due to X-ray scattering or secondary emissions. BESSY II is an electron storage ring, used as a source of synchrotron radiation generated by feeding electron packets through undulators. The PTB soft X-ray beamline uses a plane grating monochromator to produce an X-ray beam with a very high Q-factor of roughly 1000 which means when set to have a beam energy of 1000 eV, the beam energy spectrum peak has a FWHM of

1 eV (Scholze et al., 2003). The beam can be used to perform QE measurements with the use of a primary standard reference diode periodically inserted into the beam to measure photon flux.

During experimental campaigns to confirm the QE of the CIS221-X for THESEUS (Townsend-Rose et al., 2023) the opportunity arose to operate the CIS221-X in a photon counting mode, enabling testing relevant for AXIS. This included photon counting at energies from 200 eV to 1900 eV with the detector operated at -40 °C and with a framerate of 20 Hz. While there are regions of the beam with far too high intensity for photon counting measurements, beam non-uniformities and diffracted X-rays, shown in Figure 7.1, result in regions of lower intensity in which there are many X-rays detected by the CIS221-X that can be isolated for further analysis.

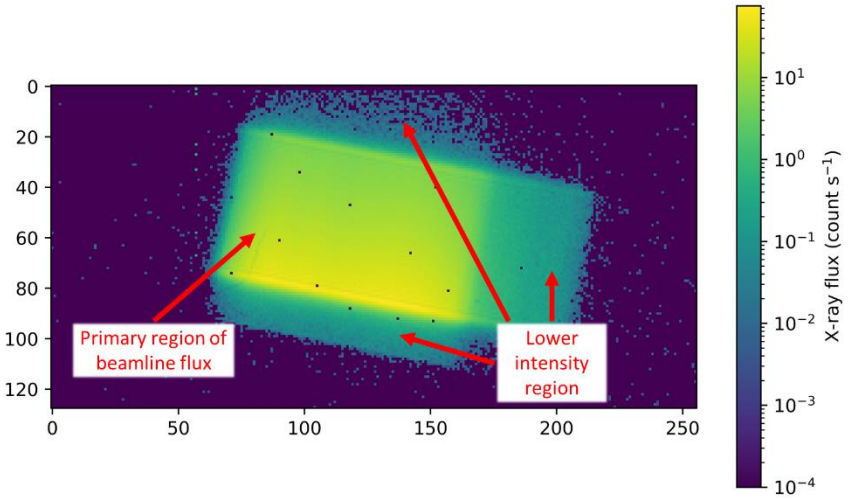

Figure 7.1. Observed X-ray photon flux of the 500 eV X-ray beam at BESSY-II measured with the BSI CIS221-X. Diffracted X-rays form the regions above, below and to the right of the main beam as labelled. Only the variant 3 region of the 221-X was read out during these trials. The dark spots are hot pixels that have been masked out of data.

Photon counting in these regions produced spectra of excellent quality, many X-rays could be isolated for photon counting and FWHM values of less than 100 eV were obtained across the range of energies tested. Figure 7.2 shows a spectrum produced using data collected while exposed to a 1400 eV X-ray beam, using the event reconstruction techniques discussed in section 4.3. The five traces of Figure 7.2 are intended to demonstrate the stages of X-ray event processing. They show histograms of: all pixel values; all pixel values above a given detection threshold (150 eV); pixel values after filtering to ensure that only the highest value pixel of an event is selected (choosing only the highest value in any 5x5

region of pixels); event values following event reconstruction by summing all pixels above the reconstruction threshold (86 eV) in the 3x3 pixel regions centred on the highest value pixel; and finally of events identified as occupying a single pixel. As 1400 eV is below the silicon Kα fluorescence energies there are no contaminating escape peaks from the X-ray detector itself, and the additional X-ray peaks visible in the spectrum are pileup peaks gathered from regions of higher X-ray intensity.

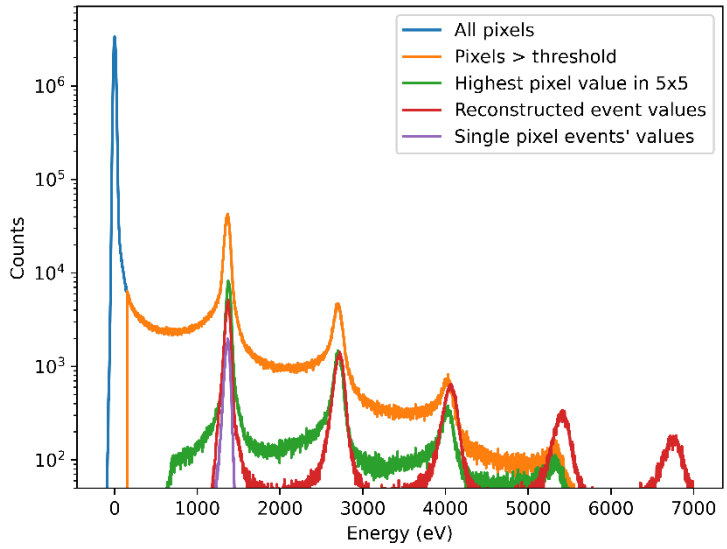

Figure 7.2. Event histogram of 1400 eV X-ray beam (at -40 °C and 20 Hz framerate) showing distinctive pileup pattern. X-rays in adjacent pixels lead to an increase in pileup observed in reconstructed event spectrum. The DN to eV conversion ratio was based on earlier testing.

Furthermore, for these tests the OBF-covered half of the CIS221-X was used, resulting in very low background signals and performance better than that exhibited during lab tests, currently thought to be due to the removal of previously unidentified light leakage sources present in the OU lab vacuum chamber.

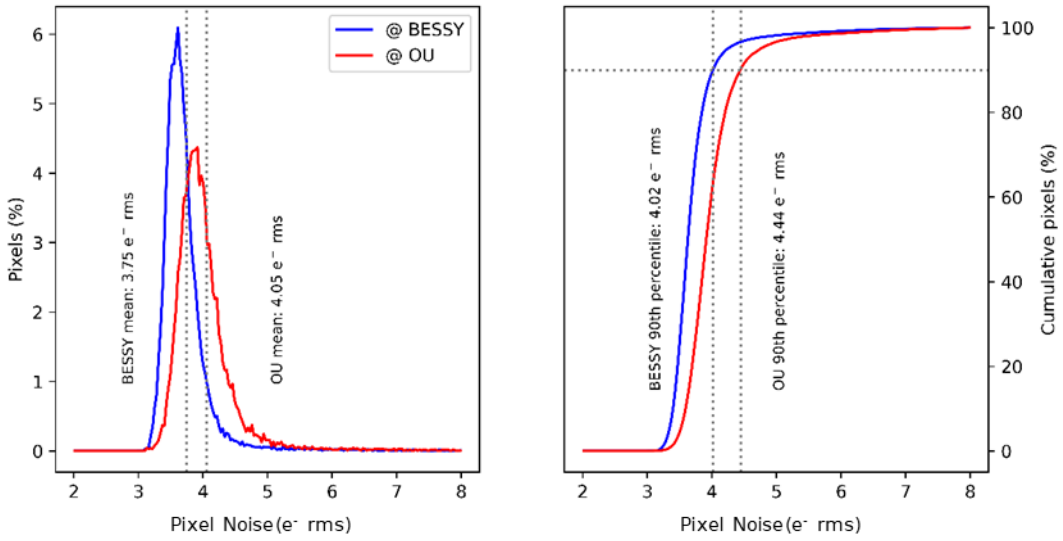

Figure 7.3. Histogram of pixel noise values at BESSY and in previous lab data. Mean readout noise measured at BESSY was 3.75 e⁻ rms.

No contaminating signals were identified and no enhancement in background noise was identified in the BESSY data (Figure 7.3), using data gathered while the beam shutter was shut. The beam shutter shut (dark) data frames were analysed with the same data pipeline later used to examine X-ray data. This revealed that the dark signal does not extend above 100 eV, once hot pixels had been identified and masked out, shown in Figure 7.4. This has built confidence that the spectral features identified later can be attributed to behaviours of X-ray interactions with the CIS221-X.

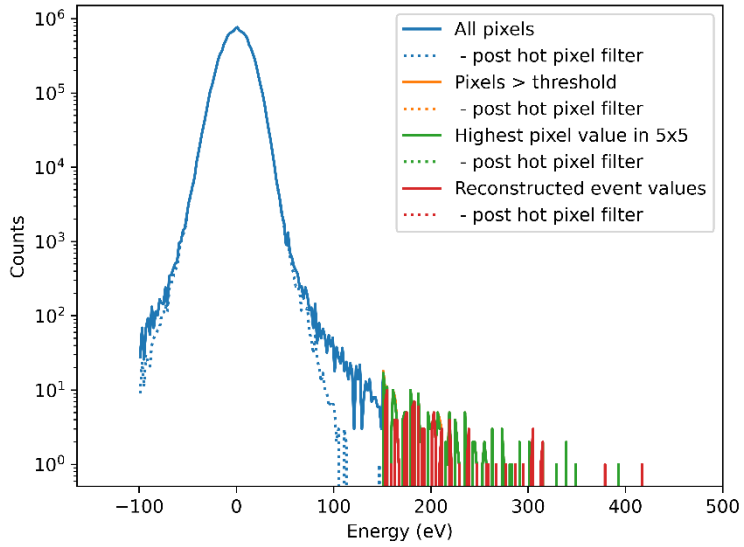

Figure 7.4. Shutter-closed X-ray spectrum at -40 °C and 20 Hz framerate. After filtering hot pixels, the all pixel histogram drops to zero at 100 eV. No false X-rays were identified, once hot (noisy) pixels had been filtered out. This builds confidence that any behaviour seen above detection thresholds is due to beamline X-rays.

A large advantage of the high-quality X-ray flux available at BESSY-II is the isolation of detector behaviours from X-ray source behaviours. As has been discussed in section 4.2.3, and the AXIS trade-off study, the response of the CIS221-X to very low energy X-rays at and below 500 eV was anticipated to diverge from expectations due to interactions close to the back surface leading to the loss of charge from X-ray events. These effects were not expected to be eliminated by fully depleting the X-ray detector because the surface dead layers are the result of the physical semiconductor-oxide boundary at the back surface of the detector and passivation implant. A well constrained population of incident X-rays has enabled the investigation of detector behaviour that would be challenging with the spectra produced by the standard test chamber setup of section 6.3.1 which generally contained peaks at many energies, often overlapping.

7.2 General observations

Despite indications that X-rays below 1 keV were indeed being absorbed closer to the back surface (discussed later), X-ray charge continued to be largely confined to a single pixel (Figure 7.5). Pixels immediately neighbouring the central pixel were included in less than 6 % of events, and pixels in the 5 × 5 pixel ring were only included in less than 1 % of events. In addition, no major asymmetries in event profiles were seen.

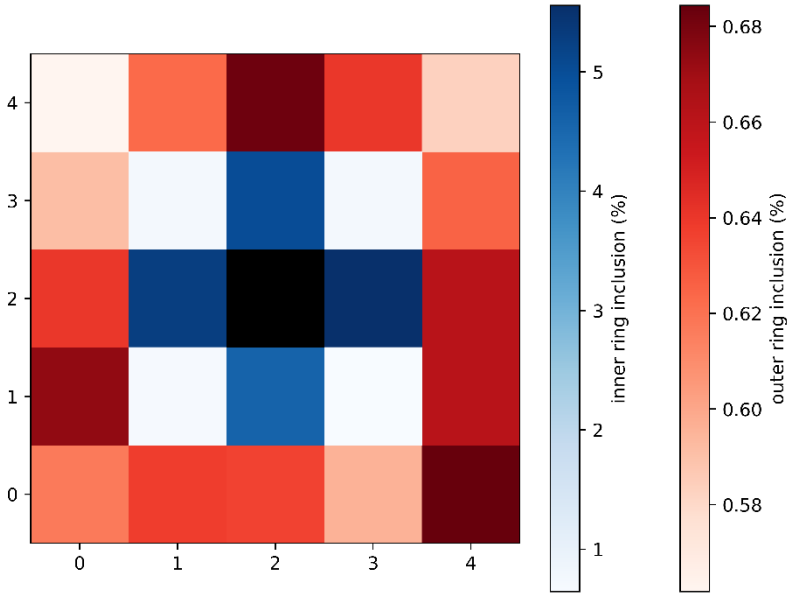

Figure 7.5. Pixel inclusion for position in 5x5 region of interest around incident pixel in the 500 eV X-ray population. For the CIS221-X, event reconstruction only uses the inner 3x3 region. Colour scales for the inner and outer rings has been split for ease of interpretation.

Finally, the behaviour of the X-ray event population behaved largely as predicted in section 6.2.2 in response to event reconstruction. The measured non-pileup X-ray peak had a stable FWHM for high reconstruction thresholds (reflecting the predictions of figure 5.10). Furthermore, the red trace of Figure 7.6 indicates that this stability is achieved while >99 % of events still have a non-zero value (all events have at least one pixel with a value greater than the reconstruction threshold), and the yellow trace indicates that, of the non-zero events >60 % are in the non-pileup peak. The FWHM advantage of selecting only the highest grade, single-pixel, events was minor, but resulted in a large number of events being excluded. Therefore, reconstructed events were included in further analysis. Following consideration of Figure 7.6, a reconstruction threshold of 86 eV was chosen for further analysis to maximise the yield of events in the main X-ray peak, while also minimising measured FWHM. This threshold was used across all energies (to mimic the expected operation of a science instrument), and adequate performance was observed across all energies of interest.

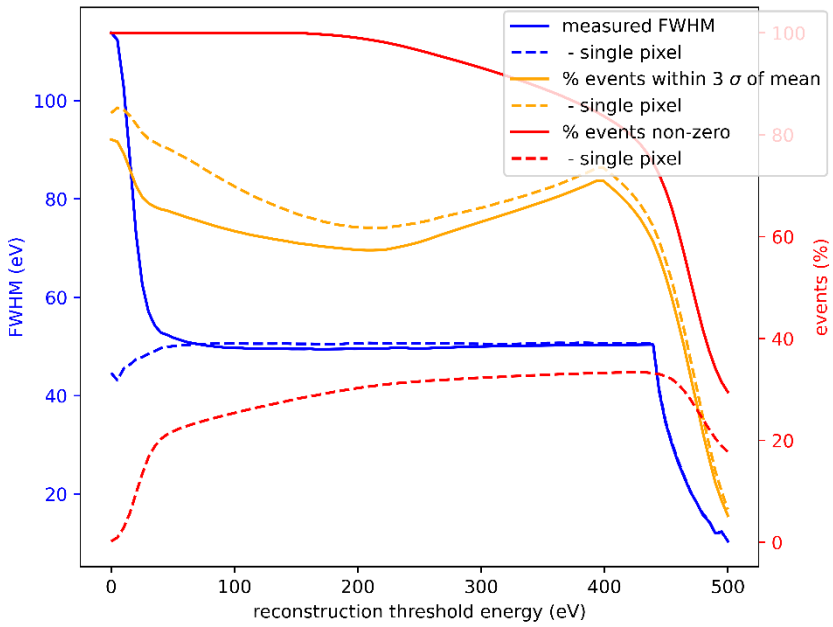

Figure 7.6. 500 eV X-ray population properties for reconstruction threshold. The properties of all events, and events graded as single pixel have been plotted in separate traces.

Under these ideal conditions processing the energy spectra to extract behavioural information was straightforward. Figure 7.7 and Figure 7.8 show spectra observed at a beam energy of 500 eV and 310 eV, respectively. These energies were selected due to the former's relevance for the energy resolution requirement and the latter's proximity to the minimum energy requirement for AXIS's science goals. Due to the materials used in the BESSY-II monochromator gratings, 300 eV is not available.

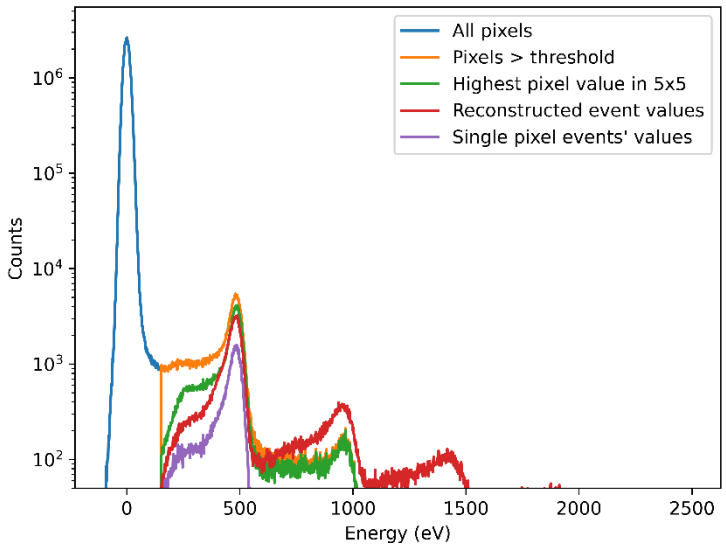

Figure 7.7. 500 eV X-ray spectrum at -40 °C and 20 Hz framerate.

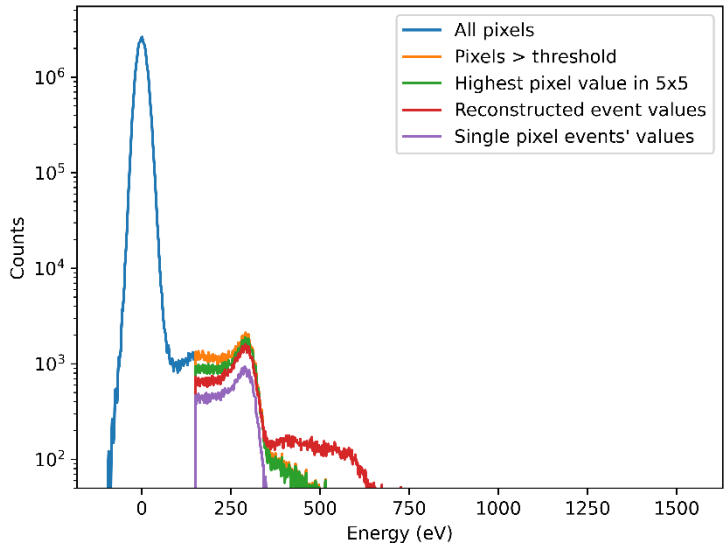

Figure 7.8. 310 eV X-ray spectrum at -40 °C and 20 Hz framerate. The peak deformation is discussed in section 7.3.

7.3 Back surface charge loss

At lower energies, shoulders were observed on the low energy side of the X-ray energy spectrum peaks, shown in Figure 7.9. These shoulders have provided an insight into the properties of the back surface dead layers in the X-ray detector.

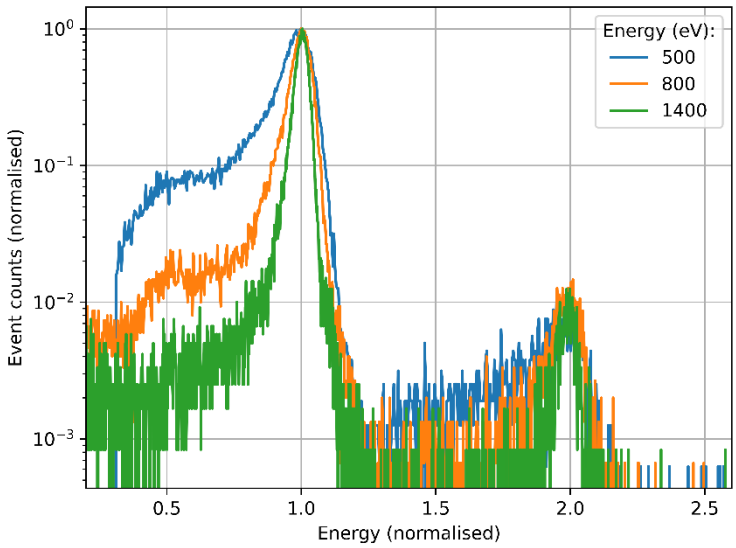

Figure 7.9. 500 eV, 800 eV, and 1400 eV spectra with energies and count rates normalised to highlight the relative size of low energy shoulder for X-ray energy.

7.3.1 Attributing charge loss to the back surface

Firstly, other potential causes of the shoulders were ruled out. The 500 eV tail was investigated first because of its distance from the event detection threshold at 150 eV. Spot-checking events within the

low energy tail did not reveal any obvious issues with the way event values had been reconstructed. Two such events have been represented in Figure 7.10, with a colour scale intended to highlight pixels close to the reconstruction threshold. The two events are not obviously spread across different, sub-threshold, pixels, though both have experienced the loss of hundreds of eV worth of charge.

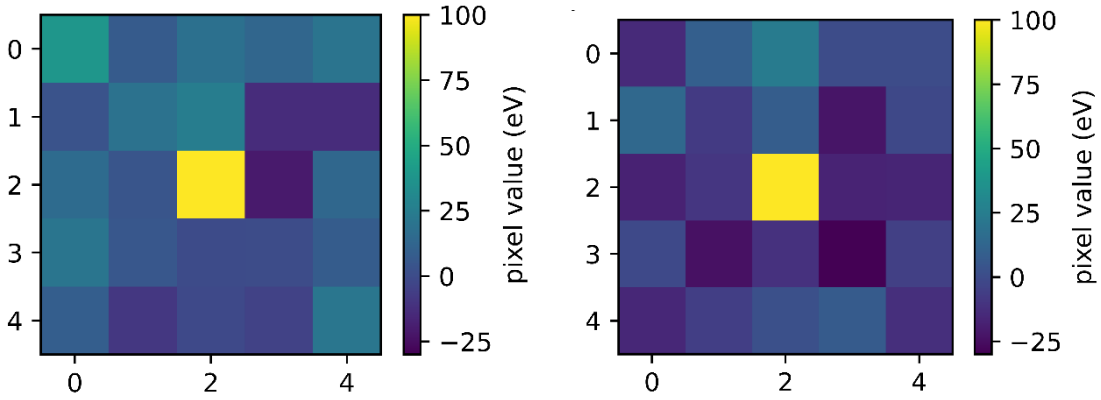

Figure 7.10. Two example low energy tail events from 500 eV X-ray population. Colour scale has been set to highlight pixel values close to 80 eV reconstruction threshold. Centre pixel value in a) is 233 eV and in b) is 189 eV, which would have resulted in 285 eV and 311 eV worth of charge appearing in neighbouring pixels if event reconstruction had erroneously reconstructed an event in which charge spreading had occurred.

Image lag was not expected to be an issue, as the variant 3 pixels have previously been demonstrated to have very low lag (Townsend-Rose et al., 2023). As confirmation, the population of 500 eV X-rays was mapped with a 2D histogram using the reconstructed event value and the value of the incident pixels in the subsequent frame. Figure 7.11 showed that there is no correlation between these two values.

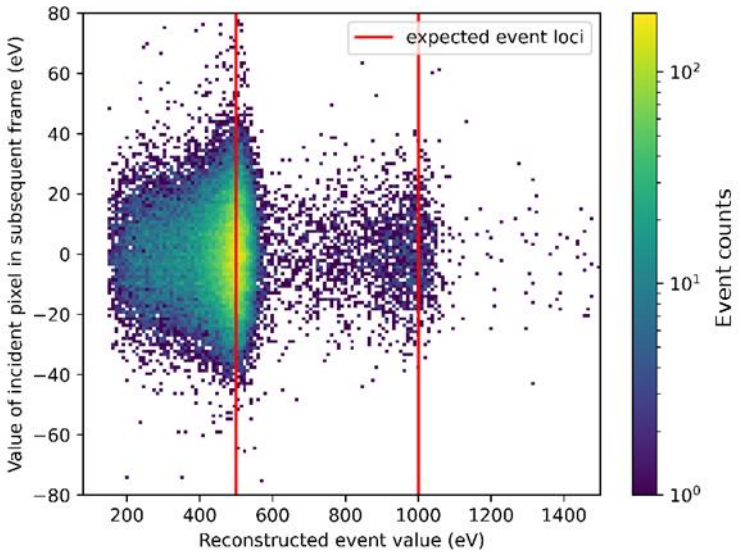

Figure 7.11 Histogram of 500 eV X-ray event population, with event coordinates determined by the reconstructed event values and the value of the incident pixels in their respective subsequent frame. Lack of correlation between these two values suggests image lag is not responsible for charge loss.

Instead, the probability of X-rays being absorbed close to the back surface (P_{loss}) was predicted using an alternative form of the layer-cake QE model (outlined in section 3.4.1.3):

$$P_{loss} = \left(1 - e^{-\frac{r_i + t_{dead}}{l_{att}}}\right) + \alpha \tag{7.1}$$

Where the initial charge cloud radius r_i is equal to $0.0012 \times \left(\frac{E_{ph}}{1\text{keV}}\right)^{1.75}$ µm after Pavlov and Nousek (1999), t_{dead} is the adjustable partial collection depth parameter, l_{att} is the attenuation length of a photon with energy E_{ph} in silicon (for example at 500 eV the attenuation length is 430 nm), and α is an adjustable offset term (which generally took a low value of less than 2 %). The offset term is thought to represent interaction depth independent (across the range of energies tested) loss mechanisms such as image lag. The number of X-ray events experiencing charge loss was measured in experimental data, as per Figure 7.12. A gaussian peak was fitted to the higher energy side of the non-pileup X-ray peak and used to generate an expected number of X-rays per histogram bin. The number of events with charge loss was inferred by the difference between the expected and measured bin values. In practice only bins representing X-rays with less than 90 % of the expected energy value for each X-ray peak could be counted. This 'tail threshold' is explored further below. The number of events expected to have experienced charge loss was compared to the number of events in the low energy tail (as per Figure 7.12). The measured and calculated (using a fit to equation (7.1)) values for P_{loss} are shown in Figure 7.13. The fitted parameters were t_{dead} = 155 nm and α = 2 %.

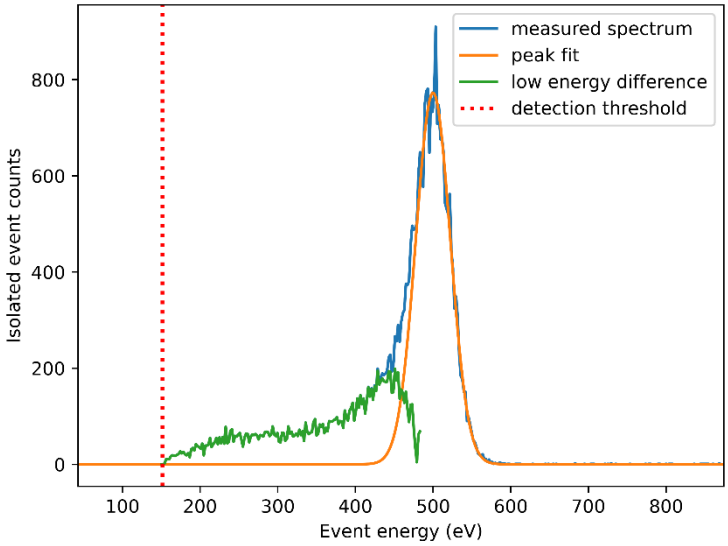

Figure 7.12. Histogram, peak, fit, and histogram of the number of events above the peak fit tail in the 500 eV dataset.

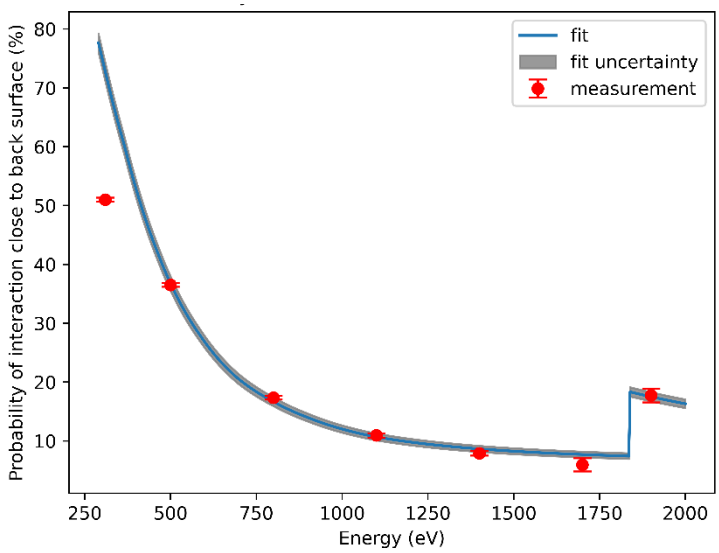

Figure 7.13. Measurement and fit to back surface X-ray events. Fitted partial collection depth is 155 nm, using equation (6.4) in which the probability of an interaction close to the back surface is equal to the probability of experiencing charge loss.

At 310 eV a significant number of X-ray events with charge loss are expected to have fallen below the event detection threshold, illustrated in Figure 7.14. This confounds the back surface interaction measurements, but also has important implications for the CIS221-X sensitivity, discussed below.

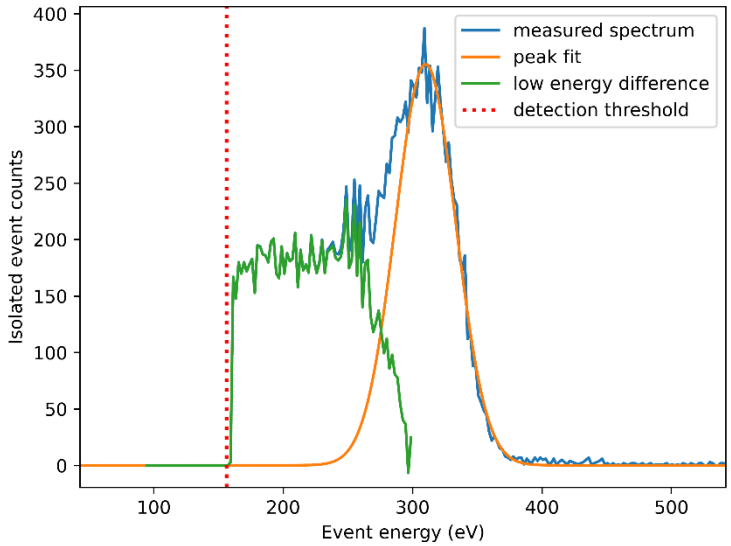

Figure 7.14. Single pixel event spectrum at 310 eV showing low energy tail truncated by the event detection threshold.

7.3.2 Application of charge loss measurements

The most immediate outcome of knowing the thickness of the partial collection region is the ability to refine the QE prediction from the trade-off study to indicate the number of events expected to be well recovered and reconstructed. By increasing the initial dead layer thickness from the nominal value to the calculated 155 nm, the dashed traces of Figure 7.15 can be introduced. This indicates that the effective QE when considering only events with good charge collection is 35% (at 390 eV) with an OBF, as opposed to the initially predicted 60%. This is relevant for AXIS, as the lower end of the energy range also includes some of the most interesting signals from N Kα (390 eV) and O Kα (520 eV) fluorescence.

The calculated value of 155 nm is far larger than the expected back surface pinning implant thickness (< 40 nm (Heymes, Soman, et al., 2020)), which was expected to be the primary driver of the partial charge collection region (Bailey et al., 1990).

This suggests that back surface structures developed for UV instruments may be required for the performance required of AXIS. UV detector design optimisations intended to improve sensitivity are directly relevant to AXIS, because the issues encountered are similar. The attenuation length of UV photons can be smaller still than those of soft X-ray photons, therefore improvements in charge collection at the back surface intended for UV will also improve a detector's sensitivity at soft X-ray energies. In particular, delta doping techniques developed at the Jet Propulsion Laboratory result in dead layer thicknesses of less than a nanometre (Hoenk et al., 1992, 2022; Nikzad et al., 1994).

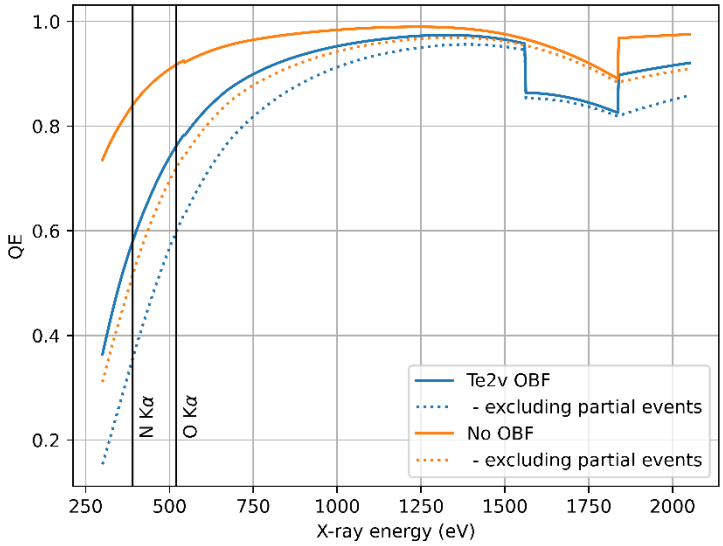

Figure 7.15. Effective QE of CIS221-X, with the effect of excluding partially recovered events indicated.

7.3.3 Reproducing tails for further investigation

The initial charge loss measurements attempted to measure the entirety of the charge tail, to assess the thickness of the layer in which charge loss is thought to have occurred. More information was extracted by only measuring a smaller part of the tail.

This was done by counting the number of excess X-rays, as before, but with values less than some fixed percentage of the expected energy (a tail threshold), rather than attempting to count all X-rays displaying charge loss. The number of X-rays observed at each energy with charge loss greater than the tail threshold continued to have a relationship well described by equation (7.1), fitting the equation to the data as before yielded a value for t_{dead} and α for each tail threshold. Sweeping the tail threshold (in % of expected charge) resulted in a smooth decrease in the depth parameter fitted with equation (7.1), shown in Figure 7.16. This suggests that there is a relationship between interaction depth and the charge loss that may be expected from an X-ray event.

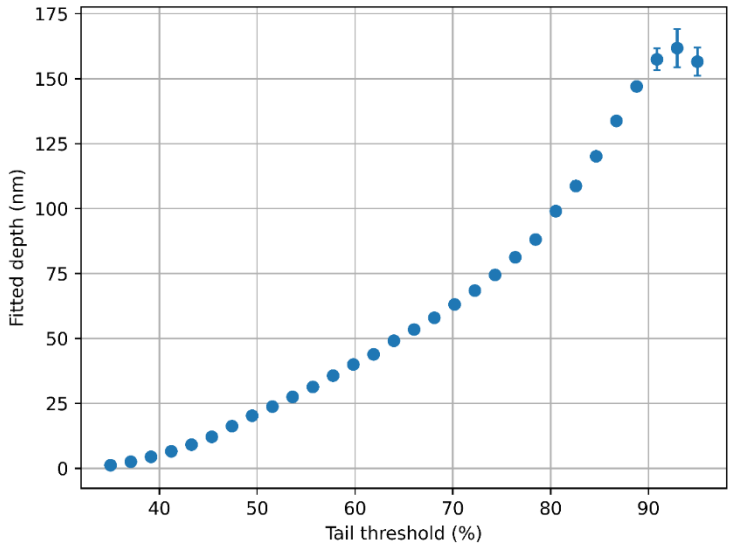

Figure 7.16. Fitted depth for tail threshold, showing even behaviour and low error up to a threshold of 90 %.

The range of thresholds that can be probed in this way are defined by the lower cut-off, itself a function of the 150 eV detection threshold relative to the 500 eV peak, and other charge loss and noise mechanisms affecting the shape of the main X-ray peak. Fits for near 100% tail thresholds resulted in poor depth certainty and an increasing reliance on the offset parameter of equation (6.4) to achieve a good fit. This indicates that there are other, smaller, charge loss mechanisms at work that mean for depths with almost complete collection a more complex description is required.

By inverting the axis and interpolating between the measured tail thresholds a function of charge loss for interaction depth may be derived. The expected peak shape may then be predicted by integrating the product of the expected charge loss and probability of interaction at a given depth across the complete thickness of the X-ray detector:

$$q_{expected}(E_{ph}) = \int f_{e^-_{loss}}(d) \ . \ P(d|E_{ph})\,\delta d \tag{7.2}$$

This expression accurately recreates many of the properties of the back surface charge loss shoulders, shown in Figure 7.17, though some divergence is seen close to the main X-ray peak. This divergence is thought to be due to the lack of measurements at tail thresholds close to 100 %. The prediction can be extended to any energy in the AXIS sensitivity range, shown in Figure 7.18.

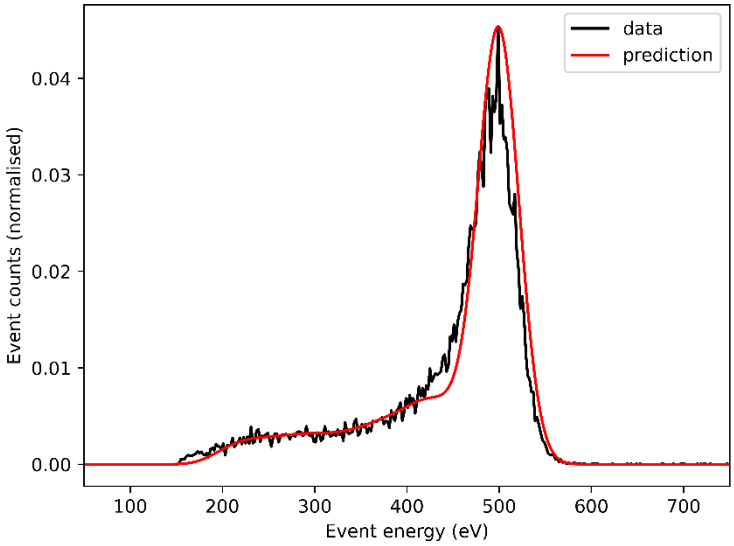

a)

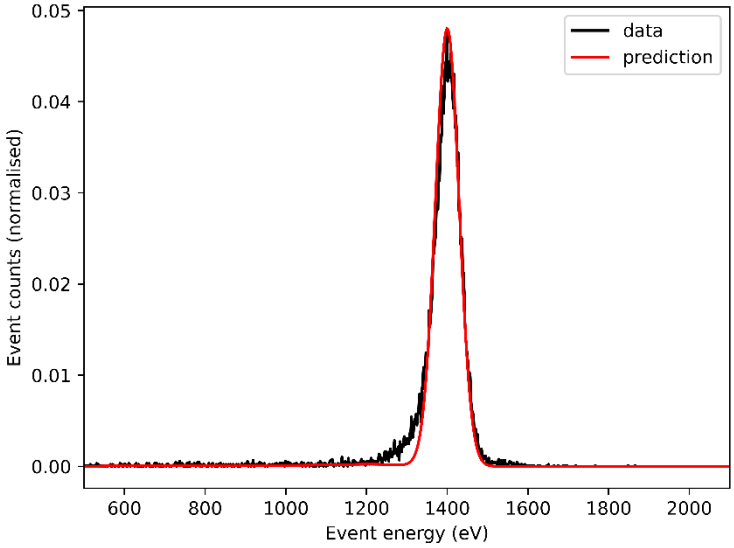

b)

Figure 7.17. Comparison of peak profile reconstructed from loss-for-depth information and X-ray attenuation length at a) 500 eV, and b) 1400 eV.

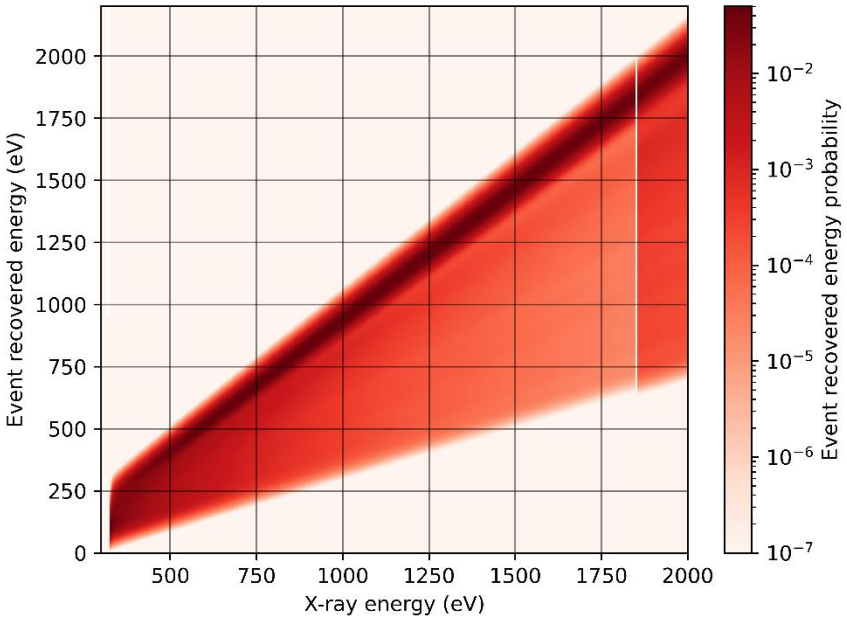

Figure 7.18. Predicted peak profiles at arbitrary energies in AXIS energy range. The discontinuity at 1847 eV is associated with the silicon absorption edge at that energy.

This effectively recreates the models of internal charge collection efficiency common in scientific X-ray detectors (for instance Bailey et al. (1990)) and seen in energy redistribution matrices (for instance Athiray et al. (2015)Narendranath, Pillai, and Sharan (2019), or Smith (2022 pp. 13)).

7.4 Comparison to EMCCD

The data collected with the CIS221-X can be compared to archived data collected during a similar test campaign of the CCD97 (Moody et al. (2017)), an EMCCD very similar to the CCD201-20 considered during the AXIS trade-off study (chapter 6). The worse energy resolution of the CCD97 due to the introduction of the EM register, and its stochastic gain elements, is immediately evident in comparisons of the spectra measured by the two X-ray detectors (Figure 7.19).

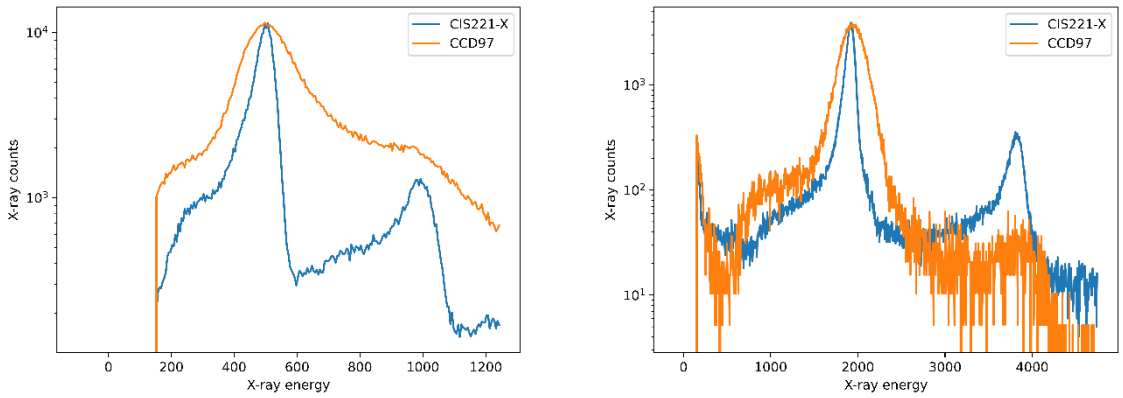

a) *b)*

Figure 7.19. Comparison of CIS221-X and CCD97 energy spectra from data collected at BESSY: a) 500 eV and b) 1900 eV X-rays.

One of the largest differences between the two X-ray detectors is best presented with a map of the distribution of X-ray event populations, using the centre pixel value, and summed value in the immediately adjacent 3x3 ring of pixels as the x and y coordinates (Figure 7.20). Plotted in this way X-rays with no charge loss or noise would be expected to form diagonal stripes from bottom right to top left along loci corresponding to summed values at multiples of the X-ray energy (shown in red, following loci of $y = n.E_{ph} - x$,$n = 1,2,3$ …). In the CIS221-X most X-rays are recorded with a single pixel, even at low energies. There is therefore a large concentration of X-rays with a centre pixel value corresponding to the expected X-ray energy, spread vertically as the value of the 3x3 ring is dominated by random noise.

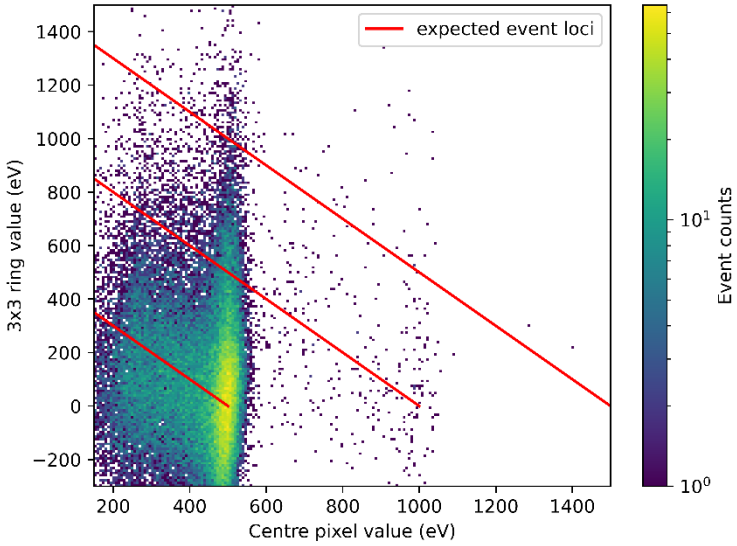

Figure 7.20. Distribution of 500 eV X-ray population in CIS221-X, mapped according to the value recorded in incident pixel and value recorded in all immediately adjacent pixels. Axes limits have been chosen to show behaviour of pileup populations (or lack thereof).

In the CCD97, however, there are no recorded single pixel events at 500 eV. Shown in Figure 7.21, the event population is made entirely of events with significant charge in the 3x3 ring. The axis of this plot have been set to match those of Figure 7.20, though the distribution of the event population suggests that there are more 500 eV X-rays to be identified if the central pixel event detection threshold was reduced below 150 eV, though this would leave the event detection algorithm more susceptible to identifying false X-ray events.

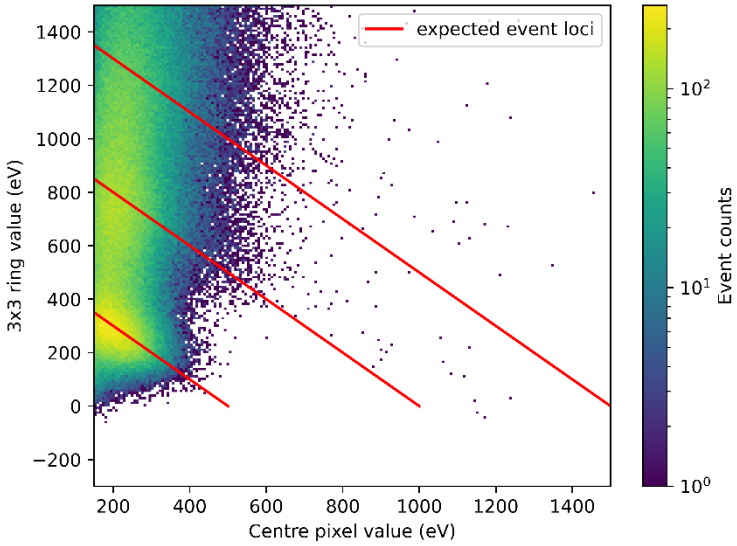

Figure 7.21. Distribution of 500 eV X-ray population in CCD97, mapped according to the value recorded in incident pixel and value recorded in all immediately adjacent pixels.

The result of the spread of X-ray charge beyond the incident pixel matches the expectations of the event reconstruction model of section 6.2.2. Increased charge spreading was expected because of the CCD97's field free region and smaller pixel size (16 µm). Sweeping the event reconstruction threshold for the CCD97 data (Figure 7.22) demonstrated an increase in measured FWHM, without the initial decrease seen in the CIS221-X.

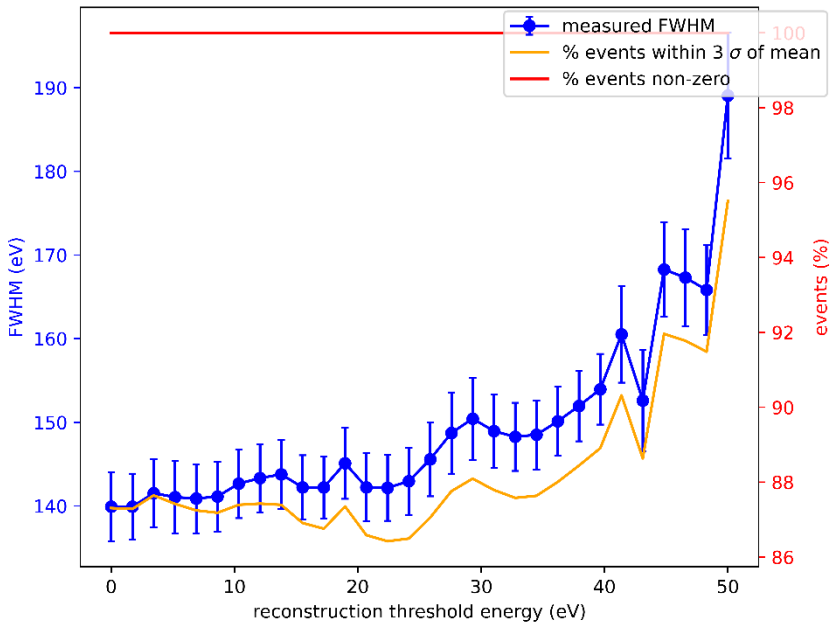

Figure 7.22. 500 eV event population properties for reconstruction threshold. Measured in CCD97 data collected for Moody et al. (2017). Event charge spreading is so prevalent in the CCD97 at this energy that higher reconstruction thresholds produce spurious results, and no single pixel events could be identified.

Finally, the low energy charge shoulders observed in the CIS221-X are present in the CCD97 too. Applying the same methods to the CCD97 data as was done for the CIS221-X (Figure 7.23) reveals similar behaviour, though the higher FWHM prevents charge loss being probed above 75 % charge loss. The fitted depths show a similar profile to the values measured in the CIS221-X, shown in Figure 7.24 The greater depth required for a given charge collection percentage in the CCD97 may be indicative of effects associated with the partial depletion of the CCD97. Both devices have similar backside processing, therefore a large degree of similarity was expected.

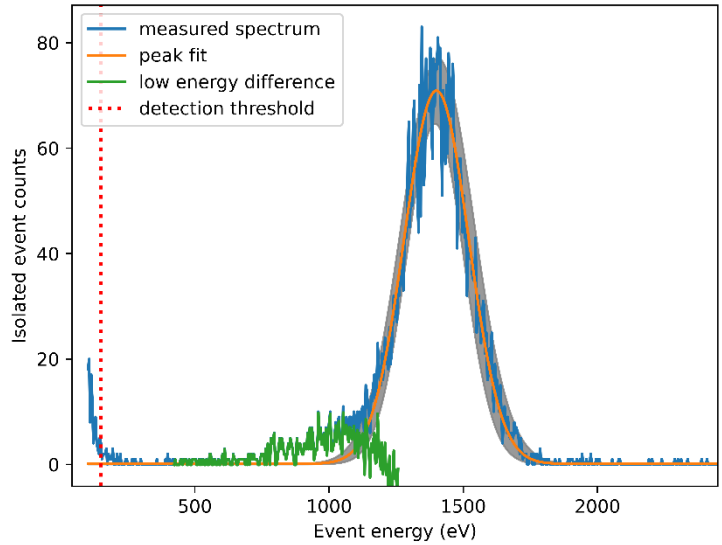

Figure 7.23. Energy tail measurement at 1400 eV for the CCD97, equivalent to the measurement of Figure 7.12.

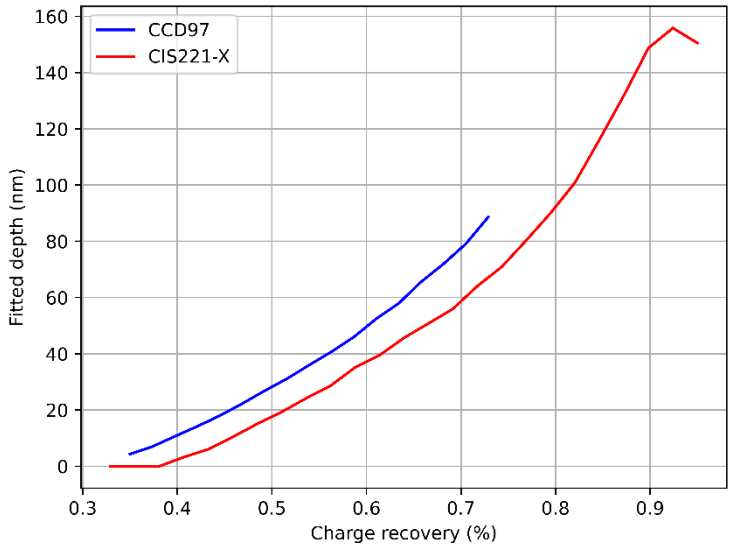

Figure 7.24. Comparison of fitted charge loss depths in the CCD97 and CIS221-X.

7.5 FWHM measurements using optimised operating conditions

The FWHM was measured from 310 eV to 1900 eV whilst operating the CIS221-X at -40 °C and 20 Hz framerate (Figure 7.25), by fitting a Gaussian profile to the energy spectrum peak for non-pileup events. These values are close to a best case of the performance that may be expected from the CIS221-X. The FWHM values closely matched the model derived for the lab based FSI CIS221-X by Heymes et al. (2022), with the readout noise adjusted to match the value measured in the BSI CIS221-

X sensor used (SN: 21094-07-23, 90th percentile: 4.02 e$^-$ rms) and accounting for the BESSY X-ray beam energy dispersion.

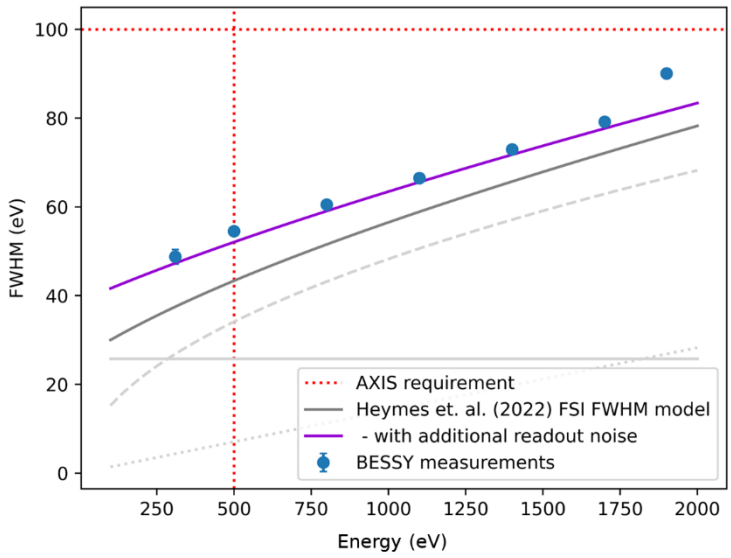

Figure 7.25. CIS221-X FWHM from 310 to 1900 eV at -40 °C and 20 Hz framerate, compared to the model of (Heymes et al., 2022). *The Heymes model components (Fano noise, pixel readout noise and PRNU, in decreasing size order at 500 eV) are indicated with the fainter grey lines.*

The Heymes et. al. model is based on the performance of an FSI device and observations of higher energy X-rays available from lab fluorescence targets' (from 1400 eV to 8900 eV) agreement at these lower energies builds confidence that the X-ray detector operation is largely unchanged between the FSI and BSI variants. Crucially the FWHM of the detector at 500 eV was 54 eV, significantly below the 100 eV AXIS requirement. Work is ongoing to reduce the FWHM contribution of the PRNU, which will potentially lead to further improvements in energy resolution.

7.6 Conclusions

The performance of the CIS221-X at soft X-ray energies has largely matched expectations. The lowest energy X-rays are the hardest to identify and measure properly for the science goals of AXIS because they are most affected by the properties of the back surface and detection and reconstruction thresholding.

The CIS221-X has demonstrated some concerning issues associated with charge loss in the back surface dead layers, which may reduce the effective QE of the detector below 50 % up to 450 eV. These issues are not specific to the CIS221-X because they relate to the properties of the detector's back surface. Design features commonly used in UV photon detectors, to reduce the back surface dead

layers, may help mitigate presence and potential consequences of the charge loss region. UV detectors must counteract the even shorter attenuation length of the UV photons.

The measured FWHM of the X-ray peaks was consistent with previous models of the CIS221-X and far better than the energy resolution requirements of AXIS: 54 eV at 500 eV, as opposed to the required 100 eV. Data collected at BESSY-II compares favourably to previous data gathered at the same facility with an EMCCD with a greater proportion of single pixel X-ray events and better energy resolution being the primary improvements.

Therefore, the CIS221-X continues to be a recommended option for the AXIS instrument. The experiments of this chapter have increased understanding of the device and built confidence in its performance. Furthermore, the identification of the back surface charge loss region in the device indicates that in the AXIS application, where the low energy X-rays are critical to the science objectives (specifically the 390 eV N Kα line), design optimisations generally considered for UV photon detectors should be considered.

This chapter has not explored the post-irradiation behaviour of the CIS221-X, which will be critical for its use in the space environment. Such testing is expected for THESEUS, and the results from the THESEUS investigations could be re-analysed in future work with AXIS in mind.

8 CIS221-X dark signal temperature optimisation

The strength of the recommendation for the CIS221-X at the end of the trade-off study was not based solely on its meeting the quantitative performance requirements. Consideration of the CIS architecture was also driven by the potential for increased operation temperatures, reducing the size, mass, and complexity of the instrument. The high readout rate of the CIS221-X could allow the X-ray detector operating temperature for AXIS to be raised above the baseline design temperature of -60^{o} C (213^{o}K). The baseline temperature has been determined by the requirement to supress dark current, however the increased framerates possible with the CIS221-X reduce the impact of the dark signal. The readout rate improvement, as previously covered, is a result of the CIS architecture that permits row-wise parallel readout, as opposed to the baseline EMCCD readout which must be performed serially at one output. This chapter covers the investigation into the performance of CIS221-X at higher operating temperatures and the impact for AXIS.

The trade-off study investigated the effect of noise on X-ray energy resolution (6.2.1.3), and event detection probability at the lowest energies required (6.2.1.2). There is a third factor to consider, the rate of false positive X-rays due to noise. As X-ray detector temperature increases, per-pixel noise is generally observed to increase due to an increase in dark current shot noise. Therefore, there is a maximum operation temperature at which the additional shot noise results in the X-ray detector producing enough false positive X-ray detections to obscure science signals.

This results in three mechanisms for a limit on the acceptable dark current:

1. Energy resolution
2. False negatives, or event detectability
3. False positives, or false X-ray events

These factors have been considered during the development of other X-ray instruments, for instance the THESEUS SXI (McHugh et al. 2020).

The proposed operating temperature of the CIS221-X for AXIS has been calculated by first predicting the effect of dark current on the three performance limits, and then comparing the derived dark current limit to the observed dark current for temperature behaviour of the CIS221-X during

experimental testing. The investigation began with a characterisation of the dark current in the CIS221-X.

8.1 Dark current measurements in the CIS221-X

Dark current was measured in an OBF BSI CIS221-X (SN: 21094-07-23) in a temperature range between -30 °C to +20 °C at 2 °C intervals. This was done by building stacks of images at integration times from 0 ms to 2 s, and then using a least-squares fit to determine the gradient of average pixel signal against integration time.

As is common, the dark current is not uniform across the X-ray detector. Shown in Figure 8.1, a log-normal fit describes the distribution of dark current values well. The pixels occupying the log normal tail displayed consistently high dark current at all other temperatures.

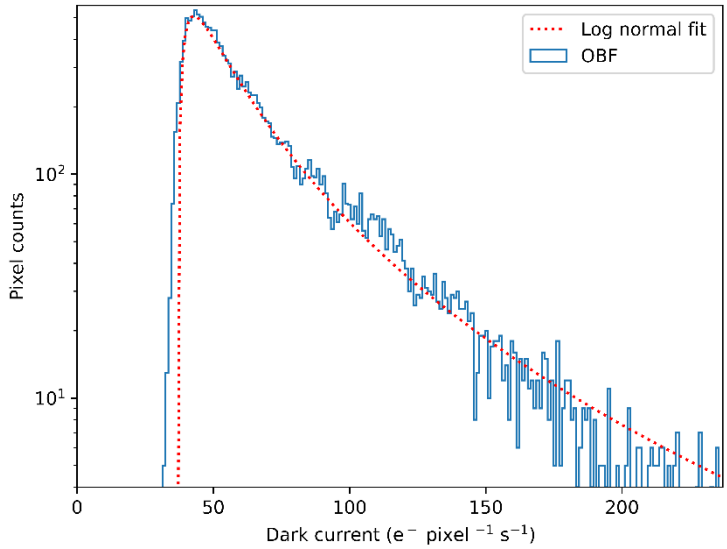

Figure 8.1. Per-pixel dark current histogram at – 40 °C showing log normal fit to distribution of dark current values (in the OBF covered half of the detector).

The mean of the pixel distribution was used as a figure of merit for the dark current. The dark current dropped to only a few tens of electrons at around -10° C. The dark current was fitted to a dual slope in log space, described by equation (8.1), equivalent to an exponential fit.

$$e_{dc}^{-} = 10^{a_1 t + b_1} + 10^{a_2 t + b_2} \tag{8.1}$$

Where:

$$a_1 = 0.022 \pm 0.000$$
$$b_1 = 2.55 \pm 0.01$$
$$a_2 = 0.072 \pm 0.002$$

$$b_2 = 2.19 \pm 0.03$$

And t is the CIS temperature in Celsius.

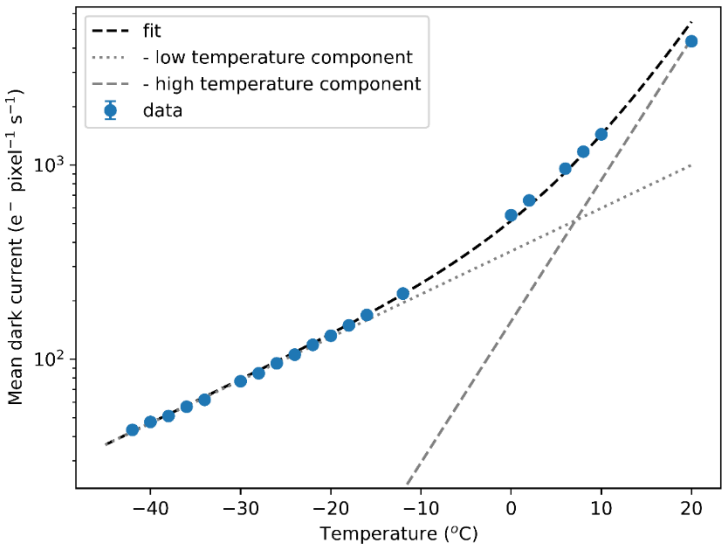

Figure 8.2. Measured and model fitted dark current for temperature in the CIS221-X 40 µm variant 3 pixels.

This initial characterisation provided a fit for the for dark current at an arbitrary temperature within the tested range, and the identification of a stable population of hot pixels.

Ongoing work characterising the CIS221-X has identified that the mean activation energy of the dark current is 0.3 eV, half of the expected 0.6 eV for depletion dark current. Furthermore, testing of the CIS221-X for the THESEUS SXI has identified that the dark current per unit pixel area of the 10 µm pixels is approximately 80 % higher, per unit surface area, than in the 40 µm pixels. Further investigation is ongoing to understand the cause of the high dark current.

8.2 Initial prediction

An initial prediction of acceptable operating temperature was made based on measured CIS221-X performance values and the three limiting factors.

8.2.1 Energy resolution

Energy resolution has been modelled with equation (5.2), based on the noise budget model of section 3.5.8, which can be rewritten to provide the number of dark signal electrons required to achieve a set FWHM, equation (8.3).

$$FWHM = 2.355 \times 3.65 \times \left(\frac{0.115\, E_{photon}}{3.65} + e_{dc}^{-} + {e_{ro,rms}^{-}}^{2} \right)^{0.5} \tag{8.2}$$

$$e_{dc}^{-} = \left(\frac{FWHM}{2.355 \times 3.65} \right)^{2} - \left(\frac{0.115\, E_{photon}}{3.65} + {e_{ro,rms}^{-}}^{2} \right) \tag{8.3}$$

Using the $e_{ro,rms}^{-}$ of the CIS221-X (3.2 e^-), and the spectral resolution requirement (100 eV at 500 eV) the maximum permissible dark signal per pixel is 107.3 e^- $pixel^{-1}frame^{-1}$. To convert this into an acceptable dark current for seconds this figure is multiplied by the device framerate, in Hz. For example, operating at a 20 Hz framerate this indicates that the acceptable dark current is 2190 $e^-pixel^{-1}s^{-1}$.

8.2.2 False negatives

The population of false negative events, X-rays erroneously classified as non-events, is expected to be dominated by events with charge loss, however there is also the potential for gaussian noise sources to reduce the recorded value of an incident pixel below detection thresholds.

The event detection rate was modelled with equation (8.4), derived from equation (6.2) of the trade-off study.

$$\sigma_{pix} = \frac{\gamma_{\mathrm{thresh}} - \gamma_{\mathrm{pix}}}{\mathrm{erf}^{-1}(1 - 2\mathrm{P}_{\mathrm{detect}})\sqrt{2}} \tag{8.4}$$

And:

$${\sigma_{pix}}^{2} = \frac{0.115\, E_{photon}}{3.65} + e_{dc}^{-} + \left(e_{ro,rms}^{-}\right)^{2} \tag{8.5}$$

For AXIS the value of γ_{thresh} is likely to be 150 eV. The greatest probability of an X-ray falling below the detection threshold will occur at the lowest X-ray energy of 300 eV. The maximum acceptable dark signal for a given probability of an X-ray being ignored is illustrated in Figure 8.3.

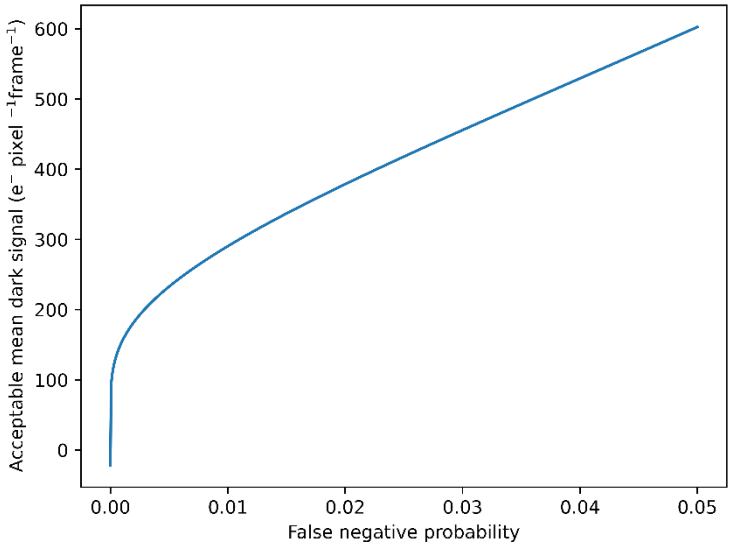

Figure 8.3. Acceptable dark signal for desired false negative probability from equations (8.4) and (8.5).

If a 99% detection rate is required, this results in a maximum e_{dc}^{-} of 292 e^{-} pixel^{-1} frame^{-1}. When operating at a 20 Hz framerate the acceptable dark current is then 5840 e^{-}pixel $^{-1}s^{-1}$.

However, the number of events expected to be excluded because their signal is too low due to loss of charge at the back surface is far higher. Using the charge loss model of section 7.1.3 the probability of a 300 eV event being recorded as a false negative is shown in Figure 8.4. This shows that at least 13 % of X-rays would be excluded as false negatives once split pixel events are accounted for.

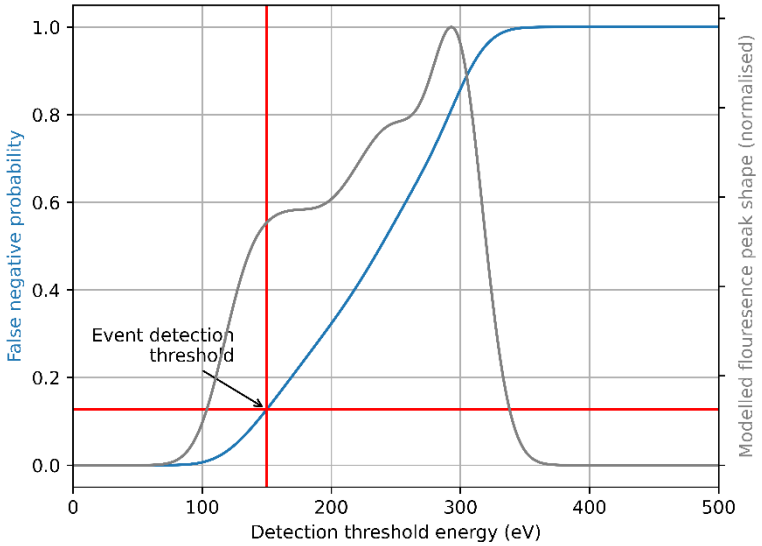

Figure 8.4. False negative probability for event detection threshold predicted with the back surface charge loss model of chapter 7.

The back surface charge loss model used in Figure 8.4 was derived using from a CIS221-X operating at 20 Hz framerate at -40 °C. At that framerate and temperature, the dark-current driven false negative rate is expected to be negligible. Furthermore, back surface charge loss is largely temperature invariant. Therefore, the false negative rate from dark current in not expected to be the dominant mechanism for the loss of X-ray events.

8.2.3 False positives

A false positive X-ray will be the result of noise in a pixel measurement. Therefore, the expected rate of false positive events has been calculated by integrating the probability distribution function of the noise in all pixels between the minimum and maximum pixel signals considered by the event detection algorithm. In the case of AXIS, this will be for pixels with signals corresponding to 150 eV's worth of charge (to account for split event detection) up to 2000 eV's worth of charge. As previously discussed, the dark current distribution per-pixel is non-uniform and has a large tail. The objective of optimising the temperature for the rate of false positive events is not to eliminate them, but rather to control them at a level that does not affect the science return.

The acceptable probability of a false detection depends on the framerate, the number of pixels per frame, and the number of false detections permitted compared to the expected count rate. The acceptable false count rate is:

$$R_{acc.false} = R_{X-ray} \cdot \eta_{false\ yield} \tag{8.6}$$

Where $R_{acc.false}$ is the acceptable false count rate in counts s^{-1},R_{X-ray} is the expected X-ray count rate (8 counts s^{-1} for AXIS), $\eta_{falseyield}$ is the proportion of all events that are permitted to be false positives. For the following analysis $\eta_{falseyield}$ has been set to 1 %. The false detection rate can also be defined in terms of a per-pixel false detection probability:

$$R_{false} = P_{falsedetection} \cdot n_{pix} \cdot f_{framerate} \tag{8.7}$$

Where n_{pix} is the number of pixels per frame, $f_{framerate}$ is the framerate in Hz, and $P_{falsedetection}$ is the false X-ray probability in counts $pixel^{-1}$ $frame^{-1}$. The permissible false count rate, assuming pixel uniformity, is therefore:

$$P_{falsedetection,acc} = \frac{R_{false}}{n_{pix} \cdot f_{framerate}} \tag{8.8}$$

For the anticipated 512 x 512 pixel CIS221-X derived X-ray detector, and framerates between 5 Hz and 20 Hz the probability of a false positive detection, per pixel, varies between 6.1 x 10^{-8} and 1.5 x 10^{-8}. Assuming that the noise of each pixel is roughly gaussian, the mean false detection rate should be lower than the acceptable rate or:

$$P_{falsedetection,acc} > \frac{1}{n_{pix}} \sum_{i=0}^{n_{pix}} P_{falsedetection,i} \tag{8.9}$$

That is, the average value of per pixel noise (of all pixels) should be such that the average pixel only has a probability of being falsely identified $P_{falsedectection,acc}$ amount of the time. Therefore, using equation (8.11)

$$\sigma_{acc,avg} = \frac{\gamma_{thresh}}{erf^{-1}(1-2P_{falsedetection,acc}) \cdot \sqrt{2}} \tag{8.10}$$

The acceptable mean pixel noise for acceptable false count rate, for a 150 eV detection threshold, calculated using (8.10) is shown in Figure 8.5.

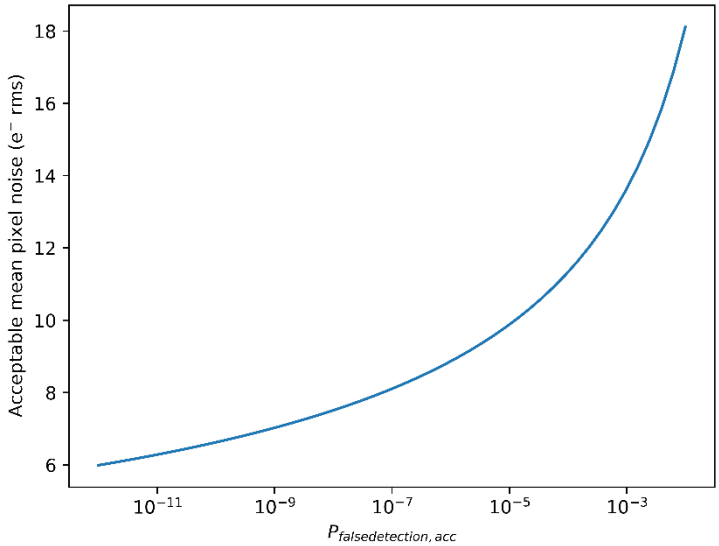

Figure 8.5. Acceptable mean per-pixel noise for acceptable false count rate.

This can be used to determine the acceptable dark signal, assuming uniform readout noise:

$$e^{-}_{dc,acc} = \left(\sigma^2{}_{\mathrm{acc},avg} - \sigma^2_{readout} \right) \tag{8.11}$$

Assuming a readout noise of 3.5 e^-, and γ_{thresh} of 150 eV, 840 e^- s^{-1} $pixel^{-1}$ dark current would be acceptable at 20 Hz.

8.2.4 Recommended operation temperature

Using the calculated maximum permissible dark currents and the measured temperature dependence of dark current of the CIS221-X it was possible to derive the maximum X-ray detector operating temperature. The first step was to calculate which of the three (temperature dependent) performance limiting factors imposes a maximum acceptable dark current. In the case of the unirradiated CIS221-X this was the rate of false positives (Figure 8.6).

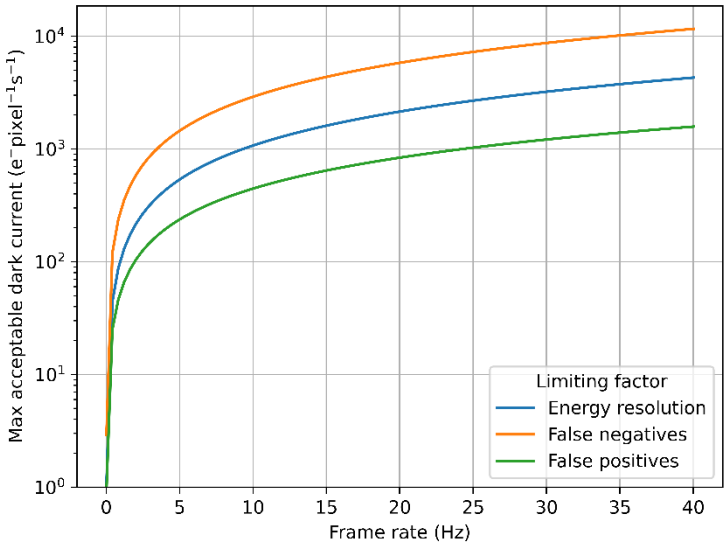

Figure 8.6. Maximum acceptable dark current according to three performance criteria.

The maximum acceptable dark current could then be compared to the dark current model derived from experimental measurements to work out the maximum operating temperature at a given frame rate, shown in Figure 8.7. The model indicated a framerate of 20 Hz would permit an operating temperature of 7.3° C ± 0.6 ° C.

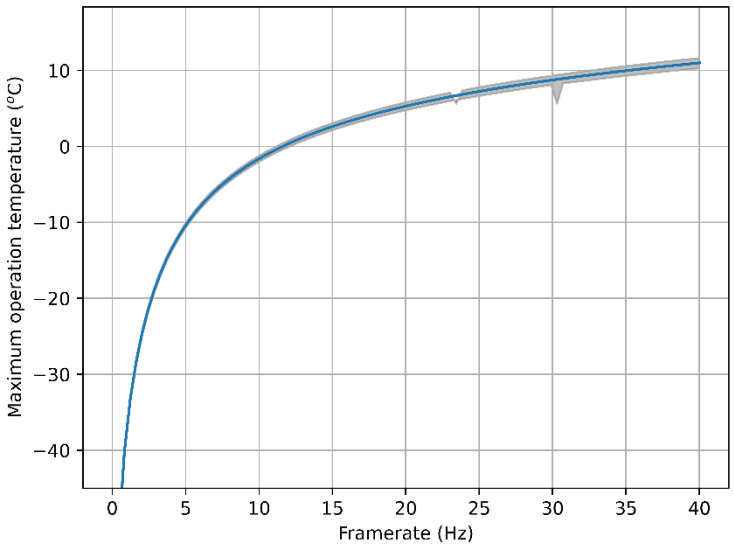

Figure 8.7. Maximum operating temperature of AXIS for frame rate of the CIS221-X.

8.3 Experimental demonstration

The BSI CIS221-X characterised in section 8.1 was used to measure the performance of the CIS221-X at higher operating temperatures. There were two aims for these trials: the first was demonstration

of false-positive behaviour, as the expected limiting factor for AXIS; the second was demonstration of X-ray measurements at higher operating temperature.

8.3.1 High temperature fluorescence tests

Measurement of energy resolution as a function of temperature was completed a SiO_2 fluorescence target. The spectra measured at different temperatures are shown in Figure 8.8. In addition to the broadening Si Kα peak, the effect of increasing noise leading to increased background X-ray counts can be seen: the small O Kα peak is obscured at and above 0 °C. At temperatures much greater than 0 °C the Al Kα and Si Kα fluorescence peaks merge and make FWHM measurements complex. The FWHM measured at different temperatures has been shown in Figure 8.9.

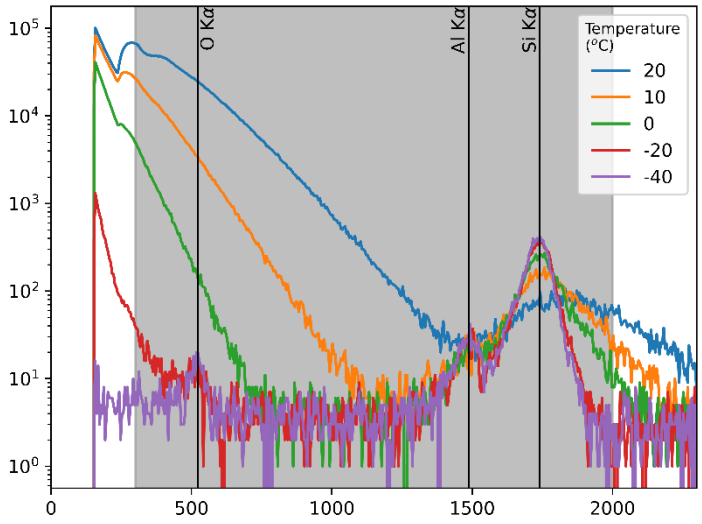

Figure 8.8. Comparison of SiO fluorescence spectrum measured at a range of operation temperatures. While the silicon Kα peak remains well defined well above 0 °C, the background spectrum of false positive X-rays obscures the faint oxygen Kα peak at higher temperatures.

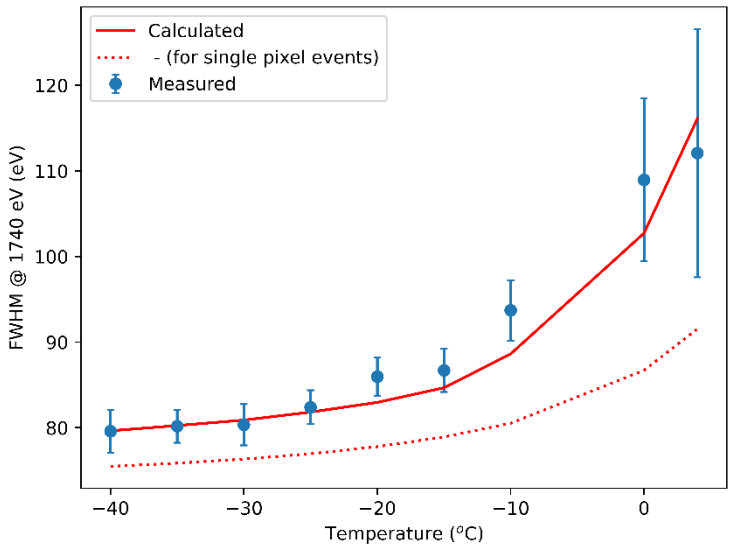

Figure 8.9. Si Kα fluorescence peak FWHM measurement for temperature.

The temperature dependence of the energy resolution can be correctly predicted using the expected Fano noise (at 1740 eV), shot noise of the dark signal (of section 8.1), known readout noise (4.55 e^- rms in CIS221-X SN: 21094-07-23), and accounting for the mean number of pixels included in each event (also shown in Figure 8.9) .

This does not match the initial energy resolution behaviour prediction, which was based on a single pixel's worth of dark current per event. This means the measured energy resolution, when using the AXIS recommended event reconstruction method at the time of writing is worse (has a larger value) than might be implied by the initial modelling. However, by accounting for the energy dependant noise (Fano noise and 1 % PRNU) using the FWHM model of J Heymes et al. (2022) and verified in section 7.1.5 of the previous chapter these Si Kα measurements can be used to predict the FWHM at 500 eV, shown in Figure 8.10. This indicates that the energy resolution of the CIS221-X only becomes an issue above 0 °C.

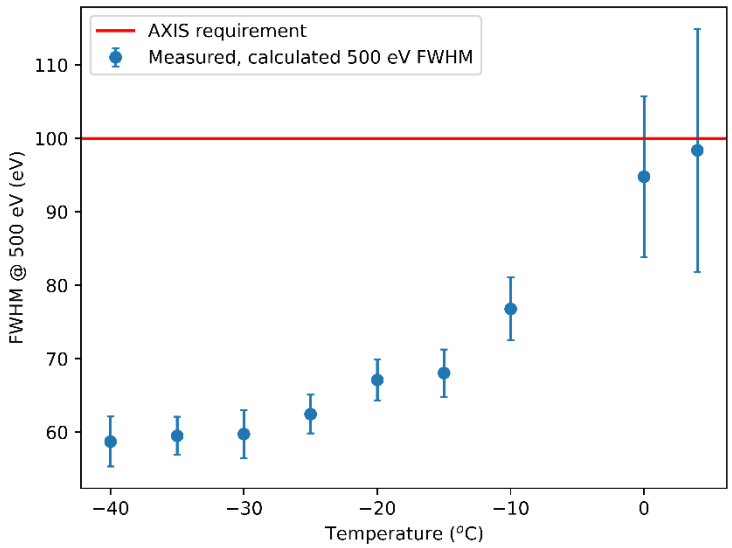

Figure 8.10. 500 eV FWHM implied by Si Kα FWHM of Figure 8.9.

8.3.2 False positive measurement

Measurement of the false positive X-ray rate reused data collected for measuring dark current. The X-ray event detection pipeline was run on each of the dark frame stacks of around 200 images. The results of this test were expected to match the predicted false positive rate obtained by rearranging the terms in equation (8.10) and multiplying by the number of pixels in the experiment's region of interest, plotted in Figure 8.11.

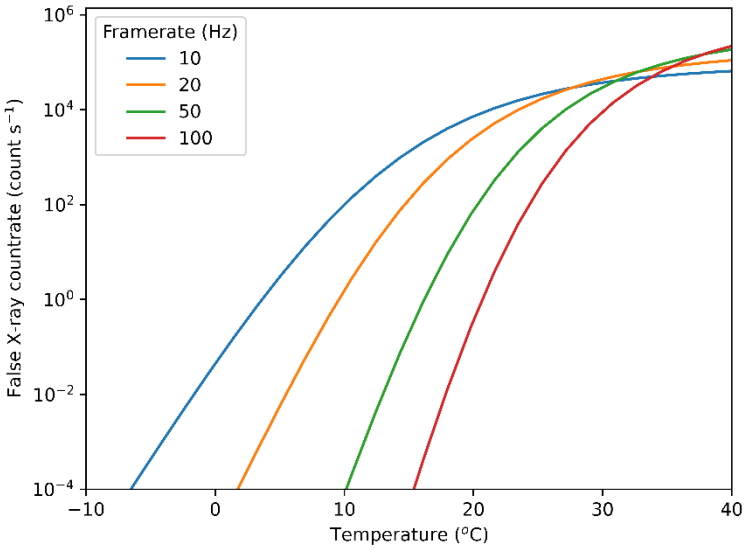

Figure 8.11. Expected false X-ray count rate for temperature at a variety of reported framerates.

Figure 8.12 shows the false positive count rate against temperature at four framerates. The inversion in the relationship between count rate and framerate (so that lower framerates are more optimal) observed in the model was seen in the experimental data. Measured values were significantly higher than expected.

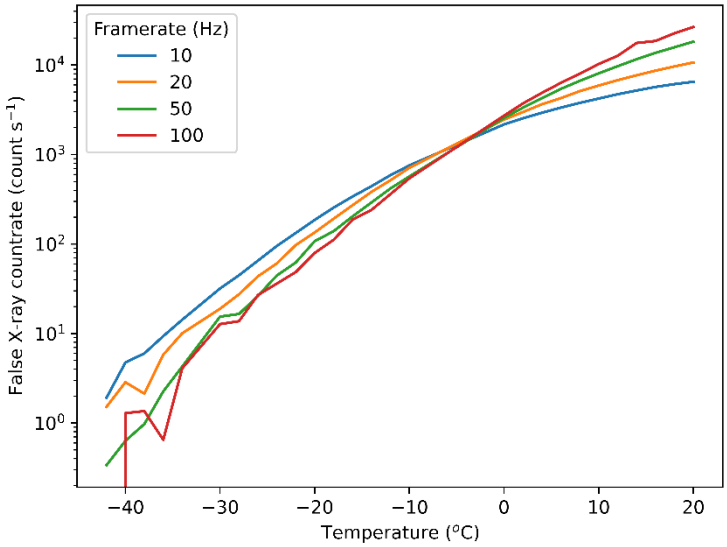

Figure 8.12. False X-ray count rate for temperature at a variety of reported framerates. Accuracy of framerate measurement > 50 Hz is low. Similarity between framerates indicates that pixels with a consistently higher chance of being identified are at cause of high false positive X-rays.

Analysis of the false X-ray counts revealed that most were the result a small number of high noise pixels, as expected from the hot pixel tail. Filtering the events to remove detections in these pixels improved performance, shown in Figure 8.13. Excluding false positive events from identified hot pixels was highly effective, at colder temperatures.

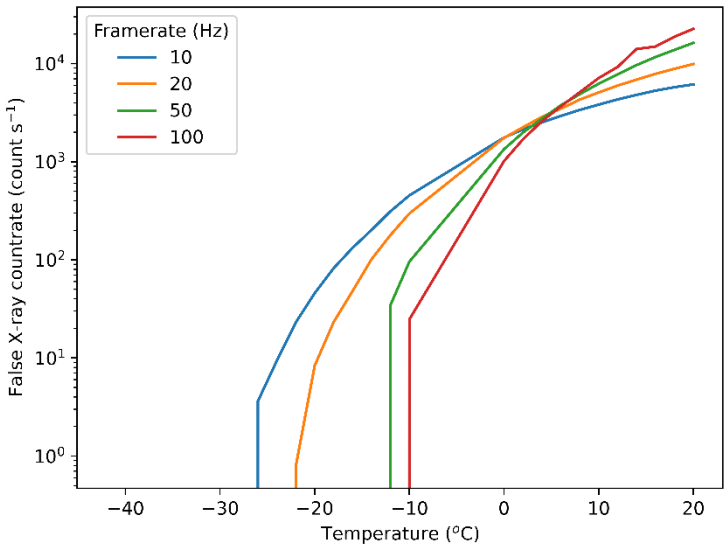

Figure 8.13. False count rate for temperature after removal of noisiest pixels. CIS221-X reaches acceptable false X-ray count rates at approximately -20 °C.

To match the specification for the THESEUS SXI the number of rejected pixels was capped at 1% of all pixels (Heymes, Stefanov, et al., 2020). At low temperatures, the total number of pixels to be excluded was less than 1 % of all pixels, at higher temperatures, the number of pixels that could be excluded increased, until greater than 1 % of pixels could be excluded, in which case only the worst pixels were. There is a good correlation between the number of excludable pixels increasing to more than 1 % of all pixels and an increase in the number of false X-rays identified (illustrated in Figure 8.14). It is possible that increasing the maximum number of rejected pixels could improve the quality of science data, however there is an impact of masking out too many hot pixels, both in terms of loss of overall sensitivity and loss of critical portions of the field of view. With the 1 % limit on pixel exclusion operation at 20 Hz achieved low enough false positive count rates at -22 °C. This is still a much lower temperature than the expected 7 °C.

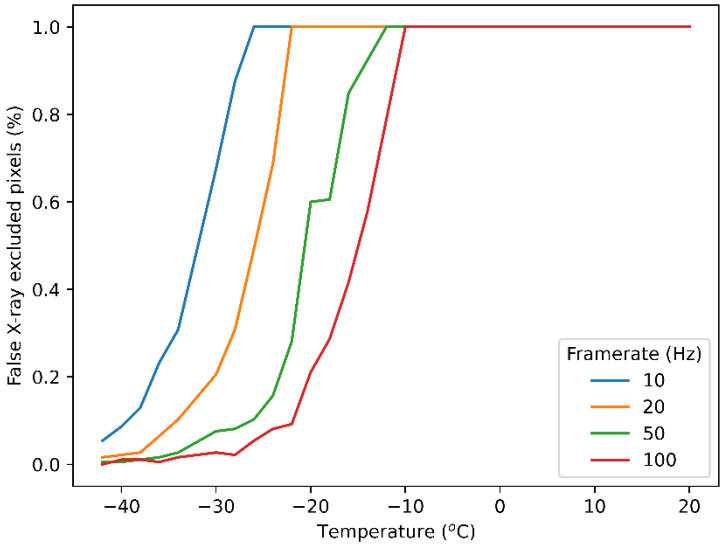

Figure 8.14. Excluded pixel count for temperature. Exclusion limited to 1% of all pixels.

The continued discrepancy between the expected behaviour and observed behaviour is thought to be due to pixels affected by RTS. As described in section 3.5.5 RTS noise results in meta-stable pixels experiencing larger changes in output value at a sub-framerate frequency, which could be generating bursts of false positive X-ray events.

8.4 Conclusions

The maximum operating for the CIS221-X to achieve adequate performance, unirradiated, for AXIS derived in this study was -22 °C, driven by the false positive X-ray count rate. The operating temperature dependant performance is derived from experimental results which showed a large population of very noisy pixels. Increased understanding of this population could be a key to bringing predictions in line with the experimental results or processing data to suppressthese pixels and achieve lower false positive count rates.

Testing of this performance after irradiation is required, to determine the required operating temperature after an expected lifetime dose. Radiation induced dark current and hot pixels are expected to lower the required operating temperature. Initial modelling using the methods of Crews et. al. (2019) to estimate the effect of radiation damage is ongoing.

Ultimately, it is highly likely that the CIS221-X, because of the high framerates achievable, could be operated warmer than the baseline -60 °C. This is a useful finding for AXIS and provides further

evidence to support a design change from the CCD201-20 baseline, to the CIS221-X. This claim requires further testing of irradiated devices.

9 Conclusions

9.1 Summary of results

The work of this thesis has had two major foci: the CLASS SCD X-ray spectrometer, and the AXIS Earth observation X-ray imaging spectrometer. Both instruments make use of new, innovative, technology to push their science capabilities. As an instrument under development, the CIS technology being considered for AXIS is at the leading edge of X-ray detection technology, while analysis of CLASS results provided confirmation of the performance of SCD detectors based on more mature CCD technology.

Chapter 5 addressed work completed at the request of the CLASS instrument operators. The change in X-ray spectroscopy performance was compared to expectations based on testing conducted for CLASS, and an estimation of the radiation dose received by the detectors. The change in energy resolution observed in calibration data was consistent with an 8.5 e^- rms increase in device noise. Dark current was estimated to have increased by 2×10^5 e^- s^{-1}. Both measurements matched expectations. This increased confidence in the continuing science operation of the instrument.

Chapter 6 summarised the methods, findings, and conclusions of the X-ray detector trade-off study for the AXIS instrument of DISHA-H. This sought to provide quantitative comparisons of different X-ray detector architectures, the outcome of which was the recommendation of a lower TRL CIS, over a more mature EMCCD. The primary advantages of the CIS were seen to be increased energy resolution (from 110 eV FWHM to 56 eV at 500 eV) the increase in X-ray flux that would be possible with the increased CIS sensitive area (from 8 count/s to 19 count/s). Initial practical trials of the X-ray detectors did not identify any behaviours of particular concern.

Chapter 7 sought to provide greater detail on soft X-ray behaviour, energy resolution and back surface charge loss, factors identified as critical during the trade-off conclusion. This made use of data collected at the BESSY-II soft X-ray beamline. Findings included: a verification of energy resolution across the AXIS energy range (including a measurement of 54 eV at 500 eV); a characterisation of back surface charge losses (in a region adjacent to the CIS illuminated surface to a depth of 155 nm) and the generation of a predictive model for further work; and observation of event reconstruction uncertainty across a wide range of energies, with properties matching expectations (optimum

reconstruction threshold was seen to be 86 eV, as opposed to 54 eV predicted by the reconstruction model analogue).

Chapter 8 sought to begin the process of answering one of the larger unanswered questions at the end of the trade-off study, by making an initial quantitative prediction of the maximum permissible operation temperature for the CIS221-X (theoretical 7 ^{o}C, experimental -22 ^{o}C). This was identified to be largely a function of the rate at which device noise generated false-positive X-ray detections, which resulted in behaviour defying explanation via mean dark current. The rate at which false positive X-rays were generated was higher than could have been expected from the initially measured dark current. Further investigations into the noise mechanisms and pixels displaying excess dark current and RTS noise was strongly recommended to provide a better understanding of the experimental conclusions.

9.2 Recommendations for AXIS

The benefits of a CIS X-ray detector for AXIS were found to be extensive. Even an experimental device, the CIS221-X, has shown good performance characteristics for a detector of this architecture. Performing well during the initial comparative study, the CIS221-X has continued to demonstrate certain favourable performance characteristics, including energy resolution, X-ray charge collection, and high temperature operation.

Therefore, from the results of this work it is recommended that AXIS should adopt a CIS-based X-ray detector over the baseline EMCCD. This will permit science goals to be achieved with a warmer and therefore lighter, less power hungry, and less complex instrument. Whether this detector is the CIS221-X itself, or a CIS221-X derived X-ray detector is an open question that will be determined largely by the expected timelines of mission development and X-ray detector availability.

9.3 Recommended future work

Recommended future work can be split by instrument, with recommendations relating to CLASS involving further monitoring of radiation damage, and recommendations for AXIS suggesting investigations into improvements or anomalous behaviour.

9.3.1 CLASS

The datasets analysed during the investigation of CLASS indicated little damage had been experienced. However, the period since the final dataset used has seen an increase in solar activity and an increase in the dose expected to have been experienced by the SCDs. Analysis of more recent data with prominent X-ray peaks fluoresced from the lunar surface may permit the identification of any new

radiation damage with a higher degree of certainty than the collimator fluorescence has permitted. Furthermore, continued monitoring of performance to the end of the mission may permit the behaviour of the SCDs at a range of radiation doses to be determined, allowing for the confirmation of expected performance trends identified during pre-flight work.

9.3.2 AXIS

For AXIS, experimental testing of CIS221-Xs at EOL doses is a priority for AXIS, and other CIS221-X applications. This should be targeted at both determining how standard performance parameters change (mean dark current, image lag, readout noise, energy resolution, QE) and the additional sources of uncertainty encountered during exploration of high temperature operation.

Additionally, analysis of monochromatic X-ray data indicated that there is a performance penalty associated with the current method of back surface passivation. This is due to 155 nm thick layer at the back of the X-ray detector in which incomplete charge collection has been inferred to occur. It may be necessary to adopt design solutions commonly used for UV detectors, though compatibility with X-ray science goals and detector design would need consideration and investigation.

Operating the CIS221-X at higher temperatures has indicated that operation at -22 ^{o}C results in adequate performance for the purposes of AXIS. However, noise behaviour exhibited has proven challenging to explain or characterise within the timeframe of the current work. Further investigation could reveal mitigation strategies for the false positive count rate to permit further improvements or identify ways to reduce the anomalous dark current exhibited.

The AXIS study has investigated a single use of the technology developed in the CIS221-X. A high temperature, high framerate, high energy resolution X-ray detector could be used in many other fields and applications. Early work has begun investigating the use of the technology in X-ray interferometry for astronomy, X-ray diffraction for planetary rover instruments, and in a medical setting. There are clear motivations to continue to further push the performance, maturity, and reliability of this technology.

9.3.3 Test apparatus

Finally, expanding available test facilities to enable X-ray imaging tests will increase the range of behaviours that can be examined. This would also permit higher-level verification of X-ray detector performance in scenarios that are more instrument-representative.

Initial trials of a potential approach have been conducted, using simple pinholes punched into a copper sheet. These pinholes can be easily attached to the current X-ray detector mount with no extra

components. The tools available resulted in a minimum pinhole diameter of 700 µm, which is far larger than would be required for X-ray detector limited tests. Despite this, the pinholes were used with a CIS221-X to demonstrate imaging spectroscopy, correctly identifying copper, aluminium, and chromium fluorescence (Figure 9.1).

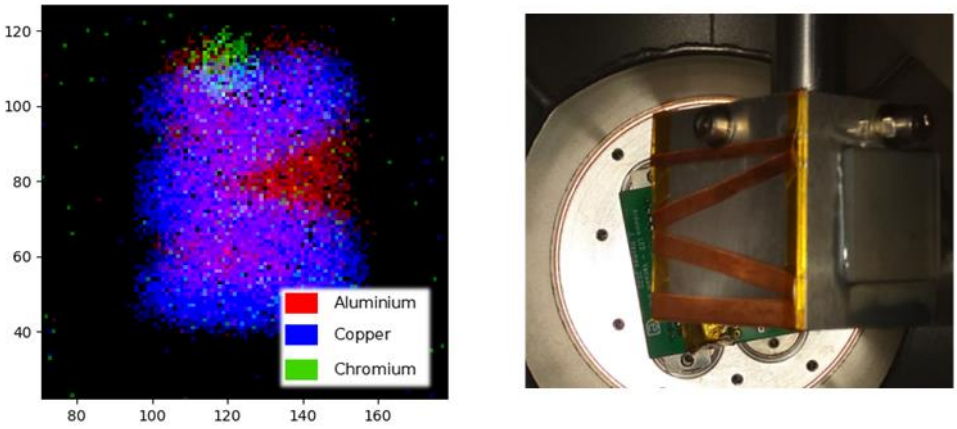

a) *b)*

Figure 9.1. a) 'M' target fluorescing X-rays, imaged by CIS221-X, where Al Kα X-rays have been mapped to the red colour channel, Cu Kα X-rays have been mapped to the blue colour channel, and Cr Kα X-rays have been mapped to the green colour channel. b) Photo of target taken with a handheld camera during chamber maintenance.

Further development of the apparatus could permit experiments testing of X-ray detector spatial resolution, to help train X-ray detection and rejection algorithms, and to produce data analogous to the expected science data for further evaluation.

9.4 COVID-19

The timeframe for this thesis project has, unfortunately, included a long period affected by the COVID-19 pandemic and associated social distancing measures. The author is supremely grateful that the impacts of the period can be relegated to a small section of the conclusion but wishes to provide some insight into the undeniable impact it has had on the overall body of work.

The primary impact, from the point of view of the experimental work required to characterise and explore the behaviours of the various X-ray detectors of the thesis, was the complete cessation of practical experimental activities for a period of 12 months. This was followed by a further 12 months of severe, but loosening, restrictions including a lack of access to experiment apparatus. This is reflected in the use of datasets not collected by the author, most dramatically from the CLASS

instrument, but also all EMCCD data including the experimental data for the trade-off study (collected at the direction, but not by the physical actions of, the author) and the archived CCD97 BESSY-II dataset.

The author will gladly concede that the effects felt both of COVID-19 and social distancing were comparatively light when compared to the experiences of others.

9.5 Conclusion

The implementation of imaging spectroscopy of soft X-rays is a scientific activity undergoing change with the introduction of new X-ray detectors. The lower in-flight resource requirements of CIS X-ray detectors able to achieve performance comparable with the current state-of-the-art CCD X-ray detectors, without the compromises required by earlier innovations like the SCD, are likely to open new opportunities for X-ray instruments.

In the latter half of the body of work of this thesis an investigation conducted for the AXIS Earth observation X-ray instrument has successfully demonstrated advantages of CIS X-ray detectors at their current state of development, and highlighted areas in which improvement would lead to increased scientific capability. This body of work and its conclusions has resulted in the adoption of CIS technology for AXIS, a major step in the technology's development.

References

Alig, R. C., Bloom, S., & Struck, C. W. (1980). Scattering by ionization and phonon emission in semiconductors. *Physical Review B*, *22*(12), 5565–5582.

Amati, L., O'Brien, P., Götz, D., Bozzo, E., Tenzer, C., Frontera, F., Ghirlanda, G., Labanti, C., Osborne, J. P., Stratta, G., Tanvir, N., Willingale, R., Attina, P., Campana, R., Castro-Tirado, A. J., Contini, C., Fuschino, F., Gomboc, A., Hudec, R., … Zicha, J. (2018). The THESEUS space mission concept: science case, design and expected performances. *Advances in Space Research*, *62*(1), 191–244.

Athiray, P. S., Narendranath, S., Sreekumar, P., & Grande, M. (2014). C1XS results — First measurement of enhanced sodium on the lunar surface. *Planetary and Space Science*, *104*, 279–287.

Athiray, P. S., Sreekumar, P., Narendranath, S., & Gow, J. P. D. (2015). Simulating charge transport to understand the spectral response of Swept Charge Devices. *Astronomy & Astrophysics*, *583*, A97.

Bailey, P., Cross, M., Pool, P. J., Castelli, C. M., Holland, A. D., Lumb, D. H., van Essen, P., Verhoeve, P., Jansen, F. A., & De Korte, P. A. J. (1990). Soft x-ray performance of back-illuminated EEV CCDs. *EUV, X-Ray, and Gamma-Ray Instrumentation for Astronomy*, *1344*(November 1990), 356.

Bhardwaj, A., Randall Gladstone, G., Elsner, R. F., Østgaard, N., Hunter Waite, J., Cravens, T. E., Chang, S. W., Majeed, T., & Metzger, A. E. (2007). First terrestrial soft X-ray auroral observation by the Chandra X-ray Observatory. *Journal of Atmospheric and Solar-Terrestrial Physics*, *69*(1–2), 179–187.

Bootsma, T. M. V., Van Zwet, E. J., Brinkman, A. C., Den Herder, J. W., De Jong, L., De Korte, P. A. J., & Olsthoorn, S. M. (2000). Synchrotron calibration and response modelling of back-illuminated XMM-RGS CCDs. *Nuclear Instruments and Methods in Physics Research, Section A: Accelerators, Spectrometers, Detectors and Associated Equipment*, *439*(2), 575–581.

References

Boyle, W. S., & Smith, G. E. (1970). Charge Coupled Semiconductor Devices. *Bell System Technical Journal*, *49*(4), 587–593.

Branduardi-Raymont, G. (2017). X-ray studies of solar system objects: Past, present, and the next decade. *Astronomische Nachrichten*, *338*(2–3), 188–194.

Buggey, T. W. (2021). *Effects Of The Space Environment On The Performance Of SMILE SXI CCDs*. PhD Thesis; The Open University.

Bush, N. (2017). *The Impact of Radiation Damage on Electron Multiplying CCD Technology for the WFirst Coronagraph*. PhD Thesis; The Open University.

Bush, N., Heymes, J., Hall, D. J., Holland, A. D., & Jordan, D. (2021). Measurement and optimization of clock-induced charge in electron multiplying charge-coupled devices. *Journal of Astronomical Telescopes, Instruments, and Systems*, *7*(01), 1–24.

Cevik, I., Huang, X., Yu, H., Yan, M., & Ay, S. (2015). An Ultra-Low Power CMOS Image Sensor with On-Chip Energy Harvesting and Power Management Capability. *Sensors*, *15*(3), 5531–5554.

Cheremukhin, G. S., Dmitriev, A. B., Mandelshtam, S. L., Sorokin, L. S., & Tindo, I. P. (1968). X-radiation of the moon and Roentgen cosmic background according to data of AMS Luna-12 (A. L. Brichant, Trans.). *Cosmic Research*, *6*(1), 119–127.

Crews, C., Soman, M.R., Lofthouse-Smith, D.D., Allanwood, E.A.H., Stefanov, K.D., Leese, M., Turner, P. and Holland, A.D. (2019). Predicting the effect of radiation damage on dark current in a space-qualified high performance CMOS image sensor. *Journal of Instrumentation*, *14*(11), C11008

Cropper, M. S., Pottinger, S., Azzollini, R., Szafraniec, M., Awan, S., Di Giorgio, A. M., Sciortino, A., Bozzo, E., Genolet, L., Philippon, A., Hailey, M., Hunt, T., Swindells, I., Holland, A. D., Gow, J. P. D., Murray, N. J., Hall, D. J., Skottfelt, J., Amiaux, J., … Castelli, M. (2018). VIS: the visible imager for Euclid. In H. A. MacEwen, M. Lystrup, G. G. Fazio, N. Batalha, E. C. Tong, & N. Siegler (Eds.), *Space Telescopes and Instrumentation 2018: Optical, Infrared, and Millimeter Wave* (p. 78). SPIE.

Davis, C. S. W. (2021). *The Simulation, Composition and Shielding of Radiation-Induced X-ray-like Background in Space-Based X-ray Astronomy Missions*. PhD Thesis; The Open University.

Dryer, B. J. (2013). *Characterisation of CMOS APS Technologies for Space Applications*. PhD Thesis; The Open University.

e2v Technologies. (2007). *CCD236-20 Datsheet* (Issue Draft A, PJP).

References

Eastwood, J. P., Hietala, H., Toth, G., Phan, T. D., & Fujimoto, M. (2015). What controls the structure and dynamics of Earth's magnetosphere?. *Space Science Reviews*, 188, 251-286.

Einstein, A. (1905). Über einen die Erzeugung und Verwandlung des Lichtes betreffenden heuristischen Gesichtspunkt. Translated by A. Arons and M. Peppard, American Journal of Physics, 33, 5, May 1965. (A. B. Arons & M. B. Peppard, Trans.). *Annalen Der Physik*, *322*(6), 132–148.

ESA. (2022). *Athena factsheet*. https://www.esa.int/Science_Exploration/Space_Science/Athena_factsheet

Fano, U. (1947). Ionization Yield of Radiations. II. The Fluctuations of the Number of Ions. *Physical Review*, *72*(1), 26–29.

Fossum, E. R. (1993). Active pixel sensors: are CCDs dinosaurs? In M. M. Blouke (Ed.), *Charge-Coupled Devices and Solid State Optical Sensors III* (Vol. 1900, pp. 2–14).

Fossum, E. R. (1997). CMOS Image Sensors : Electronic Camera-On-A-Chip. *IEEE Transactions on Electron Devices*, *44*(10), 1689–1698.

Ginet, G. P., O'Brien, T. P., Huston, S. L., Johnston, W. R., Guild, T. B., Friedel, R., Lindstrom, C. D., Roth, C. J., Whelan, P., Quinn, R. A., Madden, D., Morley, S., & Su, Y. J. (2013). AE9, AP9 and SPM: New models for specifying the trapped energetic particle and space plasma environment. *Space Science Reviews*, *179*(1–4), 579–615.

Gladstone, G. R., Waite, J. H., Grodent, D., Lewis, W. S., Crary, F. J., Elsner, R. F., Weisskopf, M. C., Majeed, T., Jahn, J.-M., Bhardwaj, A., Clarke, J. T., Young, D. T., Dougherty, M. K., Espinosa, S. A., & Cravens, T. E. (2002). A pulsating auroral X-ray hot spot on Jupiter. *Nature*, *415*(6875), 1000–1003.

Gow, J. P. D., Holland, A. D., & Pool, P. J. (2009). Proton radiation damage study of the next generation of swept charge devices. *UV, X-Ray, and Gamma-Ray Space Instrumentation for Astronomy XVI*, *7435*, 74350V.

Gow, J. P. D., Holland, A. D., Pool, P. J., & Smith, D. R. (2012). The effect of protons on the performance of second generation Swept Charge Devices. *Nuclear Instruments and Methods in Physics Research, Section A: Accelerators, Spectrometers, Detectors and Associated Equipment*, *680*, 86–89.

References

Gow, J. P. D., Smith, P. H., Pool, P. J., Hall, D. J., Holland, A. D., & Murray, N. J. (2015). Proton irradiation of a swept charge device at cryogenic temperature and the subsequent annealing. *Journal of Instrumentation*, *10*(1).

Grande, M., Browning, R., Waltham, N., Parker, D., Dunkin, S.K., Kent, B., Kellett, B., Perry, C.H., Swinyard, B., Perry, A. and Feraday, J., (2003). The D-CIXS X-ray mapping spectrometer on SMART-1. *Planetary and Space Science*, *51*(6), 427-433.

Grande, M., Kellett, B. J., Howe, C., Perry, C. H., Swinyard, B., Dunkin, S., & Huovelin, J. (2007). *The D-CIXS X-ray spectrometer on the SMART-1 mission to the Moon — First results*. *55*, 494–502.

Grande, M., Maddison, B.J., Howe, C.J., Kellett, B.J., Sreekumar, P., Huovelin, J., Crawford, I.A., Duston, C.L., Smith, D., Anand, M. and Bhandari, N., (2009). The C1XS X-ray spectrometer on Chandrayaan-1. *Planetary and Space Science*, *57*(7), 717-724.

Hall, D. J., Keelan, J., Davis, C. S. W., Hetherington, O., Leese, M., & Holland, A. D. (2018). *Predicting the particle-induced background for future x-ray astronomy missions: the importance of experimental validation for GEANT4 simulations*. 124.

Hall, D. J., Skottfelt, J., Soman, M. R., Bush, N., & Holland, A. D. (2017). Improving radiation hardness in space-based Charge-Coupled Devices through the narrowing of the charge transfer channel. *Journal of Instrumentation*, *12*(12).

Hall, R.N., (1952). Electron-Hole Recombination in Germanium. Phys. Rev. 87, 387–387.

Harding, L. K., Demers, R. T., Hoenk, M. E., Peddada, P., Nemati, B., Cherng, M., Michaels, D., Neat, L. S., Loc, A., Bush, N., Hall, D. J., Murray, N. J., Gow, J. P. D., Burgon, R., Holland, A. D., Reinheimer, A., Jorden, P. R., & Jordan, D. (2015). Technology advancement of the CCD201-20 EMCCD for the WFIRST coronagraph instrument: sensor characterization and radiation damage. *Journal of Astronomical Telescopes, Instruments, and Systems*, *2*(1), 011007.

Henke, B. L., Gullikson, E., & Davis, J. C. (1993). X-ray interaction: photoabsorbtion, scattering, transmission, and reflection at E=50-30000 eV, Z=1-92. *Atom. Data Nucl. Data*, *181*, 54.

Heymes, J., Ivory, J., Buggey, T. W., Hetherington, O., Soman, M. R., & Holland, A. D. (2022). Characterisation of a soft X-ray optimised CMOS Image Sensor. *Journal of Instrumentation*, *19*(05), P05003.

Heymes, J., Soman, M. R., Randall, G., Gottwald, A., Harris, A., Kelt, A., Moody, I., Meng, X., & Holland,

A. D. (2020). Comparison of Back-Thinned Detector Ultraviolet Quantum Efficiency for Two Commercially Available Passivation Treatments. *IEEE Transactions on Nuclear Science*, *67*(8), 1962–1967.

Heymes, J., Stefanov, K. D., Soman, M. R., Gorret, D., Hall, D. J., Minoglou, K., Morris, D., Pratlong, J., Prod'homme, T., Tsiolis, G., & Holland, A. D. (2020). Development of a photon-counting near-fano-limited x-ray CMOS image sensor for THESEUS' SXI. In A. D. Holland & J. Beletic (Eds.), *X-Ray, Optical, and Infrared Detectors for Astronomy IX* (Issue December 2020, p. 19). SPIE.

Heynderickx, D., Quaghebeur, B., & Evans, H. D. R. (2002). The ESA Space Environment Information System (SPENVIS). *IAF Abstracts, 34th COSPAR Scientific Assembly*, 475.

Hoenk, M. E., Grunthaner, P. J., Grunthaner, F. J., Terhune, R. W., Fattahi, M. M., & Tseng, H. (1992). Growth of a delta-doped silicon layer by molecular beam epitaxy on a charge-coupled device for reflection-limited ultraviolet quantum efficiency. *Applied Physics Letters*, *61*(9), 1084–1086.

Hoenk, M. E., Jewell, A. D., Kyne, G., Hennessy, J. J., Jones, T. J., Cheng, S. R., Nikzad, S., Morris, D., Lawrie, K., & Skottfelt, J. (2022). *2D-doped silicon detectors for UV/optical/NIR and x-ray astronomy*. *1219113*(August 2022), 38.

Holland, A. D. (2013). X-ray CCDs. In *Observing Photons in Space* (Issue Ccd, pp. 443–453). Springer New York.

Holland, A. D., & Pool, P. J. (2008). A new family of swept charge devices (SCDs) for x-ray spectroscopy applications. *High Energy, Optical, and Infrared Detectors for Astronomy III*, *7021*(July 2008), 702117.

Imhof, W. L., Spear, K. A., Hamilton, J. W., Higgins, B. R., Murphy, M. J., Pronko, J. G., Vondrak, R. R., McKenzie, D. L., Rice, C. J., Gorney, D. J., Roux, D. A., Williams, R. L., Stein, J. A., Bjordal, J., Stadsnes, J., Njoten, K., Rosenberg, T. J., Lutz, L., & Detrick, D. (1995). The Polar Ionospheric X-ray Imaging Experiment (PIXIE). *Space Science Reviews*, *71*(1–4), 385–408.

Ivory, J. (2021). *CMOS Sensors for Precision Astronomy.* PhD Thesis; The Open University.

Janesick, J. R. (2001). *Scientific charge-coupled devices*. SPIE press Bellingham.

Jerram, P., Pool, P. J., Bell, R., Burt, D. J., Bowring, S., Spencer, S., Hazelwood, M., Moody, I., Catlett, N., & Heyes, P. S. (2001). The LLCCD: low-light imaging without the need for an intensifier. *Sensors and Camera Systems for Scientific, Industrial, and Digital Photography Applications II*,

4306(May 2001), 178.

Johnson, J. B. (1928). Thermal Agitation of Electricity in Conductors. *Phys. Rev.*, *32*(1), 97–109.

Johnston, A. H. (1993). Mechanisms for single-particle latchup in CMOS structures. *RADECS 93. Second European Conference on Radiation and Its Effects on Components and Systems (Cat. No.93TH0616-3)*, 433–437.

Jones, L. S., Crews, C., Endicott, J., & Holland, A. D. (2022). Evaluation of the performance of the CCD236 swept charge devices in lunar orbit using in-flight data. *Journal of Instrumentation*, *17*(07), C07013.

Jones, L. S., Crews, C., Soman, M. R., Ivory, J., & Holland, A. D. (2022). Evaluation of sensors for the detection of energy resolved very soft x-ray fluorescence. In A. D. Holland & J. Beletic (Eds.), *X-Ray, Optical, and Infrared Detectors for Astronomy X* (Vol. 8848, Issue August, p. 43). SPIE.

Kotov, I. V., Hall, S., Gopinath, D., Barbour, A., Li, J., Gu, Y., Holland, K., Holland, A. D., Jarrige, I., Pelliciari, J., Soman, M. R., Wilkins, S., & Bisogni, V. (2021). Analysis of the EMCCD point-source response using x-rays. *Nuclear Instruments and Methods in Physics Research, Section A: Accelerators, Spectrometers, Detectors and Associated Equipment*, *985*, 1–10.

LaMarr, B. J., Prigozhin, G. Y., Miller, E. D., Thayer, C., Bautz, M. W., Foster, R. F., Grant, C. E., Malonis, A., Burke, B. E., Cooper, M., Donlon, K., & Leitz, C. (2022). Measurement and simulation of charge diffusion in a small-pixel charge-coupled device. *Journal of Astronomical Telescopes, Instruments, and Systems*, *8*(01), 1–19.

Lifshin, E. (Ed.). (1999). *X-ray Characterization of Materials*. Wiley.

Lofthouse-Smith, D.-D. (2021). *Characterising the CMOS Image Sensor for the JANUS Camera on ESA ' s JUICE Mission to Jupiter*. PhD Thesis; The Open University.

Lowe, B. G., Holland, A. D., Hutchinson, I., Burt, D. J., & Pool, P. J. (2001). The swept charge device, a novel CCD-based EDX detector: first results. *Nuclear Instruments and Methods in Physics Research Section A: Accelerators, Spectrometers, Detectors and Associated Equipment*, *458*(1–2), 568–579.

Luhmann, J. G. (1976). Aurora electron spectra in the atmosphere. *Journal of Atmospheric and Terrestrial Physics*, *38*, 605–610.

Luhmann, J. G., & Blake, J. B. (1977). Calculations of soft auroral bremsstrahlung and Kα line emission

at satellite altitude. *Journal of Atmospheric and Terrestrial Physics*, *39*(8), 913–919.

Luhmann, J. G., Rugge, H. R., Blake, J. B., & Christopher, L. A. (1979). Low latitude atmospheric X-rays observed by HEAO-1. *Geophysical Research Letters*, *6*(1), 25–28.

Lumb, D. H., Eggel, H., Laine, R., & Peacock, A. J. (1996). X-ray Multimirror Mission: an overview. In O. H. W. Siegmund & M. A. Gummin (Eds.), *EUV, X-Ray, and Gamma-Ray Instrumentation for Astronomy VII* (Vol. 2808, Issue October 1996, pp. 326–337).

Lumb, D. H., & Holland, A. D. (1988). Event recognition techniques in CCD X-ray detectors for astronomy. *Nuclear Instruments and Methods in Physics Research Section A: Accelerators, Spectrometers, Detectors and Associated Equipment*, *273*(2–3), 696–700.

Lumb, D. H., Jansen, F. A., & Schartel, N. (2012). X-ray Multi-mirror Mission (XMM-Newton) observatory. *Optical Engineering*, *51*(1), 011009.

Lumb, D. H., Warwick, R. S., Page, M., & De Luca, A. (2002). X-ray background measurements with XMM-Newton EPIC. *Astronomy & Astrophysics*, *389*(1), 93–105.

Mazziotta, M. N. (2008). Electron-hole pair creation energy and Fano factor temperature dependence in silicon. *Nuclear Instruments and Methods in Physics Research, Section A: Accelerators, Spectrometers, Detectors and Associated Equipment*, *584*(2–3), 436–439.

McHugh, M., Hutchinson, I., Lerman, H. N., O'Brien, P., Willingale, R., Feldman, C., Beardmore, A., Speight, R., Lodge, A., Drumm, P., Waltham, N., & Clapp, M. (2020). Development of an imaging system for the THESEUS SXI instrument. In J.-W. A. den Herder, K. Nakazawa, & S. Nikzad (Eds.), *Space Telescopes and Instrumentation 2020: Ultraviolet to Gamma Ray* (Issue December 2020, p. 284). SPIE.

Metzler, S. D., Bowsher, J. E., Smith, M. F., & Jaszczak, R. J. (2001). Analytic determination of pinhole collimator sensitivity with penetration. *IEEE Transactions on Medical Imaging*, *20*(8), 730–741.

Millan, R. M., von Steiger, R., Ariel, M., Bartalev, S., Borgeaud, M., Campagnola, S., Castillo-Rogez, J. C., Fléron, R., Gass, V., Gregorio, A., Klumpar, D. M., Lal, B., Macdonald, M., Park, J. U., Sambasiva Rao, V., Schilling, K., Stephens, G., Title, A. M., & Wu, J. (2019). Small satellites for space science. *Advances in Space Research*, *64*(8), 1466–1517.

Moody, I., Watkins, M., Bell, R., Soman, M. R., Keelan, J., & Holland, A. D. (2017). *CCD QE in the Soft X-ray Range*. 1–16.

Morrissey, P., Harding, L., Bush, N., Bottom, M., Nemati, B., Daniel, A., Jun, B., Martinez, L. M. S., Desai, N., Barry, D., Davis, R., Demers, R. T., Hall, D. J., Holland, A. D., Turner, P., & Shortt, B. (2023). Flight photon counting electron multiplying charge coupled device development for the Roman Space Telescope coronagraph instrument. *Journal of Astronomical Telescopes, Instruments, and Systems*, *9*(01), 1–25.

Moseley, H. G. J. (1913). XCIII. The high-frequency spectra of the elements. *The London, Edinburgh, and Dublin Philosophical Magazine and Journal of Science*, *26*(156), 1024–1034.

Murray, N. J. (2008). *Improvements to MOS CCD Technology for Future X-ray Astronomy Missions Improvements to MOS CCD Technology for Future X-ray Astronomy Missions*. PhD Thesis; The Open University.

Narendranath, S. (2019). *AXIS Baseline Design document*. Space Astronomy Group, ISRO.

Narendranath, S., Athiray, P. S., Sreekumar, P., Kellett, B. J., Alha, L., Howe, C. J., Joy, K. H., Grande, M., Huovelin, J., Crawford, I. A., Unnikrishnan, U., Lalita, S., Subramaniam, S., Weider, S. Z., Nittler, L. R., Gasnault, O., Rothery, D., Fernandes, V. A., Bhandari, N., … Wieczorek, M. A. (2011). Lunar X-ray fluorescence observations by the Chandrayaan-1 X-ray Spectrometer (C1XS): Results from the nearside southern highlands. *Icarus*, *214*(1), 53–66.

Narendranath, S., Pillai, N. S., & Sharan, V. (2019). *Class user manual*.

Narendranath, S., Pillai, N. S., Tadepalli, S. P., Sarantos, M., Vadodariya, K., Sarwade, A., V, R., & Tyagi, A. (2022). Sodium Distribution on the Moon. *The Astrophysical Journal Letters*, *937*(2), L23.

Narendranath, S., Pillai, N. S., Vadodariya, K., Dhingra, D., Bhatt, M., Thangjam, G., Radhakrishna, V., & Tyagi, A. (2021). New Insights from Chandrayaan-2 Large Area Soft X-Ray Spectrometer. *52nd Lunar and Planetary Science Conference*, 2230.

Narukage, N., Ishikawa, S., Sakao, T., & Wang, X. (2020). High-speed back-illuminated CMOS sensor for photon-counting-type imaging-spectroscopy in the soft X-ray range. *Nuclear Instruments and Methods in Physics Research Section A: Accelerators, Spectrometers, Detectors and Associated Equipment*, *950*(May 2019), 162974.

NASEM. (2016). *Achieving Science with CubeSats: Thinking Inside the Box*. The National Academies Press.

Nikzad, S., Hoenk, M. E., Grunthaner, P. J., Terhune, R. W., Grunthaner, F. J., Winzenread, R., Fattahi,

M. M., Tseng, H., & Lesser, M. P. (1994). Delta-doped CCDs: high QE with long-term stability at UV and visible wavelengths. In D. L. Crawford & E. R. Craine (Eds.), *Instrumentation in Astronomy VIII* (Vol. 2198, Issue June 1994, pp. 907–915).

Nyquist, H. (1928). Thermal Agitation of Electric Charge in Conductors. *Phys. Rev.*, *32*(1), 110–113.

Østgaard, N., Stadsnes, J., Bjordal, J., Germany, G. A., Vondrak, R. R., Parks, G. K., Cummer, S. A., Chenette, D. L., & Pronko, J. G. (2001). Auroral electron distributions derived from combined UV and X-ray emissions. *Journal of Geophysical Research: Space Physics*, *106*(A11), 26081–26089.

Owens, A., Mineo, T., McCarthy, K. J., & Wells, A. (1994). Event recognition in X-ray CCDs. *Nuclear Inst. and Methods in Physics Research, A*, *346*(1–2), 353–365.

Parsons, S., Hall, D. J., Holland, A. D., Verhoeve, P., Sembay, S., Randall, G., Hetherington, O., Yeoman, D., Buggey, T. W., & Soman, M. R. (2020). Radiation damage testing status of the CCDs for the SMILE SXI. In A. D. Holland & J. Beletic (Eds.), *X-Ray, Optical, and Infrared Detectors for Astronomy IX* (p. 27). SPIE.

Pavlov, G. G., & Nousek, J. A. (1999). Charge diffusion in CCD X-ray detectors. *Nuclear Instruments and Methods in Physics Research Section A: Accelerators, Spectrometers, Detectors and Associated Equipment*, *428*(2–3), 348–366.

Pigot, C., Sauvageot, J. L., Ferrando, P., & Belsole, E. (2000, December 13). Optimization of spectral performances of the XMM-EPIC MOS camera systems : event schemes tested on calibration data. *Proc. SPIE 4140, X-Ray and Gamma-Ray Instrumentation for Astronomy XI*.

Plucinsky, P. P., Bogdan, A., & Marshall, H. (2022). The evolution of the ACIS contamination layer on the Chandra X-ray Observatory through 2022. In J.-W. A. den Herder, K. Nakazawa, & S. Nikzad (Eds.), *Space Telescopes and Instrumentation 2022: Ultraviolet to Gamma Ray* (Issue August 2022, p. 160). SPIE.

Prigozhin, G. Y., Kissel, S. E., Bautz, M. W., Grant, C. E., LaMarr, B. J., Foster, R. F., & Ricker, Jr., G. R. (2000). Characterization of the radiation damage in the Chandra x-ray CCDs. In K. A. Flanagan & O. H. W. Siegmund (Eds.), *X-Ray and Gamma-Ray Instrumentation for Astronomy XI* (Vol. 4140, Issue December 2000, p. 123).

Raab, W., Branduardi-Raymont, G., Wang, C., Dai, L., Donovan, E., Enno, G., Escoubet, P., Holland, A. D., Jing, L., Kataria, D., Li, L., Read, A. M., Rebuffat, D., Romstedt, J., Runciman, C., Sembay, S., Spanswick, E., Sykes, J., Thornhill, J., … Zheng, J. (2016). SMILE: a joint ESA/CAS mission to

investigate the interaction between the solar wind and Earth's magnetosphere. In J.-W. A. den Herder, T. Takahashi, & M. Bautz (Eds.), *Space Telescopes and Instrumentation 2016: Ultraviolet to Gamma Ray* (Vol. 9905, p. 990502).

Radhakrishna, V., Tyagi, A., Narendranath, S., Vadodariya, K., Yadav, R., Singh, B., Balaji, G., Satya, N., Shetty, A., Kumar, H. N. S., Vaishali, S., Pillai, N. S., Tadepalli, S. P., Raghavendra, V., Sreekumar, P., Agarwal, A., & Valarmathi, N. (2020). Chandrayaan-2 Large Area Soft X-ray Spectrometer. *Current Science*, *118*(2), 219–225.

Randall, G., Parsons, S., Hall, D. J., Buggey, T. W., Hetherington, O., Leese, M., Holland, A. D., Yeoman, D., & Soman, M. R. (2020). Processing x-ray data on board the SMILE SXI. In A. D. Holland & J. Beletic (Eds.), *X-Ray, Optical, and Infrared Detectors for Astronomy IX* (Issue December, p. 30). SPIE.

Robbins, M. S., & Hadwen, B. J. (2003). The noise performance of electron multiplying charge-coupled devices. *IEEE Transactions on Electron Devices*, *50*(5), 1227–1232.

Rothschild, R., Boldt, E., Garmire, G., & Agrawal, P. (1978). *The Cosmic X-Ray Experiment Aboard HEAO-1*.

Rushton, J. E. (2018). *Radiation Damage in CMOS Image Sensors for Space Sensors for Space Applications*. PhD Thesis; The Open University.

Scholze, F., Tümmler, J., & Ulm, G. (2003). High-accuracy radiometry in the EUV range at the PTB soft x-ray beamline. *Metrologia*, *40*(1), S224–S228.

Schubert, G., & Soderlund, K. M. (2011). Planetary magnetic fields: Observations and models. *Physics of the Earth and Planetary Interiors*, 187(3-4), 92-108.

Sedra, A. S., & Smith, K. C. (1998). *Microelectronic Circuits* (4th ed.). Oxford University Press.

Selva, D., & Krejci, D. (2012). A survey and assessment of the capabilities of Cubesats for Earth observation. *Acta Astronautica*, *74*, 50–68.

Sexton, F. W., Fleetwood, D. M., Shaneyfelt, M. R., Dodd, P. E., & Hash, G. L. (1997). Single event gate rupture in thin gate oxides. *IEEE Transactions on Nuclear Science*, *44*(6), 2345–2352.

Shin, B., Park, S., & Shin, H. (2010). The effect of photodiode shape on charge transfer in CMOS image sensors. *Solid-State Electronics*, *54*(11), 1416–1420.

Shockley, W., Read, W.T., (1952). Statistics of the Recombinations of Holes and Electrons.

Phys. Rev. 87, 835–842.

Shokouhi, S., Metzler, S. D., Wilson, D. W., & Peterson, T. E. (2009). Multi-pinhole collimator design for small-object imaging with SiliSPECT: A high-resolution SPECT. *Physics in Medicine and Biology*, *54*(2), 207–225.

SILSO World Data Center. (n.d.). *The International Sunspot Number*. International Sunspot Number Monthly Bulletin and Online Catalogue. Retrieved February 21, 2021, from http://www.sidc.be/silso/

Smith, M. J. S. (2022). EPIC status of calibration and data analysis. In *XMM-Newton Calibration Technical Note: Vol. 3.13*.

Smith, P. H. (2014). *The CCD236 Swept Charge Device for the Chandrayaan-2 Lunar X-ray Spectrometer*. PhD Thesis; The Open University.

Smith, P. H., Gow, J. P. D., Murray, N. J., Holland, A. D., Anand, M., Pool, P. J., Sreekumar, P., & Narendranath, S. (2012). Performance of new generation swept charge devices for lunar x-ray spectroscopy on Chandrayaan-2. *High Energy, Optical, and Infrared Detectors for Astronomy V*, *8453*, 84530R.

Smith, P. H., Gow, J. P. D., Murray, N. J., Tutt, J. H., Soman, M. R., & Holland, A. D. (2014). Quantum efficiency measurements in the swept charge device CCD236. *Journal of Instrumentation*, *9*(4).

Smith, P. H., Gow, J. P. D., Pool, P. J., & Holland, A. D. (2015). Charge Transfer Inefficiency in the pre- and post-irradiated Swept Charge Device CCD236. *Journal of Instrumentation*, *10*(3).

Soman, M. R. (2014). *High-resolution detectors for soft X-ray spectroscopy*. PhD Thesis; The Open University.

Soman, M. R., Allanwood, E. A. H., Holland, A. D., Stefanov, K. D., Pratlong, J., Leese, M., Gow, J. P. D., & Smith, D. R. (2016). Electro-optic and radiation damage performance of the CIS115, an imaging sensor for the JANUS optical camera onboard JUICE. *High Energy, Optical, and Infrared Detectors for Astronomy VII*, *9915*, 991515.

Soman, M. R., Hall, D. J., Holland, A. D., Burgon, R., Buggey, T. W., Skottfelt, J., Sembay, S., Drumm, P., Thornhill, J., Read, A. M., Sykes, J., Walton, D., Branduardi-Raymont, G., Kennedy, T., Raab, W., Verhoeve, P., Agnolon, D., & Woffinden, C. (2018). The SMILE Soft X-ray Imager (SXI) CCD design and development. *Journal of Instrumentation*, *13*, C01022--C01022.

Soman, M. R., Hall, D. J., Tutt, J. H., Murray, N. J., Holland, A. D., Schmitt, T., Raabe, J., & Schmitt, B. (2013). Improving the spatial resolution of soft X-ray detection using an Electron-Multiplying Charge-Coupled Device. *Journal of Instrumentation*, *8*(01), C01046–C01046.

Srour, J. R., Marshall, C. J., & Marshall, P. W. (2003). Review of displacement damage effects in silicon devices. *IEEE Transactions on Nuclear Science*, *50*(3), 653–670.

Stadsnes, J., Aarsnes, K., & Bjordal, J. (1997). X-ray imaging of the aurora. *Advances in Space Research*, *20*(4–5), 1043–1054.

Stefanov, K. D. (2022). *CMOS Image Sensors*. IOP Publishing.

Stefanov, K. D., Clarke, A. S., Ivory, J., & Holland, A. D. (2018). Design and performance of a pinned photodiode cmos image sensor using reverse substrate bias. *Sensors (Switzerland)*, *18*(1).

Stefanov, K. D., Townsend-Rose, C., Buggey, T. W., Ivory, J., Hetherington, O., Holland, A. D., Heymes, J., Pratlong, J., Tsiolis, G., Morris, D., Minoglou, K., Prod'homme, T., & Soman, M. R. (2022). *A CMOS image sensor for soft x-ray astronomy*. *August*, 22.

Sze, S. M. (1985). *Semiconductor Devices: Physics and Technology*. Wiley.

Teledyne e2v. (2017). *CIS120 Datasheet* (No. 1).

Townsend-Rose, C., Buggey, T. W., Ivory, J., Stefanov, K. D., Jones, L. S., Hetherington, O., & Holland, A. D. (2023). Characterization, quantum efficiency, and radiation hardness of a CMOS image sensor optimized for soft x-ray astronomy. *SPIE Optical Engineering + Applications*, 12678–25.

Tutt, J. H., Holland, A. D., Hall, D. J., Harriss, R. D., & Murray, N. J. (2012). The noise performance of electron-multiplying charge-coupled devices at X-ray energies. *IEEE Transactions on Electron Devices*, *59*(1), 167–175.

von Kienlin, A., Eraerds, T., Bulbul, E., Fioretti, V., Gastaldello, F., Grant, C. E., Hall, D. J., Holland, A. D., Keelan, J., Meidinger, N., Molendi, S., Perinati, E., & Rau, A. (2018). Evaluation of the Athena/WFI instrumental background. In J.-W. A. den Herder, K. Nakazawa, & S. Nikzad (Eds.), *Space Telescopes and Instrumentation 2018: Ultraviolet to Gamma Ray* (Issue May, p. 53). SPIE.

Watkins, G. D. (2000). Intrinsic defects in silicon. *Materials Science in Semiconductor Processing*, *3*(4), 227–235.

Widenhorn, R., Blouke, M. M., Weber, A., Rest, A., & Bodegom, E. (2002). Temperature dependence of dark current in a CCD. In M. M. Blouke, J. Canosa, & N. Sampat (Eds.), *Sensors and Camera*

Systems for Scientific, Industrial, and Digital Photography Applications III (Vol. 4669, Issue April 2002, pp. 193–201).

Wilkins, D. R., Allen, S. W., Miller, E. D., Bautz, M. W., Chattopadhyay, T., Foster, R. F., Grant, C. E., Herrmann, S. C., Kraft, R. P., Morris, G., Nulsen, P., & Schellenberger, G. (2022). Reducing the background in x-ray imaging detectors via machine learning. In J.-W. A. den Herder, K. Nakazawa, & S. Nikzad (Eds.), *Space Telescopes and Instrumentation 2022: Ultraviolet to Gamma Ray* (p. 155). SPIE.

Wu, Q., Ling, Z., Wang, X., Zhang, C., Yuan, W., & Zhang, S.-N. (2023). Improving the X-Ray Energy Resolution of a Scientific CMOS Detector by Pixel-level Gain Correction. *Publications of the Astronomical Society of the Pacific*, *135*(1044), 025003.

Yao, Z., Dunn, W. R., Woodfield, E. E., Clark, G., Mauk, B. H., Ebert, R. W., Grodent, D., Bonfond, B., Pan, D., Rae, I. J., Ni, B., Guo, R., Branduardi-raymont, G., Wibisono, A. D., Rodriguez, P., Kotsiaros, S., Ness, J., Allegrini, F., Kurth, W. S., … Bolton, S. J. (2021). Revealing the source of Jupiter's x-ray auroral flares. *Science Advances*, *7*(28), 1–9.